THE UNIVERSITY *of* EDINBURGH

Computational techniques to interpret the neural code underlying complex cognitive processes

Rufus Mitchell-Heggs

Doctor of Philosophy

THE UNIVERSITY OF EDINBURGH

2023

"Enjoy when you can, and endure when you must." - To my darling girlfriend Holly, thank you for making each step a joy.

Abstract

Advances in large-scale neural recording technology have significantly improved the capacity to further elucidate the neural code underlying complex cognitive processes. This thesis aimed to investigate two research questions in rodent models. First, what is the role of the hippocampus in memory and specifically what is the underlying neural code that contributes to spatial memory and navigational decision-making. Second, how is social cognition represented in the medial prefrontal cortex at the level of individual neurons. To start, the thesis begins by investigating memory and social cognition in the context of healthy and diseased states that use non-invasive methods (i.e. fMRI and animal behavioural studies). The main body of the thesis then shifts to developing our fundamental understanding of the neural mechanisms underpinning these cognitive processes by applying computational techniques to analyse stable large-scale neural recordings. To achieve this, tailored calcium imaging and behaviour preprocessing computational pipelines were developed and optimised for use in social interaction and spatial navigation experimental analysis. In parallel, a review was conducted on methods for multivariate/neural population analysis. A comparison of multiple neural manifold learning (NML) algorithms identified that non-linear algorithms such as UMAP are more adaptable across datasets of varying noise and behavioural complexity. Furthermore, the review visualises how NML can be applied to disease states in the brain and introduces the secondary analyses that can be used to enhance or characterise a neural manifold. Lastly, the preprocessing and analytical pipelines were combined to investigate the neural mechanisms involved in social cognition and spatial memory. The social cognition study explored how neural firing in the medial Prefrontal cortex changed as a function of the social dominance paradigm, the "Tube Test". The univariate analysis identified an ensemble of behavioural-tuned neurons that fire preferentially during specific behaviours such as "pushing" or "retreating" for the animal's own behaviour and/or the competitor's behaviour. Furthermore, in dominant animals, the neural population exhibited greater average firing than that of subordinate animals. Next, to investigate spatial memory, a spatial recency task was used, where rats learnt to navigate towards one of three reward locations and then recall the rewarded location of the session. During the task, over 1000 neurons were recorded from the hippocampal CA1 region for five rats over multiple sessions. Multivariate analysis revealed that the sequence of neurons

encoding an animal's spatial position leading up to a rewarded location was also active in the decision period before the animal navigates to the rewarded location. The result posits that prospective replay of neural sequences in the hippocampal CA1 region could provide a mechanism by which decision-making is supported.

Lay Summary

The human brain consists of 100 billion neurons subdivided into specialised functional regions that drive sensation, perception, planning, decision-making, movement and action for diverse and changing scenarios. Research using non-invasive neural recording technologies such as fMRI and EEG has enabled us to pinpoint regions of functionality in the human brain and enabled us to observe how they inter-connect. However, little is currently known about how individual neurons within and across these regions combine as a neural population to evoke such functions. For this, human studies remain very difficult to execute.

This thesis addresses the need for recording from single cells by employing a high-resolution neural imaging technique known as calcium imaging to simultaneously record from hundreds of neurons within isolated brain regions of rodent models. Scientific conclusions drawn from animal models whilst not entirely interchangeable with humans, provide an illustrative means by which the neural code underlying complex functions can be inferred.

This thesis consists of a series of published papers and aimed to leverage computational techniques to answer two research questions. First, what is the role of the hippocampal brain region in memory and specifically what is the underlying neural code that contributes to spatial memory and navigational decision-making. Second, how is social cognition represented in the medial prefrontal cortex at the level of individual neurons. For each question, non-invasive methods were first used to investigate how they arise, how they become impaired in instances of Alzheimer's disease and Autistic Spectrum Disorder and the ways that they can be treated.

The main body of the thesis then dives into how large populations of neurons can be imaged and the computational methods that can be used to understand them. Using these methods, two cognitive processes were investigated, and the findings also published. The first explored the neural code underlying social cognition by analysing neural recordings from the rat medial prefrontal cortex (an area of the brain linked to executive function) during a social dominance task. The study identified populations of neurons that encoded each of the animal's own unique social behaviours, as well as that of its interaction partner, in a social dominance situation. The findings add to our existing knowledge of the role of the medial prefrontal cortex in action planning

and shed light on how the neural population encodes these actions. The second study explored the neural mechanisms underlying spatial memory and its role in decision-making. To achieve this, over 1000 Hippocampal CA1 neurons (known for their role in spatial memory) were recorded from five rats whilst they completed a spatial recency task. A key finding revealed sequences of neural activity that changed across days and could be used to predict the future reward destination of the animal, therefore implicating the Hippocampus as a potential precursor to spatial decision-making.

Overall, the thesis demonstrates the potential of advanced neural recording technology, and tailored analysis pipelines to gain insights into the neural code underlying complex cognitive processes such as memory and social cognition."

Acknowledgements

To Professor Richard G Morris - thank you for giving me this great opportunity, for guiding me, teaching me and supporting me every step of the way. I will continue to be inspired by your kindness, generosity and passion towards all that you work with and encounter. To Professor Simon R Schultz - thank you for teaching me, supporting me and giving me the opportunity to grow. The countless sessions with you on neural analysis form the backbone of what I have achieved today and what I will carry forward. Finally, I'd like to thank my friend and colleague Francesco Gobbo for his unwavering dedication to collecting high-quality data and also for his countless hours spent discussing analysis, results, and philosophy - it's been a great pleasure.

Declaration

I declare that this thesis was composed by myself, that the work contained herein is my own except where explicitly stated otherwise in the text, and that this work has not been submitted for any other degree or professional qualification except as specified.

Rufus Mitchell-Heggs

Introduction

This thesis aimed to investigate two research questions in rodent models. First, what is the role of the hippocampus in memory and what is the underlying neural code that contributes to spatial memory and navigational decision-making? Second, how is social cognition represented in the medial prefrontal cortex at the level of individual neurons. To answer these questions, I led the computational analysis of large-scale neural recordings collected from rodent brains during tasks involving spatial recall or social behaviour. This involved the research and development of tailored computational pipelines in Python to preprocess and analyse large-scale neural recordings. These pipelines were subsequently deployed to understand the neural code underpinning memory and social cognition.

This thesis begins with a critical review to sequentially introduce and review the six published research papers that comprise the body of the research. Each paper will consist of a short overview, that will outline the background literature and research gaps, then proceed to discuss the paper's aims, objectives, high-level methodology, and results. Lastly, a brief summary is provided of the research contribution to the expansion of scientific knowledge.

The order in which the papers are introduced and reviewed falls into four chapters. The first three introduce and review the papers and the fourth chapter consists of all seven papers collated.

Chapter 1 – "Cognition: An Insight from Neurodegenerative and Neurodevelopmental Disorders" forms the background motivation for developing our understanding of the brain's neural circuitry. The chapter begins by introducing high-level concepts such as memory and social cognition, before diving into neural conditions such as Alzheimer's Disease (AD) and Autistic spectrum disorder (ASD). The chapter features two papers linked to these topics as follows:

- **Paper 1: Changes in brain activity and connectivity as memories age** (Co-first author, Commentary). The commentary contributes to the first question of the thesis by introducing the broader topic of memory, defining the competing theories of memory consolidation and outlining hippocampal involvement. This adds to the existing pool of literature surrounding the hippocampus and introduces my research on elucidating the neural code of spatial navigation in rodent

models. My contribution to the commentary was to concisely summarize the key findings/ claims of the Tallman et al research paper. Then, with my co-authors, I conducted desk research to review the findings supported by competing theoretical models of memory consolidation and how the experimental/analytical robustness could be further improved to support their claims.

- **Paper 2: Experiential modulation of social dominance in a SYNGAP1 rat model of autism spectrum disorder** (Contributing author, research article). This paper contributes to the second research question of the thesis by introducing a model of Autisic Spectrum Disorder (ASD) in rats and reveals how behaviour can be altered in a social dominance experimental paradigm. The discovery of the asymmetries in behaviour between Wild-Type (WT) and ASD rats contributed to a preliminary understanding of the expected behaviour in a similar set up in paper 5 and identified the primary windows of behaviour to investigate the neural-code using single photon calcium imaging. Thus, the paper's conclusions were leveraged to define concrete starting hypotheses discussed in paper 5. The research article was part of a lab-wide effort to increase the understanding of how behaviour and neural activity differ between healthy and ASD rats in social scenarios (see Paper 5). My contribution to the research article was to bring my experience from a parallel workstream that used the same experimental paradigm. I reviewed and guided the analytical write-up, over a series of internal revisions contributing to the clarity of behavioural categorization and how the findings connected with the existing literature.

Chapter 2 – "1P-Calcium Imaging Analysis" introduces the primary tool throughout the thesis – "single photon (1P) calcium imaging". The chapter provides a brief background on the types of large-scale neural recording technologies available and explains why 1P-Calcium imaging was selected in subsequent experiments. Furthermore, the chapter aims to give the reader a complete understanding of the competing preprocessing pipelines available for extracting neural event traces. Preprocessing provides a mandatory precursor to any primary or secondary analysis and has been a significant research component in my contribution to subsequent papers. The section introduces two papers that aim to help experimenters overcome a common data-collection problem in calcium imaging and equip researchers with increasingly large-scale data with dimensionality reduction methods.

- **Paper 3: iHELMET: A 3D-printing solution for safe endoscopic Ca2+ recording in social neuroscience** (Contributing author, research article). This paper contributes to the second question of this thesis by generating a means to capture stable neural recordings in rats during a social dominance experimental paradigm. Furthermore, it holds a crucial step in the iterative development of the preprocessing pipeline used to reliably identify and record from the maximum number of neurons. The validated iHELMET was subsequently used in paper 5 enabling reliable neural recording in the tube test context. In addition, the preprocessing pipeline was further iterated upon for use in papers 5 and 6. The tube-test social dominance paradigm described in the methods article was the first implementation of single-photon calcium imaging in the lab with freely moving animals. My contribution to the article began by discovering the existence of motion artefacts within our dataset. This prompted the first author of the paper Dr Saxena to investigate additional ways in which aggressive motion could be reduced during imaging. Upon the creation of the iHELMET, I developed and deployed the motion analysis comparison, validating the efficacy of the tool. I then iterated on, co-wrote and reviewed the paper, primarily contributing to the summary of analytical findings and all the methods sections that involved the computational preprocessing and analysis of 1P calcium imaging recordings.
- **Paper 4: Neural manifold analysis of brain circuit dynamics in health and disease** (Co-First author, Review article). This review contributes to both questions of the thesis by exploring how neural manifold analysis techniques can be used as a top-down hypothesis testing strategy for large-scale neural recordings. The review categorised and compared existing NML algorithms across varying datasets across multiple brain regions including the hippocampus. By comparing multiple techniques, I was able to identify and develop subsequent computational analysis pipelines relevant for paper 6 that could be used to investigate the population code involved in spatial navigation. Furthermore, by exploring hippocampus CA1 neural recordings, I was able to develop a preliminary understanding of the dimensionality of hippocampal activity and how to optimally process and visualize subsequent data. My contribution to the review article was to lead a team of four researchers in the description and comparison of published neural manifolds algorithms. This included developing the review structure, dividing and reviewing each section and leading collaborations with external groups for the collection of comparative datasets. The specific

sections that I led were the introduction, the description of multiple Neural manifold and secondary analysis techniques and the comparative discussion. I also created all, excluding the first figures, which included co-developing and deploying visualisation and analysis code.

Chapter 3 – "Application of 1P-Calcium Imaging to Study Mechanisms of Sociability and Spatial Memory" introduces the primary focus of the thesis. The chapter commences by providing the background logic for using rats as a model of social cognition and spatial memory. It then dives into each cognitive process, its surrounding literature and two papers that leverage 1P-calcium imaging and computational techniques to further the field's knowledge of the neural circuitry underlying these processes. The two papers first explore social cognition, and then spatial decision-making.

- **Paper 5: Ca2+ imaging of self and other in medial prefrontal cortex during social dominance interactions in a tube test** (Co-First author, research article). This paper contributes to the second research question of the thesis. The research identified specific neural ensembles in the rat medial prefrontal cortex that correlate with an animal's own and another animal's behaviour. This added to a growing body of existing literature implicating the role of the medial prefrontal cortex in social coding. Furthermore, by leveraging a similar computational technique to that used in paper 6, the paper introduced a robust methodology for the identification of socially-tuned neurons. My contribution to the research article was with the experimental design, the preprocessing and analysis of the 1P calcium-imaging recordings. For experimental design, I identified ways to capture robust calcium imaging recordings (see paper 3) and created a standardized project structure for organising raw data, processed files, and figure panels. For calcium imaging preprocessing, I researched and developed a robust processing pipeline to accurately identify neurons, extract their calcium traces and align them with labelled behaviour. This involved running a rigorous review of available algorithms and collaborations with multiple research groups for best practise, algorithm and parameter sharing. Next, for the analysis, I developed multiple algorithms for univariate analysis and statistical comparison. This included the development of a mutual information pipeline used for the identification of behaviourally tuned neurons for the animal's behaviour and its interaction partner's behaviour. For each neural ensemble, I then quantified and characterised them by observing their consistency within and across imaging

sessions. Lastly, I contributed to the writing of the manuscript, including the iterative interpretation and discussion of the results and the methods for calcium imaging preprocessing and neural analysis algorithms. This included many successive drafts, with regular reviewing and refinements.

- **Paper 6: Neuronal signature of spatial decision-making during navigation by freely moving rats by using calcium imaging** (Co-First author, research article). This paper contributes to the first question of the thesis. The research captures single photon calcium imaging in the rat hippocampus CA1 region whilst the animal completes a spatial recency task. The results confirm a neural population that correlated with the animal's spatial position when exploring a 2-dimensional arena. Further, by isolating key decision-making windows within the paradigm, sequences of neural activity were identified that correspond to an animal's future destination. These results contributed to existing research into hippocampal function in encoding spatial memory, but also indicated how the neural code in the hippocampus could act as a driver for navigational decision-making. My contribution to the research article was with the experimental design, the preprocessing and analysis of the 1P calcium-imaging recordings - like paper 5. For experimental design, I co-developed a procedure for aligning calcium imaging traces to the animal's specific location. This involved extracting the animal's head position in space using Deep Lab Cut (DLC), then using a Light Emitting Diode (LED) triggered in the experiment to align neural calcium imaging to the rat head location. For the analysis, firstly, I developed the place cell identification pipeline. Given the 2D nature of our experimental paradigm, I had to overcome spatial sampling constraints, this led me to research and compare multiple mutual information estimators and develop additional measures to ensure non-biased estimation. Next, for trial neural analysis – I developed an automated software to select each correct vs incorrect trial. Then, I developed and deployed a neural manifold learning pipeline to assess the recurrence of population activity and to identify clusters of similar activity (notably a reward location and decision-making window). Upon identifying notable clusters, I developed and deployed code and visualization techniques to characterise and decode them. For the manuscript, I interpreted and co-wrote the calcium imaging results section, wrote the methods section for the calcium imaging preprocessing analysis and contributed to the structuring

and iterative reviewing of the introduction and discussion. Lastly, following reviewer comments, I led the development of a series of analyses and supporting controls that were subsequently included in the manuscript and added to the supplementary information.

Papers 4-6 were first/co-first authored publications that will therefore be discussed in more detail.

Contents

Chapter 1

Cognition: An insight from neurodegenerative and neurodevelopmental disorders

1.1 Memory

Memory falls into several categories, usually classified according to their duration and their content. For example, working memory encodes information from seconds to minutes, whilst long-term memory can encode information for days, months and years. Long-term memory can be further subdivided and includes episodic memory. This refers to an individual's ability to store and recall a specific event in time, typically characterised by what, where, who and when of the event.

Long-term memory typically starts by being encoded in medial temporal lobe structures (MTL) such as the hippocampus as a neural representation with its stability dictated by its synaptic connections. Memory consolidation takes place anywhere between months to years becoming hippocampus independent by duplicating the memory representation and committing it to neocortical areas. A holistic understanding of the neuromechanics involved in memory encoding, consolidation and recall is therefore crucial when studying how neurodegenerative diseases such as AD disrupt memory circuits.

1.2 Changes in brain activity and connectivity as memories age

The (Gobbo et al., 2022) Commentary was to review and discussed the (Tallman et al., 2022) findings of functional connectivity as a memory age. There is currently much debate as to how the Hippocampus is involved in long-term memory and how and where memory consolidation occurs. The commentary aimed to introduce and compare the paper's findings with competing theories, including the standard model of memory consolidation (SMC), Multiple trace theory (MTT) and memory schemas. A key result of the paper was no significant changes in hippocampus activity during memory retrieval at different time points, thus indicating SMC as a candidate theory. Interestingly, analysis of a subset of memory retrievals with high confidence reported no significant change to hippocampal activity over time. The commentary suggested that the reason for this was due to the metamemory component of the test (i.e. confidence score) generating a mental "time travel" to the time of memory learning and thus hippocampal involvement. Consequently, future studies would need to disentangle this component to confidently back up an SMC theory.

The commentary aims to contribute to the expansion of our understanding of memory consolidation by adding to the discussion on hippocampal involvement in long-term memory consolidation and retrieval, supporting the SMC theory and suggesting future experiments that can help provide further validation.

Personal contribution: As a co-first author, my main contributions were to summarize the key findings of (Tallman et al., 2022) paper, to review them alongside competing literature and to provide input on future directions.

1.3 Alzheimer's Disease

AD is a progressive and irreversible neurological disorder that affects memory, cognitive functions, and behaviour. It is characterized by the extracellular aggregation of Amyloid beta (Aβ) plaques and intra-cellular Tau protein tangles. Globally, it is estimated that over 50 million people have dementia, and about two-thirds of these cases are due to AD (WHO, 2023). As the population ages, the disease burden of

Alzheimer's is expected to increase, making it a significant public health concern. The reduced quality of life, the strain on families and the associated healthcare costs put the annual global cost of dementia above 1.3 trillion US dollars, a number that is expected to more than double by 2030 (WHO, 2021).

Currently, there is no cure for Alzheimer's disease, but there are therapies available to help manage symptoms and improve quality of life. The most used medications for AD are cholinesterase inhibitors and memantine (Parsons et al., 2013), both can help alleviate symptoms, improve cognition and delay progression. The treatments achieve this in different ways, with memantine working as a competitor receptor antagonist to free up NMDA receptors and increase synaptic transmissibility. Meanwhile, cholinesterase inhibitors work by inhibiting acetylcholinesterase function, thus increasing levels of free acetylcholine (Parsons et al., 2013). Additionally, there are several non-pharmacological interventions that can help manage symptoms, including cognitive and behavioural therapies, physical exercise, and social engagement. It's also important for individuals with Alzheimer's disease to receive comprehensive care, including management of coexisting medical conditions, support for caregivers, and planning for future care needs.

1.4 Social Cognition

Social cognition is an umbrella term that can be used to describe the ability of an individual to decipher the intentions of other conspecifics and to prepare and execute their actions accordingly. Encompassing many behaviours, it involves integrating and transmitting information between multiple brain regions of varying functionality. Notably, the prefrontal cortex has been identified as a key player due to its involvement in high-order executive functionality such as decision-making, attention and working memory (Bicks et al., 2015). Unsurprisingly, disruption to neural circuitry involved in social cognition (i.e. changes in the excitation/inhibition ratio) can lead to neural disorders such as Schizophrenia or ASD (Ferguson and Gao, 2018).

1.5 Autistic Spectrum Disorder

ASD is a neurodevelopmental disorder that affects 16% of children and 0.76% of people worldwide (Hodges et al., 2020). The disorder is characterised by impairments in communication and social interaction skills that can significantly impact an individual's ability to navigate daily life activities. People with ASD may also suffer from coexisting conditions such as anxiety, depression, and intellectual disability all of which can increase their reliance upon family and societal support. The high prevalence of ASD, along with the need for specialized services and support, can render it a difficult disorder to manage and one that results in substantial economic and societal costs.

The exact causes of ASD are still under investigation, but research suggests that a combination of genetic and environmental factors may contribute to the development of the disorder. Two genetic factors that have been linked with more severe cognitive and behavioural impairments include Synaptic Ras GTPase-Activating Protein 1 (SYNGAP1) (Berryer et al., 2013) and Fragile-X syndrome (FXS) (Hagerman et al., 2017). Whilst many studies have validated the local neurological impact of these variants, few explore these variants in the context of rodent models of sociability. Crucially, these types of experiments enable connections to be drawn between genetic variants and their effects on the associated behavioural phenotypes needed to develop and maintain relationships.

Among the prior experimental paradigms that model social interactions in ASD rodents, "Crawley's sociability test" enabled researchers to discover that rodents with SYNGAP1 variants displayed deficits in social recognition (Guo et al., 2009; Nakajima et al., 2019). In addition, a Fragile-X study using the "Tube Test", observed FMR1 knockout (KO) rats as more likely to be subordinate to Wild-type (WT) and as lacking behavioural flexibility (Saxena, Webster et al., 2018).

1.6 Experiential modulation of social dominance in a SYNGAP1 rat model of autism spectrum disorder

With SYNGAP1 sharing similar known deficits to FXS, (Harris et al., 2021) aimed to investigate the differences between SYNGAP1 and WT rats in a Tube Test context, like that of (Saxena, Webster et al., 2018). The experiment was split into two Phases, Phase 1 facilitating intra-cage competition between four cages of four animals (10

sessions) and Phase 2 inter-cage competitions (16 sessions). For each competition, animals would participate in 5 trials - entering a transparent tube from opposing directions and competing to push the animal out of the tube. Aside from winning and losing, animals displayed multiple behaviours including Pushing, Moving Forward, Resisting, Retreating, Withdrawal and Stillness. The results revealed that in Phase 1, where cages contained 4x KO, a typical social hierarchy would form. Conversely, in mixed cages (2x KO and 2x WT), KOs were more likely to occupy the lower ranks in the social hierarchy. Importantly, a very different pattern was observed when the animals faced contests with animals from different cages who they had never met. Specifically, when exposed to new conspecifics in Phase 2, KO animals exhibited a form of behavioural hyperstability, with high-ranked dominant animals typically winning against high-rank WTs, thus remaining high-rank and low-rank KOs continuing to lose and remain low-rank. This latter result is likely due to learnt patterns of behaviour in Phase 1 being rigidly and inflexibly carried on Phase 2. Both results are consistent with (Saxena, Webster et al., 2018) and reflect an important validity to what has been observed in ASD individuals.

The study contributes to furthering researcher knowledge by first validating SYNGAP1 rat models of ASD. Secondly, it highlights the use of an additional social test – the Tube Test, that can be used to expose key social behaviours that discriminate WT and SYNGAP1 animals. Finally, findings on behavioural hyperstability in SYNGAP1 rats reinforce surrounding mouse literature on social memory impairment.

Personal contribution: Having worked on a parallel tube test study on Fragile-X syndrome with Dr Kapil Saxena and Professor Richard Morris, I helped guide the project, suggested suitable behavioural categories and contributed to the main text.

Chapter 2

1P-Calcium Imaging Analysis

The three papers presented so far focus on the foundations of our understanding of memory and social cognition and how they can become impaired in commonly known neurodegenerative diseases and neural disorders. From this point, the thesis aims to expand on these processes by observing how changes in neural circuitry change as a function of behaviour. The following sections, focus on the methodology to record from the neural circuitry, the landscape of computational techniques required to analyse large-scale neural recordings and how applications of neural population recordings test rat models of social cognition and memory.

2.1 Large-scale neural recording

The landscape of neural recording technologies has been rapidly growing. Today, there are several techniques that can be used to record from large populations of neurons. Electrophysiology, one of the most common, is well known for its ability to record simultaneously from hundreds of neurons with high temporal precision. Furthermore, the introduction of Neuropixel has increased the number of neurons that can be imaged by an order of magnitude, with recent studies recording from over 6000 neurons (Gardner et al., 2022). Importantly, one of the shortfalls of electrophysiology is its inability to robustly identify and record from the same neurons across days due to the movement of neurons or the electrodes. To overcome this, technologies such as calcium and voltage imaging have been developed. Both enable neurons to be tracked over days, with calcium imaging capable of recording from similar orders of magnitude of neurons to that of electrophysiology. Like electrophysiology, progress in the development of imaging hardware is steadily increasing, with Mesoscopes now enabling up to 10,000 neurons to be imaged simultaneously (Stringer et al., 2019).

2.2 Calcium Imaging

Calcium imaging capitalizes on the influx of calcium ions (Ca2+) into neurons following an action potential or a series of action potentials. Neurons are genetically modified to express a fluorescent calcium indicator protein such as GCaMP6f that can bind free Ca2+ using a calmodulin-binding site. A laser is then used to excite the “activated” protein causing it to emit photons with a typical emission spectrum that can then be captured and visualised using a microscope. Importantly, there are multiple ways to perform calcium imaging, including single-photon (1P), two-photon (2P) and three-photon (3P) imaging. The number of photons refers to the quantity used to excite fluorophores such as the calcium indicator. Using more photons focuses the excitation volume, rendering the resulting fluorescence signal less prone to scattering and out-of-focus fluorescence. Longer wavelength photons travel the biological tissue further, therefore allowing the imaging of deeper brain areas. Imaging deeper structures, be it at 1P or at 2P, requires relay lenses (e.g. GRIN lenses) to convey light to and from these regions. Most GRIN lenses have sub-optimal optical properties compared to microscope objectives, which results in a decrease in effective spatial resolution. 2-photon calcium imaging therefore typically exhibits increased spatial resolution compared to that of 1P imaging. However, a key trade-off is that it often requires an animal to be head-fixed (i.e., its head movement is restrained). Using a head-mounted miniaturised microscope (Miniscope), 1P imaging technology allows an animal to move around freely. This is crucial in enabling animals to exhibit more naturalistic behaviour, especially during social interaction paradigms such as the Tube Test, or Crawley’s social interaction test. Given the social element and the natural representation of 2-dimensional space, 1P-calcium imaging was selected and optimised for neural recordings in this thesis. My contribution to the subsequent studies was to guide experimental design for optimal data collection, to review and validate a robust preprocessing pipeline and to develop and apply computational pipelines for univariate and population-level neural analysis. This follows a trend across neuroscience research that shows a growing collection of large neural datasets requires specialised personnel to conduct analysis.

2.3 Calcium Imaging Preprocessing

After performing experiments generating calcium imaging recordings, preprocessing is required to identify regions of interest (ROIs) - i.e. neurons within the microscopes Field of View (FOV). Neuronal traces are subsequently extracted from the ROIs and converted into event trains. Due to the great recent advancements in the applications of calcium imaging to neuroscience and an increasingly large number of neurons that can be recorded, there is a relatively competitive landscape of pre-processing pipelines with varying degrees of efficiency, accuracy and tailoring to specific calcium-imaging technologies. Typical pipelines begin by spatial-temporal downsampling of the FOV to remove noisy pixels, followed by applying a motion correction algorithm to align frames. Next, ROIs are identified, and each neuron's signals are extracted and isolated. This step tends to differ the most between pipelines, with top performers including PCA/ICA (Mukamel et al., 2009), CaImAn CNMF-e (Giovannucci et al., 2019; Zhou et al., 2018), EXTRACT (Inan et al., 2021) and Suite-2P (Pachitariu et al., 2017). CaImAn CNMF-e was selected due to its high performance, its tailoring to 1P-calcium imaging and its modular and Python-based implementation that allowed it to be optimized for our specific datasets. Events are extracted with the CaImAn integrated OASIS algorithm (Friedrich et al., 2017), using a parameter set optimised for 1P-calcium imaging. Neural "events" recorded with calcium imaging do not in general translate 1-to-1 into action potentials. This is due to the biophysical properties of binding and unbinding kinetics of calcium indicators, to a certain nonlinearity of calcium influx, and to detection sensitivity. This leads to temporally close action potentials to merge at high frequency, and the failure to identify isolated single action potentials. Finally, neural event trains are aligned with the animal's behaviour that arises as a function of a targeted protocol. Depending on the targeted behaviour, different approaches can be used for labelling. For example, where an animal's position in space requires tracking, software's such as ANY-maze and Deeplabcut (DLC) provide a fast and precise automated process. Post-hoc behavioural analysis can then build on the 2D position, enabling spatial binning or the selection of zones of interest. Alternatively, for more complex categorical data such as social behaviours, manual labelling remains in high use.

2.4 iHELMET: A 3D-printing solution for safe endoscopic Ca2+ recording in social neuroscience

1P-calcium imaging allows rodents to move around and interact freely within social interaction paradigms such as the Tube Test. Prior studies with mouse models have shown successful coupling of calcium imaging with the tube test context (Kingsbury et al., 2019), however upon performing these experiments in rats, dramatic FOV motion artefacts in calcium recordings were observed due to the greater strength of rats. Currently, only a few methods exist to reduce this motion, the main one being to insert a barrier between interacting animals. The (Saxena, Spooner et al., 2021) methods paper aimed to minimize motion artefacts by introducing the iHELMET, a 3D printed lightweight helmet designed to fit over a portable miniscope and in doing so protect it and decrease miniscope motion. The paper applied a simple method for quantifying dominant motion and demonstrated that the iHELMET could be worn to minimise major motion problems. Consequently, a novel solution was proposed that would maintain naturalistic interaction between rats and ensure quality neural recordings. Obtaining stable neural recordings is a useful requirement when observing neural circuitry, particularly when imaging across multiple days. Therefore, whether standalone or combined with other techniques, iHELMET provides an incremental way for researchers working with freely moving animals to achieve robust data collection. To date, the iHELMET has been used in experiments in the lab involving rat social interaction and calcium imaging (See (Garcia-Font et al., 2022)). Furthermore, the design and 3D printing instructions have been shared with several interested parties.

Personal contribution: As the lead data analyst for this project my contribution initially consisted of discovering and flagging the motion artefacts, then aiding in the quantification of motion before and after iHELMET and finally developing the calcium imaging preprocessing pipeline. I also helped write and review the main text and figures.

2.5 1P-Calcium Imaging Data Analysis

Up until recently, univariate analyses have dominated research on neural recordings. Classical analyses use peri-event time histograms and changes in a neuron's firing rate to identify tuning towards stimuli, usually referred to as the neuron's field. These approaches have been used with great success, identifying neurons with sensory tuning (e.g. neurons selective to visual orientation or auditory frequencies), spatial tuning (e.g. place cells (O'Keefe, 1976), grid cells (Moser et al., 2014), head-direction cells (Muller et al., 1996)), behavioural tuning (e.g. social cells (Liang et al., 2018), action cells (Kingsbury et al., 2019)) as well as decision and confidence tuning ((Kobak et al., 2016). Univariate analysis thus provides an excellent bottom-up approach for characterising the neural population by separating it into digestible ensembles and observing how they change as a function of experimental conditions. However, one thing that is ignored in univariate analyses is the emergent properties of a neural population and how they may contribute to the function of the brain region.

Progress in neural recording technologies has led to the increased capacity to record simultaneously from large populations of neurons. This opens the field to novel analytical techniques that explore changes in the neural population in addition to univariate analyses. Subsequently, researchers can draw more holistic conclusions between the changes of individual neurons and how they are incorporated into/drive the neural population code. Importantly, a holistic approach is crucial when investigating the disruption caused to neural circuity by neurological diseases and disorders. By breaking down the analysis into univariate and population analysis, researchers are becoming increasingly equipped with tools that can close the gap of understand how genetic misregulation can impact downstream neural circuitry and thus behavioural phenotypes.

2.6 Neural manifold analysis of brain circuit dynamics in health and disease

As the size of neural population recordings increases, so does the demand for analytical techniques that can describe population activity and how it changes as a function of behaviour, disease or disorder. The (Mitchell-Heggs et al., 2022) review aims to address this demand, by introducing and comparing some of the most common neural

population analysis methods, and in particular, diving into the popular dimensionality reduction methods of Neural Manifold Learning (NML). This method takes high-dimensional neural activity as input and aims to represent it in a lower-dimensional form that maintains the information content of the original activity. This enables high-dimensional neural population data to be more comprehensibly visualised and interpreted. Both linear and non-linear methods were sequentially introduced, breaking down how they work and highlighting the literature in which they have been used. Seven of the most common algorithms (2 linear, 5 non-linear) were then compared across three datasets collected from different brain regions and displaying varying behavioural complexity. The review concluded that the NML algorithm selection is highly dependent on the research goals and the data being examined. For example, most of the seven algorithms compared (linear and non-linear) performed equally well for linear neural representations such as those that arise during hippocampal spatial encoding. Conversely, non-linear algorithms tended to generalize better across datasets, particularly those that contain highly non-linear neural representations or tasks of high behavioural complexity. The review went on to compare the top-performing linear and non-linear algorithms (MDS and UMAP) in the context of a simulated model of AD – displaying how they can be used for hypothesis testing and to identify asymmetries between healthy vs diseased brain states. Finally, the review discussed a range of large range of manifold secondary analysis algorithms that can be used to characterize and parameterize NMLs.

This review builds on previous works such as the highly cited (Cunningham and Yu, 2014) review of dimensionality reduction algorithms by introducing additional published research that includes novel NML algorithms, their applications and the techniques that aim to characterize/parameterize them. NML provides one of many dimensionality reduction techniques that will be crucial when interpreting large-scale neural recordings. With the introduction of novel technologies such as the Neuropixel and Mesoscopes, there is a trend of increasingly large neural datasets, thus demanding ever more sophisticated analysis methods that can make use of the full dataset and remain interpretable. Finally, looping back to NML in the context of neurodegenerative diseases and disorders, much is already known at the level of molecular and cellular dysfunction, but there is still a large gap in knowledge at the network level. By comparing NML algorithms and sharing their application with secondary analysis to an AD dataset (along with the open-source code), this review hopes to equip researchers with the necessary toolkit to investigate network dysfunction.

Personal contributions: As a co-first Author, I oversaw the planning of the review structure and coordinated the authors. Researched, compared and wrote up different NML algorithms and uses in neuroscientific literature, namely tSNE and trial-structured algorithms (e.g. dPCA and mTDR). Researched topological data analysis algorithms (e.g. persistent cohomology) and co-wrote the abstract introduction and discussion. Furthermore, I led the collaboration with two research groups, to collect two of the three datasets presented and compared Yu et al., 2007 and Rubin et al., 2019. Designed code for figures 3 - 5 and co-prepared figures 1, 3, 4, 5, 6.

Chapter 3

Application of 1P-Calcium Imaging to Study Mechanisms of Sociability and Spatial Memory

As previously mentioned in the introduction and in the prior section, 1P calcium imaging was used as the primary technique for two workstreams investigating the neurocircuitry of social cognition and spatial navigation in rats. Both projects aim to contribute to the fundamental understanding of how their respective processes are executed and provide a means of hypothesis testing for subsequent disruptive diseases and disorders (e.g. AD or ASD).

For both papers, rat models were used to investigate the neural circuitry. Previous disease models have been established in mice, largely due to their high-throughput capacity and a strong understanding of their genetic code and its manipulation. However, due to the steadily improving understanding of the rat genome, it is increasingly possible to perform similar manipulations in rats. The benefit of using rats over mice is that they are known to display a more complex spectrum of behaviours (Ellenbroek and Youn, 2016). This may reflect additional insights when conducting studies of social cognition, as shown in paper 6. Furthermore, rats have been long privileged as the model of choice to study navigation and decision-making, with monkeys reserved for the most complex tasks. For instance, studies on spatial memory using the Morris watermaze (Morris, 1981) exposed that rats have a better ability than mice to correctly remember the location of the platform (Ellenbroek and Youn, 2016). This alludes to more sophisticated hippocampal activity and thus provides a better model when linking to human spatial memory. The final paper 7, thus leverages rat models, becoming one of the first calcium imaging papers to be published in rat hippocampus.

3.1 Ca2+ imaging of self and other in medial prefrontal cortex during social dominance interactions in a tube test

Continuing from Section 2, paper 3, the (Garcia-Font et al., 2022) study aimed to develop the characterisation of neural activity linked to social cognition. The study builds on prior social studies that investigate the neural coding of social cognition, such as the (Murugan et al., 2017; Liang et al., 2018) social interaction experiment and the (Kingsbury et al., 2019), social dominance experiment. The paper characterised social cognition by running a rat social dominance experiment in the Tube Test and simultaneously conducting calcium recording in the Prelimbic cortex (PrL). The rat PrL was chosen due to its containing some functional homology to the human medial Prefrontal Cortex (mPFC), a brain region, known for its association with social cognition in the form of empathy, theory of mind, planning (of self and others) and decision making (Euston et al., 2012). Intra-cage competitions were explored, with rats competing against their cage mate for 5 sessions of 5 trials. Leveraging the previously described iHELMET, robust and continuous recordings were captured and aligned with five classes of behaviour, that consisted of the animal moving forward, pushing, resisting, retreating, withdrawing or remaining still. The paper revealed two findings - the first was that strongly dominant animals showed increased population activity compared to clear losers. The second was that a specific ensemble of neurons fires preferentially during an animal's own behaviour and/or during the competitor's behaviour. Furthermore, when observing the consistency of these behaviourally tuned neurons over multiple sessions the majority showed around 33% consistency, indicating a dynamic neural code. The study extends the findings of (Kingsbury et al., 2019), by acknowledging the existence of coincident cells – neurons that are tuned to both to the animal's own behaviour and the other animal's (e.g. tuned to PUSH own and RETREAT other). Furthermore, the paper introduces a robust univariate methodology that may be used to discriminate and characterise the effects of ASD-induced behavioural hyperstability (Saxena, Webster et al., 2018; Harris et al., 2021). Understanding the stability and consistency of neural ensembles may provide valuable insights into how ASD alters neural functionality.

Personal contributions: As a co-first author, my first contribution was to the preprocessing and analysis of the calcium imaging recordings. This included thoroughly researching and optimising parameters for the preprocessing pipeline (described above) and developing the analytical pipelines for identifying and characterising behaviourally tuned cells. Upon completion of this, I contributed to the writing and editing of the manuscript and producing figures 2a, d, e and 3,4,5.

3.2 Spatial Navigation

The neural encoding of space is thought to be largely attributed to ensembles of specialised neurons that work in unison to generate an internal map of the environment and the position of an individual within it. Processing commences in the visual cortex with the input of sensory signals and subsequently feeds into a neural circuit involving the retrosplenial and postrhinal cortex that subsequently feed into bidirectional interactions between the hippocampus and entorhinal cortex, eventually leading to the action execution in the motor cortex (Alexander et al., 2023). Within this circuit, boundary cells, head direction cells, grid cells and place cells all contribute to providing an internal representation of the environment and the animal moving through it. Current research seeks to further uncover the precise interactions in this circuit and how the different components come together when spatial memory becomes activated in scenarios of spatial navigation, action planning and decision-making. For example, the hippocampal CA1 region has been found to replay sequences of neurons at theta rhythm for upcoming trajectories (Widloski and Foster, 2022). This implies that the hippocampus may play a role in guiding the action planning of where to go next.

3.3 Neuronal signature of spatial decision-making during navigation by freely moving rats by using calcium imaging

The (Gobbo et al., 2022) study aimed to further develop the understanding on the neural code for spatial navigation and how it may impact decision-making. In the paper, 1P-calcium imaging data from rat hippocampal CA1 region was collected during an event arena task. The event arena apparatus consisted of a startbox and an open

arena containing 3 sandwell locations. The paradigm followed multiple sessions, each consisting of three stages, Exploration – the animal spends 10 minutes exploring the arena with empty sandwells. Sample – pellets are introduced into one of the three sandwells, the animal then samples each well and builds an association of the rewarded location. Choice – after a 30-minute delay, all three sandwells are covered and homogenised for visual and olfactory cues and pellets introduced into the sandwell from the previous “Sample” stage. The animal is then placed into the startbox and learns to recall the rewarded location. Both the Sample and Choice stages can be further broken down into individual trials. For each trial, the animal begins in the startbox, journeys outbound to one of the three sandwells to recover a pellet and returns inbound to the startbox to consume the pellet. Importantly, in the short window before the animal leaves the startbox the neural activity linked to the decision-making process can be observed.

The results showed that during the Exploration stages, animals formed a stable cognitive map of the environment in the form of place cells. These cells experienced a heightened probability of firing in certain locations within the arena, enabling the animal to precisely position itself relative to proximal and distal cues. Importantly, during the Choice stage, place cells that usually fired in the arena also fired in the decision-making window before the animal left the startbox. The ensemble of neurons that fired in the startbox formed a distinct neural code that could be accurately used to predict the prospective reward well location. These Neurons were found to encode locations along the outbound path towards and including the rewarded well. These were distinct compared to trials of alternative reward wells and suggest a form of prospective coding of the upcoming trajectory or location. This aligns with the findings of (Widloski and Foster, 2022), that observed hippocampal CA1 region replay sequences of neurons at theta rhythm for upcoming trajectories.

This paper contributes to the steady progress in understanding the role of the hippocampus CA1 region in spatial decision-making. By observing its role in prospectively replaying cells that represent the space around specific reward destinations, it can be deduced that it may play a part in guiding the animal’s decision. This poses a future research question on the causal effects of the hippocampus in decision-making. Furthermore, there are two well-known strategies by which animals navigate known as egocentric and allocentric navigation. Egocentric navigation involves an animal representing space and landmarks in a way that is relative to its current position, for example, path distance and direction. Meanwhile, in allocentric representations,

an animal will represent landmarks relative to each other that can be defined by the grid and place cells (Wang et al., 2020). This research asks the question as to whether there are differences in prospective replay for an egocentric vs allocentric spatial representation.

Personal contributions: As a co-first author, my first contribution was on the pre-processing and analysis of the calcium imaging recordings. The primary analysis steps included creating a place cell identification and characterisation pipeline that conformed with literature standards. Furthermore, I conducted thorough population analyses including neural manifold learning and decoder analysis to visualise the distinct predictive codes of the rewarded locations. The panels for these analyses are shown in Figures 1,2,3, Supplementary Figures 6 to 19.

Bibliography

Alexander, A. S., J. C. Robinson, C. E. Stern and M. E. Hasselmo (May 2023). "Gated transformations from egocentric to allocentric reference frames involving retrosplenial cortex, entorhinal cortex, and hippocampus". In: *Hippocampus* 33.5, pp. 465–487. DOI: 10.1002/hipo.23513.

Atrián-Blasco, E., L. d. Cremoux, X. Lin, R. Mitchell-Heggs, L. Sabater, S. Blanchard and C. Hureau (15th Feb. 2022). "Keggin-type polyoxometalates as Cu(II) chelators in the context of Alzheimer's disease". In: *Chemical Communications* 58.14. Publisher: The Royal Society of Chemistry, pp. 2367–2370. DOI: 10.1039/D1CC05792H.

Berryer, M. H. et al. (2013). "Mutations in SYNGAP1 Cause Intellectual Disability, Autism, and a Specific Form of Epilepsy by Inducing Haploinsufficiency". In: *Human Mutation* 34.2. _eprint: https://onlinelibrary.wiley.com/doi/pdf/10.1002/humu.22248, pp. 385–394. DOI: 10.1002/humu.22248.

Bicks, L. K., H. Koike, S. Akbarian and H. Morishita (2015). "Prefrontal Cortex and Social Cognition in Mouse and Man". In: *Frontiers in Psychology* 6.

Cunningham, J. P. and B. M. Yu (Nov. 2014). "Dimensionality reduction for large-scale neural recordings". In: *Nature Neuroscience* 17.11. Number: 11 Publisher: Nature Publishing Group, pp. 1500–1509. DOI: 10.1038/nn.3776.

Das, N., J. Raymick and S. Sarkar (1st Oct. 2021). "Role of metals in Alzheimer's disease". In: *Metabolic Brain Disease* 36.7, pp. 1627–1639. DOI: 10.1007/s11011-021-00765-w.

Ellenbroek, B. and J. Youn (1st Oct. 2016). "Rodent models in neuroscience research: is it a rat race?" In: *Disease Models & Mechanisms* 9.10, pp. 1079–1087. DOI: 10.1242/dmm.026120.

Euston, D. R., A. J. Gruber and B. L. McNaughton (20th Dec. 2012). "The Role of Medial Prefrontal Cortex in Memory and Decision Making". In: *Neuron* 76.6, pp. 1057–1070. DOI: 10.1016/j.neuron.2012.12.002.

Ferguson, B. R. and W.-J. Gao (2018). "PV Interneurons: Critical Regulators of E/I Balance for Prefrontal Cortex-Dependent Behavior and Psychiatric Disorders". In: *Frontiers in Neural Circuits* 12.

Friedrich, J., P. Zhou and L. Paninski (Mar. 2017). “Fast online deconvolution of calcium imaging data”. In: *PLoS computational biology* 13.3, e1005423. DOI: 10.1371/journal.pcbi.1005423.

Garcia-Font, N. et al. (2nd Aug. 2022). “Ca2+ imaging of self and other in medial prefrontal cortex during social dominance interactions in a tube test”. In: *Proceedings of the National Academy of Sciences of the United States of America* 119.31, e2107942119. DOI: 10.1073/pnas.2107942119.

Gardner, R. J., E. Hermansen, M. Pachitariu, Y. Burak, N. A. Baas, B. A. Dunn, M.-B. Moser and E. I. Moser (Feb. 2022). “Toroidal topology of population activity in grid cells”. In: *Nature* 602.7895. Number: 7895 Publisher: Nature Publishing Group, pp. 123–128. DOI: 10.1038/s41586-021-04268-7.

Giovannucci, A. et al. (17th Jan. 2019). “CaImAn an open source tool for scalable calcium imaging data analysis”. In: *eLife* 8. Ed. by D. Kleinfeld and A. J. King. Publisher: eLife Sciences Publications, Ltd, e38173. DOI: 10.7554/eLife.38173.

Gobbo, F., R. Mitchell-Heggs and D. Tse (2nd Oct. 2022). “Changes in brain activity and connectivity as memories age”. In: *Cognitive Neuroscience* 13.3. Publisher: Routledge _eprint: https://doi.org/10.1080/17588928.2022.2076076, pp. 141–143. DOI: 10.1080/17588928.2022.2076076.

Guo, X., P. Hamilton, N. J. Reish, J. D. Sweatt, C. A. Miller and G. Rumbaugh (June 2009). “Reduced expression of the NMDA receptor-interacting protein SynGAP causes behavioral abnormalities that model symptoms of schizophrenia”. In: *Neuropsychopharmacology : official publication of the American College of Neuropsychopharmacology* 34.7, pp. 1659–1672. DOI: 10.1038/npp.2008.223.

Hagerman, R. J. et al. (29th Sept. 2017). “Fragile X syndrome”. In: *Nature Reviews Disease Primers* 3.1. Number: 1 Publisher: Nature Publishing Group, pp. 1–19. DOI: 10.1038/nrdp.2017.65.

Harris, E., H. Myers, K. Saxena, R. Mitchell-Heggs, P. Kind, S. Chattarji and R. G. M. Morris (2021). “Experiential modulation of social dominance in a SYNGAP1 rat model of Autism Spectrum Disorders”. In: *European Journal of Neuroscience* 54.10. _eprint: https://onlinelibrary.wiley.com/doi/pdf/10.1111/ejn.15500, pp. 7733–7748. DOI: 10.1111/ejn.15500.

Hodges, H., C. Fealko and N. Soares (Feb. 2020). “Autism spectrum disorder: definition, epidemiology, causes, and clinical evaluation”. In: *Translational Pediatrics* 9 (Suppl 1), S55–S65. DOI: 10.21037/tp.2019.09.09.

Inan, H. et al. (25th Mar. 2021). *Fast and statistically robust cell extraction from large-scale neural calcium imaging datasets*. Pages: 2021.03.24.436279 Section: New Results. DOI: 10.1101/2021.03.24.436279.

Kingsbury, L., S. Huang, J. Wang, K. Gu, P. Golshani, Y. E. Wu and W. Hong (July 2019). "Correlated Neural Activity and Encoding of Behavior across Brains of Socially Interacting Animals". In: *Cell* 178.2, 429–446.e16. DOI: 10.1016/j.cell.2019.05.022.

Kobak, D. et al. (12th Apr. 2016). "Demixed principal component analysis of neural population data". In: *eLife* 5, e10989. DOI: 10.7554/eLife.10989.

Liang, B., L. Zhang, G. Barbera, W. Fang, J. Zhang, X. Chen, R. Chen, Y. Li and D.-T. Lin (7th Nov. 2018). "Distinct and Dynamic ON and OFF Neural Ensembles in the Prefrontal Cortex Code Social Exploration". In: *Neuron* 100.3, 700–714.e9. DOI: 10.1016/j.neuron.2018.08.043.

Mitchell-Heggs, R., S. Prado, G. P. Gava, M. A. Go and S. R. Schultz (22nd Mar. 2022). *Neural manifold analysis of brain circuit dynamics in health and disease*. arXiv: 2203.11874[q-bio].

Morris, R. G. M. (1st May 1981). "Spatial localization does not require the presence of local cues". In: *Learning and Motivation* 12.2, pp. 239–260. DOI: 10.1016/0023-9690(81)90020-5.

Moser, E. I., Y. Roudi, M. P. Witter, C. Kentros, T. Bonhoeffer and M.-B. Moser (July 2014). "Grid cells and cortical representation". In: *Nature Reviews Neuroscience* 15.7. Number: 7 Publisher: Nature Publishing Group, pp. 466–481. DOI: 10.1038/nrn3766.

Mukamel, E. A., A. Nimmerjahn and M. J. Schnitzer (24th Sept. 2009). "Automated analysis of cellular signals from large-scale calcium imaging data". In: *Neuron* 63.6, pp. 747–760. DOI: 10.1016/j.neuron.2009.08.009.

Muller, R. U., J. B. Ranck and J. S. Taube (1st Apr. 1996). "Head direction cells: properties and functional significance". In: *Current Opinion in Neurobiology* 6.2, pp. 196–206. DOI: 10.1016/S0959-4388(96)80073-0.

Murugan, M. et al. (14th Dec. 2017). "Combined Social and Spatial Coding in a Descending Projection from the Prefrontal Cortex". In: *Cell* 171.7. Publisher: Elsevier, 1663–1677.e16. DOI: 10.1016/j.cell.2017.11.002.

Nakajima, R., K. Takao, S. Hattori, H. Shoji, N. H. Komiyama, S. G. N. Grant and T. Miyakawa (19th July 2019). "Comprehensive behavioral analysis of heterozygous Syngap1 knockout mice". In: *Neuropsychopharmacology Reports* 39.3, pp. 223–237. DOI: 10.1002/npr2.12073.

O'Keefe, J. (1st Jan. 1976). "Place units in the hippocampus of the freely moving rat". In: *Experimental Neurology* 51.1, pp. 78–109. DOI: 10.1016/0014-4886(76)90055-8.

Pachitariu, M., C. Stringer, M. Dipoppa, S. Schröder, L. F. Rossi, H. Dalgleish, M. Carandini and K. D. Harris (20th July 2017). *Suite2p: beyond 10,000 neurons with standard two-photon microscopy*. Pages: 061507 Section: New Results. DOI: 10.1101/061507.

Parsons, C. G., W. Danysz, A. Dekundy and I. Pulte (2013). "Memantine and Cholinesterase Inhibitors: Complementary Mechanisms in the Treatment of Alzheimer's Disease". In: *Neurotoxicity Research* 24.3, pp. 358–369. DOI: 10.1007/s12640-013-9398-z.

Rubin, A., L. Sheintuch, N. Brande-Eilat, O. Pinchasof, Y. Rechavi, N. Geva and Y. Ziv (18th Oct. 2019). "Revealing neural correlates of behavior without behavioral measurements". In: *Nature Communications* 10.1. Number: 1 Publisher: Nature Publishing Group, p. 4745. DOI: 10.1038/s41467-019-12724-2.

Saxena, K., J. Webster, A. Hallas-Potts, R. Mackenzie, P. A. Spooner, D. Thomson, P. Kind, S. Chatterji and R. G. M. Morris (13th June 2018). "Experiential contributions to social dominance in a rat model of fragile-X syndrome". In: *Proceedings of the Royal Society B: Biological Sciences* 285.1880, p. 20180294. DOI: 10.1098/rspb.2018.0294.

Saxena, K., P. A. Spooner, R. Mitchell-Heggs and R. G. M. Morris (1st May 2021). "iHELMET: A 3D-printing solution for safe endoscopic Ca2+ recording in social neuroscience". In: *Journal of Neuroscience Methods* 355, p. 109109. DOI: 10.1016/j.jneumeth.2021.109109.

Stringer, C., M. Pachitariu, N. Steinmetz, C. B. Reddy, M. Carandini and K. D. Harris (19th Apr. 2019). "Spontaneous Behaviors Drive Multidimensional, Brain-wide Activity". In: *Science (New York, N.Y.)* 364.6437, p. 255. DOI: 10.1126/science.aav7893.

Tallman, C. W., R. E. Clark and C. N. Smith (2nd Oct. 2022). "Human brain activity and functional connectivity as memories age from one hour to one month". In: *Cognitive Neuroscience* 13.3, pp. 115–133. DOI: 10.1080/17588928.2021.2021164.

Wang, C., X. Chen and J. J. Knierim (Feb. 2020). "Egocentric and allocentric representations of space in the rodent brain". In: *Current opinion in neurobiology* 60. Publisher: NIH Public Access, p. 12. DOI: 10.1016/j.conb.2019.11.005.

WHO (2021). *Global status report on the public health response to dementia*. URL: https://www.who.int/publications-detail-redirect/9789240033245 (visited on 26/04/2023).

– (2023). *WHO - Dementia*. URL: https://www.who.int/news-room/fact-sheets/detail/dementia (visited on 26/04/2023).

Widloski, J. and D. J. Foster (4th May 2022). "Flexible rerouting of hippocampal replay sequences around changing barriers in the absence of global place field remapping". In: *Neuron* 110.9, 1547–1558.e8. DOI: 10.1016/j.neuron.2022.02.002.

Yu, B. M., C. Kemere, G. Santhanam, A. Afshar, S. I. Ryu, T. H. Meng, M. Sahani and K. V. Shenoy (May 2007). "Mixture of Trajectory Models for Neural Decoding of Goal-Directed Movements". In: *Journal of Neurophysiology* 97.5. Publisher: American Physiological Society, pp. 3763–3780. DOI: 10.1152/jn.00482.2006.

Zhou, P. et al. (22nd Feb. 2018). "Efficient and accurate extraction of in vivo calcium signals from microendoscopic video data". In: *eLife* 7, e28728. DOI: 10.7554/eLife.28728.

Chapter 4

Research Papers

4.1 Changes in brain activity and connectivity as memories age

COGNITIVE NEUROSCIENCE
2022, VOL. 13, NOS. 3–4, 141–143
https://doi.org/10.1080/17588928.2022.2076076

Routledge
Taylor & Francis Group

Changes in brain activity and connectivity as memories age

Francesco Gobbo[a], Rufus Mitchell-Heggs[a,b] and Dorothy Tse[c]

[a]Centre for Discover Brain Sciences, Deanery of Biomedical Sciences, University of Edinburgh, UK; [b]Department of Bioengineering and Centre for Neurotechnology, Imperial College London, London, UK; [c]Department of Psychology, Edge Hill University, Ormskirk, UK

ABSTRACT

The role of the hippocampus during memory consolidation is not fully understood, with human and animal experiments producing conflicting conclusions. In particular, human lesion studies tend to indicate that the hippocampus gradually becomes independent from memory over years, whilst animal studies suggest that this can happen over days. Tallman et al. (this issue) used fMRI to investigate activity and functional connectivity in the brain at four different time points following memory encoding. Their findings include a decrease in functional connectivity between the hippocampus and parahippocampal cortex with memory age, which supports the system consolidation theory, but also argues against the reduced involvement of the hippocampus over time. This study sheds new light on the neurobiology of memory.

ARTICLE HISTORY
Received 21 April 2022
Published online 13 June 2022

Keywords
Memory; FMRI; functional brain activity; memory consolidation; human neuroscience

A fundamental question in neuroscience is whether recent and remote memories are represented in a similar or different way by the hippocampus, and whether this brain area is necessary for remembering in both cases. In general, most theories agree that the hippocampus is necessary for encoding, while over time the cortex acquires more importance in supporting episodic and autobiographic memories. However, the role of the hippocampus in supporting remote memories is contentious. According to the standard model of memory consolidation (SMC), older memories become gradually independent of hippocampal function. Despite experimental support in animal and human studies (Rempel-Clower et al., 1996; Zola-Morgan & Squire, 1990), the very fact that the gradient observed in several patients' retrograde amnesia can span decades has led some authors to question this model (Nadel & Moscovitcht, 1997). Another theory, multiple trace theory (MTT), postulates that the hippocampus is always involved in the storage and retrieval of episodic memories and that memory retrieval multiplies the traces associated with the earlier memory. In addition, rapid memory consolidation theory occurs when new information is readily incorporated into prior knowledge (schema) with parallel encoding in the hippocampus and prefrontal cortex (Tse et al., 2007, 2011).

Several human studies, focusing on an early time periods (hours to several months following learning) have helped us to understand the temporal dependency of hippocampal involvement in memory storage, but results have been surprisingly mixed. The results of Tallman et al. (this issue) provide a valuable comparison of brain activity and functional connectivity in memories from four different time points, the most remote being 1 month.

Tallman et al. (this issue) reported no significant changes in hippocampus activity during memory retrieval at different time points due to the lack of a monotonic increase or decrease of the FMRI signal in the hippocampal area as a function of memory age. Furthermore, they found a decrease in functional connectivity between the hippocampus and several cortical areas. This is in contrast with the prediction of the MTT, which would expect an increase in hippocampal activity over time. Instead, we argue that these findings are compatible with the predictions by the SMC consolidation theory. While some researchers (including the authors of this study) have typically interpreted a reduced involvement of the hippocampus in remote memory as evidence for the SMC, the theory does not exclude it. Rather, what it postulates is a progressive independence of memory retrieval from the hippocampus due to the involvement of cortical areas (Squire et al., 1984, 2015).

In agreement with previous literature, the authors observed increased activity in several anterior cortical areas with memory age. Unlike other longitudinal studies (Du et al., 2019; Gais et al., 2007; Stark & Squire, 2000; Suchan et al., 2008; Takashima et al., 2006; Yamashita et al., 2009), the authors did not find a significant modulation of hippocampal activity across memory age in their experimental time window of 1 month. This may reflect the use of multiple time points and a variety of memory types being implemented. For instance, the items to be

CONTACT Dorothy Tse Department of Psychology, Edge Hill University, Ormskirk, UK

remembered were words, paired associations, or images of various complexities. Some experiments test different memory time points in a single fMRI imaging session (Du et al., 2019; Tallman et al., this issue), while others use a single learning reference and perform longitudinal studies with repeated fMRI sessions (Harand et al., 2012; Takashima et al., 2006). The strongest disagreement regarding the hippocampus reactivation between recent and remote time points in the literature arises when the comparison time window spans around 1 month but is more concordant when the remote memory is 2 months or older (Tallman et al., this issue, Supplementary Table 6). This may not be surprising if the process of system consolidation occurs with a typical timescale of around a month. Different mnemonic procedures may bidirectionally influence the speed of consolidation, possibly explaining these differences.

The use of multiple time points, a strong aspect of the analysis of Tallman et al. (this issue), could be extended to incorporate both longitudinal and parallel imaging, thereby producing a fMRI imaging dataset comparing both memories of different ages at a single time point and the evolution of individual memories over time. Although challenging, such a study would allow multiple comparisons with uniform experimental parameters.

By comparing remembered versus forgotten , the authors observe that successful retrieval activates the hippocampus. A potentially relevant aspect is that the authors ask participants to evaluate the novelty or recognition of the images on a 1-to-6 scale. Even though the authors exclude variations in confidence values that significantly modulate brain activity, the measured brain activity may reflect not only memory (whether the participant has seen the image or not) but also metamemory, i.e., the participant being asked to assign a degree of confidence to the memory. This might involve areas not necessarily relevant to memory per se (Chua et al., 2009), or involuntarily promote a mental 'time travel' to the moment of learning, hence reactivating the hippocampus in the process of scene reconstruction (Barry & Maguire, 2019). Harand et al. (2012) reported continuous hippocampus involvement for images remembered in an 'episodic' way, but not for images which only produced a sense of recognition. This may explain the continuous involvement of the hippocampus observed in despite the decaying functional connectivity with a network of cortical areas, which would instead reflect consolidation.

In conclusion, the data from Tallman et al. (this issue) provide new data to the contentious topic of system consolidation in humans. While providing some support to the SMC theory, they highlight some aspects which may be regarded as challenging some formulations of this theory. This underscores the need to formalize the theoretical predictions of memory consolidation theories and variants thereof. Lastly, the data and the literature comparison presented by the authors point to the 1- to 2-month period as the most interesting time point that may coincide with critical memory maturation events, and therefore deserves further research.

Disclosure statement

No potential conflict of interest was reported by the author(s).

Funding

The author(s) reported there is no funding associated with the work featured in this article.

References

Barry, D. N., & Maguire, E. A. (2019). Remote Memory and the Hippocampus: A Constructive Critique. *Trends in Cognitive Sciences*, *23*(2), 128–142. https://doi.org/10.1016/j.tics.2018.11.005

Chua, E. F., Schacter, D. L., & Sperling, R. A. (2009). Neural correlates of metamemory: A comparison of feeling-of-knowing and retrospective confidence judgments. *Journal of Cognitive Neuroscience*, *21*(9), 1751–1765. https://doi.org/10.1162/jocn.2009.21123

Du, X., Zhan, L., Chen, G., Guo, D., Li, C., Moscovitch, M., & Yang, J. (2019). Differential activation of the medial temporal lobe during item and associative memory across time. *Neuropsychologia*, *135*, 107252. https://doi.org/10.1016/j.neuropsychologia.2019.107252

Gais, S., Albouy, G., Boly, M., Dang-Vu, T. T., Darsaud, A., Desseilles, M., Rauchs, G., Schabus, M., Sterpenich, V., Vandewalle, G., Maquet, P., & Peigneux, P. (2007). Sleep transforms the cerebral trace of declarative memories. *Proceedings of the National Academy of Sciences of the United States of America*, *104*(47), 18778–18783.

Harand, C., Bertran, F., la Joie, R., Landeau, B., Mézenge, F., Desgranges, B., Peigneux, P., Eustache, F., Rauchs, G., & Johnson, E. C. (2012). The hippocampus remains activated over the long term for the retrieval of truly episodic memories. *PLoS ONE*, *7*(8), e43495. https://doi.org/10.1371/journal.pone.0043495

Nadel, L., & Moscovitcht, M. (1997). Memory consolidation, retrograde amnesia and the hippocampal complex. *Current Opinion in Neurobiology*, *7*(2), 217–227. https://doi.org/10.1016/S0959-4388(97)80010-4

Rempel-Clower, N. L., Zola, S. M., Squire, L. R., & Amaral, D. G. (1996). Three cases of enduring memory impairment after bilateral damage limited to the hippocampal formation. *Journal of Neuroscience*, *16*(16), 5233–5255. https://doi.org/10.1523/JNEUROSCI.16-16-05233.1996

Squire, L. R., Genzel, L., Wixted, J. T., & Morris, R. G. M. (2015). Memory consolidation. *Cold Spring Harbor Perspectives in Biology*, *7*(8), a021766. https://doi.org/10.1101/cshperspect.a021766

Squire, L. R., Cohen, N. J., & Nadel, L. (1984). The medial temporal region and memory consolidation: a new hypothesis. Psychobiology of Cognition.

Stark, C. E. L., & Squire, L. R. (2000). fMRI activity in the medial temporal lobe during recognition memory as a function of study-test interval. *Hippocampus*, *10*(3), 329–337. https://doi.org/10.1002/1098-1063(2000)10:3<329::AID-HIPO13>3.0.CO;2-Z

Suchan, B., Gayk, A. E., Schmid, G., Köster, O., & Daum, I. (2008). Hippocampal involvement in recollection but not familiarity across time: A prospective study. *Hippocampus*, *18*(1), 92–98. https://doi.org/10.1002/hipo.20371

Takashima, A., Petersson, K. M., Rutters, F., Tendolkar, I., Jensen, O., Zwarts, M. J., McNaughton, B. L., & Fernández, G. (2006). Declarative memory consolidation in humans: A prospective functional magnetic resonance imaging study. *Proceedings of the National Academy of Sciences of the United States of America*, *103*(3), 756–761.

Tse, D., Langston, R. F., Kakeyama, M., Bethus, I., Spooner, P. A., Wood, E. R., Witter, M. P., & Morris, R. G. (2007). Schemas and memory consolidation. *Science (New York, N.Y.)*, *316*(5821), 76–82. https://doi.org/10.1126/science.1135935

Tse, D., Takeuchi, T., Kakeyama, M., Kajii, Y., Okuno, H., Tohyama, C., Bito, H., & Morris, R. G. (2011). Schema-dependent gene activation and memory encoding in neocortex. *Science (New York, N.Y.)*, *333*(6044), 891–895. https://doi.org/10.1126/science.1205274

Yamashita, K. I., Hirose, S., Kunimatsu, A., Aoki, S., Chikazoe, J., Jimura, K., Masutani, Y., Abe, O., Ohtomo, K., Miyashita, Y., & Konishi, S. (2009). Formation of long-term memory representation in human temporal cortex related to pictorial paired associates. *Journal of Neuroscience*, *29*(33), 10335–10340. https://doi.org/10.1523/JNEUROSCI.1328-09.2009

Zola-Morgan, S. M., & Squire, L. R. (1990). The primate hippocampal formation: Evidence for a time-limited role in memory storage. *Science*, *250*(4980), 288–290. https://doi.org/10.1126/science.2218534

4.2 Experiential modulation of social dominance in a SYNGAP1 rat model of autism spectrum disorder

Received: 12 April 2021 | Revised: 29 September 2021 | Accepted: 5 October 2021

DOI: 10.1111/ejn.15500

RESEARCH REPORT

EJN European Journal of Neuroscience FENS WILEY

Experiential modulation of social dominance in a SYNGAP1 rat model of Autism Spectrum Disorders

Emma Harris[1] | **Honor Myers**[1] | **Kapil Saxena**[1,2] | **Rufus Mitchell-Heggs**[1] | **Peter Kind**[1,2] | **Shona Chattarji**[2,3] | **Richard G. M. Morris**[1,2]

[1]Edinburgh Neuroscience, Centre for Discovery Brain Sciences, 1 George Square, The University of Edinburgh, Edinburgh, UK

[2]Simons Initiative for the Developing Brain, The University of Edinburgh, Edinburgh, UK

[3]Brain Development and Disease Mechanisms, National Centre for Biological Sciences and Institute for Stem Cell Science & Regenerative Medicine, Bangalore, India

Correspondence
Richard G. M. Morris, Edinburgh Neuroscience, Centre for Discovery Brain Sciences, 1 George Square, The University of Edinburgh, Edinburgh EH8 9JZ, UK.
Email:

Funding information
Simons Foundation for the Developing Brain

Edited by: Eilis Dowd

Abstract

Advances in the understanding of developmental brain disorders such as autism spectrum disorders (ASDs) are being achieved through human neurogenetics such as, for example, identifying de novo mutations in *SYNGAP1* as one relatively common cause of ASD. A recently developed rat line lacking the calcium/lipid binding (C2) and GTPase activation protein (GAP) domain may further help uncover the neurobiological basis of deficits in children with ASD. This study focused on social dominance in the tube test using *Syngap*$^{+/\Delta\text{-}GAP}$ (rats heterozygous for the C2/GAP domain deletion) as alterations in social behaviour are a key facet of the human phenotype. Male animals of this line living together formed a stable intra-cage hierarchy, but they were submissive when living with wild-type (WT) cage-mates, thereby modelling the social withdrawal seen in ASD. The study includes a detailed analysis of specific behaviours expressed in social interactions by WT and mutant animals, including the observation that when the *Syngap*$^{+/\Delta\text{-}GAP}$ mutants that had been living together had separate dominance encounters with WT animals from other cages, the two higher ranking *Syngap*$^{+/\Delta\text{-}GAP}$ rats remained dominant whereas the two lower ranking mutants were still submissive. Although only observed in a small subset of animals, these findings support earlier observations with a rat model of Fragile X, indicating that their experience of winning or losing dominance encounters has a lasting influence on subsequent encounters with others. Our results highlight and model that

Abbreviations: ASD, autism spectrum disorder; BLIND, when experiments are conducted without the experimenter knowing the genotype or other information about the subjects or protocol that could bias their observations (an aspect of unconscious bias); BORIS, Behavioural Observation Research Interactive Software; C2, calcium lipid binding protein; FMR1, the gene Fragile C mental retardation 1; FXS, Fragile X Syndrome; GAP, GTPase activation protein. GTPases are a large family of hydrolase enzymes that bind to the nucleotide guanosine triphosphate (GTP) and hydrolyse it to guanosine diphosphate (GDP).; Het, heterozygous knock-out animal (in this case *Syngap*$^{+/\Delta\text{-}GAP}$); LTP, long-term potentiation; MAPK/ERK, mitogen-activated protein kinases and extracellular signal-regulated kinases; mEPSC, miniature excitatory postsynaptic current; mPFC, medial prefrontal cortex; NMDA, *N*-methyl-D-aspartate; Rap, a protein named after 'Rat sarcoma virus' that belongs to a class of protein called small GTPase, which are involved in transmitting signals within cells (cellular signal transduction); Ras, also a GTPase that is similar in structure to Rap; SAGE, Sigma Advanced Genetic Engineering; SYNGAP1, a gene that makes a protein called SynGAP, which is found at the junctions (aka 'gaps') between synapses.; *Syngap*$^{+/\Delta\text{-}GAP}$, rats heterozygous for the C2/GAP domain deletion; WHO, World Health Organisation; WT, wild-type.

Emma Harris, Honor Myers and Kapil Saxena shared first authors.

even with single-gene mutations, dominance phenotypes reflect an interaction between genotypic and environmental factors.

KEYWORDS
autism spectrum disorders, cognitive compensation, social dominance, social neuroscience, tube test

1 | INTRODUCTION

According to the World Health Organisation (WHO), as of 2019, 1 in 160 children worldwide develop autism spectrum disorder (ASD) (https://www.who.int/news-room/fact-sheets/detail/autism-spectrum-disorders). This neurodevelopmental disorder is characterised by early onset of impairments in social interaction and communication, limited interest in others and the presence of repetitive or stereotypical behaviours (Parikshak et al., 2013; Yoo, 2015). Multiple studies have identified de novo mutations in the synaptic Ras GTPase-activating protein 1 (*Syngap1*) gene as a risk factor for ASD (Berryer et al., 2012; Hamdan et al., 2011; O'Roak et al., 2014).

The *SYNGAP1* gene codes for a postsynaptic density protein primarily expressed in excitatory neurons (Walkup et al., 2016). The SYNGAP protein interacts with *N*-methyl-D-aspartate (NMDA) receptors and negatively regulates both Ras and Rap GTPase. Ras signalling activates the MAPK/ERK cascade, important for the induction and maintenance of long-term potentiation (LTP) via insertion of α-amino-3-hydroxy-5-methyl-4-isoxazolepropionic acid (AMPA) receptors into the postsynaptic membrane. The Rap pathway mediates long-term depression (LTD) via p38MAPK. Hence, SYNGAP is expected to play an essential role in normal synaptic function and plasticity (Kim et al., 2003; Komiyama et al., 2002). Heterozygous *Syngap*$^{+/\Delta\text{-}GAP}$ mice display strong excitatory/inhibitory imbalance in hippocampal and forebrain neural networks (Clement et al., 2012; Ozkan et al., 2014), an imbalance that has been proposed to be a contributor to the social deficits seen in ASD and other neuropsychiatric disorders (Yizhar et al., 2011). These neurobiological disruptions are associated with behavioural and cognitive phenotypes in murine models that mimic symptoms of the human condition such as elevated locomotor activity (hyper-excitability), impaired working and spatial memory, and a decreased sensitivity to painful stimuli (Clement et al., 2012; Guo et al., 2009; Muhia et al., 2010; Nakajima et al., 2019). The implicit supposition behind this animal work is that a single-gene mutation would primarily have a genetically deterministic effect on phenotype.

Few studies have addressed the altered sociability of *Syngap* mutations in rodents. A study looking at schizophrenic-like symptoms in mutant mice found that *Syngap*$^{+/-}$ animals had reduced social memory (Guo et al., 2009). Specifically, although they gave similar results to wild-type (WT) mice in the three-chambered sociability test, they failed to distinguish between a familiar and novel conspecific mouse. Furthermore, in the laboratory, *Syngap* mutants are reported to spend more time alone than interacting with other animals (novel or familiar), and less social interaction in both novel and home environments compared with WT animals (Guo et al., 2009; Nakajima et al., 2019). As ASD is primarily a social communication disorder, further characterisation of social interaction in animals modelling *SYNGAP* mutations would be valuable. This new study is conducted using rats rather than mice, which are central to a wide-ranging Simons funded programme of research at Edinburgh.

The primary aim was to establish whether *Syngap*$^{+/\Delta\text{-}GAP}$ rats are socially submissive and display a distinct profile of specific behaviours in social dominance interactions than WTs. Establishing a dominance hierarchy requires recognising social cues. Once established, a hierarchy usefully determines access to resources while minimising the need for aggressive conflict (Cummins, 2000; Fan et al., 2019). We used the dominance tube test, which is a behavioural assay of social dominance (Wang et al., 2014). It has been widely used as an assay of social hierarchy, such as to examine the relative dominance of different mouse strains (Kunkel & Wang, 2018), the neural circuits underlying dominance behaviour (Wang et al., 2011; Zhou et al., 2017), neuropsychiatric disorders such as major depression (Yang et al., 2014) and ASD-like syndromes (Huang et al., 2018; Saxena et al., 2018). With analogous results to other dominance tests, with which rankings correlate, it has been suggested as an accurate measure of social dominance (Wang et al., 2011). Mouse models have been used predominantly, but even they have been shown to reveal similar weanling dominance patterns to those of children (Chou et al., 2021).

A secondary facet of the study concerns the opportunity in social dominance interactions to learn about and

remember the other animal/person—a dimension of social experience. One might then expect deficits arising from failures of social memory (e.g., about the identity or social status of another animal). However, that very deficit may indirectly foster the development of motor habits in social interactions that are less demanding on day-to-day memory but reflect learned patterns of dominance or submissive behaviour (Miczek & de Boer, 2005). Such habits are likely more inflexible such that, once learned, they would be expressed repetitively even in inappropriate situations. Accordingly, after the initial phase of testing interactions within each cage, we examined contests between animals from different cages that had by then assumed a particular intra-cage rank.

Rats are a species that is inherently social, which has evolved a complex social repertoire (Lore & Flannelly, 1977), and the outbred nature of the rats we used more closely mimics the genetic variation seen in humans. They may, therefore, be an appropriate model for the study of human psychiatric disorders characterised by deficits in social cognition (Ellenbroek & Youn, 2016). Saxena et al. (2018) studied *FMR1* knockout (*Fmr1*$^{-/y}$) rats as a model for Fragile X Syndrome (FXS), another monogenic cause of autism that shares many of the behavioural deficits seen in *Syngap*$^{+/-}$ animals (Ding et al., 2014; Kazdoba et al., 2014; McNaughton et al., 2008; Spencer et al., 2005). As expected, male knockout rats were submissive to WT animals in mixed-line groups living together, a finding that makes sense in terms of model 'validity'. However, a small number of high- and low-ranking FXS mutants who had lived together and formed an *intra*-cage hierarchy went on to display the same phenotype in *inter*-cage contests. Specifically, they won (or lost) social dominance contests against stranger animals regardless of stranger rank. This study explored social dominance in *Syngap*$^{+/\Delta\text{-}GAP}$ mutants using the same experimental protocols as in our earlier study of FXS mutants (Saxena et al., 2018).

2 | MATERIALS AND METHODS

2.1 | Subjects

Adult (>12 weeks, $n = 16$) male Long-Evans hooded rats were used, weighing 500 to 600 g. The rats were cohoused in groups of four per cage, from weaning, with ad libitum food/water and a 12-h light/dark cycle. The cages contained a 25-cm-long section of Perspex tube similar to the one used in the actual tube test to allow the animals to become used to being inside such a tube. The colony founders were produced by Sigma Advanced Genetic Engineering (SAGE) labs (St. Louis, MO, USA) using the zinc finger nuclease-mediated deletion (Gurts et al., 2009) of the GTPase activation protein (GAP) domain of *Syngap*. Later rats for the experiments were bred in-house; the *Syngap*$^{+/\Delta\text{-}GAP}$ rats were generated by mating female *Syngap* heterozygous rats with male WT Long-Evans hooded rats acquired from Charles River Labs, hereafter called 'Het'. The WT animals used as controls were littermates. There was one WT single-line cage ($n = 4$), one Het cage ($n = 4$) and two mixed cages ($n_{WT} = 2$, $n_{Het} = 2$ per cage; overall $n = 8$). All experiments were done blind to genotype, with animals being given a cage number on their tail and a coloured spot on their fur (using animal paint, red, green, blue and purple) to identify them; the colouring is random. The code was retained by someone independent of the study and only broken when all procedures had been completed. The genotype of the animals was confirmed externally before and after finishing the experiments by a company (Transnetyx).

2.2 | Ethics and legal statement

The studies conducted were all behavioural and did not involve surgery or the administration of drugs. We monitored the animals carefully at all stages of handling and experimentation, particularly in Phase 2 (below) when animals from different cages were tested together. The study was conducted according to the regulations of the Animals (Scientific Procedures) Act 1986, a UK Project Licence held by RGMM (I49398628), and under the supervision of the named veterinary surgeons of the University of Edinburgh.

2.3 | Apparatus

The tube-test assay was the same as used in Saxena et al. (2018). A transparent perspex tube, 1 m long and 7 cm diameter, served to connect two holding boxes (Figure 1a). In each box, bedding was placed from the home cage of the animals to help reduce anxiety (Figure 1b). The tube was large enough for the rats to move freely, but not to cross past each other or turn around. A removable metal grid was placed in the middle of the tube, this being lifted to start an encounter that ended when one animal retreated (Figure 1c). A camera provided a direct view of the tube to record the trials using OBS recording software (https://obsproject.com/). The entire apparatus was connected to custom-made-Arduino-based hardware, and we used its serial reader functionality for reading the button presses denoting the start/stop times of the trials.

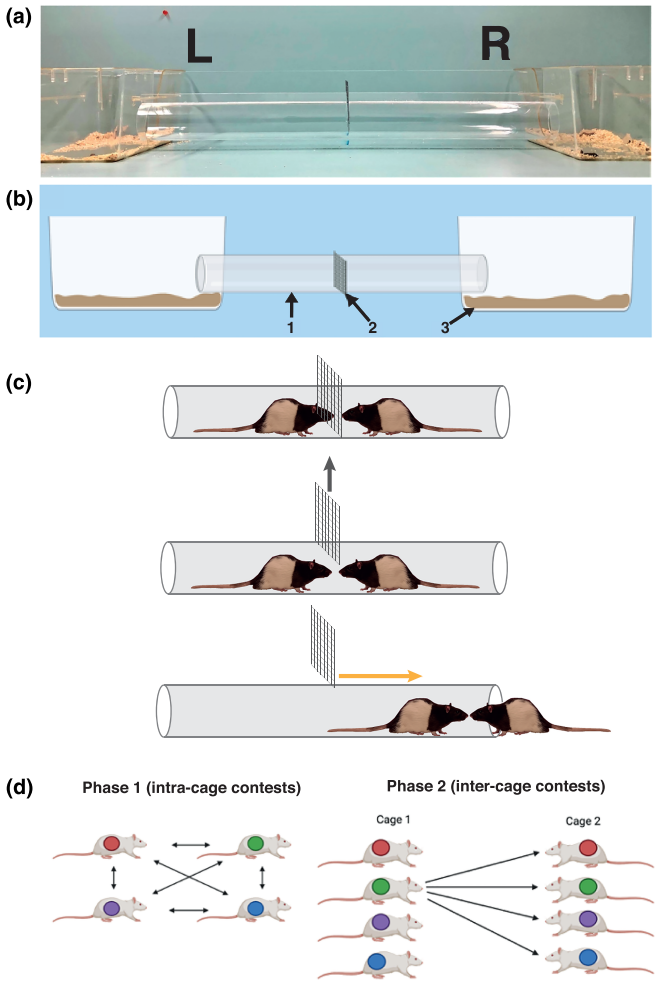

FIGURE 1 Tube-test apparatus and protocol. (a,b) The plastic, transparent tube in which dominance interactions took place (Arrow 1). A small metal grid barrier inserted at the tube centre point is used to separate the rats before the start of every trial (Arrow 2). One of two holding boxes, filled with bedding from the rats' home cages (Arrow 3). (c) Rats were placed at either end of the tube and they readily moved towards the centre point. When both rats reached the central grid barrier, the barrier was lifted and the start button pressed to begin the trial. The rats competed for dominance until the head of the 'losing rat' moved past the entrance at either end of the tube. See supplementary movie. (d) The two phases of training. Phase 1 involved contests between all animals in each cage, this being repeated across 10 sessions to secure a mean measure of within-cage ranking. Cartoon depicts all six inter-animal contests. Phase 2 consisted of competitions between cages and involved all the animals of one cage and all the animals of the other cage (4 animals [Cage 1] × 4 animals [Cage 2] = 16 animal pairs). For clarity, the cartoon depicts only one exemplar rat (green) competing against all rats of the other cage. In Phase 2, there were in four cages in total that competed against each other

2.4 | Behaviour protocols

The training protocol consisted of *Habituation*, *Phase 1 contests* between animals within a cage (intra-cage) and a *Phase 2 competition* involving all animals in one cage against all the other cages (Figure 1d; inter-cage). The experiments were performed between 9 AM to 4 PM. There were a total of 2640 competitions between individual animals.

2.4.1 | Habituation

Each animal was handled for 3 days and allowed to run freely in the apparatus (alone) for at least 10 min/day. See details of procedure in Saxena et al. (2018).

2.4.2 | Phase 1 intra-cage contests

The basic tube test consisted of two rats being placed in the holding boxes, one on each side. The rats then entered the tube and met in the middle with the metal grid present and acting as a barrier. The trial started when the barrier was removed. During the trial, the rats competed for dominance during which a variety of behaviours were observed. Typically, the animals were together, their heads side by side and relatively still for a few seconds. Thereafter, either one rat pushed the subordinate to retreat out of the tube (dominant) or the other rat withdrew of its own accord (subordinate). A trial was defined as ending when one rat backed out into the holding box from which it started. This rat was recorded as the 'loser' and the other as the 'winner'. Each pair of rats

underwent five trials each session to obtain a secure measure of dominance (3:2, 4:1 or 5:0), alternating their starting positions between left and right. All cages were tested on the same day, with the 10 sessions of 5 trials on consecutive days. The order in which the cages were trained each day was randomised in counterbalanced order.

To observe and measure intra-cage hierarchies, each animal competed against all the other animals in its cage (five runs per pair, six competitions per cage). Cage ranks were determined by adding up the number of wins or losses for each animal across all six encounters (of five trials) within a cage. The animal with the most wins was denoted as first rank. The following ranks correspond to increasing number of losses with the fourth ranked animal being the one losing the most. If two animals had the same number of losses, the relative rank was determined by which animal lost most of that pair. This daily tube-test assay was repeated over 10 sessions. There were, therefore, 4 cages $\times$ 6 encounters $\times$ 5 runs $\times$ 10 sessions ($=$ 1200). Trial latency was taken as the time (seconds) to complete one trial.

2.4.3 | Phase 2 inter-cage competitions

The procedure to conduct tube tests was exactly as above, but the animals now competed against animals in the other cages who were, effectively, stranger opponents. Each animal competed against all four animals from the other three cages. Each trial between a pair was repeated five times and all trials were repeated over three sessions. This comes up to a total of 1440 trials (6 cage interactions $\times$ 16 encounters $\times$ 5 runs $\times$ 3 sessions). We analysed only the first and third sessions for the detailed video analysis of behaviour, giving $6 \times 16 \times 5 \times 2$ contests ($=$ 960). The sequence of pairs and cages was randomised across the three sessions.

2.5 | Video analysis

Recordings from Sessions 1 and 10 of Phase 1 and Sessions 1 and 3 of Phase 2 were analysed on a frame-by-frame basis (1/20th-second resolution per frame) using Behavioural Observation Research Interactive Software (BORIS) (Friard & Gamba, 2016), with these sessions chosen for this detailed analysis as the beginning and end of each phase. Behaviours were logged for each animal as follows: PUSH (included any form of pushing, with paws, nose or body and biting), RESIST (resisting a push from an opponent), MOVE FORWARD, STILLNESS (when no displacement of the body was seen, but including other stationary activities such as sniffing or grooming), RETREAT (backing out of the tube by being pushed) and WITHDRAWAL (voluntarily backing out of the tube). It proved easy to distinguish PUSH and RESIST despite being quite similar in terms of effort.

2.6 | Statistical analysis

For all statistical analyses, we chose tests based on the data secured (wins, latency and behaviour occurrences). Values computed include total number (e.g., of wins), from which rank was derived, and means (latency and rank), occurrences of specific behaviours and measures of variability of rank (stability/variance). Stability was computed by counting the number of times an individual rat changed rank during Phase 1 without regard to whether it changed by one position of rank or more, and these data were normalised (100% stable meaning no changes in rank across the 10 sessions and 0% meaning a change every session). Variance was a similar measure and computed as the true variance of the rank scores across all 10 sessions of Phase 1. For latency and behaviour occurrences, we computed mean and standard error of the mean. For all parametric tests, the data fitted the assumptions of equal variance and were normally distributed (ANOVA and *t*-tests). For non-parametric tests, Mann–Whitney, chi-squared or a Fisher's exact test was used. The behavioural occurrences analysis for both Phases 1 and 2 required a two-way repeated measures ANOVA, with the different behaviours treated as a 'repeated measures' within subject variable. This was paired with a Sidak's multiple comparison test. The value computed in each test (e.g., *F*-ratio), significance levels and degrees of freedom are reported. GraphPad Prism v7 was used for preparing the graphs and statistics and then displayed using Adobe Illustrator.

3 | RESULTS

Qualitatively, all animals explored the tube readily during habituation and walked through it without hesitation during dominance contests. We anticipated that frequent losers might become hesitant to enter or walk through the tube over time but, surprisingly, this did not happen. We observed no signs of overt inter-animal aggression, even in contests across cages, and its absence may have contributed to the success in training of both phases of the study. All encounters were conducted and evaluated 'blind' to genotype, and the occupants of each cage were unknown to the experimenters. Although the number of animals in the study was modest ($n = 16$; WT $n = 8$,

Syngap$^{+/\Delta\text{-}GAP}$ $n = 8$), the number of contests observed was extensive ($n = 2160$).

3.1 | Phase 1 contests

The first question was whether single-line WT animals living together, and *Syngap*$^{+/\Delta\text{-}GAP}$ animals likewise (hereafter called 'Het'), would each form a hierarchy. Ranks of individual animals in single-line cages are shown in Figure 2a, with both the WTs (as expected) and Hets forming a hierarchy. The first ranked Het rat stayed at the top over all 10 sessions, all other ranks stabilising by Session 7. The mean rank was calculated from the ranks of each animal over all 10 sessions. A clear hierarchy was seen in both cages (Figure 2b); there was a statistically significant difference between ranks as determined by one-way ANOVA (WT: $F_{(3,39)} = 33.45$, $p = .0001$; Het: $F_{(3,39)} = 27.89$, $p = .0002$). No differences were observed in normalised stability (unpaired t-test, $t = .134$, df = 6, $p = .898$; Figure 2c) or variance of rank between WT and Het animals over the 10 sessions (Mann–Whitney test, $p = .829$).

The next step was to examine the hierarchies formed in each of the two mixed-line cages. Both cages showed an overall hierarchy (Figure 3a). Het rats in mixed cages won less contests than the WT animals (chi-squared test of independence, $X^2 = 68.06$, df = 1, $p < .0001$; Figure 3b). Het animals also had a lower average rank of $3.18 \pm .15$ over 10 sessions compared with WT animals with an average rank of $1.83 \pm .13$ (unpaired t-test, $t = 6.69$, df = 78, $p < .0001$; Figure 3b; the highest rank score = 1). Both comparisons were highly significant. Averaged across the two cages, there was no overlap of mean rank between the WT and Het rats (Figure 3a). With respect to trial-to-trial variability, no significant difference was detected between WT and Het animals on measures of rank stability (unpaired t-test, $t = 1.32$, df = 6, $p = .235$; Figure 3c) or variance (unpaired t-test, $t = 1.12$, df = 6, $p = .304$; Figure 3c).

The pairwise competitions took time (Figure 4). Competitions took longer at the beginning of the series of

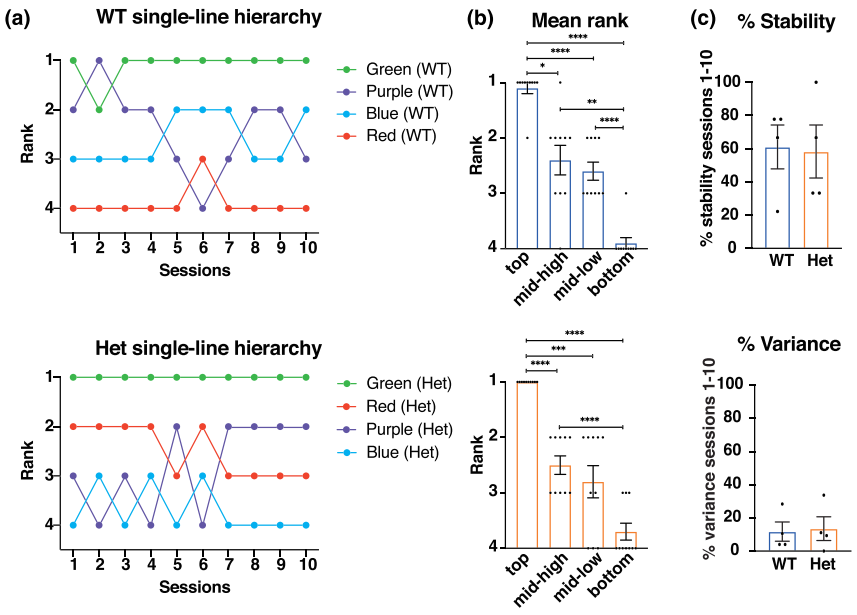

FIGURE 2 Phase 1—Establishment of intra-cage hierarchy in single line cages. (a) Cage hierarchies: Plot of individual animal rank across all 10 sessions for WT and Het single-line cages. The four colours represent each cage individual, the colour code plotted in accordance with average rank across all 10 sessions. (b) Mean ranks and individual data points (for each session) of the WT cage (blue) and *Syngap* 'Het' cage (orange) showed significant hierarchies in both cages (WT: $F_{(1.378,\ 12.40)} = 33.45$, $p \leq .0001$, with Greenhouse–Geisser correction for degrees of freedom; Het: $F_{(1.138,\ 10.24)} = 27.89$, $p = .0002$). (c) No significant differences were observed between WT and Het lines with respect to either stability (two-tailed, unpaired t-test, $t(6) = .195$, $p = .852$, $n = 4$) or variance (t-test, $t(6) = .193$, $p = .853$, $n = 4$). Means ± 1 SEM. *$p < .05$, **$p < .01$, ***$p < .001$, ****$p < .0001$, in Tukey's multiple comparison test. See main text for details

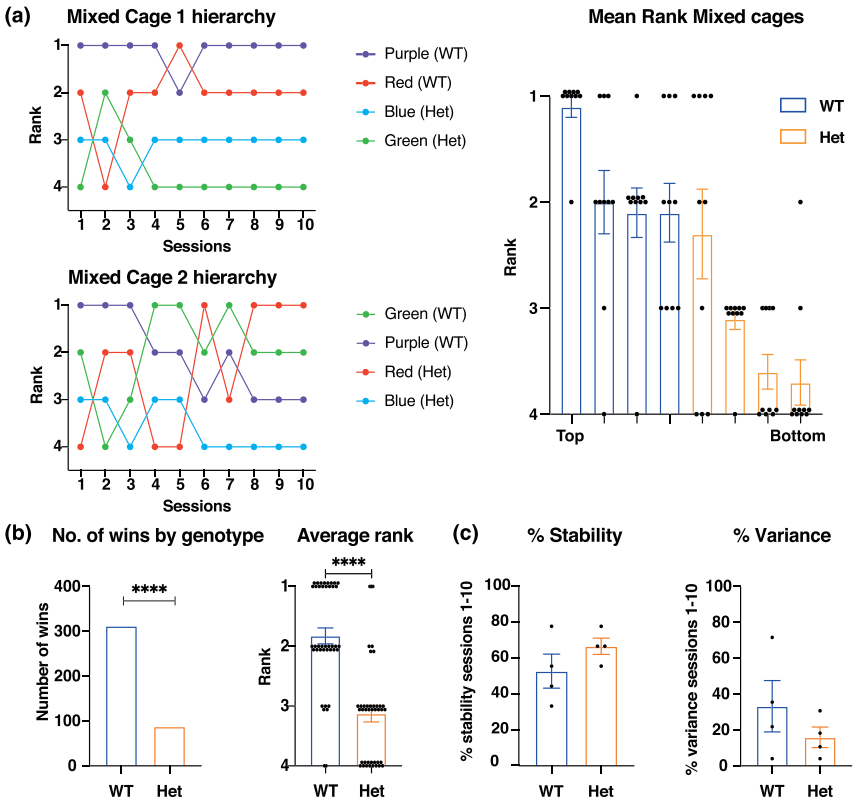

FIGURE 3 Phase 1—Establishment of intra-cage hierarchy in mixed-line cages. (a) Cage hierarchies: Plot of individual animal rank across all 10 sessions for WT and Het single-line cages. The four colours represent each cage individual, the colour code plotted in accordance with average rank across all 10 sessions. There was no overlap between the more dominant WT (blue) and more submissive Het animals (orange), although the three submissive WTs were broadly comparable with the most dominant Het. (b) Contest wins and average rank in the mixed cages: There were highly significant differences between the number of wins ($X^2 = 68.06$, df = 1, $p < .0001$) and average rank of WT and Het animals ($t = 6.73$, df = 78, $p < .0001$). (c) As in the single-line cages, there were no differences observed with respect to either stability (unpaired t-test, $t(6) = 1.321$, $p = .235$) or variance ($t(6) = 1.124$, $p = .304$). Means ± 1 SEM. ****$p < .0001$

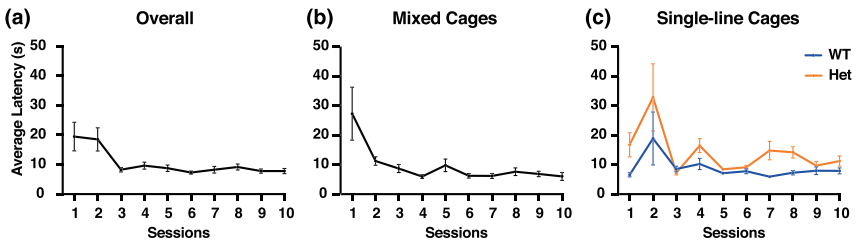

FIGURE 4 Phase 1—Time taken to complete individual contests (latency). (a) Average latency of trials (s) from all pairs of rats from all cages over 10 sessions ($n = 16$). (b,c) Average latency for mixed cages ($n = 8$) and single-line cages ($n = 8$). Note the longer time taken by Het animals in the single-line cages. For all graphs, individual latency data points for each pairing are not shown in order to increase clarity of results. Means ± 1 SEM

10 sessions, averaging 19.5 ± 4.84 s from the moment the barrier between the two animals in the tube was raised and the point when one of them fully retreated, but this time declined to less than 10 s by Session 3 (8.27 ± .74 s; Figure 4a) and then stabilised. This overall decline was significant (one-way repeated measures ANOVA, $F_{9.207} = 4.92$, $p = .0094$; Figure 4a). The pattern for latencies for the 50% subset of mixed-line cages was much the same (one-way repeated measures ANOVA, $F_{9.99} = 5.08$, $p = .032$; Figure 4b). For the single-line cages, Het animals displayed longer latencies than WT (two-way repeated measures ANOVA, $F_{1.6} = 12.3$, $p = .0056$; Figure 4c).

A key next question was whether the specific patterns of behaviour (e.g., PUSH and RETREAT) displayed during dominance encounters differed as a function of dominance or genotype. The video analysis showed a clear interaction between rank and behaviour occurrences (two-way repeated measures ANOVA, $F_{5.70} = 4.54$, $p = .0012$; Figure 5a). The trend shows that high-rank animals were more likely to PUSH and MOVE FORWARD compared with the low-rank animals who executed more RETREAT and WITHDRAWAL. In certain respects, such a pattern must occur by definition. However, the high occurrences of STILLNESS in high-rank animals were not expected a priori. One complication in quantifying the 'occurrences' of such behaviours is that PUSH behaviour may occur several times during a trial, often met by RESIST behaviour from the other animal. However, RETREAT happens less frequently and may, in the limit, happen only once to resolve a contest. Attempting to 'normalise' their relative behaviours to create a numerical 'level playing field' by examining occurrences over durations of time in order to calculate a measure of frequency does not help, as pushing can start and stop throughout a trial and thus the full duration of the trial would have to be considered the duration; but equally, retreat can happen at any time, even if only

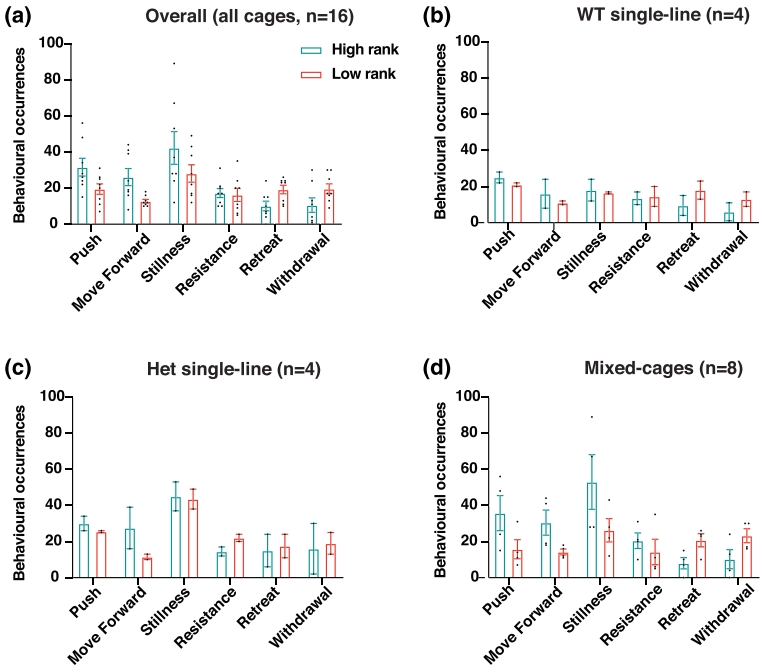

FIGURE 5 Phase 1—Patterns of behaviour observed during contests. (a) Sum of occurrences of various behaviours by individual animals plotted as a function of overall rank, together with individual animal data ($n = 16$). High rank is animals in Ranks 1 and 2 of a cage (green); low rank is animals in Ranks 3 and 4 of a cage (red). (b) Sum of occurrences of behaviours by WT animals living together ($n = 4$). (c) Sum of occurrences of behaviours by Het animals living together ($n = 4$). Note the high occurrence of 'STILLNESS' in this cage (>40) but not the WT cage (<20). (d) Sum of occurrences of behaviours by high- and low-rank WT and Het animals living together in mixed cages ($n = 8$). Note that STILLNESS is again high, but in these cages restricted to the high-rank animals (i.e., the WT rats). For all graphs, behavioural occurrences were taken as an overall count of each behaviour for each animal over 240 trials from Phase 1, Sessions 1 and 10. Means ± 1 SEM

once, and thus, the duration of time for calculating frequency is the same. However, the overall higher behaviour occurrences of the single-line Het cage than the single-line WT cage (Figure 5b,c) are consistent with the latency data of Figure 4. Moreover, the significant interaction between rank and behaviour (two-way repeated measures ANOVA, $F_{5.30} = 4.46$, $p = .0037$; Figure 5d) was observed only in the mixed-line cages in which the high-rank animals were, in practice, WT rats.

With respect to STILLNESS behaviour, frequently occurring while the two animals are in close contact and during which dominance 'decisions' may be being made, single-line Het rats animals had significantly higher STILLNESS occurrences than single-line WT animals (Sidak's multiple comparison test, $p = .0131$; cf. Figure 5c with 5b). This was not observed in the mixed cages (unpaired *t*-test, $t = .732$, df = 6, $p = .492$; data not shown), for which the primary determinant of STILLNESS was rank (Figure 5d).

3.2 | Phase 2 inter-cage competitions

The second phase of testing was an inter-cage tournament in which the animals underwent tube-test competitions against all animals from the other cages. In contrast to Phase 1 in which WT animals were clearly dominant, the phenotype now reflected some facets of the rank of the animals in Phase 1. Intriguingly, Het animals now won as equally often as WT rats (Fisher's exact test, $p = .553$; Figure 6a). In fact, the Hets in single-line cages won significantly *more* competitions against single-line WT animals from different cages (Fisher's exact test, $p = .0321$; Figure 6b), whereas mixed-cage Het rats lost more contests against stranger mixed-cage WT animals (Fisher's exact test, $p = .0152$; Figure 6c). These changes are identical to what was observed by Saxena et al. (2018) in a rat model of FXS.

One possibility is that rank was simply unstable between Phases 1 and 2 and that there are major reliability issues with the measures being quantified and the experimental approach being taken. However, rank in Phase 1 (regardless of genotype) was predictive of winning/losing in Phase 2 (Figure 6d). That is, the overall number of wins in Phase 2 by animals that were high rank in Phase 1 was significantly higher than those of Phase 1 low-rank animals (Fisher's exact test, $p < .0001$). This indicates that previous experience of winning or losing can be predictive of the outcome of competing against a stranger.

Logic then required us to distinguish high-rank and low-rank animals as a function of genotype. In a single-line cage, there will be two animals in Ranks 1 and 2, which we shall refer as 'high rank' and the other two animals (Ranks 3 and 4) as 'low rank'; this is also true of the Het single-line cage than of the WT single-line cage. One possibility is that a Het winner may 'get used' to winning and a Het loser 'get used' to losing—that is, their social dominance interactions become habits, possibly because of a deficit in social perception or memory. The 10 sessions of 5 encounters per session in Phase 1 provided 50 trials between a pair in which to develop habits in the tube test, such as habits of pushing or retreating. Interestingly from the perspective of habit versus memory, high-rank Het animals won significantly more competitions against high-rank WT rats (Fisher's exact test, $p = .0009$; Figure 6e), whereas low-rank Hets performed equivalently to low-rank WT rats when competing against them (Fisher's exact test, $p > .99$; Figure 6f). By the same argument, Het animals living in mixed cages (generally in Ranks 3 and 4) would be expected to be submissive to single-line WTs, which they were (Fisher's exact test, $p = .0321$), having a developed habit of withdrawal and retreat.

These findings in Phase 2 are statistically significant, but modest, as they entail comparisons between subsets of animals with an '*n*' of only 2, 4 and 6. Nonetheless, they raise the possibility that there may be a difference between winning when you can process social cues effectively and winning when you cannot. Variations in the occurrences of distinct behaviours in the tube may reflect these differing states of affairs. Overall, behaviour and rank interacted significantly to affect the behavioural occurrences (two-way repeated measures ANOVA, $F_{5.70} = 4.40$, $p = .0015$; Figure 7a), but there was no significant interaction between behaviour and genotype (two-way repeated measures ANOVA, $F_{5.70} = .39$, $p = .854$; Figure 7b). These data suggest that, in the inter-cage contests of Phase 2, previous experience determines future behaviour more than genotype.

As the data on combined effect of rank and genotype was revealing with respect to dominance, it might also have affected behaviour occurrences. For trials between high-ranking animals, genotype interacted significantly with behaviour (two-way repeated measures ANOVA, $F_{5.30} = 8.81$, $p < .0001$; Figure 7c), with genotype accounting for a significant amount of the variance seen in the behavioural occurrences (two-way repeated measures ANOVA, $F_{1.6} = 42.57$, $p = .006$). A trend reveals that high-ranking Het animals had a higher occurrence of PUSH, MOVE FORWARD, STILLNESS and RESIST behaviours compared with high-rank WT. This indeed complements the findings in Figure 6e as an increase in these behaviours would explain the increased number of wins. For competitions between low-ranking rats, there

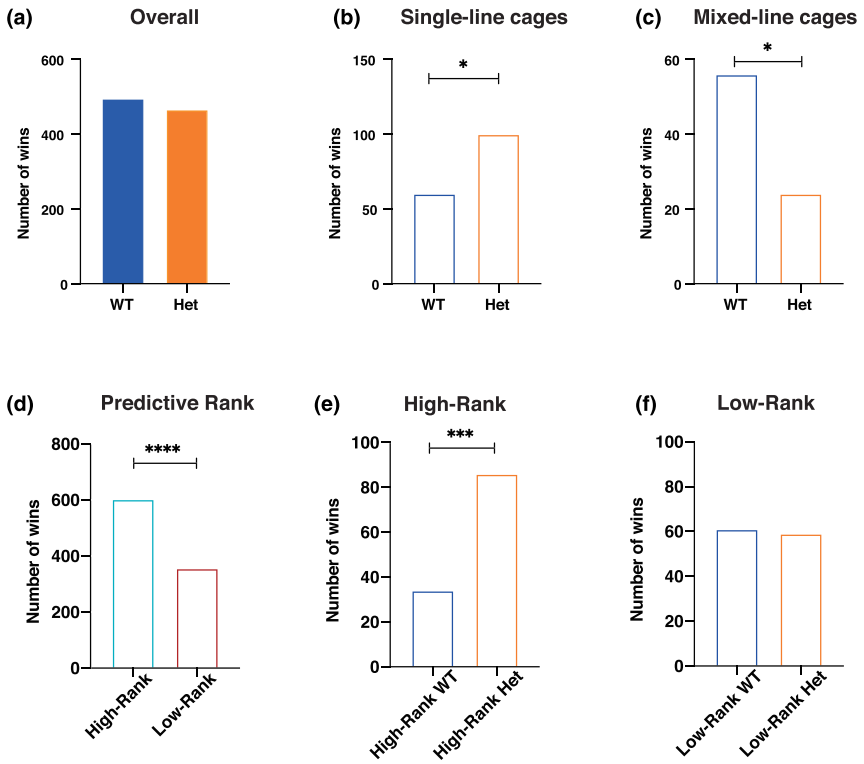

FIGURE 6 Phase 2—Competitions between animals from different cages as a function of genotype and rank predicted from Phase 1. (a) The overall phenotype of WT dominance phenotype of Phase 1 was lost in Phase 2—WT and Het animals won an equivalent number of contests. (b,c) Contests won by WT and Het animals that had lived in single-line cages (b, $n = 4$ per cage) or mixed-line cages (c, $n = 4$ per cage). Note that Het animals from single-line cages won more contests in Phase 2, whereas WT animals from mixed-line cages won more contests. (d) Predictive rank: When wins and losses in Phase 2 are plotted as a function of rank secured by animals in Phase 1 (high vs. low), the Phase 1 rank is predictive of the outcome of contests in Phase 2. (e) In contests between high-rank animals ($n = 6$ WT; $n = 2$ Het), the Het animals won far more contests. (f) In contests between low-rank animals ($n = 2$ WT; $n = 6$ Het), the total number of wins was equivalent. Means ± 1 SEM. *$p < .05$, ***$p < .001$, ****$p < .0001$. See text for details and comments on numbers of animals

was also a significant interaction between genotype and behaviour but in the opposite direction (two-way repeated measures ANOVA, $F_{5.30} = 19.0$, $p < .0001$; Figure 7d). The overall behavioural occurrence was now relatively higher in WTs (two-way mixed-model ANOVA, $F_{1.6} = 78.7$, $p = .0001$; Figure 7d), and specifically, low-rank WT animals had a higher occurrence of PUSH behaviour (mean ± SE = 68.0 ± 1.41) than low-rank Het animals (mean ± SE = 21.7 ± 2.26) (Sidak's multiple comparison test, $p < .0001$; Figure 7d). This would suggest that the WT should be dominant over the Het animals, but, as shown in Figure 6f, it was not the case. The reason may be that low-rank WT animals also had a high RETREAT occurrence (Sidak's multiple comparison test, $p = .0091$).

4 | DISCUSSION

The aim of this study was to examine the generality of the idea that ASD model animals would show consistent changes in social dominance relative to WT animals. Using a social dominance tube-test paradigm, we observed that male Het *Syngap*$^{+/\Delta\text{-}GAP}$ animals living together form a stable hierarchy but, when living with WT animals, have a submissive phenotype compared with their WT cage-mates. This models social withdrawal and is analogous to what we observed with FXS mutants (Saxena et al., 2018). Specific behaviours exhibited during the tube test included expected facets (such as greater PUSH behaviour by dominant animals), but also a striking increase in STILLNESS behaviour by the Het animals

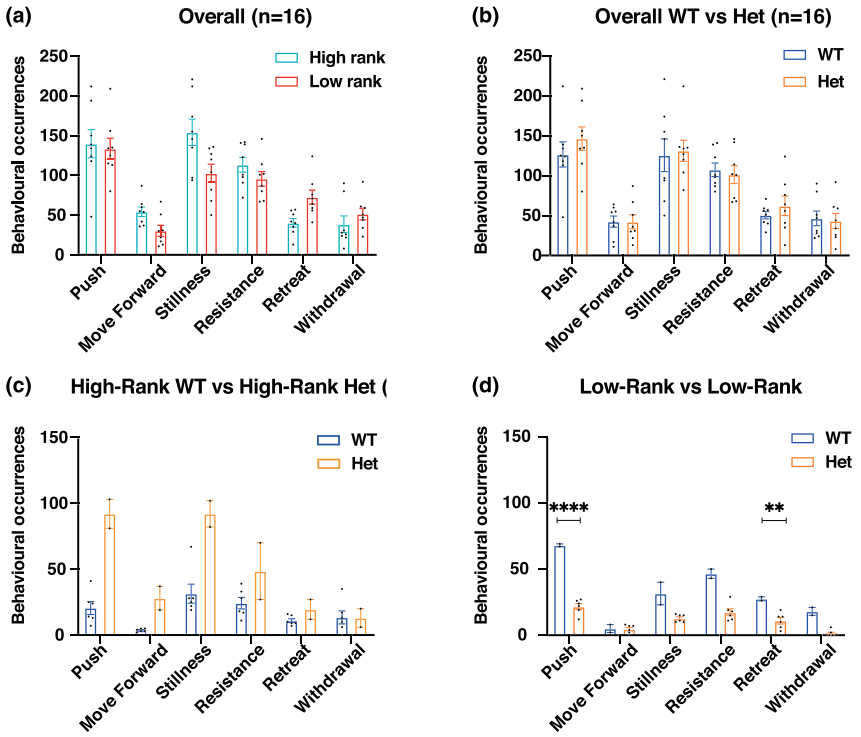

FIGURE 7 Phase 2—Patterns of behaviour observed during contests (Sessions 1 and 3). (a) In Phase 2, there was modest but a significant difference between rank and behaviour subtypes. The trends suggest that high-ranking animals showed more moving forward and stillness but less retreat. (b) No significant difference in behaviour subtypes was observed when WT animals were compared with Het. (c) Analysis of only the contests between high-ranking WT and Het animals revealed striking interaction was found between high-ranking WT and Het animals and social behaviour subtype (ANOVA; $F_{(5,30)} = 8.807$, $p \leq .001$). The data reveal high-ranking Het displayed more of every behaviour subtype except withdrawal. (d) The opposite pattern prevailed for trials only involving the contests between low-ranking WT and Het animals (ANOVA; $F_{(5,30)} = 18.99$, $p \leq .001$). For all graphs, behavioural occurrences were taken as an overall count of each behaviour for each animal over the 960 trials of Sessions 1 and 3 of Phase 2. Means ± 1 SEM. $^{**}p < .01$, $^{****}p < .0001$

housed in the single-line cage and a higher latency to resolve conflicts when two Het animals competed, both suggestive of a social processing deficit. We also found that social dominance experience affects subsequent interactions, interacting in a subset of animals in a surprising way with genotype. Het animals ($n = 2$) that were previously dominant in single-line cages in the intra-cage analyses (Phase 1) of the study were, in the inter-cage (Phase 2) tournaments, also dominant against all animals from other cages including previously dominant WT rats ($n = 6$). Het animals ($n = 6$) that were previously submissive continued to be largely submissive. These observations are subject to the qualification of small '*n*' (2 and 6, respectively), but they do replicate in another ASD line the paradoxical reversal of phenotype observed in a much larger number of FXS mutants by Saxena et al. (2018). They also add to earlier observations of some similarities between Syngap and FXS mutant mice despite various differences (Barnes et al., 2015). We shall argue that these data collectively point to a reduced ability of *Syngap*$^{+/\Delta\text{-}GAP}$ animals to process social cues.

The patterns we observed resemble behaviours observed in ASD children. More severely impaired individuals show rigid operant learning in which they continue to use a previously learned strategy, even across different contexts (A. Stanfield, personal communication; 29 April 2020). Moreover, children with autism are both more likely to be 'bullied' by their siblings but also to 'bully' them back (Toseeb et al., 2018). Perhaps these behaviours, once they develop, become inflexible habits. The dual phenotype of *Syngap*$^{+/\Delta\text{-}GAP}$ behaviour we observed, from the *submissive* Het animals living in the

mixed cages through to the suggestion of *dominant* single-line Hets winning novel encounters, may model this facet of the apparently opposing behaviours seen in ASD children. In Katsanevaki et al.'s (2020) original study of this line of *Syngap*$^{+/\Delta\text{-}GAP}$ rats, they observed a failure to extinguish a conditioned fear response despite many sessions of 'extinction'. They saw normal sociability as measured by proximity, but the mutants showed a striking decrease in active sniffing of the other animal. Interestingly, in a study of both children and weanling mice, Chou et al. (2021) show that (normal) children who are less persistent in games, have low emotional intensity and withdraw from social encounters easily are more likely to be subordinate. They go on to show, in a demonstration of face validity, that tube-test contests between mice tend to be resolved most often by loser withdrawal. Collectively, these results highlight and model the current belief that ASD reflects environmental interactions with a genetic predisposition (Chaste & Leboyer, 2012). Thus, depending on their rearing environment and previous social history in competitive interactions, children and animals with an ASD mutation (*FMR1, SYNGAP1*) may present different behavioural phenotypes.

4.1 | The pattern of behavioural findings

Syngap1 mutations in mice lead to severe cognitive impairment, including deficits in social memory (Guo et al., 2009; Komiyama et al., 2002; Muhia et al., 2010; Ozkan et al., 2014). The *Syngap*$^{+/\Delta\text{-}GAP}$ animals living in mixed cages were clearly submissive to their WT cage-mates, and thus, both WTs were in Ranks 1 and 2. This is a similar phenotype to the *Fmr1*$^{-/y}$ rats of Saxena et al. (2018).

We also reasoned that *Syngap*$^{+/\Delta\text{-}GAP}$ rats *would* be able to form a hierarchy but that it would be *less* stable than WT animals, as seen in the *Fmr1*$^{-/y}$ model of ASD (Saxena et al., 2018). We found, however, that the Het rats were not only able to form a hierarchy but did so with statistically similar stability and variance of rank to WT. Although there are some exceptions (e.g., the purple rat in the WT single-line cage that changed its rank seven out of nine times, and the red animal in the Mixed Cage 1 and Cage 2), some of the Het rats were more stable than the WTs in the mixed cages. These results suggest that Het animals may have enough social memory to distinguish between the ranks of the conspecifics with whom they are living. It is possible that rank stability observed in Hets reflects a lack of motivation, or a tendency to 'give up' easily by rats in the lower order of hierarchy.

The *Syngap*$^{+/\Delta\text{-}GAP}$ animals living in mixed cages were submissive to their WT cage-mates. However during encounters against novel conspecifics (the inter-cage assessments in Phase 2), we found that high-rank *Syngap*$^{+/\Delta\text{-}GAP}$ animals who had lived in single-line cages with other Syngap animal won over the high-rank WTs whereas low-rank *Syngap*$^{+/\Delta\text{-}GAP}$ animals showed a different pattern. In presenting these results, we noted the qualification that the numbers of animals in these comparisons (2 and 6) were small, but it should be recognised that the number of competitions they undertook was quite large. What is suggestive is that these are very similar results to Saxena et al.'s (2018) *FXS* model, raising the possibility that both *Fmr1*$^{-/y}$ and *Syngap*$^{+/\Delta\text{-}GAP}$ rats are poorer in detecting social cues relating to the dominance status of an opponent. Faced with this cognitive deficit, they may therefore develop habits of repetitive behaviour during Phase 1 that serve them well. Specifically, high-rank *Syngap*$^{+/\Delta\text{-}GAP}$ animals would have won more frequently against low-rank animals in their single-line cage (10 sessions of 5 trials per inter-animal encounter) (i.e., 100 trials for the 2 animals in each subgroup). This training may have been sufficient to develop habits such as extensive pushing, or resisting against pushes by the other animal, and that once learned, these behaviours would have continued into Phase 2. Such habitual patterns might also have been acquired by dominant WT animals, but they could, each time, better appraise their opponent by providing and receiving social cues. Repetitive behaviours have been observed in *Syngap*$^{+/\Delta\text{-}GAP}$ mice, with the animals having a higher stereotypic count in an open field test than WT (Guo et al., 2009). In our study, high-rank *Syngap*$^{+/\Delta\text{-}GAP}$ animals PUSHED significantly more than the high-rank WT, suggesting that they simply repeated a learned PUSH behaviour, whereas the WT rats adapt flexibly to the changing social environment.

An additional point is that *Syngap*$^{+/\Delta\text{-}GAP}$ animals in single-line cages showed significantly increased STILLNESS occurrence (Figure 5d), a pattern that carried over to the inter-cage tournaments for the high-rank animals. Alterations in these animals' ability to detect social cues could be a cause of both the high STILLNESS occurrence and the longer latencies to resolve competitions when confronted by another *Syngap*$^{+/\Delta\text{-}GAP}$ animal. We recognise that it is speculative to relate these findings to the work on bullying by Toseeb et al. (2018), but worth noting nonetheless.

4.2 | Neurobiological considerations

The medial prefrontal cortex (mPFC) and adjacent anterior cingulate gyrus have been implicated in

decision-making during dominance encounters (Nelson et al., 2020; Zhou et al., 2017). Decreased connectivity between mPFC and the primary somatosensory cortex has been previously observed in Het animals (Aceti et al., 2015). A separate study noted that *Syngap*$^{+/\Delta\text{-}GAP}$ mice had lowered excitability in the upper lamina somatosensory neurons, which encode touch information (Michaelson et al., 2018). *Syngap*$^{+/\Delta\text{-}GAP}$ animals also have altered volume of cortical areas related to visual system processing (Kilinc et al., 2018). These findings suggest that *Syngap* mutants may have decreased sensory perception and processing that affects their social communication.

Accelerated maturation during development leads to enlarged mushroom-shaped spines with clusters of AMPA receptors (Aceti et al., 2015; Clement et al., 2012; Kim et al., 2003; Vazquez, 2004). In addition, they have a more than 50% reduction in the SYNGAP protein known to be important in synaptic transmission (Jeyabalan & Clement, 2016; Komiyama et al., 2002). Interestingly, striking observations have been made in human induced pluripotent stem cell (hIPSC)-derived human neurons in which *Syngap1* was deleted using CRISPR/Cas9 technology (Llamosas et al., 2020). Previous studies in normal WT mice have suggested that increased synaptic strength in the mPFC leads to more dominant behaviour and that it may be the 'neurobiological foundation for dominance-associated personality traits' (McMahon et al., 2012; Wang et al., 2011; Zhou et al., 2017). We therefore wonder whether *Syngap*$^{+/\Delta\text{-}GAP}$ rats have defective synapses in association with their submissive phenotype. It cannot, however, be a simple reduction in strength or efficacy as *Syngap*$^{+/\Delta\text{-}GAP}$ adult mice have been found to have higher occurrence and amplitude of miniature excitatory postsynaptic currents (mEPSCs) in layer 2/3 mPFC neuron slices, pointing to an increase in unitary synaptic strength (Ozkan et al., 2014). Were this to be seen also in mPFC, Zhou et al.'s (2017) data predict that these animals might even be more dominant. Based on these findings, *Syngap*$^{+/\Delta\text{-}GAP}$ animals may sometimes be capable of displaying a more dominant phenotype.

One possible explanation for this contradiction is that the submissive *Syngap*$^{+/\Delta\text{-}GAP}$ phenotype is caused by reduced LTP at mPFC synapses. Wang et al. (2011) found that transgenic manipulations that increase AMPA receptor trafficking to the postsynaptic membrane led to an increase in rank in the tube test whereas reducing it led to a decrease. Subsequently, Zhou et al. (2017) described the 'winner effect' wherein repeated winning in the dominance tube test caused strengthening of mPFC synapses via LTP and changed the rank of an animal, an effect that could be mimicked by optogenetic activation of thalamic inputs to mPFC. This suggests that an LTP-like process can be important in establishing dominance in normal animals. Multiple studies have found reduced LTP in CA1 hippocampal regions of *Syngap*$^{+/\Delta\text{-}GAP}$ rodents, associated with elevated basal levels of Ras signalling in Syngap mutants, which prevents further Ras activation upon synaptic stimulation and thereby inhibits LTP (Kilinc et al., 2018; Kim et al., 2003; Komiyama et al., 2002; Ozkan et al., 2014). If these findings from hippocampus synapses generalise to other brain regions, *Syngap*$^{+/\Delta\text{-}GAP}$ animals could have reduced LTP in other regions including the mPFC. This deficit could limit their ability to adjust their behaviour flexibly in response to experience and so cause them to fall back on well-learned habits.

4.3 | Limitations and future directions

This study builds upon previous research addressing *Syngap* mutant rodents as models for ASD, but is not without limitations. First, it would be valuable to train additional cohorts of *Syngap* animals as they become available. Second, in keeping with the 3Rs (reduction, refinement and replacement), we used a small but not inappropriate number of animals in the present study, which were all male. Although the full data set was large and many facets of the statistical findings are robust, reproducing these experiments with both genders and multiple cages might allow higher confidence in the findings. They are, nonetheless, in line with the behavioural phenotype of *Syngap* mutant mice in revealing social withdrawal, repetitive behaviour and hyperactivity. Third, additional dominance tests, using different sensory or motor properties, need to be done to be conclusive about the generality of the dominance phenotype of *Syngap*$^{+/\Delta\text{-}GAP}$ rats (Fan et al., 2019; Wang et al., 2014). Such investigations should include examining the development of habits that compensate for the loss of social flexibility. Fourth, we have relied on published data in mice with respect to three-chambered tests of social novelty to claim that *Syngap*$^{+/\Delta\text{-}GAP}$ rats may have a deficit in social memory. Clearly, this should be tested directly in rats also, but the test should include not only this classic test of social memory (Crawley, 2006) but also some way of assessing whether animals can encode and remember the dominance status of a novel opponent (and not just its identity). Finally, one interesting future test would be to examine whether changes in rank can be induced by artificial induction of winning in subordinate *Syngap*$^{+/\Delta\text{-}GAP}$ animals. This could be done by optogenetic activation in the thalamic to prefrontal cortex pathway, as seen in Zhou et al.'s (2017) study. Such a study might be conducted in conjunction with a therapeutic intervention,

such as by the reintroduction of Syngap protein in a *Syngap*$^{+/\Delta\text{-}GAP}$ line of rats, in the manner of classic 'genetic rescue' studies of Rett syndrome (Guy et al., 2007). Alternatively, it might be done pharmacologically such as by restoring Ras signalling, which is reported to improve cognitive deficits in mouse models associated with ASD (Asiminas et al., 2019; Ogden et al., 2016).

ACKNOWLEDGEMENTS

The authors thank Patrick Spooner for building the apparatus and the Simons Foundation for the Developing Brain (Edinburgh) for funding.

CONFLICT OF INTEREST

All authors declare no conflicts of interest regarding this work.

AUTHOR CONTRIBUTIONS

Emma Harris conducted the study and prepared first drafts of figures. Honor Myers conducted the study and prepared first drafts of figures. Kapil Saxena set up the apparatus, secured the animals and provided day-to-day supervision. Rufus Mitchell-Heggs advised on suitable analyses and contributed to the text. Peter Kind, grant holder, commented on drafts of the text. Shona Chattarji, grant holder, commented on drafts of the text. Richard Morris, laboratory principal investigator, designed the study, modified the figures and wrote the manuscript.

PEER REVIEW

The peer review history for this article is available at https://publons.com/publon/10.1111/ejn.15500.

Raw data for all figures (Excel) and the details of all of the statistics done along with an example video are uploaded in a data repository (https://datashare.ed.ac.uk/handle/10283/4005).

DATA AVAILABILITY STATEMENT

Raw data for all figures (Excel) and the details of all of the statistics done along with an example video are uploaded in a data repository (https://datashare.ed.ac.uk/submit?workspaceID=6884).

The videos are accessible at https://datashare.ed.ac.uk/handle/10283/4005.

ORCID

Richard G. M. Morris https://orcid.org/0000-0001-8661-1520

REFERENCES

Aceti, M., Creson, T., Vaissiere, T., Rojas, C., Huang, W., Wang, Y., Petralia, R., Page, D., Miller, C., & Rumbaugh, G. (2015). Syngap1 haploinsufficiency damages a postnatal critical period of pyramidal cell structural maturation linked to cortical circuit assembly. *Biological Psychiatry*, *77*(9), 805–815. https://doi.org/10.1016/j.biopsych.2014.08.001

Asiminas, A., Jackson, A. D., Louros, S. R., Till, S. M., Spano, T., Dando, O., Bear, M. F., Chattarji, S., Hardingham, G. E., Osterweil, E. K., Wyllie, D. J. A., Wood, E. R., & Kind, P. C. (2019). Sustained correction of associative learning deficits after brief, early treatment in a rat model of Fragile X Syndrome. *Science Translational Medicine*, *11*, eaao0498. https://doi.org/10.1126/scitranslmed.aao0498

Barnes, S. A., Wijetunge, L. S., Jackson, A. D., Katsanevaki, D., Osterweil, E. K., Komiyama, N. H., Grant, S. G. N., Bear, M. F., Nagerl, U. V., Kind, P. C., & Wyllie, D. J. A. (2015). Convergence of Hippocampal Pathophysiology in Syngap+/- and Fmr1-/y Mice. *Journal of Neuroscience*, *35*(45), 15073–15081. https://doi.org/10.1523/jneurosci.1087-15.2015

Berryer, M., Hamdan, F., Klitten, L., Møller, R., Carmant, L., Schwartzentruber, J., Patry, L., Dobrzeniecka, S., Rochefort, D., Neugnot-Cerioli, M., Lacaille, J., Niu, Z., Eng, C., Yang, Y., Palardy, S., Belhumeur, C., Rouleau, G., Tommerup, N., Immken, L., ... Di Cristo, G. (2012). Mutations in *SYNGAP1* cause intellectual disability, autism, and a specific form of epilepsy by inducing haploinsufficiency. *Human Mutation*, *34*(2), 385–394. https://doi.org/10.1002/humu.22248

Chaste, P., & Leboyer, M. (2012). Autism risk factors: Genes, environment, and gene-environment interactions. *Dialogues in Clinical Neuroscience*, *14*(3), 281–292. https://doi.org/10.31887/DCNS.2012.14.3/pchaste

Chou, Y.-J., Lu, Y.-H., Ma, Y.-K., Su, Y.-S., & Kuo, T.-H. (2021). The decisive role of subordination in social hierarchy in weanling mice and young children. *iScience*, *24*, 102073. https://doi.org/10.1016/j.isci.2021.102073

Clement, J., Aceti, M., Creson, T., Ozkan, E., Shi, Y., Reish, N., Almonte, A., Miller, B., Wiltgen, B., Miller, C., Xu, X., & Rumbaugh, G. (2012). Pathogenic SYNGAP1 mutations impair cognitive development by disrupting maturation of dendritic spine synapses. *Cell*, *151*(4), 709–723. https://doi.org/10.1016/j.cell.2012.08.045

Crawley, J. N. (2006). *What's wrong with my mouse?* (Second ed.). Wiley. 10.1002/0470119055

Cummins, D. (2000). How the social environment shaped the evolution of mind. *Synthese*, *122*(1/2), 3–28. https://doi.org/10.1023/A:1005263825428

Ding, Q., Sethna, F., & Wang, H. (2014). Behavioral analysis of male and female Fmr1 knockout mice on C57BL/6 background. *Behavioural Brain Research*, *271*, 72–78. https://doi.org/10.1016/j.bbr.2014.05.046

Ellenbroek, B., & Youn, J. (2016). Rodent models in neuroscience research: Is it a rat race? *Disease Models & Mechanisms*, *9*(10), 1079–1087. https://doi.org/10.1242/dmm.026120

Fan, Z., Zhu, H., Zhou, T., Wang, S., Wu, Y., & Hu, H. (2019). Using the tube test to measure social hierarchy in mice. *Nature Protocols*, *14*(3), 819–831. https://doi.org/10.1038/s41596-018-0116-4

Friard, O., & Gamba, M. (2016). BORIS: A free, versatile open-source event-logging software for video/audio coding and live observations. *Methods in Ecology and Evolution*, *7*, 1325–1330. https://doi.org/10.1111/2041-210X.12584

Guo, X., Hamilton, P., Reish, N., Sweatt, J., Miller, C., & Rumbaugh, G. (2009). Reduced expression of the NMDA receptor-interacting protein Syngap causes behavioral abnormalities that model symptoms of schizophrenia. *Neuropsychopharmacology*, *34*(7), 1659–1672. https://doi.org/10.1038/npp.2008.223

Gurts, A. M., Cost, G. J., Freyvert, Y., Zeitler, B., Miller, J. C., Choi, V. M., Jenkins, S. S., Wood, A., Cui, X., Meng, X., Vincent, A., Lam, S., Michalkiewicz, M., Schilling, R., Foeckler, J., Kalloway, S., Weiler, H., Menoret, S., Anegon, I., ... Buelow, R. (2009). Knockout rats via embryo microinjection of zinc-finger nucleases. *Science (New York, N.Y.)*, *325*, 433. https://doi.org/10.1126/science.1172447

Guy, J., Gan, J., Selfridge, J., Cobb, S., & Bird, A. (2007). Reversal of neurological defects in a mouse model of Rett syndrome. *Science*, *315*, 1143–1147. https://doi.org/10.1126/science.1138389

Hamdan, F., Daoud, H., Piton, A., Gauthier, J., Dobrzeniecka, S., Krebs, M., Joober, R., Lacaille, J., Nadeau, A., Milunsky, J., Wang, Z., Carmant, L., Mottron, L., Beauchamp, M., Rouleau, G., & Michaud, J. (2011). De novo SYNGAP1 mutations in nonsyndromic intellectual disability and autism. *Biological Psychiatry*, *69*(9), 898–901. https://doi.org/10.1016/j.biopsych.2010.11.015

Huang, W., Wang, D., Allen, W., Klope, M., Hu, H., Shamloo, M., & Luo, L. (2018). Early adolescent Rai1 reactivation reverses transcriptional and social interaction deficits in a mouse model of Smith–Magenis syndrome. *Proceedings of the National Academy of Sciences*, *115*(42), 10744–10749. https://doi.org/10.1073/pnas.1806796115

Jeyabalan, N., & Clement, J. (2016). SYNGAP1: Mind the gap. *Frontiers in Cellular Neuroscience*, *10*, 1–32. https://doi.org/10.3389/fncel.2016.00032

Katsanevaki, D., Till, S. M., Buller-Peralta, I., Watson, T. C., Nawaz, M. S., Arkell, D., Tiwari, S., Kapgal, V., Biswal, S., Smith, J. A. B., Anstey, N. J., Mizen, L., Perentos, N., Jones, M. W., Cousin, M. A., Chattarji, S., Gonzalez-Sulser, A., Hardt, O., Wood, E. R., & Kind, P. C. (2020). Heterozygous deletion of SYNGAP enzymatic domains in rats causes selective learning, social and seizure phenotypes. *bioRxiv*. https://doi.org/10.1101/2020.10.14.339192

Kazdoba, T., Leach, P., Silverman, J., & Crawley, J. (2014). Modeling fragile X syndrome in the *Fmr1* knockout mouse. *Intractable & Rare Diseases Research*, *3*(4), 118–133. https://doi.org/10.5582/irdr.2014.01024

Kilinc, M., Creson, T., Rojas, C., Aceti, M., Ellegood, J., Vaissiere, T., Lerch, J., & Rumbaugh, G. (2018). Species-conserved SYNGAP1 phenotypes associated with neurodevelopmental disorders. *Molecular and Cellular Neuroscience*, *91*, 140–150. https://doi.org/10.1016/j.mcn.2018.03.008

Kim, J., Lee, H., Takamiya, K., & Huganir, R. (2003). The role of synaptic GTPase-activating protein in neuronal development and synaptic plasticity. *The Journal of Neuroscience*, *23*(4), 1119–1124. https://doi.org/10.1523/JNEUROSCI.23-04-01119.2003

Komiyama, N., Watabe, A., Carlisle, H., Porter, K., Charlesworth, P., Monti, J., Strathdee, D., O'Carroll, C., Martin, S., Morris, R., O'Dell, T., & Grant, S. (2002). Syngap regulates ERK/MAPK signaling, synaptic plasticity, and learning in the complex with postsynaptic density 95 and NMDA receptor. *The Journal of Neuroscience*, *22*(22), 9721–9732. https://doi.org/10.1523/JNEUROSCI.22-22-09721.2002

Kunkel, T., & Wang, H. (2018). Socially dominant mice in C57BL6 background show increased social motivation. *Behavioural Brain Research*, *336*, 173–176. https://doi.org/10.1016/j.bbr.2017.08.038

Llamosas, N., Arora, V., Vij, R., Kilinc, M., Bijoch, L., Rojas, C., Reich, A., Sridharan, B., Willems, E., Piper, D. R., Scampavia, L., Spicer, T. P., Miller, C. A., Holder, J. L., & Rumbaugh, G. (2020). *SYNGAP1* controls the maturation of dendrites, synaptic function, and network activity in developing human neurons. *The Journal of Neuroscience*, *40*, 7980–7994. https://doi.org/10.1523/JNEUROSCI.1367-20.2020

Lore, R., & Flannelly, K. (1977). Rat societies. *Scientific American*, *236*(5), 106–118. https://doi.org/10.1038/scientificamerican0577-106

McMahon, A., Barnett, M., O'Leary, T., Stoney, P., Collins, M., Papadia, S., Choudhary, J., Komiyama, N., Grant, S., Hardingham, G., Wyllie, D., & Kind, P. (2012). SynGAP isoforms exert opposing effects on synaptic strength. *Nature Communications*, *3*(900), 1–9. https://doi.org/10.1038/ncomms1900

McNaughton, C., Moon, J., Strawderman, M., Maclean, K., Evans, J., & Strupp, B. (2008). Evidence for social anxiety and impaired social cognition in a mouse model of fragile X syndrome. *Behavioral Neuroscience*, *122*(2), 293–300. https://doi.org/10.1037/0735-7044.122.2.293

Michaelson, S., Ozkan, E., Aceti, M., Maity, S., Llamosas, N., Weldon, M., Mizrachi, E., Vaissiere, T., Gaffield, M., Christie, J., Holder, J., Miller, C., & Rumbaugh, G. (2018). SYNGAP1 heterozygosity disrupts sensory processing by reducing touch-related activity within somatosensory cortex circuits. *Nature Neuroscience*, *21*(12), 1–13. https://doi.org/10.1038/s41593-018-0268-0

Miczek, K. A., & de Boer, S. F. (2005). Aggressive, defensive, and submissive behavior. In I. Q. Whishaw & B. Kolb (Eds.), *The behavior of the laboratory rat: A handbook with tests* (pp. 344–352). Oxford University Press.

Muhia, M., Yee, B., Feldon, J., Markopoulos, F., & Knuesel, I. (2010). Disruption of hippocampus-regulated behavioural and cognitive processes by heterozygous constitutive deletion of Syngap. *European Journal of Neuroscience*, *31*(3), 529–543. https://doi.org/10.1111/j.1460-9568.2010.07079.x

Nakajima, R., Takao, K., Hattori, S., Shoji, H., Komiyama, N., Grant, S., & Miyakawa, T. (2019). Comprehensive behavioral analysis of heterozygous Syngap1 knockout mice. *Neuropsychopharmacology Reports*, *39*(3), 223–237. https://doi.org/10.1002/npr2.12073

Nelson, A. C., Kapoor, V., Vaughn, E., Gnanasegaram, J. A., Rubinstein, N. D., Murthy, V. N., & Dulac, C. (2020). Molecular and circuit architecture of social hierarchy. *bioRxiv*. https://doi.org/10.1101/838664

Ogden, K., Ozkan, E., & Rumbaugh, G. (2016). Prioritizing the development of mouse models for childhood brain disorders. *Neuropharmacology*, *100*, 2–16. https://doi.org/10.1016/j.neuropharm.2015.07.029

O'Roak, B., Stessman, H., Boyle, E., Witherspoon, K., Martin, B., Lee, C., Vives, L., Baker, C., Hiatt, J., Nickerson, D., Bernier, R., Shendure, J., & Eichler, E. (2014). Recurrent de novo mutations implicate novel genes underlying simplex autism risk. *Nature Communications*, *5*(1), 1–6. https://doi.org/10.1038/ncomms6595

Ozkan, E., Creson, T., Kramár, E., Rojas, C., Seese, R., Babyan, A., Shi, Y., Lucero, R., Xu, X., Noebels, J., Miller, C., Lynch, G., & Rumbaugh, G. (2014). Reduced cognition in Syngap1 mutants is caused by isolated damage within developing forebrain excitatory neurons. *Neuron*, *82*(6), 1317–1333. https://doi.org/10.1016/j.neuron.2014.05.015

Parikshak, N. N., Luo, R., Zhang, A., Won, H., Lowe, J. K., Chandran, V., Horvath, S., & Geschwind, D. H. (2013). Integrative functional genomic analyses implicate specific molecular pathways and circuits in autism. *Cell*, *155*, 1008–1021. https://doi.org/10.1016/j.cell.2013.10.031

Saxena, K., Webster, J., Hallas-Potts, A., Mackenzie, R., Spooner, P., Thomson, D., Kind, P., Chatterji, S., & Morris, R. (2018). Experiential contributions to social dominance in a rat model of fragile-X syndrome. *Proceedings of the Royal Society B: Biological Sciences*, *285*(1880), 20180294. https://doi.org/10.1098/rspb.2018.0294

Spencer, C., Alekseyenko, O., Serysheva, E., Yuva-Paylor, L., & Paylor, R. (2005). Altered anxiety-related and social behaviors in the Fmr1 knockout mouse model of fragile X syndrome. *Genes, Brain and Behavior*, *4*(7), 420–430. https://doi.org/10.1111/j.1601-183X.2005.00123.x

Toseeb, U., McChesney, G., & Wolke, D. (2018). The prevalence and psychopathological correlates of sibling bullying in children with and without autism spectrum disorder. *Journal of Autism and Developmental Disorders*, *48*(7), 2308–2318. https://doi.org/10.1007/s10803-018-3484-2

Vazquez, L. (2004). Syngap regulates spine formation. *Journal of Neuroscience*, *24*(40), 8862–8872. https://doi.org/10.1523/JNEUROSCI.3213-04.2004

Walkup, W. G. I. V., Mastro, T. L., Schenker, L. T., Vielmetter, J., Hu, R., Iancu, A., Reghunathan, M., Bannon, B. D., & Kennedy, M. B. (2016). A model for regulation by SynGAP-α1 of binding of synaptic proteins to PDZ-domain 'Slots' in the postsynaptic density. *eLife*, *5*, e16813. https://doi.org/10.7554/eLife.16813

Wang, F., Kessels, H., & Hu, H. (2014). The mouse that roared: Neural mechanisms of social hierarchy. *Trends in Neurosciences*, *37*(11), 674–682. https://doi.org/10.1016/j.tins.2014.07.005

Wang, F., Zhu, J., Zhu, H., Zhang, Q., Lin, Z., & Hu, H. (2011). Bidirectional control of social hierarchy by synaptic efficacy in medial prefrontal cortex. *Science*, *334*(6056), 693–697. https://doi.org/10.1126/science.1209951

Yang, C., Bai, Y., Ruan, C., Zhou, H., Liu, D., Wang, X., Shen, L., Zheng, H., & Zhou, X. (2014). Enhanced aggressive behaviour in a mouse model of depression. *Neurotoxicity Research*, *27*(2), 129–142. https://doi.org/10.1007/s12640-014-9498-4

Yizhar, O., Fenno, L., Prigge, M., Schneider, F., Davidson, T., O'Shea, D., Sohal, V., Goshen, I., Finkelstein, J., Paz, J., Stehfest, K., Fudim, R., Ramakrishnan, C., Huguenard, J., Hegemann, P., & Deisseroth, K. (2011). Neocortical excitation/inhibition balance in information processing and social dysfunction. *Nature*, *477*(7363), 171–178. https://doi.org/10.1038/nature10360

Yoo, H. (2015). Genetics of autism spectrum disorder: Current status and possible clinical applications. *Experimental Neurobiology*, *24*(4), 257–272. https://doi.org/10.5607/en.2015.24.4.257

Zhou, T., Zhu, H., Fan, Z., Wang, F., Chen, Y., Liang, H., Yang, Z., Zhang, L., Lin, L., Zhan, Y., Wang, Z., & Hu, H. (2017). History of winning remodels thalamo-PFC circuit to reinforce social dominance. *Science*, *357*(6347), 162–168. https://doi.org/10.1126/science.aak9726

How to cite this article: Harris, E., Myers, H., Saxena, K., Mitchell-Heggs, R., Kind, P., Chattarji, S., & Morris, R. G. M. (2021). Experiential modulation of social dominance in a SYNGAP1 rat model of Autism Spectrum Disorders. *European Journal of Neuroscience*, *54*(10), 7733–7748. https://doi.org/10.1111/ejn.15500

4.3 iHELMET: A 3D-printing solution for safe endoscopic Ca2+ recording in social neuroscience

Journal of Neuroscience Methods 355 (2021) 109109

Contents lists available at ScienceDirect

Journal of Neuroscience Methods

journal homepage: www.elsevier.com/locate/jneumeth

iHELMET: A 3D-printing solution for safe endoscopic Ca^{2+} recording in social neuroscience

Kapil Saxena [a], Patrick A. Spooner [a], Rufus Mitchell-Heggs [a,b], Richard G.M. Morris [a,*]

[a] Laboratory for Cognitive Neuroscience and Simons Initiative for the Developing Brain Centre for Discovery Brain Sciences, Edinburgh Neuroscience, 1 George Square, Edinburgh, EH8 9JZ, UK
[b] Centre for Neurotechnology & Department of Bioengineering, Imperial College, London, UK

ARTICLE INFO

Keywords:
Social neuroscience
Calcium imaging
Endoscopic imaging
Miniscope
Inscopix

ABSTRACT

Background: In vivo calcium imaging using a microendoscope is a state-of-the-art technique to study the cellular activity inside the brain of freely moving animals such as mice or rats. A problem that can arise in social behaviour tests in rats, or similar size rodents, is that one animal interferes with or may even damage the miniature endoscopic camera attached to the second animal.
New method: We outline an inexpensive, lightweight, 3D-printed protector (iHELMET) that surrounds but is not in physical contact with the camera, together with details of its design and construction.
Results: Using a simple design, we demonstrate successful protection of the endoscope and recording in a social situation such as the social dominance tube test.
Comparison with existing methods: The helmet's 3D-printed dimensions can be readily adjusted to work with various micro-endoscopes, which may be more difficult for the only other system of which we are aware.
Conclusions: In addition to camera protection, features of the design aid camera stability, helping to secure more optimal imaging of calcium transients in specific regions of interest during long recording sessions.

1. Introduction

Growing interest in the neurobiology of social behaviour has led to the use of optical calcium imaging as an indicator of neural activity in various brain regions. It is paramount that this is done in behaving animals that are freely interacting with each other. In calcium (Ca^{2+}) imaging, a genetically encoded calcium indicator (such as the GCaMP6 series - (Chen et al., 2013) binds with Ca^{2+} ions and reports their presence as a rapid increase in the intensity of fluorescence emissions. As the intracellular Ca^{2+} concentration decreases, the fluorescence also gradually declines (Nakai et al., 2001; Tallini et al., 2006). This sequence of events is defined as a Ca^{2+} spike or Ca^{2+} transient. As these transients are observed repeatedly in specific locations, regions of interest (ROIs) can be identified in which specific transients are observed. The implication is that such Ca^{2+} transients are likely to be from individual neurons.

The neural correlates of social interaction cannot easily be studied using 2-photon-imaging in head-fixed animals on track-balls, although limited facets of social behaviour in virtual-reality are becoming available (Stowers et al., 2017). The recently developed method of choice is the use of lightweight miniature endoscopic cameras (~2gm) which, when coupled to genetic expression of Ca^{2+} reporters such as GCaMP6 constructs (either via viral vectors or transgenic animals) with an implanted GRIN lens targeting the specific brain regions (Ziv et al., 2013), provide images of Ca^{2+}-transients in real time (Ghosh et al., 2011; Jercog et al., 2016; Fig. 1A). A key value of this approach is the ability to examine large numbers of "cells" simultaneously, use both single-cell and ensemble analyses and to image across days.

In social behaviour, such as in the tube test of social dominance, a fundamental problem is that there may be physical interference by one animal with the camera on the other animal from which recordings are being taken. This interference may only be momentary, such as a brief paw movement, or may involve recurrent somatosensory interactions between animals or even brief mildly aggressive attacks. These can be sufficient to disrupt the stability of continuous recording.

An additional type of interference may be introduced because of the confined space of the narrow tube used in the tube-test of social dominance. The diameter of the tube has to be wide enough to let each animal to walk through it easily, but should be narrow enough that the two animals cannot pass each other. This condition of confined space in the

* Corresponding author.
E-mail address: (R.G.M. Morris).

https://doi.org/10.1016/j.jneumeth.2021.109109
Received 22 April 2020; Received in revised form 26 February 2021; Accepted 1 March 2021
Available online 8 March 2021

tube test introduces a set of new problems for stable Ca^{2+} recordings. Specifically, when entering the tube, the head mounted endoscope risks becoming caught at the entrance, and even when in the tube, sideways head-movements result in the camera being pushed or even banged against the walls of the tube. Such interference has apparently not yet been a problem for studies in smaller animals such as mice (Kingsbury et al., 2019), but our experience of working with animals that are approximately ten times larger and physically much stronger indicates that it is a major problem. During an ongoing social neuroscience project, we observed good stable imaging when the rats were not interacting with each other. Social interactions may cause minor interference that can ordinarily be compensated by motion-correction software, but can increase to a level that is difficult or impossible to correct in this way (Fig. 1B,C). Additional problems can include a momentary shut-down of imaging after a robust bang of the camera against the side-walls. Such interference is undesirable given the clear cost in both workload and economic terms. Given that new gene editing techniques will likely soon enable more studies to be carried out carried on rats rather than mice (Hsu et al., 2014; Till et al., 2015; Zhang et al., 2014), it may be of interest to report how we solved these problems.

One solution is to create barriers between the interacting animals as in the classic 3-chamber sociability / social novelty test (Crawley, 2004; Moy et al., 2004). The two animals are physically separated by a permeable barrier through which they can see, smell and hear each other, but somatosensory contact is limited. In the 3-chamber task, the 'test' animal in the larger space shows social interactions with the 'enclosed' animal(s), but these interactions, including whisker contact, are limited. Neurophysiological and optical recordings have nonetheless been made of such social interactions using this and similar tasks (Liang et al., 2018; Murugan et al., 2017).

We therefore considered an alternative approach that permits physical contact between the animals by developing a lightweight 3D-printed helmet with suitable dimensions and rigidity for successful endoscopic recording. The helmet is placed on the animal daily and held rigidly to a separate 3D printed baseplate-surround cemented onto the animal. We have successfully used this system in various social situations, including the social dominance tube test.

2. Materials and methods

2.1. 3D-designing and printing

The iHELMET was designed using Fusion 360® a 3D modelling software. It is made using PLA (PolyLactic Acid) on an inexpensive Replicator 2 Desktop 3D printer (https://www.makerbot.com/3d-printers/; Fig. 2A). Ready to print .stl files are available in the attached Supplementary information. The dimensions of the plastic were determined to be, internally, no more than 2 mm larger in the x, y plane than those of the Inscopix endoscopic camera, but are easily adapted for other types and makes. The helmet is so light that it adds only 4.0 g to the typical <2.0 g of the nVISTA camera of an Inscopix system (roughly <2% of the weight of the rat). Similar considerations apply to the Doric and open-source UCLA recording systems (http://doriclenses.com/life-sciences/307-miniaturized-fluorescence-microscopy; https://www.inscopix.com; http://miniscope.org/). Including the width of the plastic and design considerations, this resulted in a final unit that was 15 mm x 28 mm (x, y), and a height of 56 mm. The costs of construction of each unit are modest, with the asset costs of the 3D Printer shared between several lab groups. In-house construction enabled us to make regular modifications of the design as the project unfolded. Once printed, these parts were dry-fit tested before using.

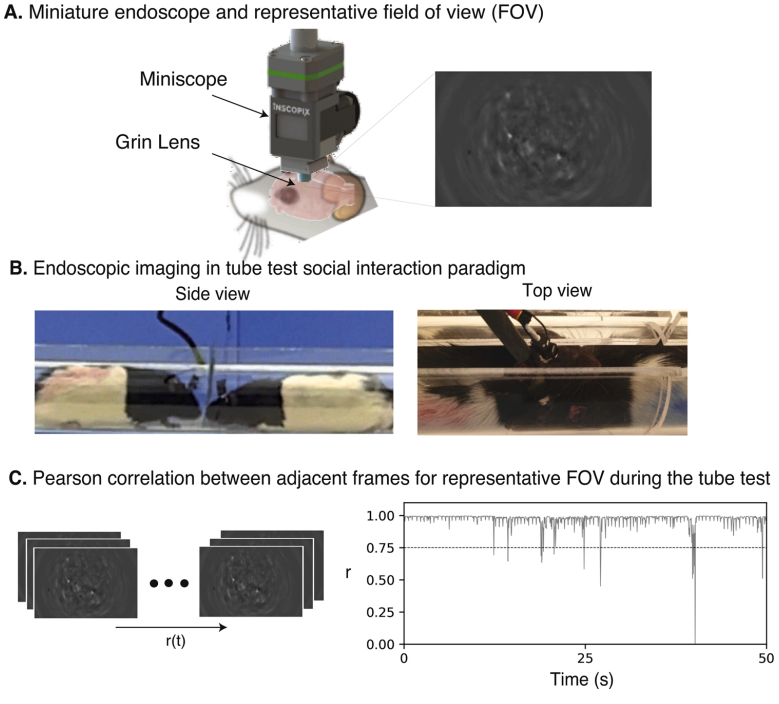

Fig. 1. The problem: situations that emerged during a calcium imaging session in the tube-test. **A)** The head-mounted endoscope as designed to be used, a representative field of view with exemplar ΔF/F measures of Ca^{2+} transients secured during recording. **B)** Two animals engaged in a contest in the tube-test of social dominance (side and top views). The acrylic tube has a 2 cm slit allowing the endoscope to move freely along its length. The unprotected scope is clearly visible in the animal on the left. The confined space puts the camera in danger of being pushed against the side-walls of the slit or of being damaged by the other animal. **C)** Pearson correlations were computed across pixels between adjacent frames (0.05 s apart) throughout a representative 50 s session.

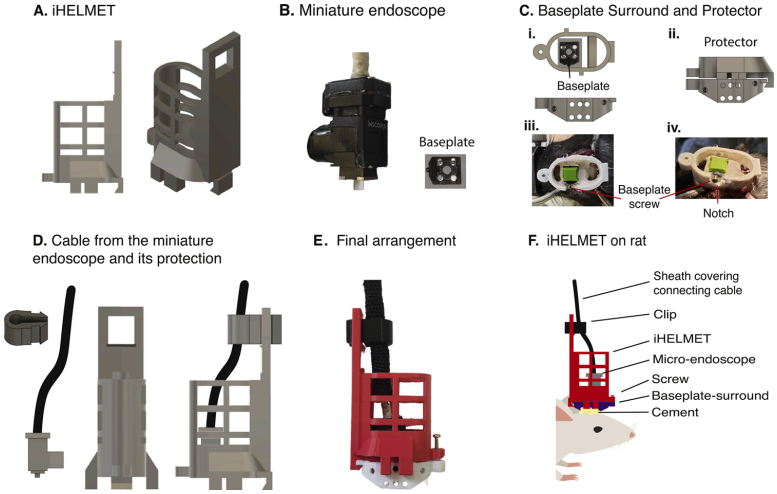

Fig. 2. The solution: design and construction of the iHELMET. **A**) A side- and partly rotated view of the final design of the 3D-printed iHELMET. Note connecting clips to the baseplate-surround at the bottom, window panels to allow free air movement, and rear post for connecting the recording cable. **B**) Photo of a typical miniature endoscope weighing < 2 gm and associated baseplate with four miniature anchoring magnets (Inscopix). **C**) Top and side view of 3D-printed baseplate-surround unit. (Ci): Side view shows holes to enable more secure anchoring with skull cement; (Cii): baseplate-protecting-cap in place (for when animals are in their home cages); (Ciii): Image of baseplate-surround on a rat's head while surgical implantation was being carried out, the green part at the centre is a small baseplate cover that protects the lens. Notice the baseplate stainless steel screw; (Civ): A notch is drilled out in the baseplate surround at the time of implantation to ease the access to the baseplate screw. **D**) Recording cable with miniature endoscope and clip, front and side-view of iHELMET, and cable grip system. **E**) Final view of the helmet with cable secured for recording. **F**) Cartoon showing iHELMET on a rat with all of the essential components.

2.2. Camera

The Inscopix endoscope which we used (Fig. 2B) has external dimensions of 11 mm x 14 mm x 20 mm and weighs 2 gm. On the animal, the 'miniscope' is normally placed into to a "baseplate" made of metal or hard plastic (with various designs in different systems), that secures the camera rigidly in the same place on each session above a miniature implanted GRIN lens (e.g. 1 mm diameter) that extends to the brain area of interest in which GCamp6f is expressed. Details of the principles behind *in vivo* endoscopic imaging are readily available at the above listed websites.

2.3. Experimental subjects

The focus of this technical note is on the helmet design but a brief comment about the experimental subjects is required. We used male Long Evans hooded rats (Charles River), typically weighing 470–600 g. The animals were typically housed in groups of 2 rats together in a social cage, with suitable protection of the GRIN lens as described below. They were maintained on *ad libitum* food and water and the study conducted under the auspices of the laboratory's UK Home Office Project and Personal Licences for animal research.

2.4. Surgery, baseplate and baseplate-surround

The first step in the use of these animals is the microinfusion of GCamp6f virus under isofluorane anaesthesia at a specific intracerebral target (the prelimbic region of the prefrontal cortex). Approximately 3 weeks later, allowing time for the virus to express, a GRIN lens is implanted under anaesthesia in a second operative stage, with full recovery thereafter. This lens is secured using a combination of skull screws, Super-bond C&B (Sun Medical Co. Ltd, Japan), and dental cement to provide firm anchoring. The miniscope requires a "baseplate" (5 mm $\times$ 5.5 mm for INSCOPIX, a different size for other suppliers) which incorporates anchoring magnets and a side-mounted screw. The magnets hold the miniscope on the head of the animal in a consistent position to retrieve the same field of view across imaging sessions. The baseplate is cemented into place on the skull of a laboratory rat under anaesthetic, being positioned while imaging with the camera to optimise the field of view of cells in which the virus is expressing.

A key feature of our innovation arises from the creation of a "Baseplate-Surround" (Fig. 2C). Specifically, the daily anchoring of the helmet requires a separate 3D-printed PLA Baseplate-Surround whose function is to hold the helmet rigidly (shown surrounding the metal baseplate in Fig. 2C(i and iii)). The baseplate-surround has its own dedicated protector cap used when the animal returns to its home cage and removed at the start of a recording session (Fig. 2C(ii)). Its purpose is to protect the GRIN lens and baseplate whilst the animals are in their social groups.

When implanting the baseplate surround, it must be aligned with the baseplate such that, when the endoscope is placed into it and the iHELMET then attached, the helmet will not be not in direct physical contact with the endoscope. A side-view of the baseplate-surround in Fig. 2C (i) bottom. Aligning the front screw-holes of the baseplate-surround to that of the baseplate screw works well, together with keeping the baseplate-surround as far back as possible in order to leave around 1–1.5 mm space between it and the baseplate (Fig. 2C (iii)). After positioning the iHELMET over the endoscope, it typically requires a few mm of forward movement to bring it to its final position (see Supplementary Video 3_procedure for the complete instructions). A design feature is that, as the baseplate-surround can limit the access to the baseplate screw, we drill out the adjacent part of the baseplate-surround to secure optimum access (Fig. 2C(iv)).

A locking nut (A2 M1.6) is embedded in the baseplate-surround and the helmet equipped with an A2 M1.6 $\times$ 5 bolt (https://www.screwsandmore.de/de; Fig. 2E). This combination of nut and bolt is suitable for the maximum torque faced by the iHELMET in the tube-test when one animal pushes on the iHELMET of the other animal with any force or while animals helmet is caught at the entry of the. This choice of screw-thread has worked flawlessly in our experiments, but other sizes of screws may be preferred in different laboratories.

2.5. Attaching the iHELMET and recording cable

After the baseplate-surround protector cap is removed on the animal, the endoscope is first attached to its baseplate, and then the helmet slid down the recording cable to lock onto the baseplate-surround and secured using the helmet screw. The lightweight cable connects the endoscope to an image capture system (DAQ), or an image illumination

system in the case of DORIC, sometimes using a ceiling-mounted commutator to enable freedom of rotational movements by the animal.

The cable is highly flexible, but there are two additional refinements to the iHELMET which emerged from its early use. One refinement is to protect the cable, the other to prevent sudden changes in cable tension affecting the camera.

The first was achieved using a short section (15−20 cm) of cable sheathing (resistant to rodent teeth) around only the lower part of the cable. This sheathing is commercially available as "split cable-sheath". We used a "wire-loom" tool to put this split sheath onto the cable, with the hollow part of the loom containing the cable and the solid part used to split the sheathing. Forward motion of the loom while holding the sheath, resulted in the sheathing being easily applied over the lower part cable (See Supplementary (Wire_Loom.stl file) to enable users to 3D print the tool). The vertical extent of the protective sheathing can be quite short as it serves to guard against any grabbing by the other animal.

The second refinement was to ensure that any change in cable tension is transmitted only to the helmet but not the camera. This was achieved by attaching the cable inside its cable-sheath to a rigid rear-mounted vertical post of the iHELMET using a cable clip (Fig. 2D and E; black in colour). It can be squeezed gently (to grip both the cable and cable sheath) and then secured to the helmet. This ensures that any change in cable tension is transmitted only to the helmet but not the camera.

2.6. Controlling movement artefacts

A separate benefit of using this particular design of helmet is improved limitation of movement artefacts. While normally the camera is held well within its baseplate, it may nonetheless be subject to very small movements (fractions of a millimetre) in both the x, y and separately the z axis, typically caused by any changes in the tension of a free-to-move cable. These may minutely change the field of view, enough to cause image instability, which may or may not be correctable by image stabilisation software. It is clearly desirable to keep these artefacts to a minimum.

The final arrangement of the endoscopic camera in its helmet is shown in Fig. 2F. Dummy cameras were also used so that, when recording from only one animal, the second animal in the social encounter had a similar helmet arrangement on its head.

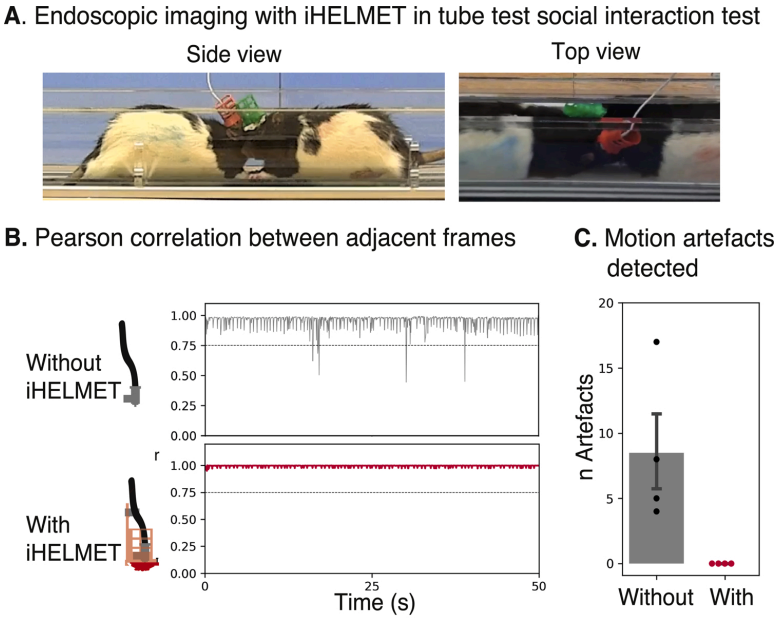

Fig. 3. The use: reduction in movement artefact when using the iHELMET. **A)** Views of animals wearing helmets during the pilot studies of its use (side and top views). Note that even when the two helmets are in contact, that contact is not transmitted to the camera inside, nor when a helmet hits against the slit in the acrylic tube used for the tube-test. **B)** Pearson correlation between pixels of adjacent frames over a representative period of 50 s recording. Cartoons display without and with-helmet conditions. Note stability (red) of the recording condition with the helmet. **C)** Display of mean and number of individual movement artefacts, these being arbitrarily defined as situations in which the frame-to-frame correlation fell below 0.75. Note striking reduction in the with-helmet condition. **D)** Representative FOV showing ROIs identified using CNMFe, together with (right) Ca2+ time-series for a select number of neurons. Mean ± 1 SEM.

3. Results

The results to be presented are in three stages. The *first* stage describes the problems we faced when we first attempted to use the endoscopes in a social situation, including the movement artefacts experienced (Fig. 1). The *second* describes our successful design, construction and use of the iHELMET (Fig. 2). The *third* presents data relevant to limitation of movement artefacts. Steps 1 and 2 are qualitative, whereas Step 3 is quantitative (Fig. 3).

3.1. The problem of movement artefacts

Fig. 1A shows the typical arrangement for the miniature endoscope and a field of view upon which brief transients are visible as the animal moves around. In our attempts to use this standard arrangement in the tube-test, we ran into the problem that the camera could hit against the slit that had been cut into the plexiglass tube or be subject to interference from the other animal in the encounter (Fig. 1B). We were nonetheless able to run a number of sessions from 4 animals before discontinuing due to concern about potential damage to the endoscope and its recording cable (Supplementary Video 1 without helmet). To quantify the extent of the movement artefact problems which arose, we computed Pearson correlations between corresponding pixels of successive video frames. In a condition of stability, the correlation coefficient (r) should be at or very close to 1.0. However, as shown in a representative set of data in Fig. 1C, the near unity value of the correlation was subject to occasional 'jolts' that coincided with the problems we were observing. We defined motion artefacts arbitrarily as any reduction of the r value below 0.75.

3.2. The iHELMET solution; design, construction and use

The design of an effective 3D printed helmet evolved through numerous design stages intended to solve key problems. The design requirements were:

- Removable and replaceable easily on a daily basis.
- Connecting rigidly to the animal in manner that surrounds but does not interfere with the camera or the base-plate holding it.
- The inner dimensions of the helmet should leave a physical gap of at least 1 mm between it and the camera, but the entire construction should still be narrow, suitable for the tube test.
- The helmet surround should not result in excessive heating of the endoscope, allowing free movement of air around it.
- The helmet should include a rigid posterior-mounted post to which the recording cable can be attached, helping to ensure the safety of the thin wires within the cable that carry power and the optical signal. In such an arrangement, any 'jerky' movements of the cable would not be transmitted beyond the helmet to the camera.
- The baseplate-surround should have a separate small 3D-printed plastic protector that can be placed after a day's recording to protect the integrity of the GRIN lens in the home cages that may house several animals.
- In cases in which imaging is done from one of two animals interacting socially, a "dummy" camera system should be installed on the test-mate from whom recordings are not being taken. This is intended to prevent technique-induced bias with respect to social interactions between animals.
- 'Retro-fittable' to the existing design features of commercial or open-source systems being used (likely requiring small 3D-printing differences for different systems).

Fig. 2 shows the various components of the final iHELMET design. The outline of the construction in Materials and Methods (above) will be seen to meet each of these conceptual requirements. In particular, we have not observed any damage to either the camera or the cable since the introduction of this iHELMET system.

3.3. Positioning the iHELMET on the animal

When an animal is removed from his home cage for a daily recording session, the first step is to remove the protective cap of the baseplate-surround. This exposes the 'clip' arrangement of the baseplate-surround to which the iHELMET attaches. The endoscope and its attached cable are then moved into position, using in the case of the Inscopix system, the 4 magnets for effective positioning in the baseplate followed by tightening of the side-mounted locking screw. The helmet is then moved down the cable and screwed into position on the baseplate-surround. The experimenter checks that its positioning results in no physical contact between the helmet and the camera and then attaches the power/recording cable using the cable clip. Once used to these steps, the experimenter can normally do these successfully in 10−30 sec. Fig. 2F shows a cartoon of the iHELMET positioned on a rat's head before entering a social situation. Either both rats will have a camera, or one will have a real camera and the other a dummy camera (Supplementary Video 2).

3.4. The benefits; limiting unexpected movement

The third facet of our results is whether such an arrangement is successful in both protecting the camera and reducing movement artefacts and enabling better motion-free recording. The temporal characteristics of Ca^{2+}-transients is a sharp rise and generally slower falling phase of a Ca^{2+}-signal. These are often plotted as a time-stamped raster with time on the x-axis once criteria for time-stamping are identified (amplitude-threshold, rise-time, fall-time etc.). These signals may then be time-locked to separately recorded behavioural signals manually, or via software such as DeepLabCut (Mathis et al., 2018; Nath et al., 2018) and the secondary analysis then undertaken examining correlations between physiological and behavioural measures. Clearly this behaviour/physiology correlation requires the imaging to be stable.

Unavoidable image motion that occurs in the nature of *in-vivo* recordings can be compensated to some extent by the 'motion correction' feature available in calcium image analysis software (such as the Inscopix Data Processing Software - IDPS). However, motion artefacts often correspond to a change in the imaging plane, rendering motion irreconcilable. A key benefit of our helmet was a striking reduction in the mean number of motion artefacts detected during imaging with iHELMET compared to without iHELMET (Fig. 3B and 3C). As in Fig. 1, the Pearson's correlation was calculated between successive frame images from the spatially band-passed recordings for eight animals (4 with iHELMET, 4 without iHELMET). Motion artefacts were identified as a correlation $r < 0.75$ (shown as a dotted line in Fig. 3B) and the total number of artefacts for each animal numerically corrected to account for recordings going first out and back into focus (dividing by 2).

An important qualification we should address is whether there are aspects of behaviour that are changed by the use of the iHELMET. Qualitatively, and mindful of the low weight of the device, there appeared to be no obvious differences. One quantitative check we made, however, was to examine social dominance in the tube test between 8 pairs of animals under conditions in which they were tested without a helmet or separately with the helmet. Supplementary Fig. 1 shows the striking correlation between these two conditions and a correlation coefficient of $r = 0.92$.

4. Discussion

The primary aim of creating a 3D-printed helmet was to protect the delicate endoscopic camera. During development of the design through various stages, the iHELMET design evolved into a constellation of three component. The helmet itself, the cable clip that restricts the changes in torque introduced by cable inertia reaching the endoscope, and the

baseplate surround that is implanted to surround the baseplate and which holds the helmet to the animal. The outlined design fulfils each of several design considerations. An added benefit was that, by anchoring the recording cable, there can be improved stability of Ca^{2+} imaging. In our experience, it enables long periods of safe, stable recordings from animals tested in social situations over long daily sessions, and several weeks or more.

Endoscopic Ca^{2+} imaging has rapidly become a method of choice for examining diverse issues - place cell stability in hippocampus (Ziv et al., 2013), time-stamping of memory ensembles (Rubin et al., 2015), contextual linking as a function of temporal proximity (Cai et al., 2016), and aspects of memory consolidation (Attardo et al., 2018). Social behaviour, however, presents a challenge. Unprotected endoscopic imaging can be successful (Liang et al., 2018; Murugan et al., 2017), but difficulties can arise. The solution proposed here is ideal for an endoscope camera for use with larger rodents such as rats, but other laboratories facing similar issues have proposed alternative methods. For example, a protective cone to protect a tetrode micro-drive for extracellular single-cell recording has been described (Nguyen et al., 2009), and others have also outlined a calcium imaging protection system (van den Boom and Bos, 2018) (https://miniscope.org/index.php/Miniscope_Baseplate_and_Protective_Cone_for_Rats).

While ingenious and suitable for mice, there are some restrictions to the van den Boom and Bos (2018) design. There is incompatibility with existing calcium imaging systems as it requires construction of a new, carefully milled, aluminium camera baseplate to which the protective cone fits. This then has consequences for the imaging. In their own words *"having a distinct baseplate design can increase the distance between the endoscope and GRIN lens, requiring the use of a relay lens"*. There appears also to be no provision to nullify the impact of sudden cable movements. The present helmet design is compatible with existing miniscope systems, but we advise laboratories to check the dimensions of the miniscope they are using and edit the provided iHELMET and baseplate-surround files (.STL) to compatible dimensions.

Beyond protection, a secondary but no less important facet of the design is its ability to limit motion artefacts when imaging. Having stable signals throughout the course of a recording session is essential and a natural feature of conventional tetrode recording but harder to realise with endoscopic recording. Using the iHELMET, the number of motion artefacts detected was significantly reduced, with minor motion observed in certain constrained and socially interactive situations. The use of the helmet may, therefore, even be desirable in situations in which only a single animal is being tested - where there is a risk of an unprotected camera hitting against some feature of the apparatus or in a large apparatus in which there may be considerable cable movement. Furthermore, the helmet can only complement other protective measures during social interaction (e.g. physical barriers).

We have now used the iHELMET in two separate social testing situations. One was a modified 3-compartment sociability/social novelty test. The animal from which imaging was taking place was free to move around a large test arena containing two small enclosures. The target animals were contained within these enclosures, but a design fault intended to increase the possibility of sensorimotor interaction was to make the enclosures in such a way as to permit the target animals inside to be able to reach a paw outside and so contact the recording animal. On one occasion, this led to unintended gripping of the recording cable and consequent damage. The new arrangement with the cable sheath and helmet clip completely prevents this type of accident without the need for any greater sensorimotor barrier between the animals. Both animals can still reach each other without danger. The second testing situation was the social dominance tube-test in which two rats meet in a tube from which the subordinate one retreats or is forced to retreat, and the dominant animal pushes or follows the subordinate. In our laboratory, the clear acrylic tube has a small 2 cm 'slit' along its long top surface wide enough for the camera and its associated recording cable, but also wide enough for a paw to reach through. In this situation, we had previously observed both frequent physical contact between the camera and one side of the slit (causing interruptions of successful imaging), and between the paw of one animal and the endoscopic camera on the other. Again, the design solves both problems. Even if the helmet makes contact or even knocks the side-walls of the tube, the camera is safely inside making no physical contact with it. Similarly, paw movements against the sides of the helmet are of no consequence.

The recordings shown in this study were from the medial prefrontal cortex (mPFC). The stereotaxic coordinates were 3.2 mm rostral from bregma and 0.8 mm lateral from the midline. The iHELMET can, in principle, be used while recording from any brain region, but prospective users should consider the possibility of the helmet interfering with the normal body movement or the behaviour of the animal. For example, recording from the olfactory bulb may be a challenge but likely not insuperable. Our tests of social dominance between 8 pairs of co-housed animals revealed a high *correlation* ($r = 0.92$) in tests with and without the helmet.

The helmet may be said to *"..kill two birds with one stone"* as the design successfully addresses two practical problems in endoscopic recording - camera protection and reducing movement artefact. It is especially suited for stronger freely-moving animals such as rats.

Credit Author Statement

Richard Morris: Conceptualization, Supervision, Writing. **Kapil Saxena:** Methodology, Construction, Figures, Experimentation. **Patrick Spooner:** Methodology, Construction, Figures, Experimentation. **Kapil Saxena:** Software, data-analysis, Visualization, Figures, Reviewing and Editing. **Rufus Mitchell-Heggs:** Software, data-analysis, Visualization, Figures, Reviewing and Editing.

Declaration of Competing Interest

The authors declare no conflicts of interest, financial or otherwise. The iHELMET system was developed in the laboratory of Prof. Richard Morris at The University of Edinburgh and is not patented. The 3D printing files are free to edit as required. We would welcome citation of this article if used.

Acknowledgements

This work was supported by grants from the Simons Institute for the Developing Brain (held by Professors Peter Kind and Adrian Bird, University of Edinburgh) and an Advanced Investigator Grant from The Wellcome Trust to RGMM. We thank Diane Damez-Werno of INSCOPIX for training and advice in the techniques of endoscopic imaging. We also want to thank members of Morris Lab who have provided valuable comments while preparing this manuscript.

Appendix A. Supplementary data

Supplementary material related to this article can be found, in the online version, at doi:https://doi.org/10.1016/j.jneumeth.2021.109109.

References

Attardo, A., Lu, J., Kawashima, T., Okuno, H., Fitzgerald, J.E., Bito, H., Schnitzer, M.J., 2018. Long-term consolidation of ensemble neural plasticity patterns in hippocampal area CA1. Cell Rep. 25, 640–650 e2.

Cai, D.J., Aharoni, D., Shuman, T., Shobe, J., Biane, J., Song, W., Wei, B., Veshkini, M., La-Vu, M., Lou, J., Flores, S.E., Kim, I., Sano, Y., Zhou, M., Baumgaertel, K., Lavi, A., Kamata, M., Tuszynski, M., Mayford, M., Golshani, P., Silva, A.J., 2016. A shared neural ensemble links distinct contextual memories encoded close in time. Nature 534, 115–118.

Chen, T.W., Wardill, T.J., Sun, Y., Pulver, S.R., Renninger, S.L., Baohan, A., Schreiter, E. R., Kerr, R.A., Orger, M.B., Jayaraman, V., Looger, L.L., Svoboda, K., Kim, D.S.,

2013. Ultrasensitive fluorescent proteins for imaging neuronal activity. Nature 499, 295–300.
Crawley, J.N., 2004. Designing Mouse Behavioral Tasks Relevant to Autistic-like Behaviors. Mental Retardation and Developmental Disabilities Research Reviews, pp. 248–258, 10.
Ghosh, K.K., Burns, L.D., Cocker, E.D., Nimmerjahn, A., Ziv, Y., Gamal, A.E., Schnitzer, M.J., 2011. Miniaturized integration of a fluorescence microscope. Nat. Methods 8, 871–878.
Hsu, P.D., Lander, E.S., Zhang, F., 2014. Development and applications of CRISPR-Cas9 for genome engineering. Cell 157, 1262–1278.
Jercog, P., Rogerson, T., Schnitzer, M.J., 2016. Large-scale fluorescence calcium-imaging methods for studies of long-term memory in behaving mammals. Cold Spring Harb. Perspect. Biol. 8.
Kingsbury, L., Huang, S., Wang, J., Gu, K., Golshani, P., Wu, Y.E., Hong, W., 2019. Correlated neural activity and encoding of behavior across brains of socially interacting animals. Cell 178, 429–446 e16.
Liang, B., Zhang, L., Barbera, G., Fang, W., Zhang, J., Chen, X., Chen, R., Li, Y., Lin, D.T., 2018. Distinct and dynamic ON and OFF neural ensembles in the prefrontal cortex code social exploration. Neuron 100, 700–714 e9.
Mathis, A., Mamidanna, P., Cury, K.M., Abe, T., Murthy, V.N., Mathis, M.W., Bethge, M., 2018. DeepLab Cut: markerless pose estimation of user-defined body parts with deep learning. Nat. Neurosci. 21, 1281.
Moy, S.S., Nadler, J.J., Perez, A., Barbaro, R.P., Johns, J.M., Magnuson, T.R., Piven, J., Crawley, J.N., 2004. Sociability and preference for social novelty in five inbred strains: an approach to assess autistic-like behavior in mice. Genes Brain Behav. 3, 287–302.
Murugan, M., Jang, H.J., Park, M., Miller, E.M., Cox, J., Taliaferro, J.P., Parker, N.F., Bhave, V., Hur, H., Liang, Y., Nectow, A.R., Pillow, J.W., Witten, I.B., 2017. Combined social and spatial coding in a descending projection from the prefrontal cortex. Cell 171, 1663-77 e16.
Nakai, J., Ohkura, M., Imoto, K., 2001. A high signal-to-noise Ca(2+) probe composed of a single green fluorescent protein. Nat. Biotechnol. 19, 137–141.
Nath, T., Mathis, A., Chen, A.C., Patel, A., Bethge, M., Mathis, M.W., 2018. Using DeepLabCut for 3D markerless pose estimation across species and behaviors. bioRxiv, 476531.
Nguyen, D.P., Layton, S.P., Hale, G., Gomperts, S.N., Davidson, T.J., Kloosterman, F., Wilson, M.A., 2009. Micro-drive array for chronic in vivo recording: tetrode assembly. J. Vis. Exp.
Rubin, A., Geva, N., Sheintuch, L., Ziv, Y., 2015. Hippocampal ensemble dynamics timestamp events in long-term memory. Elife 4.
Stowers, J.R., Hofbauer, M., Bastien, R., Griessner, J., Higgins, P., Farooqui, S., Fischer, R.M., Nowikovsky, K., Haubensak, W., Couzin, I.D., Tessmar-Raible, K., Straw, A.D., 2017. Virtual reality for freely moving animals. Nat. Methods 14, 995–1002.
Tallini, Y.N., Ohkura, M., Choi, B.R., Ji, G., Imoto, K., Doran, R., Lee, J., Plan, P., Wilson, J., Xin, H.B., Sanbe, A., Gulick, J., Mathai, J., Robbins, J., Salama, G., Nakai, J., Kotlikoff, M.I., 2006. Imaging cellular signals in the heart in vivo: cardiac expression of the high-signal Ca2+ indicator GCaMP2. Proc. Natl. Acad. Sci. U. S. A. 103, 4753–4758.
Till, S.M., Asiminas, A., Jackson, A.D., Katsanevaki, D., Barnes, S.A., Osterweil, E.K., Bear, M.F., Chattarji, S., Wood, E.R., Wyllie, D.J., Kind, P.C., 2015. Conserved hippocampal cellular pathophysiology but distinct behavioural deficits in a new rat model of FXS. Hum. Mol. Genet. 24, 5977–5984.
van den Boom, B.J.G., Bos, J., 2018. Miniscope Baseplate and Protective Cone for Rats. (http://miniscope.org/index.php/Miniscope_Baseplate_and_Protective_Cone_for_Rats).
Zhang, F., Wen, Y., Guo, X., 2014. CRISPR/Cas9 for genome editing: progress, implications and challenges. Hum. Mol. Genet. 23, R40–6.
Ziv, Y., Burns, L.D., Cocker, E.D., Hamel, E.O., Ghosh, K.K., Kitch, L.J., El Gamal, A., Schnitzer, M.J., 2013. Long-term dynamics of CA1 hippocampal place codes. Nat. Neurosci. 16, 264–266.

4.4 Neural manifold analysis of brain circuit dynamics in health and disease

Journal of Computational Neuroscience (2023) 51:1–21
https://doi.org/10.1007/s10827-022-00839-3

REVIEW

Neural manifold analysis of brain circuit dynamics in health and disease

Rufus Mitchell-Heggs[1,2] · Seigfred Prado[1,3] · Giuseppe P. Gava[1] · Mary Ann Go[1] · Simon R. Schultz[1]

Received: 21 March 2022 / Revised: 30 August 2022 / Accepted: 29 October 2022 / Published online: 16 December 2022

Abstract
Recent developments in experimental neuroscience make it possible to simultaneously record the activity of thousands of neurons. However, the development of analysis approaches for such large-scale neural recordings have been slower than those applicable to single-cell experiments. One approach that has gained recent popularity is neural manifold learning. This approach takes advantage of the fact that often, even though neural datasets may be very high dimensional, the dynamics of neural activity tends to traverse a much lower-dimensional space. The topological structures formed by these low-dimensional neural subspaces are referred to as "neural manifolds", and may potentially provide insight linking neural circuit dynamics with cognitive function and behavioral performance. In this paper we review a number of linear and non-linear approaches to neural manifold learning, including principal component analysis (PCA), multi-dimensional scaling (MDS), Isomap, locally linear embedding (LLE), Laplacian eigenmaps (LEM), t-SNE, and uniform manifold approximation and projection (UMAP). We outline these methods under a common mathematical nomenclature, and compare their advantages and disadvantages with respect to their use for neural data analysis. We apply them to a number of datasets from published literature, comparing the manifolds that result from their application to hippocampal place cells, motor cortical neurons during a reaching task, and prefrontal cortical neurons during a multi-behavior task. We find that in many circumstances linear algorithms produce similar results to non-linear methods, although in particular cases where the behavioral complexity is greater, non-linear methods tend to find lower-dimensional manifolds, at the possible expense of interpretability. We demonstrate that these methods are applicable to the study of neurological disorders through simulation of a mouse model of Alzheimer's Disease, and speculate that neural manifold analysis may help us to understand the circuit-level consequences of molecular and cellular neuropathology.

Keywords Neural manifolds · Manifold learning · Neural population analysis · Dimensionality reduction · Neurological disorders

Action Editor: Uri Eden

Rufus Mitchell-Heggs and Seigfred Prado contributed equally to this work.

✉ Simon R. Schultz

Rufus Mitchell-Heggs

[1] Department of Bioengineering and Centre for Neurotechnology, Imperial College London, London SW7 2AZ, United Kingdom

[2] Centre for Discovery Brain Sciences, The University of Edinburgh, Edinburgh EH8 9XD, United Kingdom

[3] Department of Electronics Engineering, University of Santo Tomas, Manila, Philippines

1 Introduction

While the investigation of single neurons has undoubtedly told us much about brain function, it is uncertain whether individual neuron properties alone are sufficient for understanding the neurobiological basis of behavior (Pang et al., 2016). In some cases, trial-averaging of single-neuron responses may lead to confusing or misleading interpretation of true biological mechanisms (Sanger & Kalaska, 2014; Cunningham & Yu, 2014). Additionally, single-neuron activities studied in higher-level brain areas involved in cognitive tasks (Machens et al., 2010; Laurent, 2002; Churchland et al., 2010) are highly heterogeneous both across neurons and across experimental conditions even for nominally identical trials. And finally, it may well be that task-relevant

information is represented in patterns of activity across multiple neurons, above and beyond what is observable at the single neuron level. Unfortunately, characterizing such patterns, in the worst case, may require measurement of an exponential number of parameters (the "curse of dimensionality").

However, it appears that in many circumstances, patterns of neural population activity may be described in terms of far fewer population-level features than either the number of possible patterns, or even the number of neurons observed (Churchland et al., 2012; Mante et al., 2013; Chaudhuri et al., 2019; Gallego et al., 2020; Nieh et al., 2021; Stringer et al., 2019). This underpins a paradigm shift in the studies of neural systems from single-neuron analysis to a more comprehensive analysis that integrates single-neuron models with neural population analysis.

If, as appears to be the case, the spatiotemporal dynamics of brain activity is low dimensional, or at least much lower-dimensional than the pattern space, then it stands to reason that such activity can be characterized without falling afoul of the curse of dimensionality, and on reasonable experimental timescales. Indeed, in recent years, numerous techniques have been developed to do just that. For instance, classification algorithms have been applied to neuronal ensembles to predict aspects of behavior (Rigotti et al., 2013; Fusi et al., 2016; Rust, 2014; Raposo et al., 2014). One problem with this is that the common practice is to identify "neuronal ensembles" by grouping together neurons with sufficiently highly correlated activity during the same behaviors or in response to the same stimuli. This ignores information that is transmitted collectively and might lead to (i) falsely concluding that a group of neurons do not encode a behavioral variable (when in fact they encode it collectively), (ii) incorrectly estimating the amount of information that is being encoded, and/or (iii) missing important mechanisms that contribute to encoding (Frost et al., 2021).

Alternatively, artificial neural networks (ANN) have been increasingly employed, either by (i) using a goal-driven neural network and using the embedding to compare and predict the population activity in different brain regions (Russo et al., 2018; Mante et al., 2013; Jazayeri and Ostojic, 2021), or (ii) modelling the activity of individual neurons as emanating from a feedforward or recurrent neural network architecture (Elsayed et al., 2016; Rajan et al., 2016). Whilst these methods can present powerful ways of inferring neural states and dynamics, some issues have been raised on their biological interpretability, even though recent work has addressed some of them, as we discuss in Section 2.11.

To address these shortcomings, a range of techniques which are commonly referred to under the umbrella term of "neural manifold learning" (NML) have been employed. Some of these approaches simply make use of long-established general methods for dimensionality reduction (such as principal components analysis), whereas others have been developed specifically to study high-dimensional neural datasets.

Mathematically speaking, a manifold is a topological space that locally resembles our usual Euclidean space. If we form a multivariate time-series by convolving the spike trains of a neural population with a smoothing filter, and consider the activity pattern across these time series at each time to occupy a point in a neural activity space, then over time the activity will excurse a subspace that has often been observed to appear like such a manifold. Characterizing the geometry of such structures may offer important insights into neural computation (Chung & Abbott, 2021). In practical terms, the "neural manifold" is a low-dimensional subspace within the higher-dimensional space of neural activity which explains the majority of the variance of the neural dynamics (Fig. 1). Of course, real neural population dynamics are subject to noise, and in real experiments the topological subspace that can be excursed by the dynamics of neural activity can only be sampled, often sparsely. We

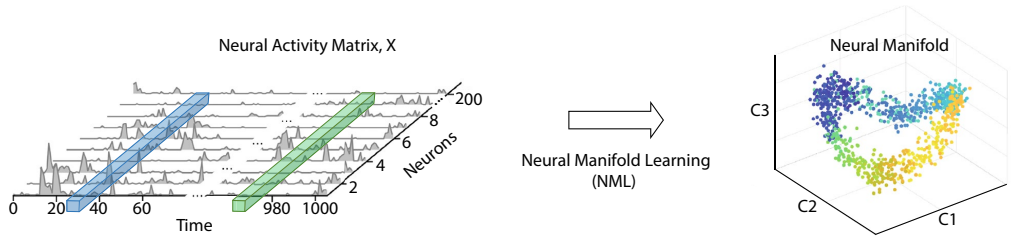

Fig. 1 Schematic showing a typical example of how a manifold learning algorithm may reduce the dimensionality of a high-dimensional neural population time series to produce a more interpretable low-dimensional representation. A high-dimensional neural population activity matrix, $\mathbf{X}$, with N neurons and T time points, is projected into a lower-dimensional manifold space and the trajectory visualized in the space formed by the first 3 dimensions, $c1$, $c2$ and $c3$

must make several important comments here: firstly, that this characterization of neural systems depends inherently upon a description of the system in which the state is continuous and determined by the instantaneous firing rates of each neuron (although those firing rates might be calculated from filters implementing shorter or longer time windows). And secondly, that what may be observed experimentally is typically a "point cloud" - however these points do not themselves constitute a manifold; instead they are normally taken as indicative of the underlying topological space which they sample. And finally, it should be noted that the term "neural manifold" is frequently used relatively loosely in neuroscience to refer to any kind of low-dimensional structure which may or may not meet the criteria of a mathematical manifold. In this survey article we will not dwell overly on this distinction, noting it but considering that utility is at this stage more important, and that it is likely that terminology will continue to evolve.

Neural manifold learning algorithms are algorithms for efficiently extracting a description of such a subspace from a sample of multivariate neural activity. Here we review how neural manifold learning can be employed to extract low-dimensional descriptions of the internal structure of ensemble activity patterns, and used to obtain insight into how interconnected populations of neurons represent and process information. Such techniques have been applied to neural population activity in a variety of different animals, brain regions and during distinct network states. In this review we compare a variety of neural manifold learning algorithms with several datasets from multi-electrode array electrophysiology and multi-photon calcium imaging experiments, to assess their relative merits in gaining insight into the recorded neural dynamics and the computations they may be underpinning.

We envisage that neural manifold learning may not only facilitate accurate quantitative characterizations of neural dynamics in healthy states, but also in complex nervous system disorders. Anatomical and functional brain networks may be constructed and analyzed from neuroimaging data in describing and predicting the clinical syndromes that result from neuropathology. NML can offer theoretical insight into progressive neurodegeneration, neuropsychological dysfunction, and potential anatomical targets for different therapeutic interventions. For example, investigating neural populations in the medial prefrontal cortex that are active during social situations while encoding social decisions may enable hypothesis testing for disorders such as Autistic Spectrum Disorder (ASD) or Schizophrenia (Irimia et al., 2018; Kingsbury et al., 2019).

In this review, we introduce NML as a methodology for neural population analysis and showcase its application to the analysis of different types of neural data with differing behavioral complexity both in healthy and disease model states. For selected algorithms, we visualize how they represent neural activity in lower-dimensional embeddings and evaluate them on their ability to discriminate between neural states and reconstruct neural data. We aim to offer the reader the prospect of selecting with confidence the type of NML method that works best for a particular type of neural data, as well as an appreciation of how NML can be leveraged as a powerful tool in deciphering more precisely the basis of different cognitive impairments and brain disorders.

2 Neural manifold learning

Neural manifold learning (NML) describes a subset of machine learning algorithms that take a high-dimensional neural activity matrix $\mathbf{X}$ comprised of the activity of N neurons at T time points and embed it into a lower-dimensional matrix $\mathbf{Y}$ while preserving some aspects of the information content of the original matrix $\mathbf{X}$ - e.g. mapping nearby points in the neural activity space $\mathbf{X}$ to nearby points in $\mathbf{Y}$ (see Fig. 1) (Cunningham & Yu, 2014; Churchland et al., 2012; Meshulam et al., 2017; Mante et al., 2013; Harvey et al., 2012; Wu et al., 2017). When projected into this lower-dimensional space, the set of neural activity patterns *observed* are typically constrained within a topological structure, or manifold, $\mathcal{Y}$, which might have a globally curved geometry but a locally linear one. For instance, if the reduced dimensionality embedding matrix $\mathbf{Y}$ is three-dimensional (3D) (often depicted on a two-dimensional (2D) page for convenience of illustration), the neural manifold $\mathcal{Y}$ might describe a closed surface within that 3D space. Another way of looking at this is that the data points in $\mathbf{X}$ lie on a lower-dimensional manifold that can be parameterised by a lower-dimensional coordinate system give by $\mathbf{Y}$, and that the task of the manifold learning algorithm is to find that coordinate system. This approach has found widespread recent use across neuroscientific studies (Fig. 2), including for understanding neural mechanisms during speech (Bouchard et al., 2013), decision-making in prefrontal cortex (Mante et al., 2013; Harvey et al., 2012; Briggman et al., 2005; Stokes et al., 2013), movement preparation and execution in the motor cortices (Churchland et al., 2012; Kaufman et al., 2014; Yu et al., 2009; Feulner & Clopath, 2021; Gallego et al., 2017) and spatial navigation systems (Chaudhuri et al., 2019; Nieh et al., 2021; Rubin et al., 2019; Gardner et al., 2022).

2.1 Manifold learning algorithms

There are several types of manifold learning algorithms that can generally be divided into linear and non-linear approaches. Although they have similar goals, they may differ in the way they transform the data and in the type of

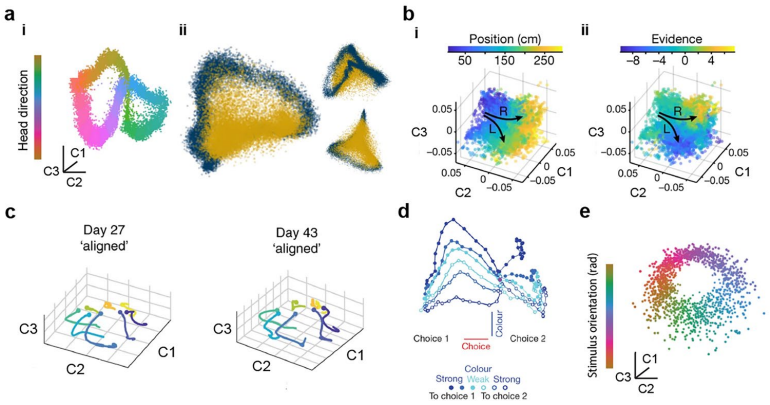

Fig. 2 Neural manifolds across different species and brain regions. **a** Population activity in the mouse head-direction circuit (Chaudhuri et al., 2019). **i** During waking, the network activity directly maps onto the head orientation of the animal. **ii** Comparison between population activity during waking (dark blue) and nREM sleep (mustard yellow); the latter does not follow the same one-dimensional waking dynamics. **b** Population activity in the mouse hippocampus during an evidence accumulation and decision making task in virtual reality (Nieh et al., 2021). Task-relevant variables such as **i** position and **ii** accumulated evidence are encoded in the manifold. **c** The motor cortical population activity underpinning a reaching task in monkeys is stable over days and years (Gallego et al., 2020). **d** Prefrontal cortical population activity in macaque monkeys during a visual discrimination task spans a low-dimensional space. Task-relevant variables such as the dots' direction and strength of motion, colour, and the monkey's choice are encoded in the manifold (Mante et al., 2013). **e** Population activity in the mouse primary visual cortex in response to gratings of different orientations, indicated by color (Stringer et al., 2021). The panel is adapted from Jazayeri and Ostojic (2021)

statistical structures or properties they capture and preserve. It is important to select the type of method most suitable for the type of neural data being analyzed, as this may have significant impact on the resulting scientific interpretation.

In this section, we describe some of the more common manifold learning methods in use in the neuroscience literature. To make a fair and informative comparison of each algorithm, we implemented them and applied them each to a number of different neural datasets, as described in Section 3. In order to facilitate comparison of the assumptions made by the different algorithms, we have attempted to adopt (where possible) a common mathematical terminology throughout; this is summarised in Table 1.

2.1.1 Linear method

Linear manifold learning is accomplished by performing linear transformations of the observed variables that preserve certain optimality properties, which yield low-dimensional embeddings that are easy to interpret biologically. Some of the most common linear manifold learning techniques are discussed below.

2.2 Principal component analysis (PCA)

One of the most common linear manifold learning methods is Principal Component analysis (PCA) (Jolliffe, 2002; Jackson, 2005; Ivosev et al., 2008). It reduces the dimensionality of large datasets while preserving as much variability (or statistical information) as possible. To obtain a neural manifold $\mathbf{Y}$, PCA performs an eigendecomposition on the covariance matrix of the neural activity matrix $\mathbf{X}$ in order to find uncorrelated latent variables that are constructed as linear combinations of the contributions of individual neurons, while successively maximising the variance. The computed eigenvectors,

Table 1 Summary of mathematical notation used throughout this manuscript

Notation	Description
N	Number of neurons
T	Number of time samples
t	Sample timestamp
$\mathbf{X}$	Population activity matrix
$\mathbf{x_t}$	Network activity state at timestamp t
k	Number of dimensions in the embedding
$\mathbf{Y}$	Manifold embedding matrix
$\mathcal{Y}$	Manifold - a topological structure within $\mathbf{Y}$
$\mathbf{D}$	Dissimilarity matrix (MDS)
$\mathbf{G}$	Graph of population activity
$\mathbf{\Lambda}$	Graph Laplacian (LEM)
$\mathbf{\Delta}$	Diagonal matrix (LEM)
$\mathbf{\Omega}$	Adjacency matrix (LEM)

or principal components (PCs), represent the directions of the axes that capture the most variance, and the corresponding eigenvalues yield the amount of variance carried by each PC.

Although PCA has been used to great effect to reduce the dimensionality of high-dimensional neural data (Churchland et al., 2010; Mazor & Laurent, 2005; Gao & Ganguli, 2015; Ahrens et al., 2012), its caveat is that it captures all types of variance in the data, including spiking variability, which may obscure the interpretation of latent variables. For example, neurons with higher firing rates typically exhibit higher variance (spike count variance being proportional to mean spike count for cortical neurons Tolhurst et al. (1983)), and therefore may skew the orthogonal directions found by PCA by accounting mostly for highly active neurons. Additionally, cortical neurons respond with variable strength to repeated presentations of identical stimuli (Tolhurst et al., 1983; Shadlen & Newsome, 1998; Cohen & Kohn, 2011). This variability is often shared among neurons, and such correlations in trial-to-trial responses can have a substantial effect on the amount of information encoded by a neuronal population. To minimise the effects of spiking variability, trial averaging or temporal smoothing of spike counts is usually done prior to performing PCA. However, this may not always be applicable to all analyses.

2.3 Multidimensional scaling (MDS)

Classical multidimensional scaling is another linear dimensionality reduction technique that aims to find a low-dimensional map of a number of objects (e.g. neural states) while preserving as much as possible pairwise distances between them in the high-dimensional space (Kruskal & Wish, 1978; Venna & Kaski, 2006; Yin, 2008; France & Carroll, 2010).

In the case of neural data, given an $N \times T$ activity matrix, $\mathbf{X}$, a $T \times T$ distance matrix, $\mathbf{D}$, is first obtained by measuring the distance between the population activity vectors for all t using a dissimilarity metric (Krauss et al., 2018). Examples of such metrics include both the Euclidean distance and the cosine dissimilarity. We will employ the latter for the MDS embeddings shown throughout this paper. For a pair of vectors $\mathbf{a}$,$\mathbf{b}$ separated in angle by θ, the cosine dissimilarity is

$$D_{\mathbf{a},\mathbf{b}} = \cos(\theta) = 1 - \frac{\mathbf{a}.\mathbf{b}}{\|\mathbf{a}\|\|\mathbf{b}\|}.$$

The dissimilarity matrix $\mathbf{D}$ is formed from the cosine dissimilarities between the neural activity patterns $\mathbf{c}_t$ at each time t for all pairs of times measured. A lower-dimensional mapping, $\mathbf{Y} \in \mathfrak{R}^{k \times T}$, where $k << N$, is then found by minimising a loss function, called the *strain*, so that the mapped inter-point distances are as close as possible to the original distances in $\mathbf{D}$. From the eigen-decomposition of the distance matrix $\mathbf{D}$, the MDS components (i.e. dimensions) are revealed by the eigenvectors, which are a linear combination of the distances across the T population activity vectors, while their respective eigenvalues report the amount of variance explained.

Multidimensional scaling has been used to study changes in neural population dynamics in both large-scale neural simulations (Phoka et al., 2012) and in neural population recordings (Luczak et al., 2009). It has been applied for characterizing glomerular activity across the olfactory bulb in predicting odorant quality perceptions (Youngentob et al., 2006), integrative cerebral cortical mechanisms during viewing (Tzagarakis et al., 2009), neuroplasticity in the processing of pitch dimensions (Chandrasekaran et al., 2007), emotional responses to music in patients with temporal lobe lesions (Dellacherie et al., 2011), and structural brain abnormalities associated with autism spectrum disorder (Irimia et al., 2018).

2.3.1 Non-linear methods

The algorithms described above can only extract linear (or approximately so) structure. Non-linear techniques, on the other hand, aim to uncover the broader non-linear structure of the neural population activity matrix $\mathbf{X}$. These insights, can come at the expense of weaker biological interpretation, as the discovered manifold is not given by a linear combination of some observed variable (e.g. individual neurons). Non-linear algorithms often attempt to approximate the true topology of the manifold $\mathcal{Y}$ within the reduced dimensionality representation $\mathbf{Y}$ by finding population-wide variables that discard the relationship between faraway points (or neural states) on $\mathbf{X}$ and focus instead on conserving the distances between neighbors.

2.4 Isomap

One of the most commonly used non-linear manifold learning algorithms is Isomap (Tenenbaum et al., 2000). Non-linear techniques aim to uncover the broader non-linear structure of the neural manifold embedding of the neural population activity, $\mathbf{X}$, by approximating the true topology of the neural manifold, $\mathcal{Y}$. To do so, Isomap first embeds $\mathbf{X}$ into a weighted graph $\mathbf{G}$, whose nodes represent the activity of the neuronal population at a given time $\mathbf{x}_t$, and the edges between them represent links to network states $\mathbf{x}_i, \mathbf{x}_j, ...$ that are the most similar to $\mathbf{x}_t$, i.e., its neighbors.

The k-nearest neighbors algorithm is usually used to estimate the neighbors for all network states $\mathbf{x}_1, ..., \mathbf{x}_T$. These neighboring relations are then encoded in a weighted graph with edges $d_{\mathbf{G}}(i,j)$ between neighboring states i, j that depends on the distance metric $d_{\mathbf{X}}$ used. $\mathbf{G}$ can then be used to approximate the true geodesic distances on the manifold $d_{\mathcal{Y}}(i,j)$ between any two points i, j (i.e. network states $\mathbf{x}_i, \mathbf{x}_j$)

by measuring their shortest path length $d_{\mathbf{G}}(i,j)$ in the weighted graph $\mathbf{G}$ using an algorithm such as Dijkstra's (Dijkstra et al., 1959).

MDS is then applied to the matrix of shortest path lengths within the graph $\mathbf{D}_{\mathbf{G}} = \{d_{\mathbf{G}}(i,j)\}$ to yield an embedding of the data in a k-dimensional Euclidean space $\mathbf{Y}$ that best preserves the manifold's estimated geometry. The quality of the reconstructed manifold $\mathcal{Y}$ depends greatly on the size of the neighborhood search and the distance metric used to build $\mathbf{G}$. Isomap is a conservative approach that seems well suited to tackle the non-linearity inherent to neural dynamics and it has in fact been used in a variety of studies, even just for visualization purposes (Mimica et al., 2018; Chaudhuri et al., 2019; Sun et al., 2019).

2.5 Locally linear embedding (LLE)

LLE is another non-linear manifold learning technique that attempts to preserve the local geometry of the high-dimensional data $\mathbf{X}$, by separately analyzing the neighborhood of each network state $\mathbf{x}_t$, assuming it to be locally linear even if the global manifold structure is non-linear (Roweis and Saul, 2000). The local neighborhood of each network state is estimated using the steps described in Section 2.4 and is connected together to form a weighted graph $\mathbf{G}$. The location of any node i in the graph corresponds to the network state $\mathbf{x}_i$, which can then be described as a linear combination of the location of its neighboring nodes $\mathbf{x}_j, \mathbf{x}_k, ...$ These contributions are summarised by a set of weights, $\mathbf{W}$, which are optimised to minimise the reconstruction error between the high-dimensional network state $\mathbf{x}_i$ and the neighborhood linear estimation. The weight w_{ij} summarizes the contribution of the j^{th} network state to the reconstruction of the i^{th} state. To map the high-dimensional dataset $\mathbf{X}$ onto a lower-dimensional one $\mathbf{Y}$, the same local geometry characterized by $\mathbf{W}$ is employed to represent the low-dimensional network state $\mathbf{y}_i$ as a function of its neighbors $\mathbf{y}_j, \mathbf{y}_k, ...$

A significant extension of LLE was introduced that makes use of multiple linearly independent weight vectors for each neighborhood. This leads to a Modified LLE (MLLE) algorithm that is much more stable than the original (Zhang & Wang, 2007). Unlike Isomap, LLE preserves only the local geometry of the high-dimensional data $\mathbf{X}$, represented by the neighborhood relationship, so that short high-dimensional distances are mapped to short distances on the low-dimensional projection. In contrast, Isomap aims to preserve the geometry of the data at all scales, long distances included, possibly introducing distortions if the topology of the manifold is not estimated well. For neural data, though, Isomap has generally been preferred for its theoretical underpinnings and more intuitive approach.

2.6 Laplacian eigenmaps (LEM)

LEM, also referred to as Spectral Embedding, is another non-linear technique similar to LLE (Belkin, 2003). The algorithm is geometrically motivated as it exploits the properties of the neighboring graph $\mathbf{G}$ generated from the high-dimensional data $\mathbf{X}$, as in Section 2.4, to obtain a lower-dimensional embedding $\mathbf{Y}$ that optimally preserves the neighborhood information of $\mathbf{X}$.

In the graph $\mathbf{G}$, any two connected nodes (network states) i and j are connected by a binary edge using a neighborhood method as in 2.4, or by a weighted edge computed via a kernel parametrising the exponential relationship of the weights with respect to the distance between the nodes in the high-dimensional space $\mathbf{x}_i - \mathbf{x}_j$. The resulting graph edges form the adjacency matrix $\mathbf{\Omega}$ that is used, together with the diagonal matrix $\mathbf{\Delta}$ containing the degree of each node of $\mathbf{G}$, to obtain the graph Laplacian $\mathbf{\Lambda} = \mathbf{\Delta} - \mathbf{\Omega}$. The spectral decomposition of $\mathbf{\Lambda}$ reveals the structure and clusters on $\mathbf{G}$. The k eigenvectors with the smallest non-zero eigenvalues of $\mathbf{\Lambda}$ are, in fact, the k dimensions of the manifold embedding $\mathbf{Y}$. Similar to LLE, Laplacian eigenmaps preserve only the local geometry of the neural population activity $\mathbf{X}$ and are therefore more robust to the construction of $\mathbf{G}$. Indeed LEM has been successfully used to unveil behaviorally relevant neural dynamics (Rubin et al., 2019; Sun et al., 2019).

2.7 t-distributed stochastic neighbor embedding (t-SNE)

t-SNE is another non-linear method that aims to match local distances in the high-dimensional space $\mathbf{X}$ to the low-dimensional embedding $\mathbf{Y}$. This is obtained by first constructing a probability distribution over pairs of high-dimensional points $\mathbf{x}_i, \mathbf{x}_j$ in such a way that nearby points are assigned a higher probability while dissimilar points are assigned a lower probability. Then t-SNE defines a similar probability distribution over the points $\mathbf{y}_i, \mathbf{y}_j$ in the low-dimensional space, and it minimizes the Kullback-Leibler divergence between the two distributions (Van der Maatea & Hinton, 2008). The Euclidean distance is used in the original algorithm to evaluate the similarity between data points, but any appropriate metric can be employed as well. This method has been applied in a wide range of domains, from genomics to signal processing, including multiple neuroscientific settings (Dimitriadis et al., 2018; Panta et al., 2016). It usually considers up to three embedding dimensions for visualization constraints, and for exploiting the Barnes-Hut approximation, which reduces the computational cost to $O(N \log N)$ from $O(N^2)$. (Van Der Maaten, 2014).

2.8 Uniform manifold approximation and projection (UMAP)

UMAP is a non-linear manifold learning technique that is constructed from a theoretical framework based on topological data analysis, Riemannian geometry and algebraic topology (McInnes et al., 2018) and it has also been used on neural data both as an NML method (Tombaz et al., 2020) and for broader dimensionality reduction purposes Lee et al. (2021). It builds upon the mathematical foundations of LEM, Isomap and other non-linear manifold learning techniques in that it uses a k nearest neighbors weighted graphs representation of the data. By using manifold approximation and patching together local fuzzy simplicial set representations, a topological representation of the high-dimensional data is constructed. This layout of the data is then optimised in a low-dimensional space to minimize the cross-entropy between the two topological representations. Compared to t-SNE, UMAP is competitive in terms of visualization quality and arguably preserves more of the global dataset structure with superior run time performance. Furthermore, the algorithm is able to scale to significantly larger data set sizes than are feasible for t-SNE.

UMAP and t-SNE have recently being employed for visualizing high-dimensional genomics data and some distortion issues have been raised (Chari et al., 2021). Although this problem is particularly apparent with t-SNE, which tends to completely disregard the global structure of the data to find clusters, any reduction to too few dimensions with respect to the original high-dimensional space will inherently distort the topology of some of the data, as indicated by the Johnson-Lindenstrauss Lemma (Johnson and Lindenstrauss, 1984). These criticisms have been made with particular reference to genomics datasets, which are intrinsically higher-dimensional than the neural datasets which manifold learning has been applied to.

2.9 Probabilistic latent variable models

Another type of NML algorithm uses probabilistic latent variable models that construct a generative model for the data in terms of mapping a low-dimensional manifold or latent space to neural responses. This type of algorithm utilizes a probabilistic framework that performs temporal smoothing and dimensionality reduction simultaneously, allowing joint optimisation of the degree of smoothing and the relationship between the original high-dimensional data and the resulting low-dimensional neural trajectory (Yu et al., 2009). A good example is Gaussian Process Factory analysis (GPFA) that uses Gaussian processes and an additional explicit noise model to account for the different independent noise variances of different neurons (i.e., spiking variability). It is a set of factor analyzers that are linked together in the low-dimensional state space by a Gaussian process prior (Rasmussen & Williams, 2006), which allows for the specification of a correlation structure across the low-dimensional states at different time points. In cases where the neural time courses are believed to be similar across different trials, smooth firing rate profiles may be obtained by averaging across a small number of trials (Mazor & Laurent, 2005; Stopfer et al., 2003; Brown et al., 2005; Broome et al., 2006; Levi et al., 2005; Nicolelis et al., 1995), or by applying more advanced statistical methods for estimating firing rate profiles from single spike trains (DiMatteo et al., 2001; Cunningham et al., 2007) Similarly, Manifold Inference from Neural Dynamics (MIND) is a recently developed NML algorithm that aims to characterize the neural population activity as a trajectory on a non-linear manifold, defined by possible network states and temporal dynamics between them (Low et al., 2018; Nieh et al., 2021).

2.10 NML algorithms for trial-structured datasets

Importantly, model selection from a computed manifold can be greatly affected by the signal-to-noise ratio (SNR) of the initial input neural data. In many cases this has been overcome by using the square root transformation of spiking data and convolving it with a Gaussian filter to yield a smoothed instantaneous firing rate (Yu et al., 2009). In addition, multiple dimensionality reduction steps have also been used to enable more interpretable visualizations (LEM on LEM (Rubin et al., 2019), UMAP on PCA (Gardner et al., 2022)). Furthermore, the NML algorithms described and visualized up until now have been general use case algorithms, used to infer neural correlates from the data. However, in experiments where specific behaviors or decisions are time-locked and run across multiple trials, some of the NMLs described above have been augmented and optimised. These include, demixed Principal Component analysis (dPCA) (Kobak et al., 2016), Tensor Component analysis (TCA) (Cohen & Maunsell, 2010; Niell & Stryker, 2010; Peters et al., 2014; Driscoll et al., 2017), Cross-Validated PCA (cvPCA) (Stringer et al., 2019) and model-based Targeted Dimensionality Reduction (mTDR) (Aoi & Pillow, 2018). These NML algorithms exploit the trial nature of an experiment to discriminate signal from trial-to-trial variability or noise, enabling the experimenter to identify the principal components that maximally correspond to a stimulus or action.

2.11 ANN-based NML algorithms

Artificial neural networks (ANN) can also be employed for manifold learning as they have the potential to extract complex non-linear structure in high-dimensional data. Autoencoders exemplify this approach as they are designed to find an optimal encoding between a high-dimensional input

and a low-dimensional representation stored in their "bottleneck" code layer, which preserves the information necessary to then reconstruct the original input from it. In this sense, auto-encoders can be thought of as a non-linear extension to PCA, where each node in the code layer is comparable to a PC. Delving deeper, the field of deep generative models such as variational auto-encoders (VAE) promise great potential at extracting low-dimensional structure in varied high-dimensional data, by constructing a stochastic model of the low-dimensional dynamics underlying the neural activity. Such methods have shown great results when inferring the neural activity trial-by-trial fluctuations, but some have raised the issue that the low-dimensional structure extracted from these models are often highly entangled and therefore, difficult to interpret (Pandarinath et al., 2018). To address these issues, VAEs that make use of external labels, such as behavioral variables or the passage of time, have been designed (Zhou & Wei, 2020). Lastly, addressing some of the shortcomings of VAEs such as interpretability, identifiability and generalizability, Consistent EmBeddings of high-dimensional Recordings using Auxiliary variables, or CEBRA, was developed. CEBRA uses an innovative approach that employs contrastive learning instead of a generative model to extract embeddings, this enables it to cope with strong data distribution shifts to yield consistent embeddings between experimental sessions, subjects and recording modalities (Schneider et al., 2022).

3 Manifold learning for the analysis of large-scale neural datasets

To demonstrate how neural manifold learning can be used in the analysis of large-scale neural datasets, we apply a number of linear and non-linear NML algorithms (PCA, MDS, LEM, LLE, Isomap, t-SNE and UMAP) to several datasets. The datasets were chosen to cover a number of different brain regions and a range of behavioral complexity. They consist of (i) two-photon calcium imaging of hippocampal subfield CA1 in a mouse running along a circular track (Section 3.1), taken from Go et al. (2021; ii) multi-electrode array extracellular electrophysiological recordings from the motor cortex of a macaque performing a radial arm goal-directed reach task (Section 3.2) from Yu et al. (2007); and (iii) single-photon "mini-scope" calcium imaging data recorded from the prefrontal cortex of a mouse under conditions where multiple task-relevant behavioral variables were monitored (Section 3.3), from Rubin et al. (2019). Lastly, we illustrate how manifold learning can be employed to characterize brain dynamics in a disease state such as Alzheimer's disease by applying these techniques to data simulated to reproduce basic aspects of dataset (i), augmented to incorporate pathology (Section 3.4).

3.1 Decoding from neural manifolds

To compare NML algorithms we evaluated the resulting manifolds according to behavioral decoding (reconstruction or classification) performance, ability to encode the high-dimensional activity (i.e reconstruction score) and intrinsic dimensionality. These quantifications make up a minor subset of the many manifold parameterization methods, of which we describe more Section 4.2). For hippocampal CA1 manifolds obtained by any of the NML methods, we computed decoding accuracy for the behavioral variable(s) as a function of the number of manifold embedding dimensions using an Optimal Linear Estimator (OLE) (Warland et al., 1997). This allows assessment of the number of dimensions necessary to encode the behavioral variable. We used a 10-fold cross-validation approach, i.e., training the decoder on 90% of the data and testing it on the remaining 10%. Decoding performance is calculated as the Pearson correlation coefficient between the actual and reconstructed behavioral variable, i.e. the mouse position, for the test data. To assess neural manifold information provided about animal behavior in the other two datasets, we built a logistic regression classifier (Hosmer et al., 1989); we evaluate its performance using the F1 score as a function of the number of manifold embedding dimensions used. The F1 score is defined as the weighted average of the precision (i.e., percentage of the results which are relevant) and recall (i.e., percentage of the total relevant results correctly classified by the algorithm), and ranges between 0 (worst) and 1 (best performance) (Blair, 1979).

3.2 Reconstruction of neural activity from a low-dimensional embedding

Another way to evaluate the degree of fidelity of the manifold embedding is to attempt to reconstruct the high-dimensional neural data from the low-dimensional embedding. This tells us how much has been lost in the process of dimensionality reduction. To obtain such a reverse mapping, we employed the non-parametric regression method originally introduced for LLE (Low et al., 2018; Nieh et al., 2021). We then obtained the reconstruction similarity by computing the Pearson correlation coefficient between the reconstructed and the original neural activity. To perform an element-wise comparison, the $N \times T$ neural activity matrices were concatenated column-wise into a single vector and the correlation coefficient calculated. To obtain the neural activity reconstruction score, we employed a 10-fold cross-validation strategy. Using 90% of the data from each session to learn the reverse mapping, the reconstruction was then evaluated on the remaining 10% the data. The final score was then obtained by averaging across folds.

3.3 Intrinsic manifold dimensionality

Estimating the number of required dimensions of the underlying manifold is a crucial part of manifold learning (Altan et al., 2021; Cunningham and Yu, 2014), as it helps one to acquire a conceptual idea of how complex the neuronal activity inside the manifold is. The intrinsic manifold dimensionality accounts for the number of independent (latent) variables necessary to describe the neural activity without suffering significant information loss (Jazayeri & Ostojic, 2021). However, it is difficult to estimate the dimensionality of neural manifolds, especially in the realistic condition of a noisy, non-linear embedding. A recent review provides a detailed evaluation of several dimensionality estimation algorithms when applied to high-dimensional neural data (Altan et al., 2021).

We acknowledge that any measure of dimensionality is strongly influenced by the timescale of the neural activity and by the size of the population recorded (Humphries, 2020), in this review we use the intrinsic dimensionality measure to compare the topologies captured by the different NML methods. To infer the manifold intrinsic dimensionality we employ a method related to the correlation dimension of a dataset (Grassberger and Procaccia, 1983). After applying NML to the original high-dimensional neural activity, for any given point (i.e., neural state) in the low-dimensional space, the number of neighboring neural states within a surrounding sphere as a function of the sphere's radius was calculated. The slope of the number of neighboring data points within a given radius on a log-log scale equals the exponent k in the power law $N(r) = cr^k$, where N is the number of neighbors and r is the sphere radius. k then provides an estimate of the intrinsic dimensionality of the neural activity. We fit the power law in the range between ∼10 to 5000 neighbors or neural states, aiming to capture the relevant temporal scale for each task and related manifold (Rubin et al., 2019; Nieh et al., 2021). Note, in fact, that we have selected a particular range for each dataset, also depending on the number of time samples T available (details in respective figure captions).

3.4 Hippocampal neural manifolds

The hippocampus is well known to be involved in memory formation and spatio-contextual representations (Scoville & Milner, 1957; O'Keefe & Conway, 1978; Morris, 2006). NML has been recently applied to hippocampal neural activity by several authors, suggesting that the rodent hippocampal activity encodes various contextual, task-relevant variables, displaying more complex information processing than spatial tuning alone (Rubin et al., 2019; Nieh et al., 2021). Here, we re-analyze published data from a dataset comprising two-photon calcium imaging of hippocampal CA1 place cells, to which previously only MDS had been applied Go et al. (2021), in order to compare manifolds extracted by different algorithms. We examine how different NML methods characterize the dynamics of hippocampal CA1 neurons along trajectories in low-dimensional manifolds as they coordinate during the retrieval of spatial memories.

The data was recorded from a head-fixed mouse navigating a circular track in a chamber floating on an air-pressurized table under a two-photon microscope (Fig. 3a). The mouse position (Fig. 3b) was simultaneously tracked using a magnetic tracker. The activity of 30 of 225 hippocampal CA1 cells recorded in the shown session is depicted in Fig. 3c. Of the 225 cells, 92 were classified as place cells by Go et al. (2021), and their normalized activity rate map, sorted according to place preference, is shown in Fig. 3d. Employing the activity of all 225 cells (both place and non-place selective), both linear (Fig. 3e) and non-linear (Fig. 3f) NML methods, revealed a cyclic pattern of transitions between network states corresponding to different locations along the circular track. The manifold formed by the dynamics of neural activity as the mice explored the full track forms a complete representation of the 2D structure of the track. We compared the algorithms in terms of decoding performance (Fig. 3g), neural activity reconstruction score (Fig. 3h) and intrinsic manifold dimensionality (Fig. 3i). All algorithms performed similarly in terms of the metrics considered, yielding almost the best possible decoding performance with just one manifold dimension and the best possible reconstruction similarity with two dimensions. Moreover, all manifolds were found to have a similar intrinsic dimensionality of around 2.

In this example, the behavioral complexity is approximately one dimensional (i.e., the mouse running in a single direction along a circular track can be mapped onto the single circular variable θ) and all NML methods produce embeddings which allow high decoding performance, with each algorithm already reaching near-maximum performance after incorporating only the first manifold dimension. This suggests that if the behavioral complexity is low and its information is broadly encoded within the neural population, any NML algorithm will yield broadly similar results. However, as we will see, this does not necessarily hold when complexity of the behavioral task is increased. In terms of the ability to capture the neural activity variance, the neural activity reconstruction score suggests that the highly non-linear tSNE and UMAP algorithms yield more informative low-dimensional embeddings.

3.5 Motor cortical neural manifolds

NML and dimensionality reduction techniques have also been applied to neural activity within motor and pre-motor cortical areas, in particular to suggest that the high variability observed in the single-neuron responses is disregarded when

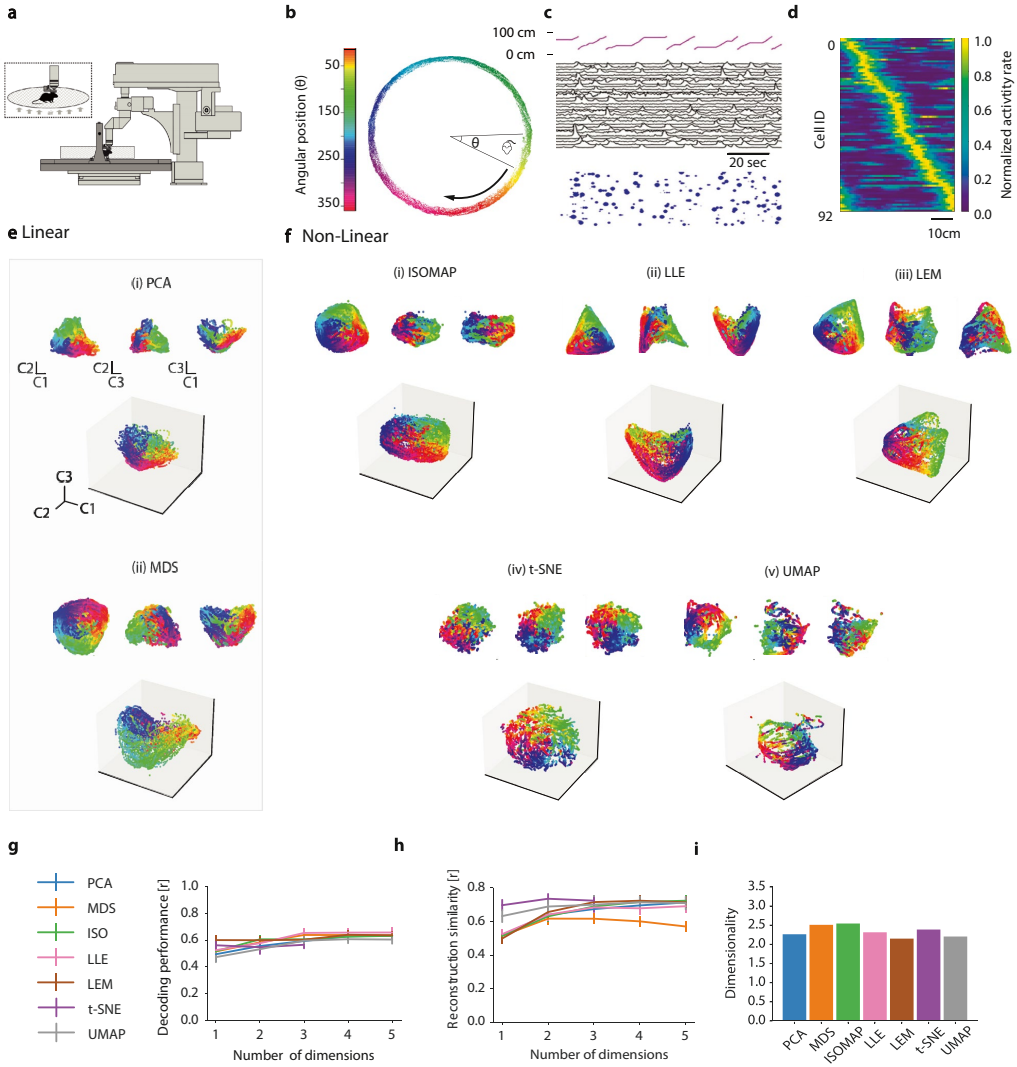

Fig. 3 Mouse hippocampalCA1 manifolds during spatial memory retrieval. Unless otherwise stated, panels adapted with permission from Go et al. (2021). **a** Schematic of experimental setup: head-fixed mouse navigates a floating circular track under a two-photon microscope. Inset: Close-up view of head-fixed mouse on floating track. **b** Spatial trajectories of the mouse, with θ (color-coded) denoting position on the track. **c** Top: Position along the track (cm), Middle: Ca^{2+} transients for 30 (of 225) randomly selected cells, Bottom: Rastergram showing events detected from the above calcium transients. Blue dots indicate time of Ca^{2+} transient onset, with dot area showing relative event amplitude (normalized per cell). **d** Normalized neural activity rate map for 92 place cells, sorted by spatial tuning around the track. **e - f** Linear vs non-linear manifold embeddings for all 225 cells (normalized). In each case the first three dimensions are visualized. Insets for each: projections on pairs of components C1 and C2 (upper left), C2 and C3 (upper middle), C1 and C3 (upper right). **e** Linear manifold embeddings (i) PCA, (ii) MDS, **f** non-linear manifold embeddings (i) Isomap, (ii) LLE, (iii) LEM, (iv) t-SNE, and (v) UMAP. (ii-v were not reproduced from Go et al. (2021). **g-i** Manifold evaluation metrics: (see: **g** Decoding performance (as used in Go et al. (2021)), **h** Neural activity reconstruction score, **i** Intrinsic manifold dimensionality

population dynamics are taken into account (Santhanam et al., 2009; Churchland & Shenoy, 2007; Churchland et al., 2012; Sussillo et al., 2015; Gallego et al., 2017). This approach has been the foundation of the "computation through dynamics" framework, which aims to characterize the neural population dynamics as trajectories along manifolds (Vyas et al., 2020). Rotational-like dynamics of motor cortex neural activity have been observed both in human and non-human primates (Churchland et al., 2012; Pandarinath et al., 2015), with stability over long periods of time (Gallego et al., 2020). Importantly, by furthering the understanding of neural population dynamics and variability, crucial steps can be made in improving performance of prosthetic devices that can be used to further enable those with nervous-system disease or injury in day-to-day tasks (Santhanam et al., 2009).

We applied NML to data from Yu et al. (2007) and Chestek et al. (2007) recorded in the caudal premotor cortex (PMd) and rostral primary motor cortex (M1) of rhesus macaques during a radial arm goal-directed reaching task (Fig. 4a). Neural data was collected for 800 successful repeats, with 100 trials for each of the 8 reaching directions (Fig. 4b). We used NML to analyze the neural activity during the 100 ms time window before the onset of the reaching movement and investigated its tuning with respect to the reaching direction (Santhanam et al., 2009). The manifold embeddings obtained using different NML methods, both linear (Fig. 4e) and non-linear (Fig. 4f), revealed different types of structures with data points clustering according to the monkey's target endpoint. All the NML algorithms tested revealed lower-dimensional structures that discriminate between each of the behavioral states along a single dimension. We used the pre-movement neural manifold to classify the behavior into one of eight different goal directions. The two linear NML algorithms yielded the most behaviorally informative embedding, requiring only two dimensions to achieve best performance (Fig. 4g). All algorithms performed equally in terms of neural activity reconstruction similarity, with only one dimension being necessary to reconstruct the original neural activity patterns (Fig. 4h). The intrinsic dimensionality of the two linear embeddings, on the other hand, was the highest (Fig. 4i). Non-linear NML algorithms extracted lower-dimensional embedding at the cost of encoding less behavioral information.

Increasingly, NML has been used to analyze neural circuits implicated in decision-making such as the prefrontal cortex (PFC) (Kingsbury et al., 2019; Mante et al., 2013) and the anterior cingulate cortex (ACC) (Rubin et al., 2019). With these multi-function brain regions, neurons are widely known for their mixed selectivity, often capturing information relating to both stimuli features and decisions (Kobak et al., 2016; Rigotti et al., 2013; Fusi et al., 2016). This moves away from the notion of highly-tuned single cells and gives rise to a dynamical, population-driven code (Pouget et al., 2000) ideally suited to NML methods. This was nicely demonstrated by Rubin et al. (2019), who visualized and quantified how NML (in their case, LEM) could be used to discriminate neural states arising from different brain regions (ACC and hippocampal area CA1) during identical tasks. The neural activity was recorded in freely-behaving mice exploring a linear track and performing various behaviors such as drinking, running, turning, and rearing (Figure 5a-c). Building on their findings, we employed various alternative NML methods, both linear (Fig. 5d) and non-linear (Fig. 5e), that revealed different neural data structures, exhibiting clustering according to the animals' behavior, with PCA and LLE producing the least clustered visualizations. Evaluation of NML behavior classification performance (Fig. 5f), reconstruction similarity (Fig. 5g) and manifold intrinsic dimensionality (Figure 5i) revealed that although there was high variability in performance, non-linear algorithms generally out-performed the linear ones. Notably, two non-linear NML algorithms t-SNE and UMAP performed the best in terms of behavioral classification and ability to reconstruct the high-dimensional neural activity from the manifold embedding, with an intrinsic dimensionality between 2 and 3, inferring that behavior is the predominant type of information encoded by the ACC network during this task.

3.6 Analysis of neural manifolds in neurological disorders

NML potentially provides a valuable tool for understanding the biology of different brain disorders. As an example, NML can be used to characterize changes in neural manifolds for spatial memory during the progression of Alzheimer's disease (AD). In AD, the hippocampus and connected cortical structures are among the first areas to show pathophysiology. Hippocampal-dependent cognitive processes such as episodic memory are particularly and prominently affected at the behavioral level. However, it is not yet understood how the pathological markers of AD, such as amyloid-beta plaques and neurofibrillary tangles, lead to specific disruptions in the network-level information processing functions underpinning memory function. While single-cell properties are obviously affected, it is believed that network properties relating to the coordination of information throughout brain circuits involved in memory may be particularly at risk (Palop & Mucke, 2016). Neural manifold learning analysis methods may thus play a useful or even crucial role in disentangling the effects of these network alterations.

The formation of extracellular amyloid plaques causes aberrant excitability in surrounding neurons (Busche et al., 2008): cells close to amyloid plaques tend to become hyperactive, whereas those further away from the plaques tend to

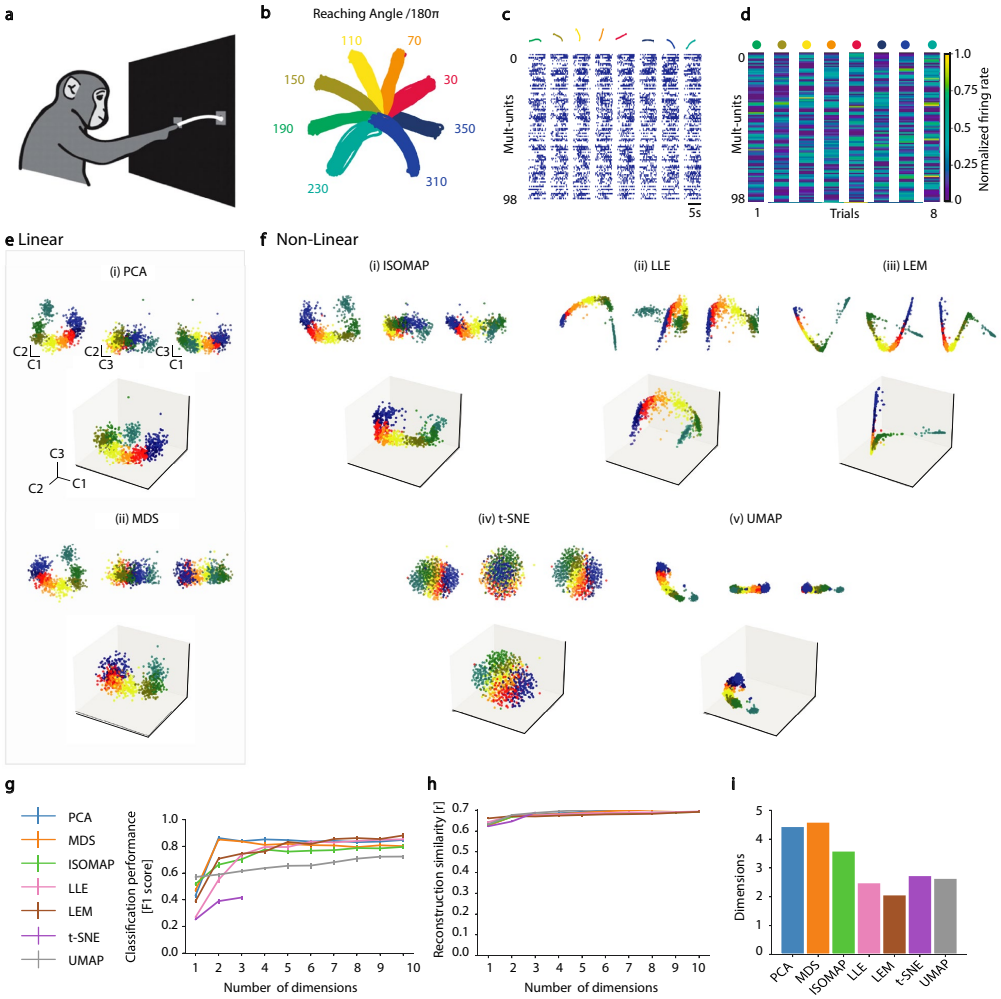

Fig. 4 Manifold analysis of motor cortical dynamicsduring a reaching task. **a** Monkey reaching task experimental setup. **b** Arm trajectories and target reaching angles - schematic and coloured trajectories adapted from Yu et al. (2007). **c-d** Neural data processing steps (adapted from Santhanam et al. (2009)) **c** Top: X,Y position of monkey arm over eight individual trials coloured according to (b). Bottom: Corresponding raster plot of spike trains recorded simultaneously from 98 neural units, sampled every 1 ms. Units include both well isolated single-neuron units (30% of all units), as well as multi-neuron units. **d** Population activity vector yielding the instantaneous firing rates of the same neural units in (c) for the 100 ms before the monkey reached out its arm (separated and coloured by trial type/arm direction as in c). **e - f** Linear vs non-linear manifold embeddings (normalized, only first three dimensions visualized). Insets: projections on pairs of components, C1 and C2 (upper left), C2 and C3 (upper middle), C1 and C3 (upper right). **(e)** Linear manifold embeddings (i) PCA, (ii) MDS. **f** non-linear manifold embeddings (i) Isomap, (ii) LLE, (iii) LEM, (iv) t-SNE, and (v) UMAP **g-i** Manifold evaluation metrics **g** Decoding performance [F1 score], **h** Neural activty reconstruction score [r], **i** Intrinsic manifold dimensionality

become hypoactive (or relatively silent). This aberrant neuronal excitability could potentially have a substantial effect on the neural manifold, and conversely, the neural manifold may provide a way to assess the overall impact of network abnormalities. To demonstrate this, we simulated neural data for the (Go et al., 2021) circular track experiment described in Fig. 3) using parameters outlined by (Busche et al., 2008), i.e., the percentages of hyperactive (α) and hyperactive cells

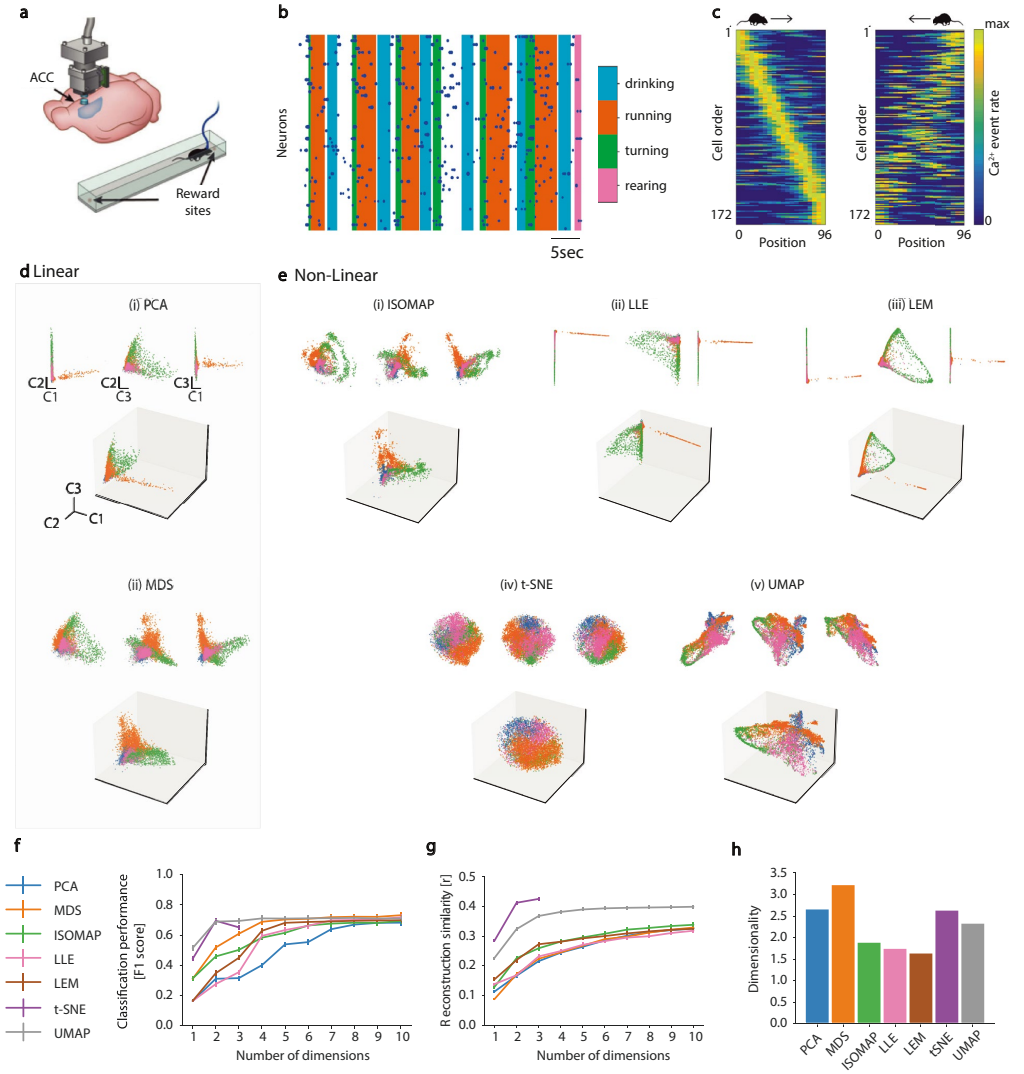

Fig. 5 Manifold analysis of prefrontalcortical dynamics during behavior. **a-c** Schematic of experimental setup from Rubin et al. (2019). The mouse navigates a linear track with rewards at both ends. **b** Raster plot of the neural activity during multiple behaviors (adapted from Rubin et al. (2019)): (1) drinking, (2) running, (3) turning, and (4) rearing. **c** Calcium event rate as the mouse runs to the right (left panel) and to the left (right panel) of the linear track (from Rubin et al. (2019)). **d-e** Linear vs non-linear manifold embeddings (normalized). In each case the first three dimensions are visualized: Insets for each: projections on pairs of components: C1 and C2 (upper left), C2 and C3 (upper middle), C1 and C3 (upper right). **d** Linear manifold embeddings (i) PCA, (ii) MDS, **e** non-linear manifold embeddings (i) Isomap, (ii) LLE, (iii) LEM, (iv) t-SNE, and (v) UMAP. **f-h** Manifold evaluation metrics **f** Decoding performance [r], **g** Reconstruction score [r], **h** Intrinsic manifold dimensionality

(β) in a given FOV, while conforming to previous studies that observed more than 20% of neurons becoming hyperactive (Busche et al., 2008; Busche & Konnerth, 2015) in transgenic AD mice. This yielded a population of hippocampal CA1 cells (with 50% normal cells, 21% hyperactive cells and 29% hypoactive cells). Hypersynchrony, which

has also been observed in AD (Palop & Mucke, 2016), was not simulated for the purposes of this exercise, to maintain simplicity. This disease model mimics the neural activity of hippocampal CA1 cells of an AD mouse (e.g. a mouse over-expressing amyloid precursor protein, (Oakley et al., 2006)) running on a circular track; we compare it with a simulated control model representing a healthy wild-type litter-mate (Fig. 6a, b). Using MDS and UMAP as exemplars (Fig. 6c, d, respectively), NML shows how the aberrant excitability of neurons distorts the neural manifolds for spatial memory in AD (bottom panel) with respect to the healthy control model (top panel). While the topological structure remains relatively intact, the boundaries of the set become fuzzier, akin to adding noise to the system. To further evaluate this, we examined manifold parameterization measures including decoding performance, neural reconstruction similarity and manifold intrinsic dimensionality for both NML approaches (Fig. 6e-m). In both cases, the AD model's manifold embeddings display worse performance than the control model, although UMAP was able to recover a more behaviorally informative and lower-dimensional embedding than MDS.

To investigate the effects of the proportions of aberrant cells on the neural manifolds, we simulated the same models with varying percentages of normal, hyperactive (α) and hypoactive (β) cells. As expected, the hyperactivity of cells close to amyloid plaques (which tends to add noise) distorts the neural manifolds more than the hypoactive cells (which is more akin to having a decreased number of neurons in the manifold), resulting in less clustering of neural states in the manifold space. This is consistent with their effects on performance in terms of the given manifold measures (Fig. 6f-g, i-j, l-m).

We suggest that on this basis, NML techniques exhibit potential for helping to improve our understanding of network-level disruption in disease phenotypes.

4 Discussion

4.1 Comparison of neural manifold algorithms

With the increase in the numbers of simultaneously recorded neurons facilitated by emerging recording technologies, the demand for methods that enable reliable and comprehensively informative population-level analysis also increases. Multivariate analyses of large neuronal population activity thus require the use of more efficient computational models and algorithms that are geared towards finding the fewest possible population-level features that best describe the coordinated activity of such large neuronal populations. These features must be interpretable and open to parameterization that enables inherent neural mechanisms to be described (as discussed in the next section).

In this review, we give insights into how NML facilitates accurate quantitative characterizations of the dynamics of large neuronal populations in both healthy and disease states. However, assessing exactly how reliable and informative NML methods are remains a challenge and is open to interpretation. An ideal NML method must be able to adapt to different datasets that span functionally different brain regions, behavioral tasks, and number of neurons being analyzed, while considering different noise levels, timescales, etc.

In many studies, linear NML methods (such as PCA and classical MDS) have been preferred, and are widely used throughout the literature because of computational simplicity and clear interpretation. However, these methods have not been sufficient when the geometry of the neural representation is highly non-linear, which might for instance be induced by high behavioral task complexity (Jazayeri & Ostojic, 2021) (see Fig. 5). As shown in (Rubin et al., 2019), low SNR can also affect the quality of some linear NML embeddings. They compared PCA and LEM algorithms and revealed that LEM required fewer neurons and lower firing rates for accurate estimation of the internal structure. To address the challenges of noisy data, many solutions have been suggested, including the development of novel linear algorithms, such as dPCA (Kobak et al., 2016), cvPCA (Stringer et al., 2019), and mTDR (Aoi & Pillow, 2018). These methods enable greater discrimination between specific clusters of neural activity, but they do rely heavily on neural responses acquired during multiple trials of time-locked behavior. However, these may not always be available, and whilst it is possible to tweak certain algorithmic parameters or fit them to manipulated forms of the data (e.g. through time-warping), the end result is an increase in computational complexity and possibly harder to interpret results.

Conversely, non-linear methods, in general, trend towards better generalization across datasets. This is particularly true for UMAP and t-SNE (see Figs. 3, 4 and 5). To discriminate clusters of neural activity, UMAP and t-SNE have been shown to be the most powerful non-linear NML techniques. However, they might not always yield an embedding that is representative of the true high-dimensional geometry. These issues are particularly relevant for inherently very high-dimensional data, such as genomics data (Chari et al., 2021). In fact, it is debated whether a low number of latent dimensions are enough to drive neural population activity and explain its variability across a range of circumstances such as brain region and task (Chaudhuri et al., 2019; Rubin et al., 2019; Nieh et al., 2021; Churchland et al., 2012; Gallego et al., 2020), or if higher dimensionality are required (Stringer et al., 2019; Humphries, 2020).

Finally, a key consideration when selecting any NML method is whether its function is for neural data

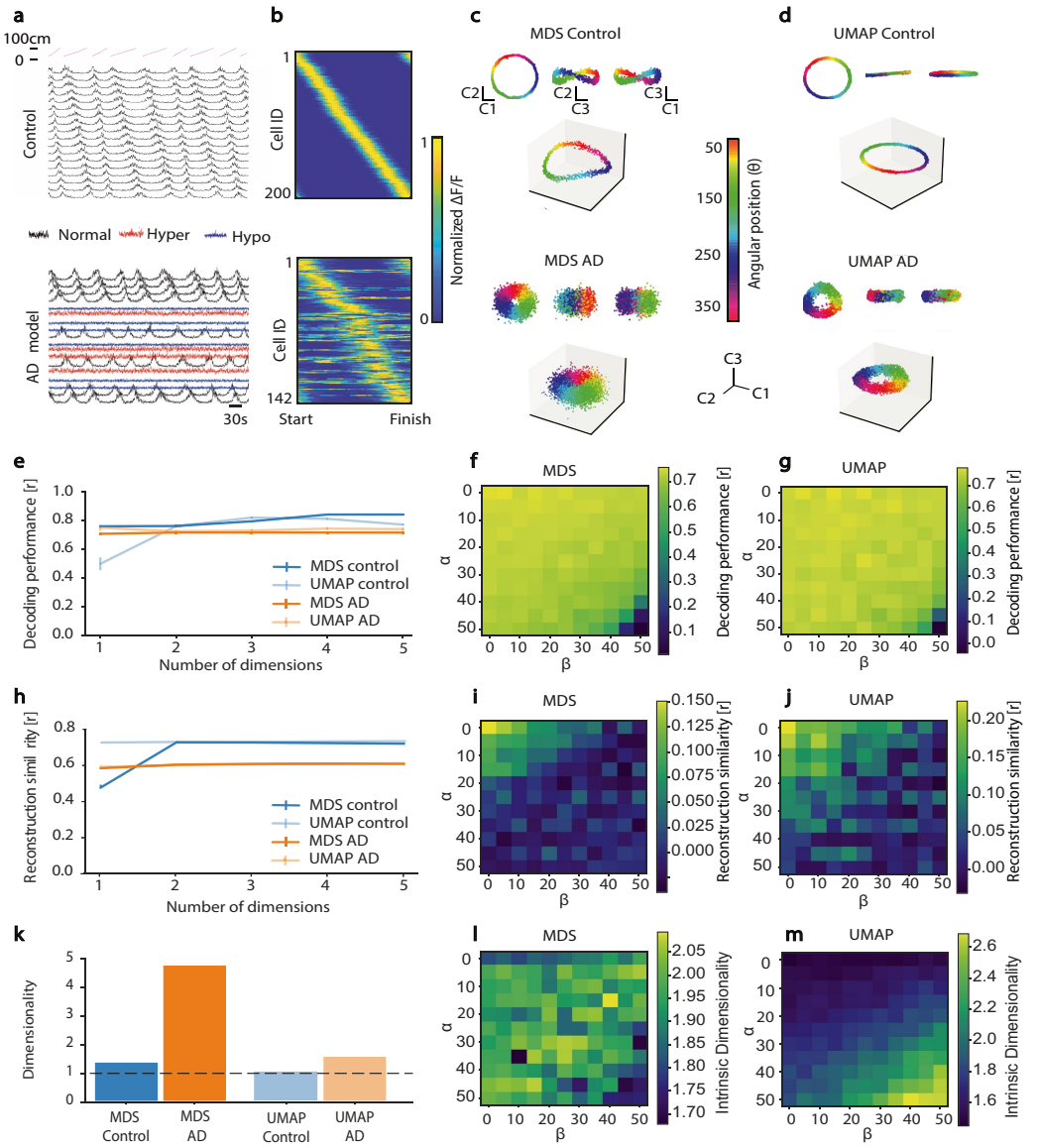

Fig. 6 Changes in neural manifolds during neurodegenerative disease states. **a** Example simulated calcium traces for a mouse traversing a circular track (simulation of real experiment in Fig. 3). Top: 20 of 200 "normal" CA1 place cells (magenta traces on top show mouse trajectory). Bottom: 20 of 200 AD-affected place cells that fall into three categories: Normal (black), Hyperactive (red) and Hypoactive (blue). **b** Normalized activity rate maps for 200 healthy and 142 (out of 200) AD hippocampal CA1 place and hyperactive cells (respectively) sorted by location of maximal activity. **c-d** 3D projection in the manifold space using (c) MDS and (d) UMAP for both healthy control and AD simulated models. Inset: 2D projections onto pairs of dimensions. **e-m** Evaluation metrics for MDS and UMAP, Control vs AD and shown as a function of varying percentages of normal, hyperactive (α) and hypoactive (β) cells. **e-g** Decoding performance [r]. **h-j** Reconstruction similarity [r]. **k-m** Intrinsic dimensionality

visualization or for structural discovery and/or quantification. For instance, many of the non-linear algorithms described above, such as UMAP, t-SNE have excellent capabilities in visualizing high-dimensional data and provide an interpretable global structure. Similarly, VAEs present themselves as great candidates for discriminating global clusters. However, obtaining a favorable global structure can often be at the expense of a loss to local structure (Chari et al., 2021) and therefore can distort any downstream structural quantification. To address these shortcomings one can use algorithms that either provide a linear solution such as PCA-based methods (Gardner et al., 2022) or that focus on local structure such as LEM (Rubin et al., 2019). ANNs may add further possibilities, with methods such as CEBRA tackling model identifiability and generalization (Schneider et al., 2022).

One message that can be taken away from our comparison of neural manifold approaches is that linear methods do provide substantial insight over a wide range of problem domains (often consistent with what is provided by non-linear methods), and even in areas where they fail to correctly capture the low-dimensional topological structure of the manifold, they can still provide insight verifiable through decoding of behavior.

4.2 Parameterization of neural manifolds

A key issue for NML approaches is that after the neural manifold has been determined, it normally needs to be analyzed further to answer a given scientific question. This process, known as parameterization, would ideally involve extraction of the equations of the manifold itself, however, out of feasibility may also be based on a more limited quantification of manifold properties. Depending on the type of neural data at hand and the scientific hypothesis to be tested, it's important to select the most suited and informative NML algorithm and parameterization measures. One challenge that has to be kept in mind is that the resulting manifolds, although often visualized in two or three dimensions for convenience, frequently involve many more dimensions (e.g. even a low-dimensional neural manifold from a recording from many hundreds of neurons might involve tens of dimensions), and many approaches that may work well in two or three dimensions do not necessarily scale straightforwardly to higher-dimensional representations.

Where transitions in the dynamics of neural states are observed over time, one approach that is useful is recurrence analysis (Marwan et al., 2007; Wallot, 2019). Recurrence analysis is a non-linear data analysis that is based on the study of phase space trajectories, where a point or element in phase space represents possibles states of the system. It is a powerful tool in characterizing the behavior of a dynamical system, especially when observing how states change over time. A recurrence plot measures and visualizes the recurrences of a trajectory of a system in phase space. Note that although the recurrent plot is inherently two-dimensional, recurrence analysis can describe dynamics in an arbitrary dimensional space - a key feature of this technique. As the respective phase spaces of two systems change, recurrence plots allow quantification of their interaction and tell us when similar states of the underlying system occur. The time evolution of trajectories can be observed in the patterns depicted in the recurrence plots, and these patterns are associated with a specific behavior of the system, such as cyclicity and similarity of the evolution of states at different epochs. Different measures can be used to quantifying such recurrences based on the structure of the recurrence plot, including recurrence rate, determinism (predictibility), divergence, laminarity, and Shannon entropy (Webber & Marwan, 2015; Wallot, 2019). These measures might be especially useful when observing neuronal responses to stimuli over repeated trials under different conditions (such as healthy and diseased states).

Another way to compare neural manifolds under different conditions is to directly quantify the similarity of trajectories in the neural manifold space (Cleasby et al., 2019; Ding et al., 2008; Alt, 2009). The most commonly used measures of trajectory similarity are Fréchet distance (FD) (Fréchet, 1906; Besse et al., 2015), nearest neighbor distance (NND) (Clark & Evans, 1954; Freeman et al., 2011), longest common subsequence (LCSS) (Vlachos, 2002), edit distance for real sequences (EDR) (Chen & Ng, 2004; Chen et al., 2005) and dynamic time warping (DTW) (Toohey, 2015; Long & Nelson, 2013). Computing such measures may allow us to characterize the differences (or similarities) among neural manifolds obtained from different models. This type of analysis may be especially useful when comparing models in health and disease states across age groups, or when comparing neural manifold representations of the same model across different environments and conditions.

Another useful measure is manifold trajectory tangling (Russo et al., 2018). Tangling is a simple way of determining whether a particular trajectory could have been generated by a smooth dynamical flow field; under smooth dynamics, neural trajectories should not be tangled. Two neural states are thus tangled if they are nearby but associated with different trajectory directions. High tangling implies either that the system must rely on external commands rather than internal dynamics, or that the system is flirting with instability (Russo et al., 2018). Thus, tangling can be compared across all times and/or conditions. It is especially useful when characterizing neural dynamics over the course of learning or development. For example, it may be interesting to examine whether neural circuits adopt network trajectories that are increasingly less tangled when learning a new skill and with increasing performance. Conversely, it may also

be interesting to investigate whether pathological conditions may be associated with increased tangling during learning.

In cases where we characterize task-specific responses, e.g., during repetitive, trial-structured motor movements, determining whether these neural responses are consistent with the hypothesised computation is important. Hence, the consistency in the geometry of the population response and/or the time-evolving trajectory of activity in neural state space (i.e., manifold space) must be examined. For such task-specific trials, manifold trajectories are considered consistent if the trajectory segments trace the same path and do not diverge. One measure that can be used for such analysis is manifold trajectory divergence (Russo et al., 2020). In contrast to manifold trajectory tangling, which assesses whether trajectories are consistent with a locally smooth flow field, manifold trajectory divergence assesses whether similar paths eventually separate, smoothly or otherwise. A trajectory can have low tangling but high divergence, or vice versa. Multiple features can contribute to divergence, including ramping activity, cycle-specific responses, and different subspaces on different cycles. Thus, manifold trajectory divergence provides a useful summary of a computationally relevant property, regardless of the specifics of how it was achieved (Russo et al., 2020).

Lastly, topological data analysis (TDA), which comprises methods such as persistent cohomology, aim to rigorously characterize the topological structure of the data. These methods are quite sensitive to noise levels and might not be adequate to investigate functionally complex neural systems, but they succeed in revealing the topology of simpler systems such as the head direction, grid cell systems and linear track representation (Chaudhuri et al., 2019; Gardner et al., 2022; Rubin et al., 2019). Similarly, Spline Parameterization for Unsupervised Decoding (SPUD) is a powerful method to characterise the manifold dynamics, which stems from a rigorous analysis of the manifold topological structure (Chaudhuri et al., 2019).

An increasing body of work using large-scale neural recording technologies is pointing towards the viewpoint that neural manifolds during spontaneous activity may be relatively high dimensional (Avitan & Stringer, 2022) [reviewed in], in comparison to the low-dimensional picture of spontaneous activity that had emerged from earlier recording technologies such as single-unit extracellular electrophysiology and functional magnetic resonance imaging. This of course provokes the question: at what dimensionality do neural manifold approaches cease to become useful? Notably, the datasets we have used as illustrations in this survey paper are (reflecting the field) intrinsically relatively low-dimensional in nature, ranging from a mouse running around a constrained environment to a monkey moving its arm in a fixed set of trajectories. Free-ranging, real-world behaviour is obviously higher dimensional in nature. Do manifold approaches cease to become useful in such cases? We would argue not, as long as the dimensionality of the manifold is much lower than the dimensionality of the neural recording (essentially determined by the number of cells that can be recorded, and which can exceed 10,000 with recently introduced technologies). Certainly two and three-dimensional visualisations may fail to capture interesting aspects of the data (which may in many cases be true already for 10-dimensional datasets). However, as we have pointed out in this section, there are many approaches for analysis of the resulting manifolds, such as recurrence plots, trajectory similarity measures, and manifold trajectory tangling, that work for higher dimensional manifolds. How these properties relate back to the predictions made by computational models of brain function is so far less clear. This area is ripe for further theoretical work.

4.3 Is neural manifold learning useful for understanding neurological disorders?

Neural manifold learning offers the prospect of aiding in our understanding of circuit neuropathologies. For instance, in mouse models of Alzheimer's disease, amyloid or tau pathologies result in changes in cortical circuitry, which are particularly evident in the hippocampus and connected structures. However, the effect of these pathologies on the dynamics of neural circuits involved in spatial and working memory at the network level are still not well understood. By analyzing the changes in the geometry of population responses and the time-evolving trajectory of activity of the associated hippocampal-cortical circuits, we can compare the neural manifolds recovered from groups of mice of different ages and/or with different health states. In particular, we can use recurrence analysis to determine whether neural states recur upon presentation of the same stimuli over repeated trials at different times across different ages of the models. Neural manifold similarity, tangling and divergence measures may also be computed to evaluate the differences (or similarity) of movement trajectories in the neural manifold space. Together, these measures can be used to compare the manifold dynamics across different age groups in both healthy and disease states.

In this review, we have demonstrated that neural manifold learning methods provide a powerful toolbox for understanding how populations of neurons coordinate in representing behaviorally relevant information. While the cellular and molecular pathologies underlying a variety of neurological disorders such as Alzheimer's Disease, Parkinson's Disease and Frontotemporal Dementia are at least beginning to be well understood, how they translate into network dysfunction and thus, into cognitive and behavioral deficits is not. Neural manifold learning techniques, in combination with new experimental technologies allowing us to record the

activity of many thousands of neurons simultaneously during behavioral tasks, potentially may allow us to assay the dynamics and Gestalt representations underlying cognition and behavior at the level of entire neural circuits. This could in turn lead to improved understanding of disease processes and more sensitive tests of therapeutic effect.

Acknowledgements We thank Krishna V Shenoy and Byron Yu for their permission to use the macaque motor cortex dataset and Alon Rubin for permission to use the mouse ACC dataset. We thank Elena Faillace for useful comments on a previous version of this manuscript.

Author contributions Rufus Mitchell-Heggs co-led and managed the project wrote and reviewed the main manuscript text, designed code for Figs. 3, 4 and 5 and co-prepared Figs. 1, 3, 4, 5 and 6. Seigfred Prado wrote and reviewed the main manuscript text, designed code for figures 6 and co-prepared Figs. 1 and 5. Giuseppe P. Gava wrote and reviewed the main manuscript text and designed the majority of manifold learning code for Figs. 3, 5 and 6 and created Fig. 2. Mary Ann Go contributed experimental data used for Fig. 3 and reviewed the main manuscript. Simon R. Schultz co-led and managed the project, wrote and reviewed the main manuscript.

Funding This work was funded by studentships from the EPSRC CDT in Neurotechnology for Life and Health (EPSRC EP/L016737/1) to S.P. and G.P.G., by Wellcome Trust Award 22152/Z/20/Z (S.R.S. and M.A.G.), by Wellcome Trust Award 207481/Z/17/Z (salary support to RM-H from R.G.M. Morris) and by Mrs Anne Uren and The Michael Uren Foundation.

Code availability Code to generate some of the figures in this paper is available at: https://github.com/schultzlab/Neural_Manifolds

Declarations

Conflicts of interest The authors declare that there are no conflicts of interest.

References

Ahrens, M. B., Li, J. M., Orger, M. B., et al. (2012). Brain wide neuronal dynamics during motor adaptation in zebrafish. *Nature, 485*(7399), 471–477.

Alt, H. (2009). The computational geometry of comparing shapes. In: Efficient Algorithms. *Springer*, p 235–248

Altan, E., Solla, S. A., Miller, L. E. et al. (2021). Estimating the dimensionality of the manifold underlying multi-electrode neural recordings. *PLoS Computational biology 17*(11), e1008591

Aoi, M. C., & Pillow, J. W. (2018). Model-based targeted dimensionality reduction for neuronal population data. *Advances in Neural Information Processing Systems, 31*, 6690–6699.

Avitan, L., & Stringer, C. (2022). Not so spontaneous: Multi-dimensional representations of behaviors and context in sensory areas. *Neuron*. https://doi.org/10.1016/j.neuron.2022.06.019

Belkin, M. (2003). Laplacian eigenmaps for dimensionality reduction and data representation. *Neural Computation, 15*(6), 1373–1396.

Besse, P., Guillouet, B., Loubes, J. M., et al. (2015). Review and perspective for distance based trajectory clustering. arXiv:1508.04904

Blair, D. C. (1979). Information Retrieval, 2nd Edition. *Journal of the American Society for Information Science*.

Bouchard, K. E., Mesgarani, N., Johnson, K., et al. (2013). Functional organization of human sensorimotor cortex for speech articulation. *Nature, 495*(7441), 327–332.

Briggman, K. L., Abarbanel, H. D., & Kristan, W. B. (2005). Optical imaging of neuronal populations during decision-making. *Science, 307*(5711), 896–901.

Broome, B. M., Jayaraman, V., & Laurent, G. (2006). Encoding and decoding of overlapping odor sequences. *Neuron, 51*(4), 467–482.

Brown, S. L., Joseph, J., & Stopfer, M. (2005). Encoding a temporally structured stimulus with a temporally structured neural representation. *Nature neuroscience, 8*(11), 1568–1576.

Busche, M. A., & Konnerth, A. (2015). Neuronal hyperactivity-a key defect in alzheimer's disease? *Bioessays, 37*(6), 624–632.

Busche, M. A., Eichhoff, G., Adelsberger, H., et al. (2008). Clusters of hyperactive neurons near amyloid plaques in a mouse model of Alzheimer's disease. *Science, 321*(5896), 1686–1689.

Chandrasekaran, B., Gandour, J. T., & Krishnan, A. (2007). Neuroplasticity in the processing of pitch dimensions: A multidimensional scaling analysis of the mismatch negativity. *Restorative neurology and neuroscience, 25*(3–4), 195–210.

Chari, T., Banerjee, J., & Pachter, L. (2021). The specious art of single-cell genomics. bioRxiv:0825457696.

Chaudhuri, R., Gerçek, B., Pandey, B., et al. (2019). The intrinsic attractor manifold and population dynamics of a canonical cognitive circuit across waking and sleep. *Nature Neuroscience, 22*, 1512–1520.

Chen, L., & Ng, R. (2004). On the marriage of lp-norms and edit distance. *Proceedings of the Thirtieth international conference on Very large data bases-Volume, 30*, 792–803.

Chen, L., Özsu, M. T., & Oria, V. (2005). Robust and fast similarity search for moving object trajectories. In: *Proceedings of the 2005 ACM SIGMOD international conference on Management of data*, pp 491–502.

Chestek, C. A., Batista, A. P., Santhanam, G., et al. (2007). Single-neuron stability during repeated reaching in macaque premotor cortex. *Journal of Neuroscience, 27*(40), 10742–10750.

Chung, S., & Abbott, L. (2021). Neural population geometry: An approach for understanding biological and artificial neural networks. *Current opinion in neurobiology, 70*, 137–144.

Churchland, M., Cunningham, J., Kaufman, M. T., et al. (2010). Cortical preparatory activity: representation of movement or first cog in a dynamical machine? *Neuron, 68*(3), 387–400.

Churchland, M., Cunningham, J., Kaufman, M., et al. (2012). Neural population dynamics during reaching. *Nature, 487*, 51–56.

Churchland, M. M., & Shenoy, K. V. (2007). Temporal complexity and heterogeneity of single-neuron activity in premotor and motor cortex. *Journal of Neurophysiology, 97*(6), 4235–4257.

Clark, P. J., & Evans, F. C. (1954). Distance to nearest neighbor as a measure of spatial relationships in populations. *Ecology, 35*(4), 445–453.

Cleasby, I. R., Wakefield, E. D., Morrissey, B. J., et al. (2019). Using time-series similarity measures to compare animal movement

trajectories in ecology. *Behavioral Ecology and Sociobiology, 73*(11), 1–19.
Cohen, M. R., & Kohn, A. (2011). Measuring and interpreting neuronal correlations. *Nature Neuroscience, 14*(7), 811.
Cohen, M. R., & Maunsell, J. H. (2010). A neuronal population measure of attention predicts behavioral performance on individual trials. *Journal of Neuroscience, 30*(45), 241–253.
Cunningham, J. P., & Yu, B. M. (2014). Dimensionality reduction for large-scale neural recordings. *Nature Neuroscience, 17*(11), 1500–1509.
Cunningham, J. P., Yu, B. M., Shenoy, K. V., et al. (2007). Inferring neural firing rates from spike trains using gaussian processes. *Advances in Neural Information Processing Systems, 20*, 329–336.
Dellacherie, D., Bigand, E., Molin, P., et al. (2011). Multidimensional scaling of emotional responses to music in patients with temporal lobe resection. *Cortex, 47*(9), 1107–1115.
Dijkstra, E. W., et al. (1959). A note on two problems in connexion with graphs. *Numerische Mathematik, 1*(1), 269–271.
DiMatteo, I., Genovese, C. R., & Kass, R. E. (2001). Bayesian curve-fitting with free-knot splines. *Biometrika, 88*(4), 1055–1071.
Dimitriadis, G., Neto, J. P., & Kampff, A. R. (2018). t-sne visualization of large-scale neural recordings. *Neural Computation, 30*(7), 1750–1774.
Ding, H., Trajcevski, G., Scheuermann, P., et al. (2008). Querying and mining of time series data: experimental comparison of representations and distance measures. *Proceedings of the VLDB Endowment, 1*(2), 1542–1552.
Driscoll, L. N., Pettit, N. L., Minderer, M., et al. (2017). Dynamic reorganization of neuronal activity patterns in parietal cortex. *Cell, 170*(5), 986–999.
Elsayed, G. F., Lara, A. H., Kaufman, M. T., et al. (2016). Reorganization between preparatory and movement population responses in motor cortex. *Nature Communications, 7*(1), 1–15.
Feulner, B., & Clopath, C. (2021). Neural manifold under plasticity in a goal driven learning behaviour. *PLoS Computational Biology 17*(2), e1008621.
France, S. L., & Carroll, J. D. (2010). Two-way multidimensional scaling: A review. I*EEE Transactions on Systems, Man, and Cybernetics, Part C (Applications and .Reviews) 41*(5), 644–661.
Fréchet, M. M. (1906). Sur quelques points du calcul fonctionnel. *Rendiconti del Circolo Matematico di Palermo (1884-1940), 22*(1), 1–72.
Freeman, R., Mann, R., Guilford, T., et al. (2011). Group decisions and individual differences: route fidelity predicts flight leadership in homing pigeons (columba livia). *Biology letters, 7*(1), 63–66.
Frost, N. A., Haggart, A., & Sohal, V. S. (2021). Dynamic patterns of correlated activity in the prefrontal cortex encode information about social behavior. *PLoS Biology, 19*(5), e3001235.
Fusi, S., Miller, E. K., & Rigotti, M. (2016). Why neurons mix: high dimensionality for higher cognition. *Current Opinion in Neurobiology, 37*, 66–74.
Gallego, J., Perich, M., Chowdhury, R., et al. (2020). Long-term stability of cortical population dynamics underlying consistent behavior. *Nature Neuroscience, 23*, 1–11.
Gallego, J. A., Perich, M. G., Miller, L. E., et al. (2017). Neural manifolds for the control of movement. *Neuron, 94*(5), 978–984.
Gao, P., & Ganguli, S. (2015). On simplicity and complexity in the brave new world of large-scale neuroscience. *Current Opinion in Neurobiology, 32*, 148–155.
Gardner, R. J., Hermansen, E., Pachitariu, M., et al. (2022). Toroidal topology of population activity in grid cells. *Nature, 602*(7895), 123–128.
Go, M. A., Rogers, J., Gava, G. P., et al. (2021). Place cells in head-fixed mice navigating a floating real-world environment. *Frontiers in Cellular Neuroscience, 15*, 19.
Grassberger, P., & Procaccia, I. (1983). Characterization of strange attractors. *Physical Review Letters, 50*(5), 346.
Harvey, C. D., Coen, P., & Tank, D. W. (2012). Choice-specific sequences in parietal cortex during a virtual-navigation decision task. *Nature, 484*(7392), 62–68.
Hosmer, D. W., Jovanovic, B., & Lemeshow, S. (1989). Best subsets logistic regression. *Biometrics* pp. 265–1270.
Humphries, M. D. (2020). Strong and weak principles of neural dimension reduction. arXiv:2011.08088
Irimia, A., Lei, X., Torgerson, C. M. et al. (2018). Support vector machines, multidimensional scaling and magnetic resonance imaging reveal structural brain abnormalities associated with the interaction between autism spectrum disorder and sex. *Frontiers in Computational Neuroscience* p. 93.
Ivosev, G., Burton, L., & Bonner, R. (2008). Dimensionality reduction and visualization in principal component analysis. *Analytical chemistry, 80*(13), 4933–4944.
Jackson, J. E. (2005). *A user's guide to principal components*. John Wiley & Sons.
Jazayeri, M., & Ostojic, S. (2021). Interpreting neural computations by examining intrinsic and embedding dimensionality of neural activity. *Current Opinion in Neurobiology, 70*, 113–120.
Johnson, W., & Lindenstrauss, J. (1984). Extensions of lipschitz maps into a hilbert space. *Contemporary Mathematics, 26*, 189–206.
Jolliffe, I. T. (2002). *Principal component analysis for special types of data*. Springer.
Kaufman, M. T., Churchland, M. M., Ryu, S. I., et al. (2014). Cortical activity in the null space: permitting preparation without movement. *Nature Neuroscience, 17*(3), 440–448.
Kingsbury, L., Huang, S., Wang, J., et al. (2019). Correlated neural activity and encoding of behavior across brains of socially interacting animals. *Cell, 178*(2), 429–446.
Kobak, D., Brendel, W., Constantinidis, C., et al. (2016). Demixed principal component analysis of neural population data. *eLife 5,* e10989.
Krauss, P., Metzner, C., Schilling, A., et al. (2018). A statistical method for analyzing and comparing spatiotemporal cortical activation patterns. *Scientific reports, 8*(1), 1–9.
Kruskal, J., & Wish, M. (1978). *Multidimensional Scaling*. Sage Publications.
Laurent, G. (2002). Olfactory network dynamics and the coding of multidimensional signals. *Nature Reviews Neuroscience, 3*(11), 884–895.
Lee, E. K., Balasubramanian, H., Tsolias, A., et al. (2021). Non-linear dimensionality reduction on extracellular waveforms reveals cell type diversity in premotor cortex. *eLife, 10*, e67490.
Levi, R., Varona, P., Arshavsky, Y. I., et al. (2005). The role of sensory network dynamics in generating a motor program. *Journal of Neuroscience, 25*(42), 9807–9815.
Long, J. A., & Nelson, T. A. (2013). A review of quantitative methods for movement data. *International Journal of Geographical Information Science, 27*(2), 292–318.
Low, R. J., Lewallen, S., Aronov, D., et al. (2018). Probing variability in a cognitive map using manifold inference from neural dynamics. bioRxiv:418939.
Luczak, A., Barthó, P., & Harris, K. D. (2009). Spontaneous events outline the realm of possible sensory responses in neocortical populations. *Neuron, 62*(3), 413–425.
Machens, C. K., Romo, R., & Brody, C. D. (2010). Functional, but not anatomical, separation of "what'' and "when'' in prefrontal cortex. *Journal of Neuroscience, 30*(1), 350–360.
Mante, V., Sussillo, D., Shenoy, K. V., et al. (2013). Context-dependent computation by recurrent dynamics in prefrontal cortex. *Nature, 503*(7474), 78–84.
Marwan, N., Romano, M. C., Thiel, M., et al. (2007). Recurrence plots for the analysis of complex systems. *Physics Reports, 438*(5–6), 237–329.

Mazor, O., & Laurent, G. (2005). Transient dynamics versus fixed points in odor representations by locust antennal lobe projection neurons. *Neuron, 48*(4), 661–673.

McInnes, L., Healy, J., & Melville, J. (2018). Umap: Uniform manifold approximation and projection for dimension reduction. arXiv: 1802.03426

Meshulam, L., Gauthier, J. L., Brody, C. D., et al. (2017). Collective behavior of place and non-place neurons in the hippocampal network. *Neuron, 96*(5), 1178–1191.

Mimica, B., Dunn, B. A., Tombaz, T., et al. (2018). Efficient cortical coding of 3d posture in freely behaving rats. *Science, 362*(6414), 584–589.

Morris, R. (2006). Elements of a neurobiological theory of hippocampal function: the role of synaptic plasticity, synaptic tagging and schemas. *European Journal of Neuroscience, 23*(11), 2829–2846.

Nicolelis, M. A., Baccala, L. A., Lin, R., et al. (1995). Sensorimotor encoding by synchronous neural ensemble activity at multiple levels of the somatosensory system. *Science, 268*(5215), 1353–1358.

Nieh, E. H., Schottdorf, M., & Freeman, N. W., et al. (2021). Geometry of abstract learned knowledge in the hippocampus. *Nature* pp. 1–5.

Niell, C. M., & Stryker, M. P. (2010). Modulation of visual responses by behavioral state in mouse visual cortex. *Neuron, 65*(4), 472–479.

Oakley, H., Cole, S. L., Logan, S., et al. (2006). Intraneuronal β-amyloid aggregates, neurodegeneration, and neuron loss in transgenic mice with five familial alzheimer's disease mutations: potential factors in amyloid plaque formation. *Journal of Neuroscience, 26*(40), 10129–10140.

O'Keefe, J., & Conway, D. H. (1978). Hippocampal place units in the freely moving rat: why they fire where they fire. *Experimental Brain Research, 31*(4), 573–590.

Palop, J. J., & Mucke, L. (2016). Network abnormalities and interneuron dysfunction in alzheimer disease. *Nature Reviews Neuroscience, 17*(12), 777–792.

Pandarinath, C., Gilja, V., Blabe, C. H., et al. (2015). Neural population dynamics in human motor cortex during movements in people with als. *Elife, 4*(e07), 436.

Pandarinath, C., O'Shea, D. J., Collins, J., et al. (2018). Inferring single-trial neural population dynamics using sequential auto-encoders. *Nature methods, 15*(10), 805–815.

Pang, R., Lansdell, B. J., & Fairhall, A. L. (2016). Dimensionality reduction in neuroscience. *Current Biology, 26*(14), R656–R660.

Panta, S. R., Wang, R., Fries, J., et al. (2016). A tool for interactive data visualization: application to over 10,000 brain imaging and phantom mri data sets. *Frontiers in Neuroinformatics, 10*, 9.

Peters, A. J., Chen, S. X., & Komiyama, T. (2014). Emergence of reproducible spatiotemporal activity during motor learning. *Nature, 510*(7504), 263–267.

Phoka, E., Wildie, M., Schultz, S. R., et al. (2012). Sensory experience modifies spontaneous state dynamics in a large-scale barrel cortical model. *Journal of Computational Neuroscience, 33*(2), 323–339.

Pouget, A., Dayan, P., & Peter, R. (2000). Information processing with population codes. *Nature Reviews Neuroscience, 1*, 125–132.

Rajan, K., Harvey, C. D., & Tank, D. W. (2016). Recurrent network models of sequence generation and memory. *Neuron, 90*(1), 128–142.

Raposo, D., Kaufman, M. T., & Churchland, A. K. (2014). A category-free neural population supports evolving demands during decision-making. *Nature Neuroscience, 17*(12), 1784–1792.

Rasmussen, C. E., & Williams, C. (2006). Gaussian processes for machine learning the mit press. Cambridge, MA.

Rigotti, M., Barak, O., Warden, M. R., et al. (2013). The importance of mixed selectivity in complex cognitive tasks. *Nature, 497*(7451), 585–590.

Roweis, S. T., & Saul, L. K. (2000). Nonlinear dimensionality reduction by locally linear embedding. *Science, 290*(5500), 2323–2326.

Rubin, A., Sheintuch, L., Brande-Eilat, N., et al. (2019). Revealing neural correlates of behavior without behavioral measurements. *Nature Communications, 10*(1), 1–14.

Russo, A. A., Bittner, S. R., Perkins, S. M., et al. (2018). Motor cortex embeds muscle-like commands in an untangled population response. *Neuron, 97*(4), 953–966.

Russo, A. A., Khajeh, R., Bittner, S. R., et al. (2020). Neural trajectories in the supplementary motor area and motor cortex exhibit distinct geometries, compatible with different classes of computation. *Neuron, 107*(4), 745–758.

Rust, N. C. (2014). Population-based representations. In: Gazzaniga MS, Mangun GR (eds) The Cognitive Neurosciences. MIT Press, chap 19, p 337.

Sanger, T. D., & Kalaska, J. F. (2014). Crouching tiger, hidden dimensions. *Nature Neuroscience, 17*(3), 338–340.

Santhanam, G., Yu, B., Gilja, V., et al. (2009). Factor-analysis methods for higher-performance neural prostheses. *Journal of Neurophysiology, 102*(2), 1315–1330.

Schneider, S., Lee, J. H., & Mathis, M. W. (2022). Learnable latent embeddings for joint behavioral and neural analysis. arXiv:2204.00673

Scoville, W. B., & Milner, B. (1957). Loss of recent memory after bilateral hippocampal lesions. *Journal of Neurology, Neurosurgery, and Psychiatry, 20*(1), 11.

Shadlen, M. N., & Newsome, W. T. (1998). The variable discharge of cortical neurons: implications for connectivity, computation, and information coding. *Journal of Neuroscience, 18*(10), 3870–3896.

Stokes, M. G., Kusunoki, M., Sigala, N., et al. (2013). Dynamic coding for cognitive control in prefrontal cortex. *Neuron, 78*(2), 364–375.

Stopfer, M., Jayaraman, V., & Laurent, G. (2003). Intensity versus identity coding in an olfactory system. *Neuron, 39*(6), 991–1004.

Stringer, C., Pachitariu, M., Steinmetz, N., et al. (2019). High-dimensional geometry of population responses in visual cortex. *Nature, 571*(7765), 361–365.

Stringer, C., Michaelos, M., Tsyboulski, D., et al. (2021). High-precision coding in visual cortex. *Cell, 184*(10), 2767–2778.

Sun, G., Zhang, S., Zhang, Y., et al. (2019). Effective dimensionality reduction for visualizing neural dynamics by laplacian eigenmaps. *Neural Computation, 31*(7), 1356–1379.

Sussillo, D., Churchland, M. M., Kaufman, M. T., et al. (2015). A neural network that finds a naturalistic solution for the production of muscle activity. *Nature Neuroscience, 18*(7), 1025–1033.

Tenenbaum, J. B., De Silva, V., & Langford, J. C. (2000). A global geometric framework for nonlinear dimensionality reduction. *Science, 290*(5500), 2319–2323.

Tolhurst, D. J., Movshon, J. A., & Dean, A. F. (1983). The statistical reliability of signals in single neurons in cat and monkey visual cortex. *Vision Research, 23*(8), 775–785.

Tombaz, T., Dunn, B. A., Hovde, K., et al. (2020). Action representation in the mouse parieto-frontal network. *Scientific reports, 10*(1), 1–14.

Toohey, K. (2015). Similaritymeasures: trajectory similarity measures. R package version 1.

Tzagarakis, C., Jerde, T. A., Lewis, S. M., et al. (2009). Cerebral cortical mechanisms of copying geometrical shapes: a multidimensional scaling analysis of fmri patterns of activation. *Experimental brain research, 194*(3), 369–380.

Van der Maaten, L., & Hinton. G. (2008). Visualizing data using t-sne. *Journal of Machine Learning Research, 9*(11).

Van Der Maaten, L. (2014). Accelerating t-sne using tree-based algorithms. *The Journal of Machine Learning Research, 15*, 3221–3245.

Venna, J., & Kaski, S. (2006). Local multidimensional scaling. *Neural Networks, 19*(6–7), 889–899.

Vlachos, M., Kollios, G., & Gunopulos, D. (2002). Discovering similar multidimensional trajectories. In: Proceedings 18th International Conference on Data Engineering, IEEE, pp 673–684.

Vyas, S., Golub, M. D., Sussillo, D., et al. (2020). Computation through neural population dynamics. *Annual Review of Neuroscience, 43*, 249–275.

Wallot, S. (2019). Multidimensional cross-recurrence quantification analysis (mdcrqa)-a method for quantifying correlation between multivariate time-series. *Multivariate Behavioral Research, 54*(2), 173–191.

Warland, D. K., Reinagel, P., & Meister, M. (1997). Decoding visual information from a population of retinal ganglion cells. *Journal of Neurophysiology, 78*(5), 2336–2350.

Webber, C., & Marwan, N. (2015). Recurrence quantification analysis. Theory and Best Practices.

Wu, A., Roy, N. A., Keeley, S., et al. (2017). Gaussian process based nonlinear latent structure discovery in multivariate spike train data. *Advances in Neural Information Processing Systems, 30*, 3496.

Yin, H. (2008). On multidimensional scaling and the embedding of self-organising maps. *Neural Networks, 21*(2–3), 160–169.

Youngentob, S. L., Johnson, B. A., Leon, M., et al. (2006). Predicting odorant quality perceptions from multidimensional scaling of olfactory bulb glomerular activity patterns. *Behavioral neuroscience, 120*(6), 1337.

Yu, B. M., Kemere, C., Santhanam, G., et al. (2007). Mixture of trajectory models for neural decoding of goal-directed movements. *Journal of Neurophysiology, 97*(5), 3763–3780.

Yu, B. M., Cunningham, J. P., Santhanam, G., et al. (2009). Gaussian-process factor analysis for low-dimensional single-trial analysis of neural population activity. *Journal of Neurophysiology, 102*(1), 614–635.

Zhang, Z., & Wang, J. (2007). MLLE: Modified locally linear embedding using multiple weights. *Advances in Neural Information Processing Systems, 19*, 1593–1600.

Zhou, D., & Wei, X. X. (2020). Learning identifiable and interpretable latent models of high-dimensional neural activity using pi-vae. *Advances in Neural Information Processing Systems, 33*, 7234–7247.

4.5 Ca2+ imaging of self and other in medial prefrontal cortex during social dominance interactions in a tube test

PNAS RESEARCH ARTICLE | NEUROSCIENCE OPEN ACCESS

Ca2+ imaging of self and other in medial prefrontal cortex during social dominance interactions in a tube test

Nuria Garcia-Font[a,1], Rufus Mitchell-Heggs[a,1], Kapil Saxena[a,b,1], Carolin Gabbert[c], Georgina Taylor[a], Giulia Mastroberardino[a], Patrick A. Spooner[a], Francesco Gobbo[a], Julia K. Dabrowska[d], Sumantra Chattarji[b,e], Peter C. Kind[b,e], Simon R. Schultz[d], and Richard G. M. Morris[a,b,e,2]

Contributed by Richard Morris; received April 30, 2021; accepted May 2, 2022; reviewed by Hailan Hu and Mark Schnitzer

The study of social dominance interactions between animals offers a window onto the decision-making involved in establishing dominance hierarchies and an opportunity to examine changes in social behavior observed in certain neurogenetic disorders. Competitive social interactions, such as in the widely used tube test, reflect this decision-making. Previous studies have focused on the different patterns of behavior seen in the dominant and submissive animal, neural correlates of effortful behavior believed to mediate the outcome of such encounters, and interbrain correlations of neural activity. Using a rigorous mutual information criterion, we now report that neural responses recorded with endoscopic calcium imaging in the prelimbic zone of the medial prefrontal cortex show unique correlations to specific dominance-related behaviors. Interanimal analyses revealed cell/behavior correlations that are primarily with an animal's own behavior or with the other animal's behavior, or the coincident behavior of both animals (such as pushing by one and resisting by the other). The comparison of unique and coincident cells helps to disentangle cell firing that reflects an animal's own or the other's specific behavior from situations reflecting conjoint action. These correlates point to a more cognitive rather than a solely behavioral dimension of social interactions that needs to be considered in the design of neurobiological studies of social behavior. These could prove useful in studies of disorders affecting social recognition and social engagement, and the treatment of disorders of social interaction.

social dominance | tube test | endoscopic imaging | prefrontal cortex | rodents

Significance

Growing interest in social neuroscience requires the development and refinement of social behavior paradigms and novel analyses of the manner in which the neural activity in one brain may reflect the behavioral activity of self or of other, or the activity of each of two interacting individuals. This study documents an approach to analyze such interactions in a social dominance encounter between rodents.

The overarching aim of this work is to develop a better understanding of the neural activity associated with social dominance interactions, including those that may be altered in autism spectrum disorders (ASDs). Social interactions occur between pairs of rodents taking part in a variety of social tests used in laboratory settings (1, 2), including tests of relative access to food, resident–intruder tests, and the widely used "tube test" of social dominance (3, 4). The latter takes the form of two animals being placed into a Plexiglas tube, confronting each other during an interanimal encounter that is resolved by one animal becoming the "winner" and the other animal the "loser." Sometimes, this involves the behavioral conjunction of "pushing" by one and "resisting" by the other, but diverse other behaviors are observed that reflect a more cognitive element of decision-making, such as "withdrawal." Extensive use of the tube test in group-living male mice has revealed it to be a stable and reliable indicator of social dominance, correlating well with other measures of dominance (2, 5). The present study is part of a larger project to use this and other tests of phenotype in animal models of ASDs because a prominent characteristic of this syndrome is social withdrawal. For example, Saxena et al. (6) showed, using wild-type (WT) and Fragile-X mutant (*Fmr1*$^{-/y}$) rats, that repeated testing over several sessions revealed a relative but not absolute social dominance of WT animals over the mutants, with gene-related differences in intersession stability. We also witnessed the development of inflexible behavioral habits that enabled overcoming failures of social awareness in some encounters. These findings are consistent with the socially withdrawn or otherwise aberrant behavior seen in humans with ASD and in animal models of Fragile-X (7) and Rett syndrome (8, 9).

In this study, we examined neural correlates of social dominance interactions from a cognitive perspective. It was guided by anatomical and physiological data revealing that the frequency of excitatory postsynaptic currents, single-unit activity, or Ca^{2+} transients in the prefrontal cortex or anterior cingulate gyrus are likely very important mediators of dominance and known to be on the causal chain of brain network activity mediating dominance and submissiveness (10). Behavior by both animals, such as pushing or resisting, has been reported that is well correlated with changes in neural activity in the prelimbic zone of the medial prefrontal cortex (PrL, mPFC) of mice (5, 11). We have successfully identified behaviors such as moving forward, pushing, resisting, retreat,

Author affiliations: [a]Laboratory for Cognitive Neuroscience, Edinburgh Neuroscience, The University of Edinburgh, Edinburgh EH8 9JZ, United Kingdom; [b]Simons Initiative for the Developing Brain and Patrick Wild Centre, The University of Edinburgh, Edinburgh EH8 9JZ, United Kingdom; [c]Institute of Neurogenetics, University of Lübeck, 23562 Lübeck, Germany; [d]Department of Bioengineering and Centre for Neurotechnology, Imperial College London, London SW7 2AZ, United Kingdom; and [e]National Centre for Biological Sciences, Tata Institute of Fundamental Research, 400005 Bangalore, India

Author contributions: P.A.S., S.C., P.C.K., and R.G.M.M. designed research; N.G.-F., K.S., C.G., G.T., and F.G. performed research; N.G.-F., R.M.-H., K.S., C.G., G.T., G.M., J.K.D., S.R.S., and R.G.M.M. analyzed data; N.G.-F., R.M.-H., and R.G.M.M. wrote the paper; P.A.S. built the apparatus; S.C. supervised K.S. and contributed ideas for experiments; P.C.K. raised the grant funds; and R.G.M.M. directed the project.

Reviewers: H.H., Zhejiang University; and M.S., Stanford University.

The authors declare no competing interest.

[1]N.G.-F., R.M.-H., and K.S. contributed equally to this work.

[2]To whom correspondence may be addressed. Email:

This article contains supporting information online at http://www.pnas.org/lookup/suppl/doi:10.1073/pnas.2107942119/-/DCSupplemental.

Published July 26, 2022.

stillness, and withdrawal. Pushing and resisting may seem similar (and are sometimes conflated) but can be readily distinguished from the video record monitored on a frame-by-frame basis at 1/20 s by a skilled observer successfully identifying the initiating animal. In rats, the typical duration of tube test interactions varies from 5 s to 60 s. Encounters can be characterized as a cycle of specific acts, followed by perception of the immediate outcome of these actions by both animals. A dominant animal cannot just unilaterally "decide" to be dominant—it may need to push to find out how the other animal will react. Such interactions fuel the interbrain correlations between two animals outlined by ref. 12. Accordingly, while a focus on overt behaviors that can be scored from a video record is clearly objective, a strictly "behaviorist" approach risks failing to provide unambiguous insight into the underlying decision-making process(es) involved in ascertaining social dominance. Studies of sociability and social recognition memory also point to cognitive aspects of social interaction (13).

A separate issue is that the standard single-animal approach to examining the neural correlates of sensation, perception, and action is to look only at the animal from which physiological recordings are being taken (14–17). A social situation, however, opens up the intriguing possibility that the activity in the brain of one animal reflects a representation of the actions or intentions of the other animal. It rapidly became apparent to us that, while differences in single-cell or multiunit activity associated with such dominance or submissive behaviors were observed, as reported previously by Hu's group (10), a neural correlate of pushing behavior by one animal could sometimes be described as the neural correlate of resistance by the other animal. Our study was conducted in the spirit of the interbrain approach, but our findings open up a separate logical issue from the concept of interbrain dynamics (12). Specifically, they include the possibility of identifying whether cell firing in animal A during encounters with animal B is specifically responsive to the actions of animal A, or of animal B, or of them both.

Results

The data take the form of Ca^{2+} imaging data, behavioral data, and the analysis of mutual information between these. We report here data from three pairs of group-living WT rats, and three pairs of group-living FXS (Fmr1-/y) rats ($n = 12$). These are part of an ongoing study that will grow to much larger groups of animals over several years, sufficient to make detailed WT vs. FXS comparisons (not yet feasible). A total of 913 cells were identified from 11 of these animals, of which five pairs were analyzed in detail. We outline the protocol and histochemical analyses, then turn to quantification of the behavior, to the global ΔF/F measure, and, finally, using event processing software, to the patterns of events across multiple individual cells.

Fig. 1 *A*–*C* shows a cartoon of the placement of a microendoscope on the head of a hooded rat, representative viral expression of GCamp6f in the prelimbic area of the prefrontal cortex, and the approximate position of the gradient refractive-index (GRIN) lens in one of the rats, and a typical camera image during recording. Fig. 1*D* shows successful expression of GCamp6f in the PrL at cellular magnification (Fig. 1 *D*, *Left*; 20×). NeuN and GAD67 expression (Fig. 1 *D*, *Left Middle*), DAPI (Fig. 1 *D*, *Right Middle*), and exemplars of superposition (Fig. 1 *D*, *Right*) show that virus expression was in excitatory neurons (identified with NeuN and GAD67) without affecting nuclear integrity (observed with DAPI). Fig. 1*E* shows the protocols consisting of 50 encounters between the six pairs of animals over 10 d of tube tests, each having five trials per day (blue shading), of which alternate days (green, red) were subject to Ca^{2+} imaging between the animals of a pair. Fig. 1*F* shows two animals in the Plexiglas tube (1 m), one animal (green) having the real camera and the other (red) having a dummy camera, both protected within iHELMETs (18).

Behavioral Findings. Fig. 2*A* shows the timelines of all pairs of animals in the tube test. In the cages of WT rats (Fig. 2 *A*, *Top*), one pair of animals displayed consistently strong dominance (H4093/H4094, dark and light green) while the other two pairs showed a more varied pattern of moderate dominance (dark and light orange); in the KO cages (Fig. 2 *A*, *Bottom*), two pairs of animals showed strong dominance, and only one pair showed a more moderate pattern (H4090/H4089). Different genotypes were hereafter pooled, but distinct dominance status retained.

Detailed frame-by-frame video analysis of the behaviors (Fig. 2*B*) revealed the behavioral profiles of the animals in each trial, plotted in terms of numbers of specific behaviors per session (averaged across 10 sessions), the relative duration of each type of behavior, and the interanimal behavior correlations (Fig. 2 *B* and *C*). The value of analysis at such fine temporal grain is that it is possible for a skilled observer to see clearly which of two animals initiates an encounter, that is, which animal first engages in PUSH behavior and which responds by RESIST or RETREAT behavior. Two of us (C.G. and G.M.) gained experience over 1,000 recorded trials of identifying these different behaviors. Fig. 2*B* considers pooled pairs of strong or moderate dominance pairs, with respect to both behavior frequency per session and normalized duration. We hypothesized that the "decision-making" in strong vs. moderate dominance pairs might be different. Excluding STILLNESS, an ANOVA of the frequency of occurrences in both strong and moderate pairs of animals showed a significant effect (Huyinh Feldt; $F = 5.05$, degree of freedom (df) 4/32, $P = 0.003$) but no significant difference between strong vs. moderate. For normalized duration, nonparametric Kruskal–Wallis tests comparing winners and losers showed that winners spent significantly longer time in MOVE FORWARD but shorter in RETREAT and WITHDRAWAL in the strongly dominant/submissive pairs (ps < 0.05, 0.037, and 0.05, respectively). In the more moderate dominance animals, only MOVE FORWARD showed a longer duration for the winners ($P < 0.05$).

In Fig. 2*C*, the correlation matrix shows the positive or negative correlations between specific behaviors of the winning animal in the series of paired encounters (rows) and those of the losing animal (columns). The color white implies that this combination of behaviors did not occur (generally, because one of the behaviors, such as RETREAT, did not occur in strong winners). RESIST behavior by a winning rat was strongly correlated with PUSH behavior by the losing animal, but, conversely, PUSH behavior by the winner correlated with both RESIST and RETREAT by the loser. This asymmetry reflects dominance. With respect to STILLNESS, there was a good but not unique correlation between the two animals. When one animal was STILL, it was likely that the other was also, but there were occasions when the winner was still and the losing animal showed WITHDRAWAL. WITHDRAWAL by the loser was also more strongly correlated with both MOVE FORWARD by the winner and, paradoxically, WITHDRAWAL by the winner. These behavioral correlations guided facets of the Ca^{2+} imaging analysis that follows.

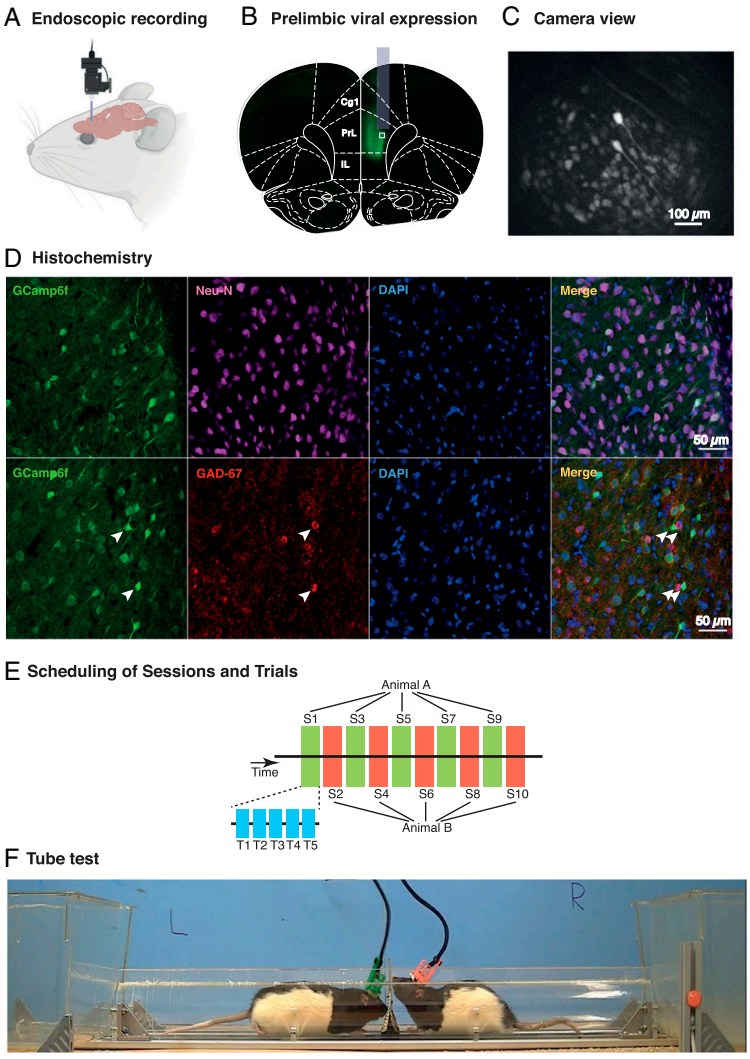

Fig. 1. Calcium imaging in rats during social dominance interactions in the tube test. (A) Cartoon depicting detachable miniature endoscope (Inscopix) that is placed daily into a head-mounted baseplate cemented to the skull. (*B*) Photomicrograph of viral expression of GCamp6f colocalized on a coronal section from Paxinos and Watson brain atlas at the AP location of the prelimbic zone (PrL) of mPFC, together with superimposed image of typical location of a GRIN lens. (*C*) Representative camera view of PrL neurons during a behavioral session (Scale bar, 100 μm. based on the size of the sensor provided by Inscopix (1050x650μm equivalent to 1280x800pixels). (*D*) Higher-power images of GCamp6f expression in single cells (*Left*), Neu-N staining (*Left Middle Top*) and GAD-67 (*Left Middle Bottom*), DAPI (*Right Middle*), and exemplar superpositions (*Right*). (Scale bar, 50 μm.) (*E*) Recordings were taken from the two animals on alternate sessions in the tube test experiments consisting of five trials per session. With only one camera, recordings were taken from odd-numbered sessions for one animal and even-numbered sessions for the other. (*F*) Two Lister-hooded male rats in the tube test, each wearing the iHELMET that serves to protect the endoscopic from physical interaction with the other animal (18).

Mean Calcium Imaging Activity (ΔF/F) across All ROIs. Successful stable recordings of Ca^{2+} transients from individual cells were secured (i.e., regions of interest [ROIs] showing multiple rapid increases in signal intensity of ΔF/F followed by slow decreases of fluorescence to baseline), with successful longitudinal registration gradually declining across successive sessions from >90% on successive session to >60% comparing session 1 (S1) and S5 (Fig. 3*A*). As we have only one endoscope in the laboratory, recordings were taken from one animal on even-numbered sessions but from the other on odd-numbered sessions. Using the CaImAn constrained nonnegative matrix factorization–extended (CNMF-e) (see *Materials and Methods* and Table 1 the total number of longitudinally registered cells identified from the 11 animals was 913 (WT = 375; KO = 538).

The first step was to examine the neural activity of individual cells using the ΔF/F measure (Fig. 3*B*) and the summated mean across all cells in each animal, as in Kingsbury et al. (11), for each 1/20-s time period of the recorded tube test sessions (25 trials per rat; exemplar for one session of five trials in Fig. 3*C*). These sessions typically lasted 100 s to 350 s of which a

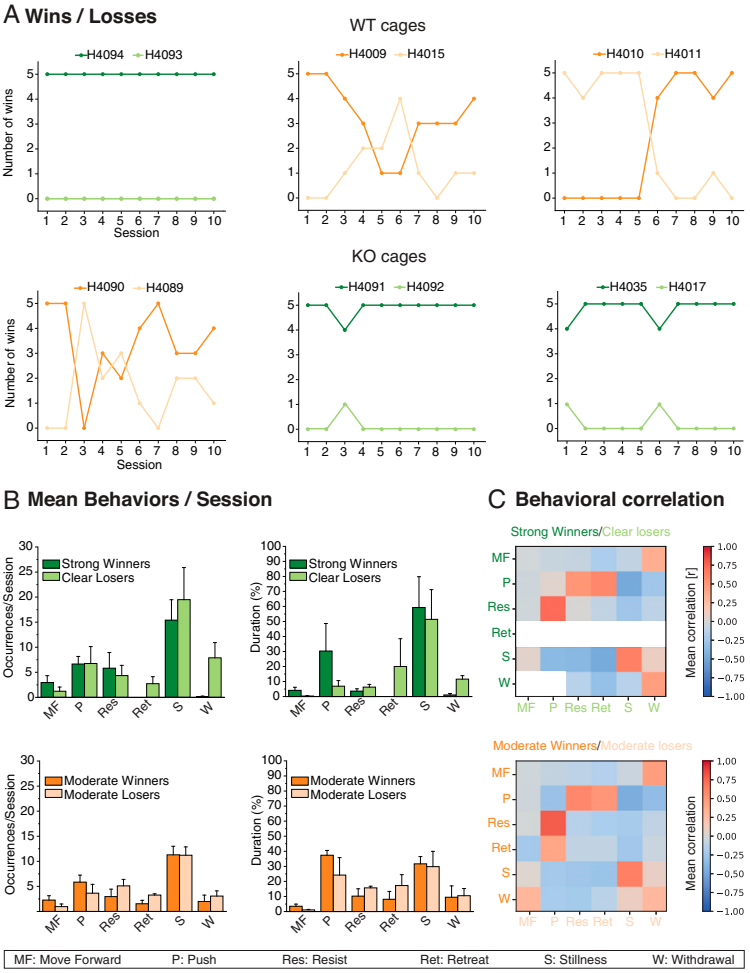

Fig. 2. Behavioral analysis. (*A*) Timeline across 10 sessions of the six pairs of animals—three WT and three FXS. Note the strong dominance in three pairs of animals but a more varied and moderate pattern of dominance in the other three pairs. (*B*) Number of occurrences of behaviors per five trial sessions over 10 sessions averaged for the three strongly dominant cages (*Top*, green) and the three more moderate dominance cages (*Bottom*, orange). Note predominance of periods of STILLNESS, that RETREAT and WITHDRAWAL were not seen in the strongly dominant animals, and that there was a more uniform pattern across winners and losers in the case of moderate dominance. (*C*) Correlation matrix showing probability of behavior of animal A as a function of the cooccurrence of different behaviors in animal B (and vice versa). Note high PUSH/RESIST correlations, and absence of RETREAT and WITHDRAWAL in strongly dominant animals. Means ±1 SEM.

large proportion was the intertrial interval when the animals were outside the Plexiglas tube (white; data from these periods was not analyzed). Time series plots of the within-tube normalized cell activity (black line, normalized scale on the *y* axis) reveal diverse patterns, including periods of quiescence, activity, and activity bursts (Fig. 3*C*). The different behaviors observed are color coded. The exemplar is a pair of rats (H4093 and H4094) in which the imaged animal was the loser of this series of contests. Trial 1 (T1) shows relative high activity and bouts of RESIST/PUSH/RESIST by the eventual loser (Fig. 3 *C*, *Top*), notably during two long PUSH periods by the winning competitor (Fig. 3 *C*, *Bottom*). Later in the same trial, PUSH by the winner is associated with RESIST/RETREAT and eventually WITHDRAWAL by the loser, with clearly detectable changes in the pattern of mean activity at any one time point. However, from T2 onward, it is quite striking how much time is spent by the winning animal (Fig. 3 *C*, *Bottom*) in STILLNESS (blue). Two examples of the complexity of the pattern are as follows: 1) In T4, the second period of PUSH by the imaged animal is accompanied by a stable low value of ΔF/F until the competitor starts to RESIST, whereupon the mean activity rises dramatically; 2) in T5, the winning animal is in STILLNESS, whereupon, at 320 s, it shows a dramatic rise in mean activity which coincides with RESIST by the other animal and then subsides, with the trial ending through WITHDRAWAL of the loser. Thus, careful inspection reveals that perception of the social dimension was apparent even in this normalized multicell activity.

Fig. 3*D* shows the normalized mean overall neural activity (ΔF/F) for all successfully recorded animals. As in Fig. 2, the strong winners/losers (green) are considered separately from the

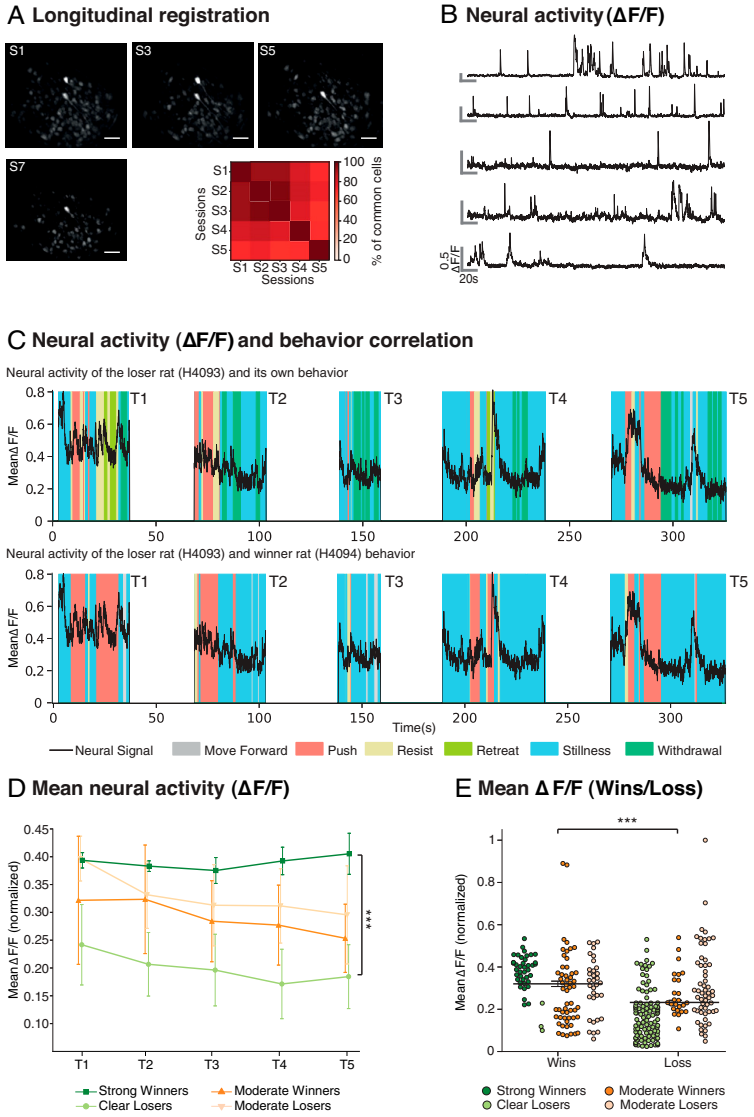

Fig. 3. Neural activity in identified regions of interest. (*A*) Mean Longitudinal registration of the animals across five sessions (S1 to S5, $n = 11$) and exemplar of longitudinal registration of ROIs with respect to maximal fluorescence in individual animals within each session (Inscopix) across four sessions. ROIs are hereafter referred to as "cells." Note the decline of likelihood of longitudinal registration across multiple sessions (Scale bar, 100 μm.). (*B*) Neural activity (ΔF/F) of an exemplar series of five individual cells showing the typical sharp rise time of luminance and slower decay time. These two parameters are conflated in any computation of mean neural activity. (*C*) Mean neural activity on each of five trials of a daily session aligned to an animal's own behavior (H4093, *Top*) or to the observed behavior of the other animal (H4094, *Bottom*). Note the striking peak during PUSH and RESIST" (respectively), and sometimes during STILLNESS, as outlined in the text. Respective behaviors are color coded beneath the two images. (*D*) Normalized mean neural activity (ΔF/F) averaged across all cells and each of the five daily trials, categorized with respect to whether the animals were strongly dominant/clearly submissive or were displaying more moderate dominance ($n = 11$, ns = 2, 3, 3, and 3, respectively). A difference in mean neural activity is shown as a function of the strength of dominance. (*E*) Normalized mean neural activity (ΔF/F) averaged across all winning and losing trials. Note that it confirms that the mean ΔF/F is related to the strength of the dominance status ($n = 11$). (***$P < 0.0001$). Means ±1 SEM.

moderate winners/losers. Mean activity is high in strong winners (a stable normalized score of circa 0.4 through the session) but much lower in the clear losers. Conversely, the mean activity patterns of the moderate subgroup ($n = 6$) are more equivalent with, if anything, the trend paradoxically showing losing animals to have slightly higher mean activity. Inhomogeneity of variance precluded the use of an ANOVAR, so we used a nonparametric test with the strong subgroup. These revealed that the difference in mean activity between winners and losers was highly significant in the case of strong dominance pairs (W = 0.39; L = 0.20; Mann–Whitney $U = 1$, df 23, $P < 0.0001$). The comparison of winners and losers in the

moderate subgroup was not significant (W = 0.29; L = 0.33; Mann–Whitney $U = 85$, df 28, $P > 0.3$). Fig. 3*E* plots the normalized mean ΔF/F of individual animals considering winning trials and losing trials separately. The mean ΔF/F on winning trials was higher than on losing trials (paired samples t test $t = 6.69$, df = 130, $P < 0.0001$). The difference appears strongest in the contrast between strong winners and losers.

Relationship of Cell Firing to Behavior. Using Online Active Set method to Infer Spikes (OASIS) of ΔF/F signals, we inferred time-stamped activity corresponding to the sharp rise in amplitude that we hereafter consider as cell firing "events" (Fig. 4*A*; see *Materials and Methods*). Sessions were characterized by multiple time-stamped events across trials from which we computed a mutual information score (MIS) to identify individual cell activity that was uniquely associated with each of the six observed behaviors. A key finding was that unique cells were identified. Fig. 4*B* shows the event train for an exemplar unique PUSH cell (overlaid with corresponding behaviors during their time periods in distinct colors), with T1 time-expanded (below) to illustrate the

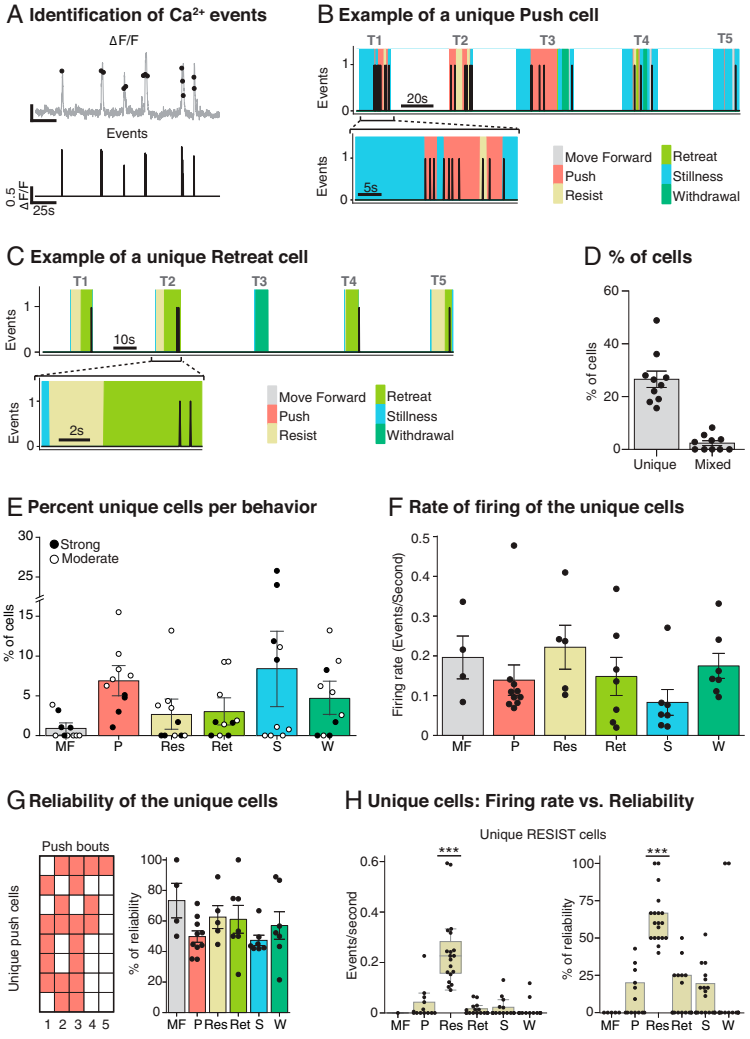

Fig. 4. Identification of Ca^{2+} events and their correlation with behavior. (*A*) Event identification software takes the smoothed ΔF/F time signal (*Top*, gray); it identifies discrete events that cross a predefined threshold (*Top*, black dots) and time stamps these events (*Bottom*). (*B*) Exemplar of a unique PUSH cell activity during one session (*Top*) and in one expanded trial (*Bottom*). All the behaviors are represented with different colors. Note that the activity of the cell clearly overlaps with the PUSH behavior. (*C*) Exemplar of the distinct category of a unique RETREAT cell activity during one session (*Top*) and in one expanded trial (*Bottom*). (*D*) Percentage of recorded cells classified as unique (26.6% ± 3.1, $n = 10$) and mixed (2.4 % ±0.9, $n = 10$). (*E*) Percentages of cells classified as unique for one behavior. Note that the moderate animals (white dots) have more cells per behavior, except for STILLNESS ($n = 10$). (*F*) Rate of firing of the unique cells. Note that, despite STILLNESS being the most frequent behavior and having the highest number of specific cells, its mean firing rate is low. (*G*) Reliability of the unique cells inside a session. (*H*) Firing rate vs. reliability plots of the unique-RESIST cells across all the behaviors. Each session was treated independently with cells pooled across sessions. Note that the values are clearly higher for the behavior that they are encoding, which illustrates a complementary way of establishing the correct behavior classification of these cells (***$P < 0.0001$, $n = 19$). Means ±1 SEM.

close correlation between the activity of this cell and the act of pushing. Similarly, Fig. 4*C* shows the event train for an exemplar unique RETREAT cell throughout an exemplar five-trial session with, again, a clear correlation between the cell activity and the retreating behavior. Unique cells were observed in all six behavior categories, although those for STILLNESS cannot be interpreted. For each session, the MIS (bits) was computed between each cell event train and the six behaviors—a cell was classified as a unique behavior-specific cell if it superseded the 95th percentile of a randomly generated MIS distribution of shuffled activity with original behavior (*SI Appendix*, Fig. S1). This was computed independently for all six behaviors, with cells classified as unique for two behaviors in a single animal and categorized as "mixed cells" (Fig. 4*D*). The total number of unique behavior-specific cells was 262 at the 95% MIS criterion (26.6%) with 26 mixed cells (2.4%). There were a further 571 nonspecific cells (57.2%), the remainder being 13.9% coincident activity cells (Fig. 5; see *Materials and Methods*). There was no relationship to the dominance status of the animals (ANOVA F = 1.13, df 2/4, P = 0.41), or to the strength of this status (ANOVA F < 1). Fig. 4*E* reveals the proportion of unique cells across the six behavior categories with a relationship to the strength of the dominant status (ANOVA F = 9.27, df 5/10, P = 0.002). Fig. 4*F* shows the mean rate of firing (circa 0.15 events per second; computed as the number of events divided by the total time that unique behaviors were occurring; not significantly different across behaviors, F < 1). Reliability was measured by examining whether the activity of a unique cell occurred on all or subset of the behavioral bouts of a single session (Fig. 4*F*). Across all unique cells, reliability was relatively high (mean = 56.5%). With the identification

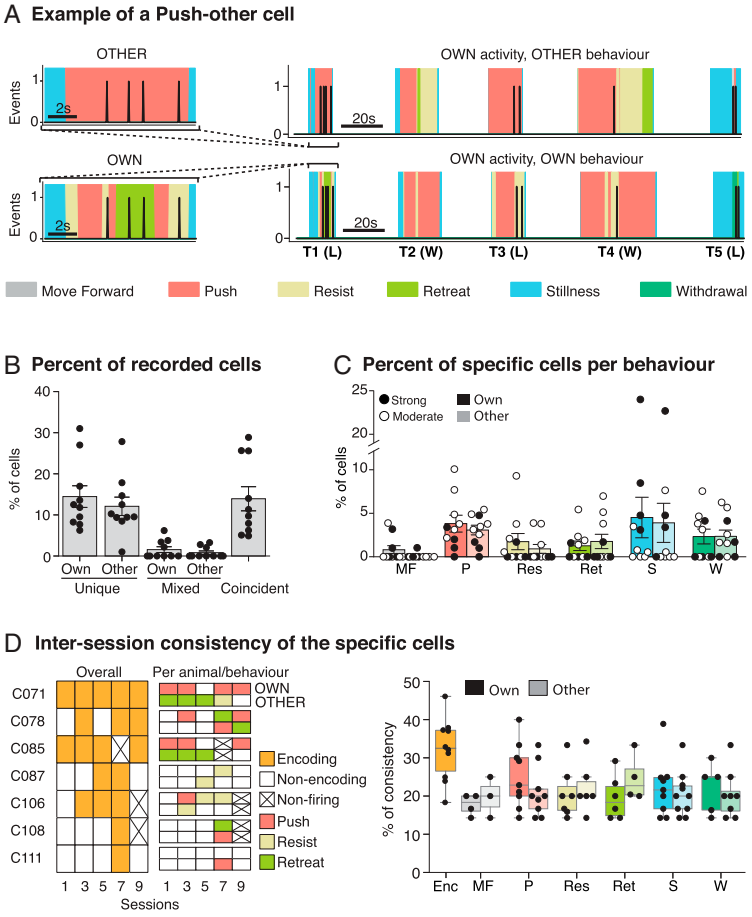

Fig. 5. Identification of Ca^{2+} events and their correlation with the behavior of the other animal. (*A*) Exemplar of a PUSH-other cell activity across one session compared to the other animal behavior (*Top Right*) and the own animal behavior (*Bottom Right*) and expanded trials (*Left*) that show that the cell is active only when the other animal pushes (*Top*). Note that the imaged animal (H4089) is the winner (W) in T2 and T4 and is the loser (L) in T1, T3, and T5, since this rat is a moderate loser. (*B*) Percentages of recorded cells classified as specific for own, other, and coincident behaviors (n = 10). (*C*) Percentages of cells per behavior distinguishing between own and other behavior. Note that the percentages are quite similar between own and other and that the moderate dominance animals have more specific cells per behavior, except for STILLNESS (n = 10). (*D*) Consistency of the specific cells across sessions. (*Left, 'Per session. Example of a single rat'*) The overall consistency of seven exemplar cells from a single animal across five sessions (S1, S3, S5, S7 and S9) and the specific encoding per animal (OWN and OTHER) and behavior. (*Right, 'Per behavior'*) The overall consistency and the consistency per behavior. Note that the consistency of the encoding cells (30%, orange) and the consistency per behavior (20%, various colors) are much lower than the reliability values in Fig. 4 (n = 10). Means ±1 SEM.

Table 1. Key resources

Reagent or Resource	Source	Identifier
Bacterial and virus strains		
AAV1.CamKII.GCaMP6f.WPRE.SV40	Addgene https://www.addgene.org/100834/#100834-AAV1	Cat#100834-AAV1
Deposited data		
Excel files of data	Laboratory	Attached
Experimental models: organisms/strains		
Rats (Male Long Evans-Fmr1$^{em1/PWC}$) referred in text as Fmr1 KO	Breeders from SAGE Labs, now https://horizondiscovery.com/	In-house breading (The University of Edinburgh) Identifier: FMR1-HRB
Software and algorithms		
IDPS	https://www.inscopix.com/software-analyzis#software_idps	Version 1.5
CNMF-e	https://github.com/zhoupc/CNMF_E	Zhou et al. (28)
OASIS	https://github.com/j-friedrich/OASIS	Friedrich et al. (29)
MATLAB	https://www.mathworks.com/products/matlab.html	Version 2019b
SPSS	https://www.ibm.com/uk-en/products/spss-statistics	Version 25
ImageJ	NIH https://imagej.nih.gov/ij/index.html	Version 53
Other		
Inscopix Miniature Microscope system (nVista)	https://www.inscopix.com/nvista	nVista v3.0
Microinjection syringe pump	https://www.wpiinc.com/var-8091-microinjection-syringe-pump-with-smartouch-controller	Order code # UMP3T-1
GRIN lens, baseplate	https://www.inscopix.com/lenses-viruses	Lens (1.0 mm x 9.0 mm) Baseplate standard
Superbond (dental cement)	https://www.prestige-dental.co.uk/product/super-bond-universal-kit/	superbond-universal-kit
iHELMET (3D printed parts)	https://www.sciencedirect.com/science/article/pii/S0165027021000443	Saxena et al. (18). .STL files are in the supplementary for this
3D printer	https://www.makerbot.com/3d-printers/	PLA printer
Normal donkey serum	Sigma Aldrich	D9663
Triton X-100	Sigma Aldrich	T8787
Mouse Anti-GAD67	Sigma Aldrich	MAB5406 clone 1G10.2
Guinea pig Anti-NeuN	SYnaptic SYstems	266 004
Donkey anti-mouse Alexa 647	Thermo Fisher	A-31571
Goat Anti-Guinea pig IgG Cy3-conjugated	Abcam	ab102370
Fluoroshield with DAPI	Sigma Aldrich	F6057

of unique cells being a key finding, we show the example of unique RESIST cells with respect to both rate of firing and reliability. Note that, even with an MIS score of >95%, there were occasional events in those same cells during other behaviors, but in all cases these were rare; the firing rate was significantly higher for RESIST cells during resistance bouts compared to during other behaviors (Kruskal–Wallis $P < 0.0001$). Moreover, the reliability of the unique RESIST cells was circa 60%, whereas the reliability of these same cells during other behaviors was low (ANOVA $F = 18.60$, $df = 5$, $P < 0.0001$). Both results together illustrate the accuracy of the cell classification based on MIS.

Up until now, we have referred to unique cells as being those whose activity has an MIS score above the 95th percentile for a specific behavior. Fig. 5 introduces a new distinction concerning whether cells show a unique relationship to the animal's own behavior or to that of the other animal. The tube test is, of course, a social situation; cell firing may be unique-own or unique-other. An exemplar of a unique-other cell is shown in Fig. 5*A*. This cell was recorded in one of the animals and fired only when the other animal pushed and went on to win in T1. A time expansion of T1 (Fig. 5 *A*, *Left*) shows this cell firing when the other animal pushed with the recorded loser sometimes resisting or retreating. This pair of animals was classified as showing only moderate dominance, with the recorded animal losing on T1, T3, and T5 but winning on T2 and T4 (Fig. 5*A*). We interpret the event train for this cell as one that uniquely encodes the other animal pushing. Fig. 5*B* shows the proportion of the different subsets of unique and mixed cells, but now including a further category called coincident cells, excluded from Fig. 4*D* for clarity. These were a further 124 cells (13.9%) that fired only when the behavior of animal A occurred simultaneously with a behavior of animal B. As shown in Fig. 5*C*, we did not observe any significant difference in the percentage of cells in each category related to the strength of the dominance status for either unique-own cells nor for unique-other cells (strength

of status x category x behavior: ANOVA F < 1). However, dominance status did interact significantly (status*category*behavior: ANOVA F = 8.35, $P = 0.002$, df 5/10). The final measure calculated was intersession consistency of the two types of unique cells. Whereas reliability refers to cell/behavior correlations within a session, consistency is a measure of engagement across sessions with respect to encoding of any behavior (orange) or of a specific behavior such as PUSH, RESIST, or RETREAT. Fig. 5 *D*, *Left* gives examples for seven cells from one animal (H4011). Cell 71 is an example of high consistency across sessions (5/5) but in which the specific behavior encoded changes from session to session. In contrast, C87 shows lower consistency with respect to encoding any behavior (2/5 sessions). Fig. 5 *D*, *Right* shows the intersession consistency which was circa 30% for the overall encoding (Enc, orange) and 20% for the specific cells per behavior, both measures being much lower than for reliability.

Discussion

There were two main findings. First, the mean cell activity (ΔF/F) across all cells in PrL of the mPFC of individual animals reflected relative dominance, being higher in strongly dominant and lower in highly submissive animals than in pairs of animals displaying more-moderate and interchanging patterns of dominance. Second, interanimal analyses revealed exacting MIS-computed correlations between Ca^{2+} activity in specific longitudinally registered regions of activity and specific behaviors. Unique cells were identified that correlated with an animal's own behavior (unique-own) or the other animal's behavior (unique-other). Coincident cells were also observed reflecting the joint behavior of the two animals competing in a tube test contest. We also made observations of within-session reliability and intersession consistency of the cell behavior correlations.

Detailed inspection of the data revealed that specific behaviors, such as pushing, resisting, and stillness, were frequent (Fig. 2). Retreat and withdrawal were more frequent in losing animals, but pushing was of a longer duration in very dominant winners. Stillness was also very frequent, but it is unclear what social engagement is happening during such periods. The focus of our analysis was on identifying whether there was cell activity in PrL that was uniquely correlated with these or other behavior categories, and the significance of the correlation assessed using a rigorous MIS (Figs. 4 and 5). Our findings of unique-own, unique-other, and coincident categories build on this concept, including that their relative frequency is reported and is surprisingly similar (Fig. 5*B*). That there are cells in PrL that are uniquely correlated to a dominant animal's own pushing behavior is unsurprising given earlier observations using tetrode recording (10). However, we also observed 3% push-other cells that fired when the other animal was pushing (exemplar cell in Fig. 5*A*), and a smaller but significant number of RETREAT-other and withdraw-other cells (Fig. 5*C*). WITHDRAW-other cells are a particularly interesting category, as they are seen in winning animals when they were not engaged in any other behavior than stillness. The stationary winning animal could have only observed the losing animal withdraw. Our use of MIS scores above the 95th percentile criterion for significance also enabled us to separately identify coincident cells, namely, cells that fired only when one animal executed behavior A while the other animal was doing behavior B. The existence of these distinct categories supports our perspective that the activity of cells in PrL during social dominance encounters reflects a cognitive rather than a purely behavioral dimension of the situation.

Whereas single-cell recording has classically been examined in relation to the perception, location, actions, or decisions of an animal from which recordings are being taken (14–17), a social situation introduces the intriguing possibility that neural activity in animal A is responding to some facet of the behavior of animal B. With growing interest in social neuroscience, a wider facet of our results is that they constitute data having theoretical and methodological implications. In studies in nonhuman primates, the discovery of "mirror neurons" introduced the concept that activity in a motor area of the brain may be responsive to a specific action of the agent from which the recordings are being taken and to the same action undertaken by a different agent (19). The representation of the actions by others has also been observed in a study of social agency between two monkeys (20). In certain game-playing situations in which two monkeys cooperate in playing a game, patterns of single-cell firing have been observed in STS that correlate with acts of cooperation (21). Related to this, the concept of "theory of mind," having to do with interpreting the intentions and actions of others, has also been intensively investigated in human neuropsychology and cognitive science, and in relation to ASDs (22).

Kingsbury et al. (11) were the first to report striking correlations of activity between the two animals in a social dominance situation, using the mean ΔF/F measure, leading to their statistical concept of interanimal "neural dynamics." Such correlations might arise, as Kingsbury et al. themselves point out, because both animals receive a common exogenous stimulus at the same time (e.g., an auditory stimulus), but they conducted relevant controls to rule out such a "common-cause" explanation. They might also arise because the two animals are effortfully pushing against each other. We recognize and accept the concept of "interbrain dynamics" (12), but their behavior analyses did not appear to distinguish between pushing by one animal during resist by the other, because they used a common behavioral category of push for both. As we did not have two endoscopic cameras, we were unable to explore or extend their central finding, but we did manage to disentangle some correlations. For example, unique-own cells for pushing in dominant animals from which imaging was being done could be distinguished from different cells that were active in one animal that were also active during, for example, resist by the other animal (our coincident cells). The mean ΔF/F activity of the two brains would likely correlate very highly during this latter condition. Kingsbury et al. did take the precaution (notably, in their figure 7) of restricting their consideration to cases in which one animal was motionless and the other animal did something. This is suitably cautious but may not be the only approach to disentangling cell firing related to self vs. other with, for example, our distinction between unique-other and coincident cells. An additional value of the behavior categorization of individual cells is that it enabled us to ask about the reliability of cell firing during an individual session, and the consistency from session to session. Our data suggest that PFC encoding is dynamic, with consistency low (circa 33% across multiple sessions) and lower for specific behaviors.

We began this program of research to investigate possible disorders in social dominance in rat models of ASDs, finding, as expected, that both Fragile-X and SynGap mutant rats are socially submissive but with dominance patterns influenced by experience (6, 23). In seeking to take this project to a neurophysiological level, we are now seeking to enlarge the cohort of animals to be able to compare Ca^{2+} signals in these different lines with those of WT normal rats. This analysis will be

complemented by studies in other social protocols such as sociability and social memory, both of which are relevant to a better understanding of the neurobiology of ASDs.

Materials and Methods

Contact for Reagents and Resources Sharing.

Further information and requests for resources and reagents should be directed to and will be fulfilled by the lead contact, R.G.M.M.).

Materials Availability. This study did not generate new unique reagents.

Data and Code Availability. The data are available at https://datashare.ed.ac.uk/handle/10283/4373, and consists of Excel files corresponding to each panel of each figure. The code to classify behaviorally tuned neurons is available at https://github.com/rufusmitchellheggs/Behavioral-Tuned-Cells.

Experimental Model and Subject Details.

Rats. Adult (n = 12) male Long-Evans Fmr1$^{em1/PWC}$ hooded rats, hereafter referred to as WT or Fmr1 KO, were used, aged 3 mo to 4 mo at the start of surgery, weighing circa 350 g. The rats were housed in groups of two per cage, with ad libitum food/water and a 12-h light/dark cycle. The Fmr1 KO rats were generated by mating female heterozygous rats with male WT Long-Evans hooded rats obtained from Sigma Advanced Genetic Engineering (SAGE) laboratories, now part of Horizon Discovery, and the offspring of the female Fmr1 heterozygotes crossed to WT Long-Evans hooded rats (Charles River Labs), thus FMRP$^{-/Y}$. The WT rats were littermate matched. There were three WT cages with $n = 2$ per cage, and three Fmr1 KO cages (ns = 2). All experiments were done blind to genotype, with animals being given a colored spot on their fur (using animal paint) and their cage number on their tail to identify them. The code was retained by someone independent of the study.

Ethical and legal issues. All procedures related to animals, including surgical procedures, involved a series of stages, each conducted under recovery anesthetic (isoflurane), according to the regulations of the Animals (Scientific Procedures) Act 1986 and under the supervision of the named veterinary surgeons of the University of Edinburgh.

Surgical Methods.

Virus injection. The animals were anesthetized using isoflurane (1 to 3%) and mounted in a stereotaxic apparatus (Kopf). A hole was drilled in the skull, targeting the prelimbic (PrL) region of the mPFC at stereotaxic coordinates AP −3.2 mm, ML 0.8 mm (unilateral infusion), and DV at both 3.7 and 4.2 mm. The virus, AAV1.CamKII.GCaMP6f.WPRE.SV40 (source: https://www.addgene.org) diluted with saline to a final dilution of 1:5 (titer: 5.77 × 10^{12} GC/mL), was infused using the 30G needle and a nanoinjector pump (previous virus dilution studies were conducted to establish an optimal dilution for this brain region). A volume of 250 nL per site was infused at the rate of 50 nL/min (5 mins). A further delay of 5 min to allow the virus to diffuse was allowed before the needle was retracted slowly. Beginning with an immediate postoperative injection of rimadyl, the animals were allowed to recover for 2 wk, with postoperative care undertaken to minimize the discomfort to the animal as per institutional guidelines.

GRIN lens implantation. Three to four weeks after virus injection, the GRIN lens was implanted at the same stereotaxic location. The animals were again anesthetized and fixed in the stereotaxic apparatus. Using a trephine bur to do a very small craniotomy above the virus injection site, followed by the creation of a small track cut into the brain tissue overlying PrL by lowering a sterile blunt needle (18G) through the hole in the brain at the target site (DV 3.25 mm from skull surface), we prepared for lowering the GRIN lens. When the needle reached its target site, we paused for 5 min, and then the needle was retracted slowly; this created a cavity which was almost the size of the lens (1-mm diameter). Using a holder assembly, the GRIN lens was lowered into the brain slowly until it reached a site 3.25 mm below the skull surface. Dental cement (Super Bond) was used to secure the lens to the skull and four skull screws that had previously been drilled into location as solid anchor points. The lens was then covered with silicon to protect it until the final step of baseplate implantation.

Baseplate implantation. A period of ∼3 wk after lens implantation is required for the lens to become clear (clearance of implantation-associated gliosis). Using anesthesia again, the baseplate containing a working endoscope was lowered so as to target the center of the GRIN lens. We followed Inscopix guidelines to lower the baseplate until the circular border of the lens is seen, and then moved up slightly until we saw cells and/or blood flow, whereupon, at this point, we used dental cement to fix the baseplate. When the cement had dried and hardened, the scope was removed gently by undoing the baseplate screw, leaving the baseplate with the GRIN lens. The baseplate was then covered with the baseplate cover.

Protecting the endoscope. Due to the social nature of our behavioral task, we find that the endoscope needs protection from the other animal to secure stable Ca^{2+} recordings. We used our three-dimensional (3D)-printed protector [called iHELMET; see Saxena et al. (18)]. Briefly, an additional plastic baseplate surround is secured permanently on the animal 1 d after the baseplate installation, care being taken to align it with the baseplate in such a way that, when the endoscope is mounted and the iHELMET is placed, it protects the endoscope without any direct contact with the endoscope. A cable clip on the helmet also prevents any sharp movements of the cable from causing force on the camera to which it is electrically connected.

Apparatus.

Behavior. The tube test assay was procedurally as in Saxena et al. (6). A 1-m transparent Plexiglas tube, 7-cm internal diameter, served to connect two holding boxes (42 × 26 × 18 cm; Fig. 1*D*). In each box, bedding was placed from the home cage of the animals to help reduce anxiety. The tube was large enough for the rats to move freely, but to neither cross each other nor turn around. The apparatus was modified from that of Saxena et al. (6) to include 1) a long slit cut into the upper central part of the Plexiglas to permit lateral movement of the head-mounted endoscope and attached cable along the axis of the tube; and 2) a moveable wire-grill separator that permitted visual, auditory, and olfactory interaction of the animals in the tube but limited somatosensory contact, running on a smoothly running trolley such that the slightest movement onto it from either animal would result in it moving effortlessly. A camera provided a direct view of the tube to record the trials using OBS recording software. The entire apparatus was connected to custom-made Arduino-based hardware, and we used its serial reader functionality for reading the button press (start/stop times of the trials) into the computer.

Calcium imaging. The Inscopix data acquisition software and Inscopix nVista imaging system (v3.0) associated with a GRIN lens are used to acquire calcium imaging videos at 20 Hz (24, 25). The procedure for implanting the virus and GRIN lens is described above. The endoscopic camera was mounted daily in exactly the same place on a head-fixed baseplate and connected, via a power/data cable, to a data receiver and then to relevant computers. Recordings were stabilized and the camera was protected using the "iHELMET" (18). During each trial, the experimenter was located in an antechamber separate from the animals to limit human–animal interference.

Procedure. The training protocol consisted of habituation followed by tube test contests between animals within each cage coupled to Ca^{2+} imaging (Figs. 1*E* and 2*A*).

Habituation. One week prior to the start of the contests, small sections of the Plexiglas tubing were placed inside each home cage, and the animals were handled daily. The two animals per cage then received their color marking, and were placed into the apparatus for 20 min. Both cage occupants were allowed to run freely through the tubes for 5 min before being returned to the home cage.

Tube test contests. A tube test contest consisted of two rats being placed in the holding boxes, one on each side. Both rats had an iHELMET (red or green) of which one contained a working camera and the other a dummy camera. Recordings were taken from both rats on alternate sessions (1, 3, 5, etc. and 2, 4, 6, etc.; we had only one endoscope). The rats then entered the tube and met in the middle at the metal grid which acted as a barrier. The trial started when the moveable barrier was unlocked. During the trial, the rats competed for dominance, during which a variety of behaviors were observed (identified blind with respect to genotype). Typically, the animals were together and relatively still for a few seconds. Thereafter, either one rat pushed the subordinate out of the tube (dominant) or the other rat withdrew of its own accord (subordinate), but various other behaviors occurred during such encounters. MOVE FORWARD occurred when either or both animals moved toward each other; PUSH occurred when animal A pushed against the metal grid and caused it to move, often stopped by animal B showing RESIST behavior. The roles of animals A and B in executing PUSH and RESIST generally alternated, but not exactly in time with each other. If animal A was showing PUSH behavior and animal B being pushed backward,

this was called RETREAT (i.e., an enforced action); however, if animal B withdrew of its own accord, this was classified as WITHDRAWAL (i.e., an unenforced action). There were sometimes periods when neither animal moved or did much else; these were classified as STILLNESS, but this could include sniffing, grooming, or other activities that do not involve forward or backward motion. A trial was defined as ending when the first rat retreated or withdrew into the holding box from which it started. This rat was recorded as the "loser," and the other was recorded as the "winner." Each pair of rats underwent five trials each session, alternating their starting positions from left or right, to obtain a secure measure of dominance (5:0 wins/losses, 4:1 or 3:2). One session of each of 10 sessions was completed each day. Randomization of the pair sequence and cage sequence was applied so that both changed every session. Trial latency was taken as the time (seconds) to complete one trial. All trials included both behavioral observation and Ca^{2+} imaging. Each animal had an iHELMET, but only one animal had a real nVista, the other wore a "dummy" camera (the camera is expensive). The animal from which recordings were being taken alternated across days. Video recordings were taken at the same time.

Data Analysis.

Behavioral labeling. The data analysis proceeded in stages. With respect to behavior, the videos of all four animals were analyzed using BORIS software (26), with the occurrence of six different categories of behavior examined on a frame-by-frame basis and time stamped to 1/20-s resolution (the same as the frame rate of the Inscopix camera). Thus, we knew when each behavior began and ended to that temporal resolution.

Single-photon calcium imaging. For Ca^{2+} recordings, the field of view was preprocessed by first applying a low and high spatial band-pass filter ($\sigma_{low} = 0.0005$ and $\sigma_{high} = 0.5$), then motion correcting by aligning each frame to a manually selected high-activity reference frame (both algorithms were used within the Inscopix data processing software [IDPS, Inscopix (27)]. The subsequent preprocessed recordings were then exported as a .tiff file, cell ROIs were extracted, and their respective $\Delta F/F$ were computed using the CNMF-e python API (28). Cells were longitudinally registered across multiple sessions by reading the CNMF-e identified ROIs into the Inscopix IDPS environment and using their internal registration algorithm to align ROIs across days. Finally, event detection was computed using the OASIS package (29) (as found in CaImAn). Care was taken to use individual animal noise thresholds (stable across sessions) to identify events. A low threshold risks assigning noise to "events," whereas a high threshold misses "events" (typically, we adapted the "s_min" parameter to be between 0.2 and 0.3). We identified an appropriate threshold to optimize the signal-to-noise ratio for each cell in each animal and maintained that threshold across all longitudinally registered sessions (the threshold changing to 0.1 and others at 0.4 in rare cases). Having identified Ca^{2+} events, and time stamped them, it was then possible to align the behavior and Ca^{2+} time series exactly. Visual inspection of output data was used to verify correct performance of the cell identification and event detection algorithms.

Behaviorally tuned neurons. Each neural event train was convolved with a Gaussian function ($\sigma = 12.5$ ms, window width of 2 σ) to obtain a time series of instantaneous firing rates. The Kraskov MIS was then calculated independently between each neuron and each behavior (30). Neurons were classified as encoding a specific behavior during a session (i.e., five trials) if they met the following criteria: 1) Calcium transient events were present in over 34% of the behavioral occurrences, and 2) the cell achieved an MIS greater than chance. Chance-level mutual information for a cell was determined by performing 2,000 shuffles of a cell event train and calculating the mutual information between each shuffled event train. The cell was considered as encoding a specific behavior cell if its MIS exceeded the 95th percentile of the values for the shuffled data. All the cells classified as encoding a specific behavior were verified with a visual inspection.

Behaviorally tuned neuron characteristics. For all behavioral encoding neurons, the "reliability" was calculated as the percentage of within-session behavioral occurrences that a neuron fired, and their "consistency" was calculated as the percentage of sessions in which the neuron was classified as encoding a specific behavior. The event rate was calculated as the number of events divided by the duration of behavior (seconds) to yield events per second–these were then averaged across behavioral occurrences and across all sessions.

Terminology. We followed standard usage in Ca^{2+} imaging studies for defining specific terms. When the camera displays a Ca^{2+} transient, we refer to this as an event, and events occur at a certain rate. Such transients happen in an ROI on the screen image of the endoscope, and these ROIs are considered as cells. Thus, events are cell firing. Longitudinal registration with respect to the *x,y* location of the ROI, identified via the stable physical location of ROIs in the camera image (31), enables a single cell to be followed across days (Fig. 3*A*). Events may occur at a single cell only during specific behaviors in the tube test (self or other or both), or during multiple behaviors, and thus their categorization was into unique cells which show specific events only during one behavior, coincident cells (unique behaviors in one animal of a pair simultaneously with a unique behavior in the other animal), mixed cells (any two behaviors in a single animal), or nonspecific cells (three or more behaviors). We distinguished unique-own, unique-other, and coincident cells. We also measured rate of firing (events per unit of time that a specific behavior was happening), and so could measure separately the number of cells by behavior category and the rate of events per category.

The critical feature of our correlational methodology was the principle of "mutual information."

Histology and Histochemistry. At the end of all recording, the animals were perfused transcardially with cold PBS (phosphate buffer saline, P4417 Sigma Aldrich) and fixed using 4% formaldehyde in PBS (prepared from Paraformadehyde, Sigma Aldrich 441244). After cryopreservation in 20% sucrose, coronal sections (60 μm thick) were cut on a cryostat and then visualized (endogenous GCaMP and staining signal) using a Nikon A1R confocal microscope. In all animals, the lens was targeted correctly to PrL as identified from the Rat Brain Atlas. For immunofluorescence staining, slices were permeabilized in PBS 10% NDS (normal donkey serum, Sigma Aldrich D9663) 0.3% Triton X-100 (Sigma Aldrich T8787) for 30 min, then incubated in PBS 10% NDS 0.1% Triton X-100 with 1:1,000 mouse Anti-GAD67 Antibody (Sigma Aldrich MAB5406 clone 1G10.2) or 1:500 guinea pig Anti-NeuN (SYSY 266 004) overnight at room temperature. The next day, three 10-min washes with PBS 0.1% Triton X-100 were performed, then slices were incubated in PBS 0.1% Triton with 1:200 donkey anti-mouse Alexa 647 (Thermo Fisher A-31571) or 1:200 goat anti-guinea pig Cy3 (Abcam ab102370), After three washes in PBS, slices are mounted in Fluoroshield with DAPI (Sigma Aldrich F6057). Confocal images were acquired with air objective 20× Plan Apo VC/NA 0.8, and the pinhole was set to 1.5 AU; 405-, 488-, 561-, and 633-nm laser lines were used to acquire the DAPI, GCaMP, Cy3, and Alexa 647 channels, respectively. Image processing was done with ImageJ (NIH).

Quantification and Statistical Analysis. Standard statistical tests were used, as data demanded, with the SPSS statistical package v25 used for these tests. Statistical significance was defined with $\alpha < 0.05$, with all F values and degrees of freedom stated. Specifications were described in the respective results and figure legends. All of the bar graphs with error bar represent mean ± SEM. Line graphs with error bars represents mean ± SEM.

Data Availability. Excel files and Python code have been deposited at https://datashare.ed.ac.uk/handle/10283/3888. The code to classify behaviorally tuned neurons is available at https://github.com/rufusmitchellheggs/Behavioral-Tuned-Cells.

ACKNOWLEDGMENTS. This work was funded by a grant held by P.C.K. and Adrian Bird of the Simons Institute for the Developing Brain, University of Edinburgh (Simons Foundation). This research was funded in whole, or in part, by a Wellcome Trust Advanced Investigator Grant (to R.M.). For the purpose of open access, the author has applied a CC BY public copyright license to any Author Accepted Manuscript version arising from this submission.

1. L. Ricceri, A. Moles, J. Crawley, Behavioral phenotyping of mouse models of neurodevelopmental disorders: Relevant social behavior patterns across the life span. *Behav. Brain Res.* **176**, 40–52 (2007).
2. J. N. Crawley, *What's Wrong with My Mouse? Behavioral Phenotyping of Transgenic and Knockout Mice* (Wiley, Hoboken, NJ, ed. 2, 2006).
3. G. Lindzey, H. Winston, M. Manosevitz, Social dominance in inbred mouse strains. *Nature* **191**, 474–476 (1961).
4. Z. Fan *et al.*, Using the tube test to measure social hierarchy in mice. *Nat. Protoc.* **14**, 819–831 (2019).
5. F. Wang *et al.*, Bidirectional control of social hierarchy by synaptic efficacy in medial prefrontal cortex. *Science* **334**, 693–697 (2011).
6. K. Saxena *et al.*, Experiential contributions to social dominance in a rat model of fragile-X syndrome. *Proc. Biol. Sci.* **285** (2018).

7. A. Asiminas *et al.*, Sustained correction of associative learning deficits after brief, early treatment in a rat model of Fragile X Syndrome. *Sci. Transl. Med.* **11** (2019).
8. J. Guy, J. Gan, J. Selfridge, S. Cobb, A. Bird, Reversal of neurological defects in a mouse model of Rett syndrome. *Science* **315**, 1143–1147 (2007).
9. A. J. Sandweiss, V. L. Brandt, H. Y. Zoghbi, Advances in understanding of Rett syndrome and MECP2 duplication syndrome: Prospects for future therapies. *Lancet Neurol.* **19**, 689–698 (2020).
10. T. Zhou *et al.*, History of winning remodels thalamo-PFC circuit to reinforce social dominance. *Science* **357**, 162–168 (2017).
11. L. Kingsbury *et al.*, Correlated neural activity and encoding of behavior across brains of socially interacting animals. *Cell* **178**, 429–446.e16 (2019).
12. L. Kingsbury, W. Hong, A multi-brain framework for social interaction. *Trends Neurosci.* **43**, 651–666 (2020).
13. F. L. Hitti, S. A. Siegelbaum, The hippocampal CA2 region is essential for social memory. *Nature* **508**, 88–92 (2014).
14. D. H. Hubel, T. N. Wiesel, Receptive fields, binocular interaction and functional architecture in the cat's visual cortex. *J. Physiol.* **160**, 106–154 (1962).
15. J. O'Keefe, J. Dostrovsky, The hippocampus as a spatial map. Preliminary evidence from unit activity in the freely-moving rat. *Brain Res.* **34**, 171–175 (1971).
16. E. V. Evarts, Brain mechanisms in movement. *Sci. Am.* **229**, 96–103 (1973).
17. M. N. Shadlen, W. T. Newsome, Neural basis of a perceptual decision in the parietal cortex (area LIP) of the rhesus monkey. *J. Neurophysiol.* **86**, 1916–1936 (2001).
18. K. Saxena, P. A. Spooner, R. Mitchell-Heggs, R. G. M. Morris, iHELMET: A 3D-printing solution for safe endoscopic Ca^{2+} recording in social neuroscience. *J. Neurosci. Methods* **355**, 109109 (2021).
19. G. Rizzolatti, L. Fogassi, V. Gallese, Mirrors of the mind. *Sci. Am.* **295**, 54–61 (2006).
20. K. Yoshida, N. Saito, A. Iriki, M. Isoda, Representation of others' action by neurons in monkey medial frontal cortex. *Curr. Biol.* **21**, 249–253 (2011).
21. R. V. Bretas, M. Taoka, H. Suzuki, A. Iriki, Secondary somatosensory cortex of primates: Beyond body maps, toward conscious self-in-the-world maps. *Exp. Brain Res.* **238**, 259–272 (2020).
22. F. G. Happé, Communicative competence and theory of mind in autism: A test of relevance theory. *Cognition* **48**, 101–119 (1993).
23. E. Harris *et al.*, Experiential modulation of social dominance in a SYNGAP1 rat model of ASD. *Eur. J. Neurosci.* **54**, 7733–7748 (2021).
24. B. A. Flusberg *et al.*, High-speed, miniaturized fluorescence microscopy in freely moving mice. *Nat. Methods* **5**, 935–938 (2008).
25. E. J. Hamel, B. F. Grewe, J. G. Parker, M. J. Schnitzer, Cellular level brain imaging in behaving mammals: An engineering approach. *Neuron* **86**, 140–159 (2015).
26. O. Friard, M. Gamba, BORIS: A free, verstaile open-source event-logging software for video/audio coding and live observations. *Methods Ecol. Evol.* **7**, 1325–1330 (2016).
27. E. A. Mukamel, A. Nimmerjahn, M. J. Schnitzer, Automated analysis of cellular signals from large-scale calcium imaging data. *Neuron* **63**, 747–760 (2009).
28. P. Zhou *et al.*, Efficient and accurate extraction of in vivo calcium signals from microendoscopic video data. *eLife*, **7** e28728 (2018).
29. J. Friedrich, P. Zhou, L. Paninski, Fast online deconvolution of calcium imaging data. *PLOS Comput. Biol.* **13**, e1005423 (2017).
30. A. Kraskov, H. Stögbauer, P. Grassberger, Estimating mutual information. *Phys. Rev. E Stat. Nonlin. Soft Matter Phys.* **69**, 066138 (2004).
31. L. Sheintuch *et al.*, Tracking the same neurons across multiple days in Ca^{2+} imaging data. *Cell Rep.* **21**, 1102–1115 (2017).

4.6 Neuronal signature of spatial decision-making during navigation by freely moving rats by using calcium imaging

PNAS RESEARCH ARTICLE | NEUROSCIENCE OPEN ACCESS

Neuronal signature of spatial decision-making during navigation by freely moving rats by using calcium imaging

Francesco Gobbo[a,1], Rufus Mitchell-Heggs[a,b,1], Dorothy Tse[a,c], Meera Al Omrani[d], Patrick A. Spooner[a,e], Simon R. Schultz[b], and Richard G. M. Morris[a,e,2]

Contributed by Richard G. M. Morris; received July 16, 2022; accepted September 20, 2022; reviewed by Denise Cai and John O'Keefe

A challenge in spatial memory is understanding how place cell firing contributes to decision-making in navigation. A spatial recency task was created in which freely moving rats first became familiar with a spatial context over several days and thereafter were required to encode and then selectively recall one of three specific locations within it that was chosen to be rewarded that day. Calcium imaging was used to record from more than 1,000 cells in area CA1 of the hippocampus of five rats during the exploration, sample, and choice phases of the daily task. The key finding was that neural activity in the startbox rose steadily in the short period prior to entry to the arena and that this selective population cell firing was predictive of the daily changing goal on correct trials but not on trials in which the animals made errors. Single-cell and population activity measures converged on the idea that prospective coding of neural activity can be involved in navigational decision-making.

hippocampus | place cells | spatial navigation

Significance

This manuscript addresses a longstanding problem about how place cell firing contributes to navigation in spatial environments, and data derived from on-line calcium imaging offer a new solution. These data support the view that prior to entering an arena where an animal will navigate to only one of several possible places on each day, a population of spatially responsive cells, including place cells, fire during the last 5 s. This population is shown to be predictive of the destination and trajectory that the animal is about to take.

A challenge in understanding spatial memory and spatial navigation is explaining how the former contributes to the latter. It is generally accepted that place cells (PCs) in the hippocampus constitute a "cognitive map" of the external space and that maps are used for navigation (1, 2). An outstanding question is how these two aspects can be linked—how information stored in the map can be accessed to guide choices about navigation. Numerous neurobiological studies have shown that laboratory animals readily learn to direct their spatial navigation accurately from one known place to another. This has been observed in diverse tasks such as the Barnes Maze (3) and the watermaze (4), with accurate navigation lost after hippocampal lesions. The cognitive map theory defines hippocampal PCs as active only in a particular position in a specific environment. How then can PCs corresponding to distal places A, B, or C contribute to appropriate navigation when the animal is starting his navigation from a remote start place S?

One solution might be to represent the animal's location in vectorial terms with respect to relevant landmarks or goals. This has found support in the discovery of object vector cells in the rat entorhinal cortex (5) and goal-oriented vector fields of PCs in the hippocampus of bats (6) and, recently, of rats (7). Modulation of in-place activity has been reported depending on future paths or goal locations (8–10). However, this solution may not explain the decision-making aspect entailed in flexible choices, such as the decision to go from place S to place A but not to other places. With respect to decision-making, one suggestion is that occasional out-of-field neural activity might be used. For example, the look-ahead activity of hippocampal CA3 PCs at decision choice points has been reported in rats running in figure-of-8 mazes (11, 12). Activity replay, a phenomenon first identified during sleep (13) or rest (14) after daytime experience, was later found to be involved in the out of-field reactivation of PCs during awake navigation to a learned home-goal from random locations (15). Replay could therefore be a possible way for the brain to selectively accesses spatial information beyond the current location. It could sometimes reflect intended navigation and has therefore been labeled as prospective replay. The role of replay during decision-making has been actively debated in the literature, with different groups suggesting that replayed events may reflect future paths (15, 16), paths to be avoided (17), new or updated learning (18), or the remembering of past trajectories (19). Hence, we sought to observe the neuronal signature of decision-making when rats learn and use newly acquired information to navigate to distinct locations across different sessions.

Four key issues guided the experimental design. The first, following Pfeiffer and Foster (15), was to visually monitor enough cells simultaneously in an individual animal because only a subset may participate in navigational planning. The second was to be sure of recording from the same cells across days in order that firing on one day, when the animal may learn to go to A, can be compared to that seen on another day when it

Author affiliations: [a]Centre for Discovery Brain Sciences, Edinburgh Neuroscience, The University of Edinburgh, Edinburgh, EH8 9JZ, UK; [b]Department of Bioengineering and Centre for Neurotechnology, Imperial College London, London, SW7 2AZ, UK; [c]Department of Psychology, Edge Hill University, Ormskirk, L39 4QP, UK; [d]MSc Program in Integrative Neuroscience, University of Edinburgh, Edinburgh, EH8 9JZ, UK; and [e]Simons Initiative for the Developing Brain, University of Edinburgh, Edinburgh, EH8 9JZ, UK

Author contributions: F.G., R.M.-H., and R.G.M.M. designed research; F.G., R.M.-H., and D.T. performed research; R.M.-H., D.T., P.A.S., and S.R.S. contributed new reagents/analytic tools; F.G., R.M.-H., and M.A.O. analyzed data; and F.G., R.M.-H., and R.G.M.M. wrote the paper.

Reviewers: D.C., Neuroscience Department, Icahn School of Medicine, New York, NY; and J.O., University College London.

The authors declare no competing interest.

See online for related content such as Commentaries.

[1]F.G. and R.M.-H. contributed equally to this work.

[2]To whom correspondence may be addressed. Email: .

This article contains supporting information online at http://www.pnas.org/lookup/suppl/doi:10.1073/pnas.2212152119/-/DCSupplemental.

Published October 24, 2022.

encodes the new location that day and remembers to go to B or C but not A. The widely used multiple single-cell tetrode recording technique addresses the first issue with excellent temporal resolution but is less suitable for the second because one cannot be certain that a specific cell on day N is also recorded on day N+1. Indeed, it is not uncommon for tetrodes to be advanced slightly from day to day in search of additional cells. The third issue was to devise a suitable behavioral task for the navigation problem in which the animal must encode which of the three distinct targets in a familiar spatial context is correct on any day and direct its navigation appropriately to the most recent correct location. The fourth issue is to ensure that the chosen technique does not pose too heavy a constraint on the behavioral protocol, with behavioral performance being minimally influenced (20). The present study meets all four challenges. It uses an event arena in which rats are trained over many days (28 or more) and thereby become familiar with the testing context. They develop a stable spatial map whose PCs can be repeatedly mapped during a daily 10-min exploration phase. The target location of A, B, or C of the animal's navigation from a start location S was varied from day to day. In effect, the daily task is a spatial "recency" task in which one location, but not the other two, is identified as the rewarded target for that session. The study deploys calcium (Ca^{2+}) imaging, which has recently been used to monitor neuronal activity during learning and neuronal reactivation (21, 22), as the recording technique of choice. This provides high cell numbers and ensures day-to-day reproducibility and stability, albeit at the expense of temporal resolution. The Ca^{2+}-transients were monitored using a gradient refractive-index (GRIN) lens directed at area CA1 of the hippocampus in freely moving rats. Using both single-cell and manifold population analyses of cell firing, we reveal a solution to the navigation problem.

Results

Calcium Imaging in Rat CA1. To record from freely moving rats performing the spatial memory/navigational task, we used miniature endoscopes (miniscopes) originally introduced by the Schnitzer group (23, 24). Successful recordings in CA1 have so far been performed in mice, but we sought to adapt the technique to rats and were successful in recording from hundreds of cells per animal (in this study, 1,146 neurons from 6 animals, mean = 191 ± 43 SEM). A key step required in rat was to aspirate beyond the fibers of the corpus callosum to invade also some of the myelinated fibers of the alveus that would otherwise limit the visibility of CA1 neurons from the GRIN lens (Fig. 1*A* and *SI Appendix*, Fig. S1). This was achieved with care resulting in minimal damage to stratum oriens. When the miniscope was fitted to its baseplate on each day (Fig. 1*B*), its view through the GRIN lens that had been lowered during surgery to the outer surface of the hippocampus allowed the imaging of Ca^{2+}-transients from pyramidal CA1 neurons (Fig. 1*C* and *SI Appendix*, Fig. S2). It proved possible to record stably from large numbers of neurons simultaneously with high signal to noise (*SI Appendix*, Fig. S2*A*). After the raw camera videos were processed (Fig. 1 *D*, *Left*), recordings were processed to identify individual regions of interest (ROIs; *Materials and Methods*) with the CaImAn constrained nonnegative matrix factorization-extended (CNMF-E) algorithm (Fig. 1 *D*, *Right*). The Ca^{2+} activity associated with individual ROIs, which likely corresponded to single cells, could be readily distinguished (Fig. 1*E*) and monitored during distinct exploration, sample, and choice phases of the daily behavioral task (see below). On the top rows of Fig. 1*F*, the correspondence between CNMF-E traces and the fluorescence profile of the resulting ROIs expressed as ΔF/F can be seen. Individual Ca^{2+} events were detected from CNMF-E traces (Fig. 1*F*). An ostensible virtue of Ca^{2+} imaging is the ability to monitor neurons across days by matching corresponding ROIs and thus explore the consistency of cell firing and its behavioral and spatial correlates across training sessions (24, 25). We were able to obtain stable fields of view and record from the same cells across periods of 4 sessions (Fig. 1*G* and *SI Appendix*, Fig. S3*A*) and for as long as 30+ days (*SI Appendix*, Fig. S3*B*). This stability is shown for two illustrative cells (nominally called 1 and 2 in Fig. 1 *G*, *Middle*) across sessions 18 to 21 of training. Around 80% of neurons could be reliably found across sessions (Fig. 1*H*). We confirmed that our recordings came from excitatory neurons expressing the calcium sensor GCaMP6f (26) from the CamKII promoter. GCaMP6f expression overlapped with the pan-neuronal marker NeuN but not with the inhibitory neuron marker GAD67 (*SI Appendix*, Fig. S4). To our knowledge, only one recent study (27) has been published using single-photon calcium imaging in rat CA1. This confirmed the presence of PCs, and our findings build on theirs as an application of this technology to freely moving rats undertaking flexible spatial choice behavior.

"Everyday Memory" Task. The concept of everyday memory (28) is that a great deal of information is encoded incidentally during daily life that is typically retained selectively for not much more than a day. In our model of this phenomenon, food-restricted rats were trained during a sample phase to retrieve food pellets from a single sandwell in a square arena whose location changed daily. There was no requirement to learn, as it was not a trial requiring discrimination between two choices, but the animals were rewarded at the daily location that was encoded. This daily training was preceded each day by an exploration phase of the entire arena in which the 3 possible locations for this rewarded sandwell were initially empty (Fig. 1*I*). Access to the arena from a startbox (blue) was via an automated entry door. The exploration phase lasted 10 min during recording sessions. The sample phase (6 trials) then began in which the animals now found that one of the possible sandwell locations had sand in it (green in Fig. 1*I*) that, were the animal to dig, would reveal accessible food pellets. The food pellets are large (0.5 g) such that the animals have a natural disposition to carry them back to the startbox to eat. All animals quickly returned to the startbox after retrieving each pellet one by one. The other two possible sandwell locations were empty, with food pellets in an underlying inaccessible compartment to ensure uniform olfactory cues (29). After 45 min, the choice phase (6 trials) began in which the animals were now confronted by 3 identical-looking sandwells, of which only the one used in the sample phase contained an accessible food reward (win-stay). The animal's path from the startbox around the arena and among the sandwells was monitored on both sample and choice trials. On the next session, one day later, the position of the correct sandwell changed to a new location in a quasi-random order. Over time, the probability that the animals would preferentially approach this sandwell during choice trials improved ($F = 2.88$, $df = 21$, $P = 0.034$; Fig. I) such that, by sessions 18 to 21 (shaded green; Fig. 1), the animals reached an asymptote of performance of 90.6 ± 3.5% correct (mean ± SEM, Student's t test $t = 11.61$ relative to chance, $df = 7$, $P < 0.0001$; here and throughout the text, full statistics information is reported in *SI Appendix*, Table S1; Fig. 1*J*, and *SI Appendix*, Fig. S5). The time taken by the animal to reach

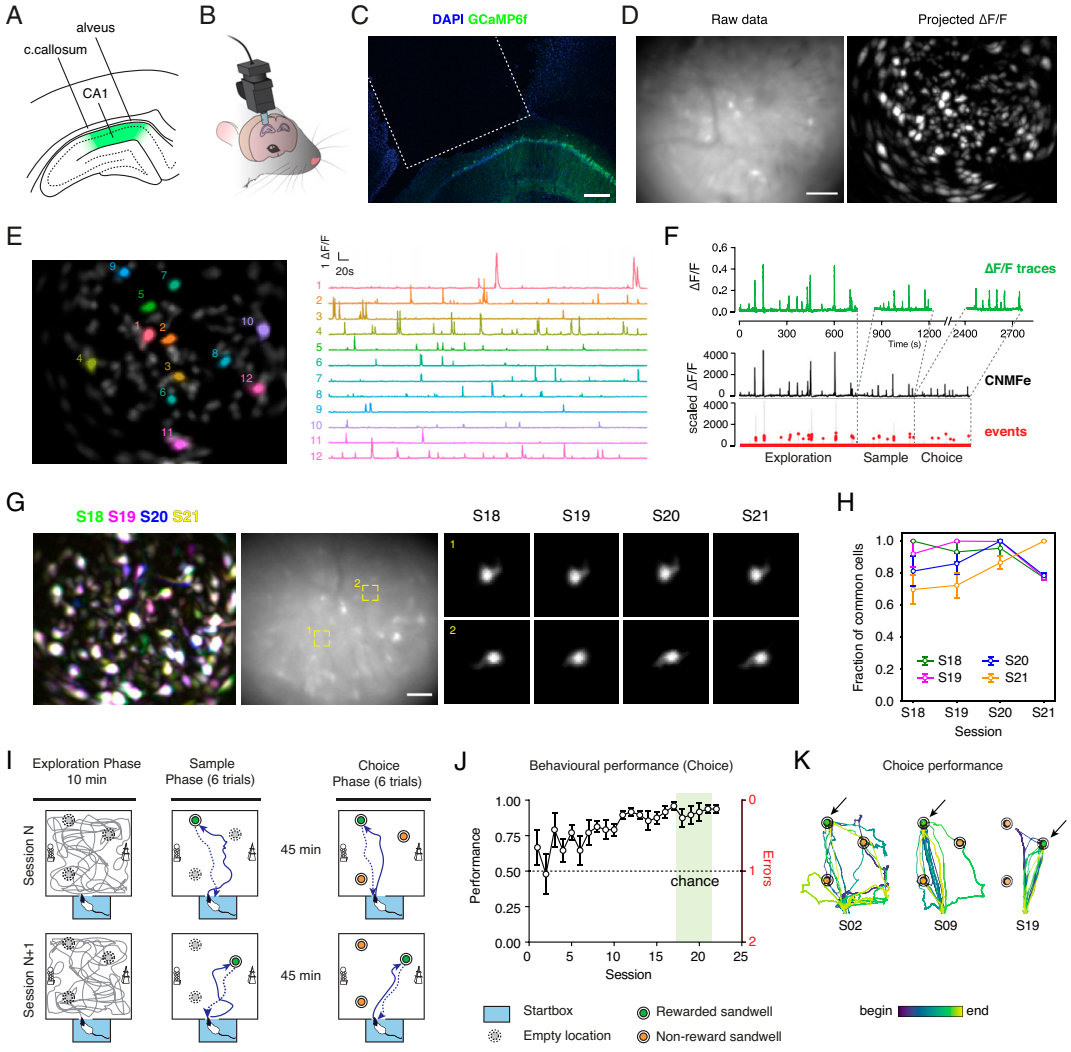

Fig. 1. Miniscope calcium imaging in rat CA1. (*A*) Schematic of rat hippocampus CA1 area. The hippocampus is overlaid dorsally by alveolar fibers and callosal fibers. GCaMP6f is expressed in CA1 pyramidal neurons (depicted in green). (*B*) The GRIN lens is implanted to reach the outer surface of CA1 and cemented to the animal's skull. A baseplate is attached externally to allow the daily positioning of the miniscope and recordings from the same neurons across multiple sessions. (*C*) Histological analysis confirmed the positioning of the GRIN lens as above stratum oriens of CA1. In green, own GCaMP6f fluorescence; in blue, DAPI staining of nuclei. Scale bar, 250 μm. The dashed line indicates the position occupied by the GRIN lens. (*D*) FOV of rat CA1 seen as recorded with the miniscope. The image displays the green fluorescence seen through the 535/50 filter from 475-nm illumination; note the occasional blood vessels and some brighter or active cells in the frame. Scale bar, 100 μm. On the *Right*, projected ΔF/F of the video on the *Left*. After processing, the signal is normalized in ΔF/F units, and maximum projection is shown to display active cells. (*E*) The CNMF-E algorithm was used to identify neurons. Representative temporal traces for 12 cells of the animal in *D*; note that the beginning of the recording is shown. The corresponding cells are highlighted on the cell map on the *Left*. (*F*) Event detection was performed with the OASIS algorithm from CNMF-E traces. The calculated ΔF/F profile of the applied mask is shown to compare the data traces with the CNMF-E output. (*G*) Longitudinal registration across consecutive sessions (S18 to S21). Superposition of the projected ΔF/F recordings for the four sessions confirms the consistency of the FOV. In the *Middle*, the corresponding FOV is presented; scale bar, 100 μm. In the two *Insets*, two representative cells are shown as they are identified in the four sessions. (*H*) Pairwise comparison of common cells between sessions. A large proportion of cells is detected and identified across multiple sessions. Average ± SEM, $n = 6$ animals. Note that the comparison of each session with itself is 1 by definition. (*I*) Schematic of the behavioral task in the everyday arena. Each session is made of three phases, as follows: exploration in the arena (10 min), sample phase (6 trials), and choice phase (6 trials). The text and *Materials and Methods* contain details. The startbox location from which the animal starts and then returns to eat the rewards is depicted in light blue. Each session, the identity of the rewarded sandwell changes. Ca^{2+} recordings are typically longer and are synchronized with the behavioral video with a transistor-transistor logic (TTL) pulse. (*J*) Behavioral performance increased over sessions, as animals committed fewer errors in identifying the correct sandwell during choice trials. Average ± SEM. For each animal, the average number of errors in the first three choice trials is expressed as performance that assumes a value of 0.5 at chance (*Materials and Methods*). The sessions highlighted in green are the recorded sessions considered in this work. Session effect, $P < 0.05$, one-way ANOVA. Here and in all later instances, full statistical details are reported in *SI Appendix*, Table S1. (*K*) Example trajectories of an animal performing in the choice phase at different stages of learning (S02, S09, and S19). Note how trials become more directed and fewer errors are committed.

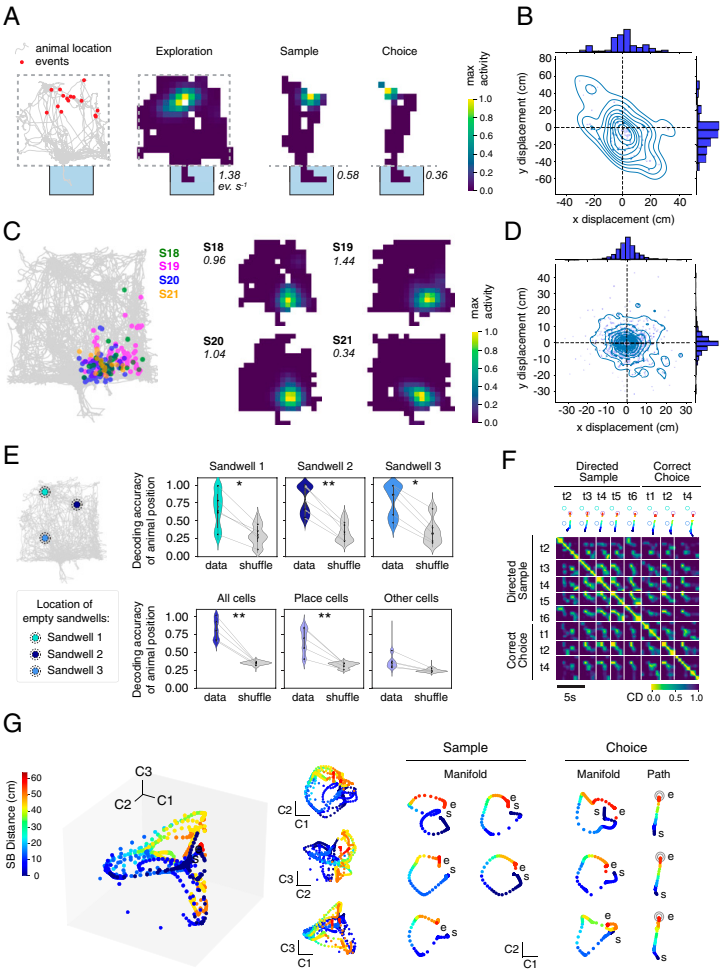

Fig. 2. Features of space representation in rat CA1. (*A*) Example cell showing the consistency of event locations between exploration, sample, and choice. On the *Left*, the position of the events of the displayed cell (red dots) are superimposed on the animal's trajectory. On its *Right*, the corresponding occupancy maps are shown for the three phases. The light-blue box is the startbox, and the dashed line indicates the arena limits. In italic is the peak value for each map (events/second). (*B*) x-y displacement of the maximum activity for all neurons in sample and choice phases compared to the exploration phase. (*C*) Individual cells display consistent location of their place fields across consecutive sessions. Displayed is one representative cell detected in S18 to S21. On the *Left* is shown the position of the events color coded by session. On the *Right*, corresponding occupancy maps are shown for the four sessions. (*D*) x-y displacement of the place center across exploration sessions. The first session where a PC is detected is taken as reference to calculate the displacements for the other sessions. (*E*) Decoding accuracy of a decoder trained on the exploration phase activity. On the *Left*, location and naming of the three sandwell locations used in this study. *Top*, the decoder correctly predicted when the animals were located in one of the three sandwells. Violin plot, points are individual animals. $*P < 0.05$, $**P < 0.01$, Student's *t* test of data vs. shuffle comparison. *Bottom*, performance of the decoder using all of the cells detected (*Left*), only PCs (*Middle*), or other spatially sensitive cells (non-PCs, *Right*). $**P < 0.01$, Student's *t* test of data vs. shuffle. *SI Appendix*, Table S1 shows for full statistics. (*F*) Cosine dissimilarity matrix for directed sample trials (trials 2, 3, 4, 5, and 6), and correct choice trials (trials 1, 2, and 3) showing repeated neuronal activity along the trajectory. Trajectories are represented on top of the graph. (*G*) Manifold representation of trials presented in *F*. The majority of variance is contained in the first two components C1 and C2. The s denotes the start of the trials in the startbox, and the e denotes the end of the outbound part of each trial at the sandwell. Note the repeated pattern assumed by the individual trial manifolds (*Right*) indicating the repetitiveness of the neural activity. The manifold assumes a circular shape even though it only corresponds to the outbound trajectory between the startbox and the sandwell (shown for choice trials), indicating a link between the startbox activity and the sandwell representation.

the sandwell that was most recently correct also declined across sessions (*SI Appendix*, Fig. S5*A*). In the last 2 sessions, a probe trial was performed in which the sandwells were covered with sand but had no accessible food reward. The animals tended to focus their digging for food preferentially on the correct sandwell (correct-incorrect effect, $P < 0.001$, two-way ANOVA; *SI Appendix*, Fig. S5*C*). It is important to note that the learning curve of Fig. 1*J* is not gradual learning of the spatial map of the arena and the 3 possible sandwell locations; such context learning is likely accomplished in the earliest sessions. Instead, it is the acquisition of the principle of using memory recall to approach the most recently rewarded location (spatial recency memory). Fig. 1*K* plots the paths taken by a representative animal at different stages of learning (in this example, sessions 2, 9, and 19). As the animal became more proficient in the task, more direct paths were taken and fewer errors were committed. Thus, the behavioral task created an ideal daily neuronal recording session in which there is a defined starting location, three geometrically distinct targets, and the opportunity to follow directed navigational paths from the start to the most recently valued target and back home again. We therefore focused our attention on sessions 18 to 21 during which the animals' asymptotic performance in the task was recorded using the miniscope.

Spatial Properties of Cells Recorded with Ca^{2+} Imaging. The next step was to conduct Ca^{2+} imaging during all three phases of the task (exploration, sample, and choice; Fig. 2). We confirmed observations from mouse experiments that miniscope Ca^{2+} imaging enables the visualization of place fields in the event arena. They were observed in individual cells during all phases of the session (Fig. 2*A*). PCs have been identified in linear and multidimensional environments (30); we also consistently observed many neurons displaying spatial selectivity (*SI Appendix*, Fig. S6). Multiple factors including directed navigation may induce global or rate remapping (31). To determine if remapping was occurring between exploration and sample or choice phases, the center of place fields identified in the exploration phase were compared with the maximum activity during sample and choice phases; there was no trend toward either global or rate remapping, taking into account the lesser space navigated during the training trials (Fig. 2*B*). Moreover, by

pooling data across sessions 18 to 21, we were able to observe a reasonably thorough mapping of the two-dimensional (2D) space of the entire event (*SI Appendix*, Fig. S6*C*).

Miniscope Ca^{2+} imaging offers the opportunity to examine stability between sessions (Fig. 2*C*). The quantification across sessions 18 to 21 showed most place-field centers displayed a spatial drift of 10 cm or less in the two arena axes (Fig. 2*D* and *SI Appendix*, Fig. S7), with the activity monitored across four separate exploration sessions of 10 min each. Thus, neurons did not significantly change the position of their place field over these four consecutive days. A neuron was considered a PC if the following four criteria were met: 1) the neuron fired more than three times during the exploration phase; 2) when computing the mutual information between its Ca^{2+} events and the animal's position, the correlation was greater than the 99th percentile of the spatial information calculated for the shuffled dataset; 3) there was no evidence of spike burstsl and 4) a minimum number of entries in the place field (*Materials and Methods* contains details). With these criteria, about a third of active cells were classified as PCs (29 ± 5%; *SI Appendix*, Fig. S7*D*), which is in line with previous reports in various environments by using different recording techniques (23, 32–35). Overall, 59 ± 8% of cells was classified as a PC in at least one session, which is in agreement with ref. 23 (*SI Appendix*, Fig. S7*E*). The majority of PCs had one place field, which is in agreement with previous reports (23, 36, 37) (*SI Appendix*, Fig. S7*F*). An exact number is likely influenced by the extent of effective behavioral sampling of the arena and the stringency of the classification criteria.

The next step was to examine whether spatial information in the activity of recorded neurons was sufficient to correctly predict the animal position. Using the data from the 10-min daily exploration phases (Fig. 2*E* and *SI Appendix*, Fig. S8), we trained a decoder to predict the animal position when at one of the three empty sandwell locations. Fig. 2 *E, Right*, shows that the probability of decoding the correct location of the animal (data) was significantly above chance performance (shuffle). Thus, the decoder correctly predicted the location of the sandwells from the unit activity (i.e., that the animal was located there; t values = 2.96, 4.56, and 3.01 for sandwell 1, 2, and 3, respectively; data vs. shuffle, df 8, all $P < 0.02$). As expected, most of the spatial information was contained in what were classified as PCs; with a decoder using only the activity from PCs, the performance was similar to the performance using all cells (all cells vs. PCs, df 8, $P = 0.43$, one-way ANOVA multiple comparisons) and above chance (data vs. shuffle, $P < 0.001$ in both cases, one-way ANOVA multiple comparisons; Fig. 2 *E, Center*, in the second row). In comparing the performance of all cells with those of defined PCs, we also observed a trend for some residual spatial information to be contained in this other subpopulation of cells. However, among this group of cells, only some may be contributing to performance (other cell data vs. shuffle, $P = 0.083$, one-way ANOVA multiple comparisons, nonsignificant).

The next issue was to examine if neurons were reliably reactivated by traversing analog portions of space during repeated outbound and then inbound trajectories between the startbox and the rewarded sandwell during sample and choice trials. The pairwise cosine dissimilarity was computed between the frames in accurately directed outbound paths of sample trials (i.e., the animal reached the rewarded sandwell first) and correct choice trials. Dissimilarity was lower in time points of corresponding positions, as presented in Fig. 2*F*. The repeated pattern of low cosine dissimilarity parallel to the diagonal indicates that as animals traversed the same space, the activity of neurons in the sample and choice phases was also similar. This repetition can be observed by expressing their distance with a multidimensional scaling (MDS) manifold representation (Fig. 2*G*). Each point on the manifold represents the neural population vector at a particular time point of the outbound path, and the distance between points represents the relative cosine dissimilarity. For both sample and choice trials, the intrinsic dimensionality (38, 39), a measure of the number of dimensions required to describe the neural activity, was on average 1.91 ± 0.36 dimensions. Indeed, the first two components contained most of the spatial information (Fig. 2 *G*, *C1-C2 Inset*; *SI Appendix*, Fig. S9), while additional dimensions typically included trial-to-trial variations such as whether a trial was correct or incorrect (*SI Appendix*, Fig. S9*A*). The manifolds of the individual trials displayed higher than chance correlation, especially in the first two components (*SI Appendix*, Fig. S9*D*), indicating that repeated traversals recruit similar activity along their length. This likely represents, in part, the population of PCs along the trajectory, but interestingly, the start of the manifold trials (the last 10 s in the startbox) was close to the end-point in 2D space (i.e., arrival at the rewarded sandwell), and the manifold assumes a circular shape, especially in the C1-C2 plane (Fig. 1 *G*, *Right*, and *SI Appendix*, Fig. S10). As the closer two points are to each other in manifold space, the lower is their cosine dissimilarity; these data point to the striking finding that the population neural activity in the startbox is similar to that of the correct sandwell.

Neuronal Activity in the Startbox Is Predictive of Spatial Decision-Making. We have seen that, over sessions 18 to 21, the animals chose the sandwell to approach upon leaving the startbox in choice tests at around 90% correct. The manifold results presented above prompted us to gather further insight into this initial part of the trial and, in particular, the last 10 s in the startbox before leaving. Note that the animal has full agency about when to leave after the door had opened. Fig. 3*A* shows that mean event rate rose steadily during this 10-s period. A decoder was then trained on the activity in the startbox in 2-s time windows (Fig. 3*B*) to see if it would correctly classify to which sandwell the animal was headed during choice trials. The prediction accuracy rose to >80% as the moment of entrance into the arena approached and was significantly higher than chance when compared to shuffled data that were, as expected for 3 sandwells, around 33% (Fig. 3*C*, breakdown of individual animals is presented in *SI Appendix*, Fig. S11). The decoder correctly identified the sandwell to which the animal was heading before leaving the startbox on trials when the animal chose correctly but poorly when the animals' choices were incorrect (i.e., they searched at a nonrewarded sandwell first in that trial). This prediction was highly significant for correct trials (ANOVA, F = 43.84, df 3/14, $P < 0.0001$).

Interestingly, the prediction was not significant for incorrect trials ($P = 0.46$ to shuffled data, one-way ANOVA multiple comparisons). Decoding performance remained poor when we reclassified the incorrect trials as leading to the appropriate sandwell (but a sandwell that was nonrewarded on that session) ($P < 0.0001$ compared to correct trials, $P = 0.49$ compared to incorrect trials, one-way ANOVA multiple comparisons). Together, these data indicate that startbox neural activity is not anticipating a different sandwell during incorrect choices but rather is not discerning between possible choices at all; the resulting outcome is perhaps a casual behavioral choice. However, if random, this choice may sometimes lead to the correct sandwells, and indeed, we noticed a small proportion of correct choice trials where decoding performance was poorer (Fig. 3*C*). A trend for better decoding performance on correct trials as a function of

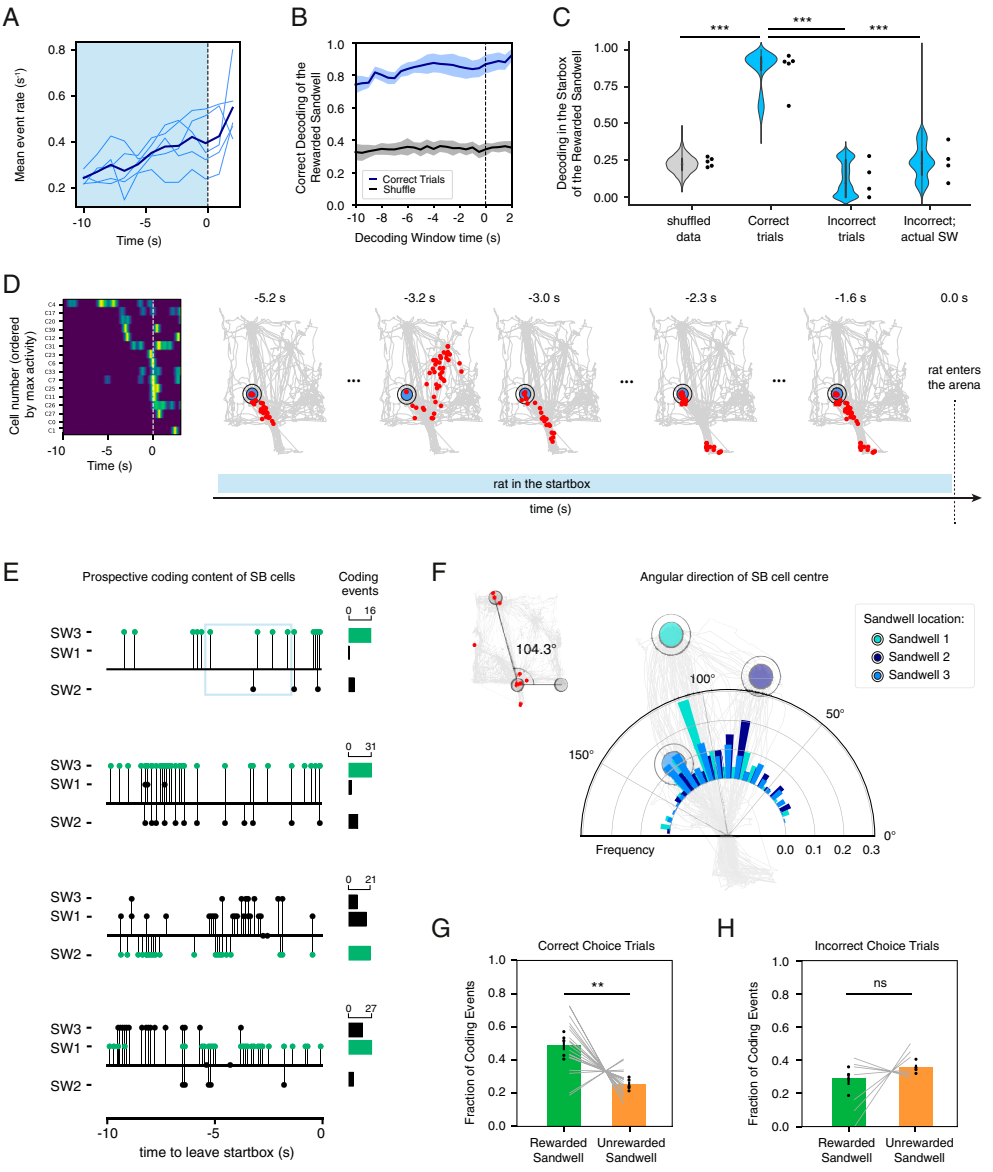

Fig. 3. Prospective coding during decision-making. (*A*) Neural activity increased as the moment of leaving the startbox approaches (dashed line). Mean event rate (events per second) in the 10 s before leaving (blue shaded area). Individual animals are shown in light blue and the population average in blue. (*B*) The success of decoding of the correct destination sandwell increases as the moment of leaving the startbox approaches (dashed line). Mean ± SEM is resented in blue and shaded area, while the mean ± SEM for the control shuffled data are represented in gray and shaded area. (*C*) Decoding the performance of the destination in choice trials from the startbox activity. The performance was highly accurate in correct trials compared to the shuffled data. In incorrect trials, instead, the performance was much worse and at chance level. For incorrect trials, the decoder performance was inaccurate also when they were relabeled with the first visited sandwell (incorrect actual) during those trials. ***$P < 0.0001$, one-way ANOVA comparison of means. (*D*) A representative example of cell events during the 0 s before leaving the startbox and the first 2 s of the trial in the arena. Cells are ordered by maximum activity. On the *Right*, we plot the spatial content of the cell activity between −5.2 s and −1.6 s. Red dots are the position of the events when the cells were active in our experiment (which includes the arena and the startbox). Importantly, during the display window, the animal was in the startbox. (*E*) Representative examples of choice trials showing the repeated prospective coding of the different sandwells (SW) in the 10 s before leaving the startbox. Prospective coding corresponding to the correct sandwell in each trial is displayed in green. Next to each graph, the frequency of each prospective coding is displayed as a histogram. The first trial on *Top* corresponds to the trial displayed in *D*; the light-blue square indicated the portion of the trial presented for display purposes. (*F*) Histogram of the angular distribution of the place centers for the cells active in the startbox divided by the identity of the rewarded sandwell (1, 2, or 3). Individual histograms are presented in *SI Appendix*, Fig. S17. (*G*) Relative number of prospective coding events for the rewarded and nonrewarded sandwells during correct trials. Black dots are individual animals and gray lines are individual sessions. **$P = 0.0057$, paired t test. (*H*) Number of prospective coding for incorrect trials. ns = 0.3033 paired t test.

the number of cells active in the startbox was observed, but overall performance was higher than 65% (*SI Appendix*, Fig. S12). Interestingly, a lower but significant performance was observed in later sample trials when the animal went to the appropriate sandwell directly, indicating that even a small number of prior exposures may be sufficient to drive memory encoding and a coherent representation during retrieval (*SI Appendix*, Fig. S13 *A* and *B*). This is unlikely to simply reflect the direction the animals were facing because we could not predict the animals' goal from the orientation of their head (*SI Appendix*, Fig. S14).

A high proportion of the cells active in the startbox was reactivated when the animal was in the arena (t = 5.98, df 4, P = 0.0039, paired Student's t test compared to cells active in the startbox only; *SI Appendix*, Fig. S15 *A* and *B*). In particular, startbox events were significantly more likely to map to the portion of the arena occupied during sample and choice phases, reflecting the paths taken to and from one of the three sandwells (t = 3.459, df = 4, P = 0.026, paired Student's t test; *SI Appendix*, Fig. S15 *C* and *D*). Moreover, the majority of startbox cells (64 ± 12.5%, mean ± SEM) represented the animals' outbound paths (with ∼22% PCs). Conversely, only 3.6 ± 0.2% (mean ± SEM) were active during the inbounds path (of which ∼6.5% were PCs) but 39 ± 6% (mean ± SEM) were active in both inbound and outbound paths (*SI Appendix*, Fig. S16). To determine the information content at each time point during the 10 s before leaving the startbox, the locations of place fields in the arena were plotted for the subset of cells active in the startbox during this time window (displayed in Fig. 3*D* is the time window from −5.2 s through to −1.6 s). Fig. 3*D* shows exemplar activity patterns at different time points before the animal left the startbox on an individual trial at specific time points. This was a trial in which the animal went to sandwell 3. The initial activity corresponds to the correct sandwell and the trajectory leading to it and then a momentary change of anticipation switching to sandwell 2 (at −3.2 s) followed by a return to the commitment to approach sandwell 3. Note that the rat was in the startbox throughout this period (*SI Appendix*, Fig. S14*F*). This exemplar pattern was quite common across different animals and sandwells, and we therefore refer to this phenomenon as "prospective coding," as the temporal resolution of calcium imaging is insufficient to use the term replay (*Discussion*). In Fig. 3*E* and *SI Appendix*, Figs. S17 and S18, further examples are displayed showing that different patterns of prospective coding occur over time, corresponding to the correct sandwell location or correct trajectory (in green) but also of the other two sandwells (black).

The direction to which startbox cells were pointing was quantified as the average angle between the spatial location of the cell events during exploration and the door of the startbox (Fig. 3*F*). As expected, the distribution of startbox directions corresponded to the angles of the directions to the three sandwells (Fig. 3 *F*, *Inset*). This distribution changed between sessions due to the use of different rewarded sandwells in a random but counterbalanced order (Kolmogorov-Smirnov comparisons between sandwells 1, 2, and 3: all D values are >0.19 with all P values of <0.0001). In particular, the distribution peaked toward the angle corresponding to the correct sandwell of that session (Fig. 3*F* and *SI Appendix*, Fig. S19). The number of prospective coding events in the startbox was strikingly higher on correct than incorrect trials (Fig. 3 *G* and *H*; paired Student's t test, repeated measures, t = 5.41, df = 4, P = 0.0077). Note that the number of prospective coding events associated with the other sandwells was not zero—consistent with the pattern jumping around during the startbox decision-making period. On incorrect trials, the number of prospective coding events was similar for the correct and incorrect sandwells (paired Student's t test, repeated measures, t = 1.239, df = 3, P = 0.3023). On average, prospective coding events corresponding to the recall of the correct sandwell in the startbox were longer and recruited a larger number of cells than those of the incorrect locations (paired Student's t test, repeated measures, t = 4.372 df = 4, P = 0.0119) (*SI Appendix*, Fig. S20 *A* and *B*). Furthermore, the number of events for the correct sandwell was relatively constant on all 6 trials in the choice phase (*SI Appendix*, Fig. S20*C*). However, this was markedly different for sample trials during which the animal has to encode the new daily location, for which the first three trials are closer to chance, while the last three show more frequent prospective coding of the correct sandwell (*SI Appendix*, Fig. S20*C*).

Discussion

There are four main findings. First, calcium imaging of large numbers of cells in freely navigating rats in an open arena has confirmed years of electrophysiological data showing that PCs and other cells with spatial selectivity can be observed, with no global remapping of place field locations observed between exploration, sample, and choice phases. Second, neural activity in the startbox increases during the waiting period before a trial starts with population coding activity preferentially correlating with any correct target or path to which the animal is about to run. Third, startbox activity is not predictive of the goal on trials when the animal performs incorrectly. Fourth, population coding of cell activity reveals that the activity in this time period prospectively codes the trajectories to possible goal locations, with the correct goal location being overrepresented. These data collectively reveal that neuronal activity corresponding to possible destinations or the paths to them is reactivated in the time period before a decision is made, which is a pattern of neural activity that could inform decision-making by displaying alternative scenarios.

These observations were possible through the successful optical recording with miniscopes in the CA1 hippocampal region of rats performing a complex, naturalistic navigational task in a large environment. The application of this technique to the rat required the careful aspiration of a very small strip of myelinated alvear fibers overlying the hippocampus, as well as those of the corpus callosum (as used in the mouse; *SI Appendix*, *Supplementary Discussion*), in such a manner as to leave stratum oriens undamaged (Fig. 1). In this way, there was minimal damage to the hippocampus itself, CA1 cell imaging was feasible, and we realized successful, reliable recordings over many days with stable regions of interest. Rats typically exhibit a wider range of behaviors and are better suited for demanding neuroscience protocols such as those employed in the study of spatial and episodic memory (40–42). Compared to electrophysiology, calcium imaging allows the identification of neurons across different sessions and for prolonged periods of time (23), although at the expense of time resolution and sensitivity. Ref. 37 also provides a detailed comparison of data from the rat and mouse, and our joint introduction of the technique to one of the most studied areas of the brain in one of the main model organisms is particularly important.

Our first finding confirms that this technique is effective in the detection of PCs in the rat. With our criteria (*Materials and Methods*; 99% mutual information), a third of cells were classified as PCs, with the remaining population of cells also exhibiting some degree of spatial selectivity (Fig. 2*E*). Different reports estimate PCs to range from 20% (43) to 35% (35) to 80% (32), although the number is markedly influenced by task factors, which are the criteria used to define PCs and which cells can be

included in population encoding. Our results are broadly in line with reports on rat hippocampus using electrophysiology in 2D environments, despite certain parameters (such as rate of firing) being different in optical recording. Shifts between environments (2, 44, 45) or prominent changes in environmental cues (46) are known to induce global, partial, or rate remapping of PCs. Here, we did not observe global remapping between exploration, sample, and choice trials, although we cannot exclude some level of rate remapping in the firing rate of PCs between the different phases. Indeed, in related experiments, it has been reported that even the introduction of barriers in a well-known environment can allow stable place fields to be maintained (16). With receptive fields stable across days, this greatly expanded the neuronal dataset with which to assess navigational trials and train a decoder. In our experiment, place fields remained largely stable across days (Fig. 2 *C* and *D*) as also reported in ref. 27. This stability is likely to be due to the animals' extensive training in the same arena. While large day-to-day variability has been reported between early epochs of an environment (23), correlation in the neural representation between sessions increased as the animals became acquainted with the environment upon repeated presentations (25).

Second, before the animals take any action to move toward one of the sandwells, neural activity increases in frequency such that, by the time animal chooses to leave the startbox, there is enough information in population measures of activity to correctly predict the animal's destination, at least for correct trials (Fig. 3 *B* and *C*). Interestingly, similar measures on the first or second sample trial, before the animals had fully encoded which is the correct location that day, were poorer, but activity thereafter assumed a predictive pattern (*SI Appendix*, Fig. S20*C*). Thus, spatial recency within a well learned context can be encoded and accessed remarkably fast, which is reflected also in the reduced number of behavioral errors after the initial sample trials (Fig. 1*J* and *SI Appendix*, Fig. S5). In at least a fraction of cells (65 ± 3%), the information contained in the startbox neuronal activity reflects spatial information about one of the sandwell locations or the outbound trajectory to reach it (*SI Appendix*, Figs. S15 and S16 and Fig. 3 *D*–*H*). These observations are consistent with a report by Komorowski et al. (47) that showed that PCs may become engaged by the task on which animals are trained such as the spatial recency task here .

Third, we observed that startbox activity was different on behaviorally incorrect trials. The relatively higher representation of the correct sandwells likely reflects a focus on the imminent destination (Fig. 3 *E*–*G*). At the beginning of incorrect trials, and in early sample trials, the proportions of prospective coding events for the correct and incorrect sandwells were statistically indistinguishable (Fig. 3*H*). This finding is consistent with the results obtained using the decoder (Fig. 3*C*) where neither the correct nor the actual destination could be decoded from the neural activity in the startbox on incorrect trials.

Fourth, population coding enabled the analysis of activity patterns using state-of-the-art, multidimensional manifolds to represent neural population activity in multidimensional spaces. It was observed that two dimensions were sufficient to capture most of the variance of the cosine dissimilarity in the neural activity recorded in the animals' trajectories to the sandwell. A striking observation was that, on the outbound path of correct choice trials, these visualizations assumed a circular appearance suggesting a relationship between the population firing in the startbox and at the correct sandwell. This was confirmed by observing the spatial content contained in the activity of the population of cells active in the startbox. Such representation cannot be measured using only single cells and reflects a potential strength of calcium imaging. Compared to electrophysiology, calcium imaging allows the identification of large numbers of neurons across different sessions and for prolonged periods of time (23, 24), although at the expense of time resolution and sensitivity. While replay has been traditionally recorded by means of electrophysiology because of its good temporal resolution, there have been reports of replay with calcium imaging (21, 22). Although it is likely that replay detected with electrophysiology and cell reactivation detected in this work represent the same biological phenomenon, we deemed it prudent to refer to our finding as prospective coding.

These observations of spatially predictive activity collectively support findings that suggest that prospective coding could be used to guide future behavior (48, 49). While some authors have proposed this, other reports have argued that replay may rather reflect past memory, as past trajectories seem to be overrepresented in reward-switch tasks (19). Here, we find that prospective coding not only maps onto future, correct trajectories but also includes momentary mapping onto the other sandwells during decision-making in the startbox (Fig. 3 *D*–*H*). Our proposal is that such activity can sometimes serve to anticipate possible scenarios during decision-making. Accordingly, different outcomes may be weighed during decision-making to guide correct goal-directed behavior.

The behavioral task used, now referred to as everyday memory, has the defining characteristic of the episodic encoding of information (e.g., during nondiscrimination sample trials) that can be accessed for a period but is typically forgotten quickly—a common everyday experience. By session 18, the animals were completely familiar with the spatial context and likely had a consolidated representation in long-term memory of the environment. Their task was to update each day which area of space mattered—spatial recency. The free choice and the flexibility of this task are extra factors to encourage the animal to think about the desired destination. When the choice is more forced by the configuration of the task, as in the case of radial mazes (19), the replay of past trajectories may be preferred to avoid choosing a wrong arm that precludes access to the rewards by not allowing rerouting, in analogy to what has been reported in experiments with fear conditioning (17). Indeed, the data by Gillespie et al. (19) show that, after repeated trials, the representation of the rewarded arm increases. Our data therefore support a role for prospective coding to inform decision-making rather than only guide future behavior, as also theoretically suggested by others (50, 51). Prospective coding by hippocampal CA1 cells may hence prioritize paths that are most immediately relevant for on-going behavior (52). This would also explain how prospective coding can even construct mental scenarios that have never actually been experienced (11). It has been reported that differential activity along common paths can reflect a future choice (8, 9). However, most cells we identified in the startbox were also active in the arena at some point; it is possible that the different configuration of our behavioral setup does not promote differential firing because there are no obliged common tracks reaching the various sandwells. Indeed, cells only active in the startbox were a smaller proportion of the total (*SI Appendix*, Fig. S15*A*), and their activity may be differentially regulated by the animal's destination (9). An alternative possibility is that via the prospective coding of different trajectories, the brain is performing evidence accumulation until some threshold is reached, possibly with conjunctive coding by other brain regions, e.g., in anticipation of a reward (53). Indeed, Fig. 3*E* suggests that as the decision point approaches, the number of

prospective coding events for the correct sandwell increase. Future work will elucidate this aspect.

There are limitations to our observations. One is that, due to technical reasons, it is difficult to reconstruct sequences of recorded neurons or to ascertain their ordered activity below the frame-rate detection of 20 Hz. Accordingly, we use the neutral term of content of neural activity rather than considering them as sequences. One additional caveat is sensitivity, such that realistically isolated action potentials are not detected by GCamp6f. This likely results in an underestimation of the number of prospective coding events and of the number of cells involved. Nonetheless, we find that a third of cells active in the startbox at the beginning of trials are common in any other trial (*SI Appendix*, Fig. S13 *C–E*). This should affect all activity in an equal manner, so we doubt it introduces significant bias to our analysis; if anything, our results provide a conservative estimate of the frequency of such prospective coding events.

In conclusion, we have presented an application of miniscope imaging of the rat CA1 to the study of decision-making in spatial navigation. This offered the possibility of comparing the neuronal activity across multiple sessions in which animals encode the most recent rewarded location and engage in memory prospective coding to go to it. Before any action is taken to navigate toward one of the possible destinations, the activity corresponding to three possible locations or trajectories is prospectively coded by hippocampal neurons. Our results suggest that such coding may be used by the animals to recall alternative destinations and, possibly, to evaluate their suitability. Our data provide information regarding the role of prospective coding during remembering/action planning. Future directions will further clarify how the animals use this information to plan and simulate possible paths and how the choice is made from these possibilities. Furthermore, it will be interesting to test how allocentric or egocentric spatial features of the task influences prospective coding.

Materials and Methods

Animal Subjects. Lister-Hooded rats ($n = 8$) were 2 to 3 mo old at the start of the experiments. Animals were purchased from Charles River and group housed until surgery; after surgery, animals were housed in single cages. During the behavioral task, they were food deprived to 85 to 90% of the free-feeding weight against a growth curve, with free access to water, on a 12:12-h light-dark cycle with training in the light phase. Care of the animals complied with the UK Animals (Scientific Procedures) Act conducted under a Project License (PPL P7AA53C3F). Two animals were excluded from the recordings due to insufficient quality of the field of view (FOV; low number of detected cells). One further animal (H0487) could only be recorded in sessions 18 and 19 due to technical issues and was excluded from the analysis on prospective coding because we could not compare the three possible destinations.

Immunohistochemistry. At the end of the experiments, the animals were anesthetized with 200 mg/mL pentobarbital and perfused transcardially with cold PBS (phosphate buffer saline; P4417 Sigma Aldrich) and 4% formaldehyde in PBS (Sigma Aldrich 441244). Heads were postfixed for 24 h in formaldehyde, and then the brains were extracted and postfixed overnight. They were transferred in 20% sucrose PBS and cut with a cryostat (Bright Instruments). After being washed in PBS, slices were permeabilized in PBS supplemented with 10% NDS (normal donkey serum; Sigma Aldrich D9663) and 0.1% Triton X-100 (Sigma Aldrich T8787) for 30 min, and then incubated in PBS supplemented with 10% NDS 0.1%, Triton X-100, mouse anti-GAD67 antibody (Sigma Aldrich MAB5406 clone 1G10.2) 1:1,000, and guinea pig Anti-NeuN (SYSY 266 004) 1:500 overnight at room temperature. The next day, three washes with PBS with 0.1% Triton X-100 were performed, and then slices were incubated in PBS with 0.1% Triton, 1:200 donkey anti-mouse Alexa 647 (Thermo Fisher A-31571) and 1:200 anti-guinea pig Alexa 555. After three washes in PBS, the slices were mounted in Fluoroshield with DAPI (Sigma Aldrich F6057).

Microscopy. Multichannel images were acquired using a Nikon A1R Ti:E inverted confocal microscope with 1AU pinhole dimension, using a 40× Plan Apo/numerical aperture (NA) 1.25 oil objective (histological staining) or 10× Plan Flour/NA 0.3 (GCaMP6f/DAPI acquisition). Sequential acquisition of the four channels was performed with the laser lines DAPI 402 nm, GCaMP6f 488 nm, NeuN/Alexa555 562 nm, GAD67/Alexa647 639 nm, and 450/50; and with 525/50 and 595/50 filter cubes. Histological sections stained with DAPI were images with a Leica DMR upright microscope with Retiga 2000R camera using an epifluorescence mercury lamp and PL FLUOTAR 10×/0.30 and PL FLUOTAR 20×/0.50 objectives.

Surgical Procedures. Surgical procedures were performed under sterile conditions and according to best practice. Animals were maintained under 3 to 2% isoflurane (Covertus absis01) reversible anesthesia and 0.5 mL rimadyl (Zoetis) administered as an analgesic at the beginning of each surgery. In the first surgery, 1 μL of AAV1.CaMKII.GCaMP6f.WPRE.SV40 (UPenn Vector Core, then Addgene 100834-AAV1) diluted with sterile PBS (Sigma-Aldrich) to a final concentration of 5.7 10^{12} vg/mL was injected in the CA1 region of each hemisphere (stereotaxic coordinates from bregma AP (Antero-Posterior) 3.6, ML (Medio-Lateral) ± 2.2, DV (Dorso-Ventral) 2.2 from dura) at 100 nL/min using an automated injection pump and a Hamilton syringe equipped with a Nanofil needle (World Precision Instruments). The GRIN lens was implanted 7 to 10 d after the first surgery. In the second surgery, three surgical screws were implanted in the skull (Screws and More, DIN 84 A2 M1 × 3). A circular craniotomy was performed with a trephine for microdrill (Fine Science Tools 18004-18) at AP 3.8, ML 2.4. A cylindrical volume of cortical tissue was then aspirated manually with a sterile blunt needle in the 27G to 30G range. Constant irrigation with cold saline is performed during aspiration to prevent swelling and clean blood. A small portion of alveolar (anteroposterior) and callosal (coronal) fibers was then removed with the same blunt needle with mild aspiration to expose but leave undamaged the outer surface of the hippocampus (corresponding to CA1 stratum oriens). Cold saline irrigation and soaked sterile gelatin sponge (we successfully used Pfizer Gelfoam or Delta Surgical [Newcastle Under Lyme] Gelita-Spon GS-110) were used to keep the hole clean until complete stop of the bleeding. A 1-mm-wide, 9-mm-long GRIN lens (Inscopix) was then lowered with a 5-degree angle in position AP 3.8, ML 2.4, DV 1.9 from dura (the dura is measured before the aspiration). Two stainless-steel rods (0.09-mm diameter; CrazyWire UK) are attached to side of the GRIN lens with superglue before implantation, with around 3 mm of rods protruding from the surface of the GRIN lens. A thin layer of surgical silicone (KWIK-SIL, World Precision Instruments) was applied to the sides of GRIN lens to prevent cement to enter in contact with the brain tissue. The GRIN lens was cemented in place with Super Bond dental cement (Prestige Dental) to cover the skull and included the skull screws.

Calcium Recordings. The Inscopix nVista system was used to perform calcium imaging experiments. At least 3 weeks after the GRIN lens implantations, the animals were anesthetized temporarily and the FOV checked with the Inscopix miniscope. The baseplate support for the miniscope was scored with a scalpel blade to provide better attachment with SuperBond cement. With the miniscope, the optimal position for the baseplate above the skull was determined by looking for the FOV containing neurons. Some brighter neurons are usually seen along with capillaries, and some neural activity could be sometimes detected by very briefly lowering the anesthesia depth to 0.5 to 1% isoflurane before raising it again. The baseplate was then cemented in place with SuperBond using the pre-existing layer of cement. Scoring the previous cement surface with a scalpel blade is recommended to ensure optimal adhesion. After the cement had hardened, the miniscope could be removed with the baseplate now anchored to the animal skull. A small piece of duct tape can be used to prevent dirt and dust to enter the cavity between the baseplate and the lens while not recording.

When recording, the miniscope is positioned on the baseplate and secured with a miniature screw attached to the baseplate, taking care that the animal movement does not displace the miniscope from the correct position. Proper handling of the animals is fundamental in our experience, and extensive habituation is required so that the miniscope can be attached to the animals' head without the need to completely immobilize them or use anesthesia. Rather, a mild restraint of the animal's head at jaw level, without causing distress, is often enough to enable the positioning of the miniscope. The miniscope cable was

connected to a commutator on the ceiling that enables full animal rotation. The commutator was connected to the nVista imaging system (v 3.0) that controls the miniscope functioning and stores the recorded data. Because we were recording from a large 2D area (1 to 2 m wide), the cable should be long enough to allow easy access to the whole arena. To prevent the cable being uncomfortable, elastic wires were used to connect the two extremities of the cable. On the first day of recording, the exact FOV was chosen by fine tuning the eFocus parameter on the miniscope that controls the focus of the internal lens.

Ca^{2+} recordings were collected at 20 Hz for a 1,061 × 800-pixel FOV using the Inscopix nVista imaging system (v3.0) and synchronized with the camera behavior via an electronic signal in one of the GPIO channels timestamping the time of a small light-emitting diode (LED) light in the camera FOV at the beginning and end of the recording. The camera has a pixel size of 0.82 μm.

Apparatus. All experiments were conducted using a modified event arena (29) that was 1-m × 1-m square. The walls (40 cm high) are transparent, and the floor is composed of 20-cm × 20-cm removable white tiles (for regular cleaning purposes). Three Plexiglas sandwells (6-cm diameter, 4-cm depth) that contained the hidden reward pellets were placed in one or a subset of the panels with holes. To mask the smell of the food, the sandwells were filled with clean rodent bedding material. Each sandwell had a spherical plastic bowl that enabled rewarded sandwells to contain one or more reward pellets (BioServ F0171) (0.5 g). Nonrewarded sandwells contained an equal number of reward pellets in a space underneath, thereby serving as inaccessible food. These plastic bowls had holes ensuring that the rewarded and nonrewarded sandwells contained the same number of reward pellets at approximately the same depth in the sand and thus should exude the same smell. Extensive randomizing and counterbalancing were also arranged to minimize olfactory artifacts, as follows: 1) the sandwells used in the encoding trial were not used for the recall trial of the same session; 2) all sandwells were used as rewarded or nonrewarded sandwell across days; and 2) the arena floor was regularly wiped with a 70% alcohol-impregnated towel between sessions, and before recall and probe trials. Animals entered the arena from a single startbox located nominally in the south. Two intramaze cues were positioned inside the arena on the west and east walls, namely, a multicolor toy and a clean yellow mustard dispenser, respectively. Two prominent extramaze cues were present outside the arena.

Habituation. Rats were first taught to dig for food in sandwells inside their home cages. In a first habituation session in the arena, the rats were permitted to explore the arena with two intra-arena cues and surrounding extra-arena cues for 10 min. They were also habituated to being put in a startbox and given a 0.5-g food pellet to eat. When the pellet was eaten (typically around 30 s), the rats were allowed 10 min access to the arena. On the second and third habituation, one 0.5-g pellet was placed on top of the sandwell; rats collected the pellet and took it back to the startbox; rats were then allowed to retrieve other food pellets buried close to the surface of the sandwell. If rats had difficulties in retrieving the hidden food pellets, they were helped by exposing one further pellet in front of them.

Behavior. Rats were trained in a modified form of the event arena task (29). In this task, animals learn to retrieve food pellets from one of the three sandwells in the everyday arena, whose position changes from one session to the next (sandwell 1, 2, or 3). The task is divided in three parts. During exploration. animals explore the arena for 10 min without any reward present and the sandwells are empty. During encoding (sample phase) one sandwell chosen at random is rewarded and contains 0.5-g food pellets. Animals are trained to retrieve six pellets from the sandwell, entering the arena from the startbox after the door opens, retrieve one pellet from the sandwell, and return to the startbox to consume it. During the choice trial, all sandwells were filled with bedding and appeared identical on the outside. The correct sandwell had pellets in the accessible bowl, while the other sandwells had their equal number of pellets in the nonaccessible compartment. The choice trial was performed 30 min after the end of the sample trial. During the choice phase, the animals retrieved six pellets, returning to the startbox to eat each one. A 0.5 s, a 2,300-Hz tone was played 5 s before the door opened.

Data Analysis.

Behavior performance. For each trial, latency and the number of errors were quantified. Latency is the time that occurred between the moment that the animal leaves the startbox to when it starts digging at the correct sandwell. The number of errors is the number of incorrect sandwells the animal dug at before reaching the correct sandwell, and in this experiment, we can assume values 0 (the correct sandwell is the first choice) or 1 or 2 (the animal dug at all sandwells before reaching the correct one). The performance was defined as

$$Performance = 1 - \frac{n}{n_{max}}, \quad [1]$$

where n is the number of errors. Hence, if the animal performs at chance it results in Performance = 0.5, as shown in Eq. 2.

$$\mathbb{E}(n) = \sum_i n_i \mathbb{P}(n_i) = 0(1/4) + 1(1/2) + 2(1/4) = 1 \quad [2]$$

Single-photon calcium imaging. For each subsequent Ca^{2+} recording, the Inscopix data processing software (IDPS; Inscopix v1.6) environment was used to denoise the recording by applying a low and high filter spatial bandpass (σ_{low} = 0.0005 and σ_{high} = 0.5). IDPS was then used to correct motion artifacts by using a rigid motion correction algorithm (54, 55). Preprocessed recordings were then imported into the CNMF-E python application programming interface (API) (56), their cell ROIs identified and their respective calcium transients computed as the change in fluorescence over baseline fluorescence as $\Delta F/F = (F - F_0)/F_0$, where F_0 is the mean fluoresce over the trace. All ROIs and their respective traces were manually inspected, with any duplicates or artifacts discarded. Neural events were then computed from the calcium traces using the Online Active Set method to Infer Spikes (OASIS) package (57, 58). For each animal, calcium traces were manually assessed for levels of noise and a unique noise threshold applied (typically an "s_min" parameter of between 0.2 and 0.3 was used). Longitudinal registration was performed in the IDPS. Individual recordings from the same sessions were first aligned generating one dataset for each session (S18 to S21) and then the four datasets were aligned together. Correct alignment was verified by screening a random subset of an individual set from the correspondence table generated by the system.

Animal positional tracking. Behavioral recordings of the task are performed with a camera placed on the ceiling (black and white, 20 fps). A small LED light outside the arena was used for the alignment and switched on briefly while an electrical signal was sent to one of the nVista GPIO channels. The ON time can be easily detected by a change in intensity in the corresponding pixels. Rat positional trajectories were tracked using the Python image recognition deep convolutional neural network Deeplabcut (DLC) (59).

Training dataset. A training set of 180 distinct frames of the animals in the arena in all stages (60 frames from 3 rats) were extracted based on *k*-means derived quantization. This involved downsampling the video and modeling individual frames as vectors and then randomly selecting frames from different clusters. Each frame in the dataset was then manually labeled using the point between the animal's ears as reference.

Network training. A 50-layer deep pretrained convolutional neural network (ResNet-50) was then refined by training it for 500,000 iterations on the training dataset and evaluated using the mean average Euclidean error between manually labeled frames and those predicted by DLC. Accuracy was also manually checked and corrected by referring to a DLC-labeled video. The position of the animal is translated using one corner of the arena as the reference origin.

PC identification. Spatial tuning was inferred using custom Python scripts. For each neuron, the Kraskov Spatial Information (SI) was calculated between the binarized event train and the vector of the animals binned spatial activity (obtained by binning the arena into 4- × 4-cm spatial bins). A neuron was classified as a PC if it met the following criteria: 1) the neuron had at least three events during the imaging stage, 2) the animal traversed bins in which the neuron was active at least three times, 3) a neural event occurred in at least 20% of traversals, and 4) the neurons' SI exceeded the 99th percentile of a distribution of SI for 5,000 shuffled neural event trains.

Place fields. A neuron's place field was defined by calculating its rate map and normalizing by the animal's occupancy map and then selecting all contiguous bins that surrounded the place field center (i.e., the bin with maximum activity). Place field size was then calculated as the number of 4-cm bins squared in the place field.

Decoders. A Gaussian naive Bayes (GNB) python algorithm from Sckit-learn was used for sandwell classification using neural activity first within the arena and subsequently from within the startbox. In both cases, neural event trains were convolved with a Gaussian kernel ($\sigma = 200$ ms, window width of 4σ) to obtain a time series of instantaneous event rates.

Sandwell classification arena. For sandwell classification within the arena, sandwell regions were first defined as the area within a 5-cm radius of the well center. All exploration sessions were concatenated and sandwell activity isolated to produce an N × T matrix of instantaneous event rates (X), where N is the number of neurons that are active across all sessions and at least one sandwell and T is the amount of time the animal spent in the sandwell. Then X was labeled with the animal's corresponding sandwell (y) at each point in time. The number of observations for each sandwell class was balanced by downsampling the number of samples for each well to that of the least visited and repeated 10 times to enable random sampling of the sandwell activity. Finally, a 10-fold cross-validation strategy was conducted with a 70:30 train: test split. For each training set, GNB assumes that the class-conditional densities, $\mathbb{P}(x_i \mid y)$, are normally distributed (as shown in Eq. 3, with μ_y and σ_y the mean population vector and stanard deviation for class y, respectively). Finally, the Maximum A Posteriori estimation (as shown in Eq. 4) was used for each sample, yielding a predicted sandwell for each point in time:

$$\mathbb{P}(x_i \mid y) = \frac{1}{\sqrt{2\pi\sigma^2}} \exp\left(-\frac{(x_i - \mu_y)^2}{2\sigma_y^2}\right), \quad [3]$$

and

$$\hat{y} = \text{argmax } \mathbb{P}(y) \prod_{i=1}^{n} \mathbb{P}(x_i \mid y). \quad [4]$$

SB classification of sandwell. Using correct sample and choice trials, a GNB decoder was trained to identify the animal's prospective sandwells (the sandwell that the animal was about to visit). For each trial (six sample, six choice), the startbox activity was isolated as the 10-s period before the animal left the startbox and entered the arena. Trial activity was merged into a single matrix (Trial × N × T_{SB}) and temporally split into 5 × 2-s windows, starting with a delay of −10 to −8 ($\tau = -10$ to -8) and finishing at -2 to 0, where 0 is the point at which the animal left the startbox and entered the arena. For each 2s window (Trial × N × $T_{SB,\tau}$), a GNB decoder was run using a 10-fold cross validation strategy using a 70:30 train: test split. Correct trials were subsequently compared to incorrect trials using the temporal window of $\tau = -2$ (the time during which the animal was most likely to be looking out into the arena) and a 1,000-fold cross-validation strategy.

Performance was evaluated by calculating the fraction of correctly predicted sandwells based on the actual label. Furthermore, the F1-score was calculated from the precision (the number of true positive results divided by the number of all positive results) and recall (the number of true positive results divided by the number of all samples that should have been identified as positive); see Eq. 4.

$$\text{F1} = 2 \times \frac{(precision \times recall)}{(precision + recall)} \quad [5]$$

Finally, for each training set, a comparable control was computed. This was achieved by training the GNB using X labeled with shuffled sandwell classes. Decoder performance was then tested on the same test sets as described above, generating a performance or F1-score expected at chance level (~33%).

Cosine distance. For each animal, all neurons that were active in the outbound trajectory of correct sample or choice trials were collated into the data structure (trial × N × $T_{\text{outbound correct}}$) and their neural event trains convolved with a Gaussian kernel ($\sigma = 200$ ms, window width of 4σ) to obtain a time series of instantaneous event rates. The cosine distance adjacency matrix $D_C \in T \times T$ was subsequently computed by treating each point in time as neural population vector (x_i) with dimension N and calculating its cosine distance from all other time points within and across all trials (as shown in Eq. 5).

$$D_C(x_i, x_{i+n}) = 1 - \frac{x_i \cdot x_{i+n}}{|x_i||x_{i+n}|} \quad [6]$$

MDS. Dimensionality reduction or neural manifold learning takes a high dimension neural activity matrix, $X \in N \times T$, and transforms it into the low dimension mapping $Y \in k \times T$ (where $k \ll N$). Classical MDS is a linear dimensionality reduction algorithm based on based on the MATLAB cmdscale function applied to the previously computed cosine distance matrix $D_C \in T \times T$ to yield the lower dimension embedding $Y \in k \times T$. This is computed through the minimization of a strain parameter that aims to preserve the relative cosine distances of D_C in the manifold embedding Y. In parallel to this, an eigen-decomposition of the distance matrix D_C is performed, with the resultant eigenvalues (or dimensions) sorted according to how much of the variance they explained with the top three dimensions selected for visualization.

Event rate. For correct and incorrect sample and choice trials, neurons that were active in the 10-s period before the animal left the startbox up until 2 s into the arena were isolated and the event rate over time calculated. Event rate was calculated as the number of events per seconds.

Fraction of cell firing inside trajectory. The arena was first binned into 4- × 4-cm spatial bins. A "trajectory mask" was then constructed using sample and choice trials, selecting bins that the animal traversed when leaving from the startbox to each of the three sandwells and back. The trajectory mask was then applied to all sessions and stages with any spatial activity outside the trajectory mask considered to be part of the "arena mask" (note, only bins that were visited were not included in the analysis). The fraction off cells firing inside the trajectory was subsequently calculated as the fraction of times a cell fired in the trajectory mask vs. the arena mask, normalized by the animal's bin occupancy.

Angle of cell firing. For each trial of sample and choice, we selected the cells active in the 10 s before leaving the startbox. We calculated the angle of cell firing θ as the average angle between the startbox door and the events recorded in the arena. Following convention in circular statistics, the origin was in the nominal east direction and positive angles were calculated anticlockwise so that a cell firing on the wall on the right of the door of the startbox has $\theta = 0°$. The distribution was calculated for the cells active in the startbox in trials where the correct sandwell was 1, 2, or 3.

Cell trajectory classification. For each trial of sample and choice, we selected the cells active in the 10 s before leaving the startbox. For each cell, we plotted the event positions of the neuron activity in the arena as recorded in the pretraining, sample, and choice phases. Each instance of prospective coding (cell, time) was classified as one of the sandwells if the event position was located either on the sandwell or in the trajectory between the startbox and the sandwell. In a minority of instances where pretraining events differed from the sample/choice (4.9%), mainly because of additional events outside the possible trajectories, only the sample and choice events were considered. Where the events mapped onto an area that did not correspond to any of the sandwells, the prospective coding event was classified as other (3.9%) and were not taken into account in the final calculations. The fraction of prospective coding for the correct sandwell was calculated as $n_{\text{correct}}/(n_{\text{correct}}+n_{\text{incorrect}})$ where n is the number of prospective coding occurrences. Compound prospective coding events was considered if multiple cells represented the same sandwell (either as goal or trajectory) and were part of consecutive prospective coding events (≤100 ms), i.e., two prospective coding events were considered to be part of the same compound event if they were happening on the same time frame or the following one after binning at 100 ms. Clustering into compound prospective coding events was linearly additive; if coding events occurred at t, t+100ms, or t+200ms, a single compound prospective coding event of length = 3 was considered.

Software. Confocal and microscope images were open and processed with Fiji/ImageJ v2.1 (NIH); linear transformation of brightness and contrast was applied uniformly and equally to all compared images or channels. Calcium video processing was performed as described above using IDPS v1.6 and publically available or custom Python code. Statistical analysis was performed with GraphPad Prism v7.

Note. While this manuscript was in preparation, an independent report of calcium imaging in rats running along a linear track was published (27). This report showed that a high proportion of cells can be PCs in such an apparatus. Our study confirms this finding by using a rigorous mutual information criterion to identify PCs and goes on to deploy this imaging technology to gather insight into hippocampal function during decision-making.

Spatial recency within a well-learned context can be encoded and accessed remarkably fast. These observations complement those in another report, which was published while this manuscript was in preparation, to the effect that hippocampal representations can emerge after only a limited number of trials (48).

Data, Materials, and Software Availability. All study data are included in the article and/or *SI Appendix*. The data are available at https://datashare.ed.ac.uk/handle/10283/4760. The software used for data analysis is available at https://github.com/rufusmitchellheggs/Neural-Predictive-Spatial-Coding (60).

ACKNOWLEDGMENTS. We are grateful to all current and former members of the R.G.M.M. and S.R.S. laboratories for fruitful discussion and support. We also thank Mark Schnitzer (Stanford) and his laboratory colleagues for their expert opinion on the projects and support on the analysis. The Inscopix team members were fantastic, in particular Diane Damez-Werno's insight during the initial phase of this project. Thanks also to Emma Wood and Matt Nolan (Edinburgh) and to Paul Dudchenko (Stirling) for useful insight and discussion. We also thank Giuseppe Gava (Imperial College, Oxford) for his expert guidance on PC identification. This work was financially supported by a Wellcome Trust Advanced Investigator Grant to R.G.M.M. (Grant 207481/Z/17/Z). For the purpose of open-access, the corresponding author has applied a CC BY public copyright license to the Authors Accepted Manuscript arising from this submission.

1. J. O'Keefe, J. Dostrovsky, The hippocampus as a spatial map. Preliminary evidence from unit activity in the freely-moving rat. *Brain Res.* **34**, 171–175 (1971).
2. R. U. Muller, J. L. Kubie, The effects of changes in the environment on the spatial firing of hippocampal complex-spike cells. *J. Neurosci.* **7**, 1951–1968 (1987).
3. C. A. Barnes, Memory deficits associated with senescence: A neurophysiological and behavioral study in the rat. *J. Comp. Physiol. Psychol.* **93**, 74–104 (1979).
4. R. G. M. Morris, P. Garrud, J. N. P. Rawlins, J. O'Keefe, Place navigation impaired in rats with hippocampal lesions. *Nature* **297**, 681–683 (1982).
5. Ø. A. Høydal, E. R. Skytøen, S. O. Andersson, M. B. Moser, E. I. Moser, Object-vector coding in the medial entorhinal cortex. *Nature* **568**, 400–404 (2019).
6. A. Sarel, A. Finkelstein, L. Las, N. Ulanovsky, Vectorial representation of spatial goals in the hippocampus of bats. *Science* **355**, 176–180 (2017).
7. J. Ormond, J. O'Keefe, Hippocampal place cells have goal-oriented vector fields during navigation. *Nature* **607**, 741–746 (2022).
8. E. R. Wood, P. A. Dudchenko, R. J. Robitsek, H. Eichenbaum, Hippocampal neurons encode information about different types of memory episodes occurring in the same location. *Neuron* **27**, 623–633 (2000).
9. J. A. Ainge, M. Tamosiunaite, F. Woergoetter, P. A. Dudchenko, Hippocampal CA1 place cells encode intended destination on a maze with multiple choice points. *J. Neurosci.* **27**, 9769–9779 (2007).
10. R. M. Grieves, E. R. Wood, P. A. Dudchenko, Place cells on a maze encode routes rather than destinations. *eLife* **5**, e15986 (2016).
11. A. S. Gupta, M. A. A. van der Meer, D. S. Touretzky, A. D. Redish, Hippocampal replay is not a simple function of experience. *Neuron* **65**, 695–705 (2010).
12. A. Johnson, A. D. Redish, Neural ensembles in CA3 transiently encode paths forward of the animal at a decision point. *J. Neurosci.* **27**, 12176–12189 (2007).
13. M. A. Wilson, B. L. McNaughton, Reactivation of hippocampal ensemble memories during sleep. *Science* **265**, 676–679 (1994).
14. M. P. Karlsson, L. M. Frank, Awake replay of remote experiences in the hippocampus. *Nat. Neurosci.* **12**, 913–918 (2009).
15. B. E. Pfeiffer, D. J. Foster, Hippocampal place-cell sequences depict future paths to remembered goals. *Nature* **497**, 74–79 (2013).
16. J. Widloski, D. J. Foster, Flexible rerouting of hippocampal replay sequences around changing barriers in the absence of global place field remapping. *Neuron* **110**, 1547–1558.e8 (2022).
17. C.-T. Wu, D. Haggerty, C. Kemere, D. Ji, Hippocampal awake replay in fear memory retrieval. *Nat. Neurosci.* **20**, 571–580 (2017).
18. D. Dupret, J. O'Neill, B. Pleydell-Bouverie, J. Csicsvari, The reorganization and reactivation of hippocampal maps predict spatial memory performance. *Nat. Neurosci.* **13**, 995–1002 (2010).
19. A. K. Gillespie *et al.*, Hippocampal replay reflects specific past experiences rather than a plan for subsequent choice. *Neuron* **109**, 3149–3163.e6 (2021).
20. G. Chen, J. A. King, Y. Lu, F. Cacucci, N. Burgess, Spatial cell firing during virtual navigation of open arenas by head-restrained mice. *eLife* **7**, e34789 (2018).
21. A. Malvache, S. Reichinnek, V. Villette, C. Haimerl, R. Cossart, Awake hippocampal reactivations project onto orthogonal neuronal assemblies. *Science* **353**, 1280–1283 (2016).
22. A. D. Grosmark, F. T. Sparks, M. J. Davis, A. Losonczy, Reactivation predicts the consolidation of unbiased long-term cognitive maps. *Nat. Neurosci.* **24**, 1574–1585 (2021).
23. Y. Ziv *et al.*, Long-term dynamics of CA1 hippocampal place codes. *Nat. Neurosci.* **16**, 264–266 (2013).
24. D. J. Cai *et al.*, A shared neural ensemble links distinct contextual memories encoded close in time. *Nature* **534**, 115–118 (2016).
25. A. Attardo *et al.*, Long-term consolidation of ensemble neural plasticity patterns in hippocampal area CA1. *Cell Rep.* **25**, 640–650.e2 (2018).
26. T. W. Chen *et al.*, Ultrasensitive fluorescent proteins for imaging neuronal activity. *Nature* **499**, 295–300 (2013).
27. H. S. Wirtshafter, J. F. Disterhoft, In vivo multi-day calcium imaging of CA1 hippocampus in freely moving rats reveals a high preponderance of place cells with consistent place fields. *J. Neurosci.* **42**, 4538–4554 (2022).
28. R. G. M. Morris, Elements of a neurobiological theory of hippocampal function: The role of synaptic plasticity, synaptic tagging and schemas. *Eur. J. Neurosci.* **23**, 2829–2846 (2006).
29. T. Bast, B. M. da Silva, R. G. M. Morris, Distinct contributions of hippocampal NMDA and AMPA receptors to encoding and retrieval of one-trial place memory. *J. Neurosci.* **25**, 5845–5856 (2005).
30. J. O'Keefe, Place units in the hippocampus of the freely moving rat. *Exp. Neurol.* **51**, 78–109 (1976).
31. P. Latuske, O. Kornienko, L. Kohler, K. Allen, Hippocampal remapping and its entorhinal origin. *Front. Behav. Neurosci.* **11**, 253 (2018).
32. A. A. Fenton *et al.*, Unmasking the CA1 ensemble place code by exposures to small and large environments: More place cells and multiple, irregularly arranged, and expanded place fields in the larger space. *J. Neurosci.* **28**, 11250–11262 (2008).
33. A. P. Maurer, S. L. Cowen, S. N. Burke, C. A. Barnes, B. L. McNaughton, Phase precession in hippocampal interneurons showing strong functional coupling to individual pyramidal cells. *J. Neurosci.* **26**, 13485–13492 (2006).
34. Z. N. Talbot *et al.*, Normal CA1 place fields but discoordinated network discharge in a Fmr1-null mouse model of fragile X syndrome. *Neuron* **97**, 684–697.e4 (2018).
35. E. J. Markus, C. A. Barnes, B. L. McNaughton, V. L. Gladden, W. E. Skaggs, Spatial information content and reliability of hippocampal CA1 neurons: Effects of visual input. *Hippocampus* **4**, 410–421 (1994).
36. A. T. Keinath *et al.*, Precise spatial coding is preserved along the longitudinal hippocampal axis. *Hippocampus* **24**, 1533–1548 (2014).
37. X. Mou, J. Cheng, Y. S. W. Yu, S. E. Kee, D. Ji, Comparing mouse and rat hippocampal place cell activities and firing sequences in the same environments. *Front. Cell. Neurosci.* **12**, 332 (2018).
38. P. Grassberger, I. Procaccia, Characterization of strange attractors. *Phys. Rev. Lett.* **50**, 346–349 (1983).
39. R. Mitchell-Heggs, S. Prado, G. P. Gava, M. A. Go, S. R. Schultz, Neural manifold analysis of brain circuit dynamics in health and disease. arXiv [Preprint] (2022). https://arxiv.org/abs/2203.11874 (Accessed 10 October 2022).
40. I. Q. Whishaw, A comparison of rats and mice in a swimming pool place task and matching to place task: Some surprising differences. *Physiol. Behav.* **58**, 687–693 (1995).
41. V. Hok, B. Poucet, É. Duvelle, É. Save, F. Sargolini, Spatial cognition in mice and rats: Similarities and differences in brain and behavior. *Wiley Interdiscip. Rev. Cogn. Sci.* **7**, 406–421 (2016).
42. H.-P. Lipp, D. P. Wolfer, Genetically modified mice and cognition. *Curr. Opin. Neurobiol.* **8**, 272–280 (1998).
43. L. T. Thompson, P. J. Best, Place cells and silent cells in the hippocampus of freely-behaving rats. *J. Neurosci.* **9**, 2382–2390 (1989).
44. J. K. Leutgeb *et al.*, Progressive transformation of hippocampal neuronal representations in "morphed" environments. *Neuron* **48**, 345–358 (2005).
45. T. J. Wills, C. Lever, F. Cacucci, N. Burgess, J. O'Keefe, Attractor dynamics in the hippocampal representation of the local environment. *Science* **308**, 873–876 (2005).
46. M. I. Anderson, K. J. Jeffery, Heterogeneous modulation of place cell firing by changes in context. *J. Neurosci.* **23**, 8827–8835 (2003).
47. R. W. Komorowski, J. R. Manns, H. Eichenbaum, Robust conjunctive item-place coding by hippocampal neurons parallels learning what happens where. *J. Neurosci.* **29**, 9918–9929 (2009).
48. B. E. Pfeiffer, Spatial learning drives rapid goal representation in hippocampal ripples without place field accumulation or goal-oriented theta sequences. *J. Neurosci.* **42**, 3975–3988 (2022).
49. H. F. Ólafsdóttir, F. Carpenter, C. Barry, Task demands predict a dynamic switch in the content of awake hippocampal replay. *Neuron* **96**, 925–935.e6 (2017).
50. B. E. Pfeiffer, The content of hippocampal "replay". *Hippocampus* **30**, 6–18 (2020).
51. H. F. Ólafsdóttir, D. Bush, C. Barry, The role of hippocampal replay in memory and planning. *Curr. Biol.* **28**, R37–R50 (2018).
52. M. G. Mattar, N. D. Daw, Prioritized memory access explains planning and hippocampal replay. *Nat. Neurosci.* **21**, 1609–1617 (2018).
53. A. Johnson, M. A. van der Meer, A. D. Redish, Integrating hippocampus and striatum in decision-making. *Curr. Opin. Neurobiol.* **17**, 692–697 (2007).
54. E. A. Mukamel, A. Nimmerjahn, M. J. Schnitzer, Automated analysis of cellular signals from large-scale calcium imaging data. *Neuron* **63**, 747–760 (2009).
55. S. L. Resendez *et al.*, Visualization of cortical, subcortical and deep brain neural circuit dynamics during naturalistic mammalian behavior with head-mounted microscopes and chronically implanted lenses. *Nat. Protoc.* **11**, 566–597 (2016).
56. P. Zhou *et al.*, Efficient and accurate extraction of in vivo calcium signals from microendoscopic video data. *eLife* **7**, e28728 (2018).
57. J. Friedrich, P. Zhou, L. Paninski, Fast online deconvolution of calcium imaging data. *PLOS Comput. Biol.*13, e1005423 (2017).
58. A. Giovannucci *et al.*, CaImAn an open source tool for scalable calcium imaging data analysis. *eLife* **8**, e38173 (2019).
59. A. Mathis *et al.*, DeepLabCut: Markerless pose estimation of user-defined body parts with deep learning. *Nat. Neurosci.* **21**, 1281–1289 (2018).
60. F. Gobbo *et al.*, Neuronal signature of spatial decision-making during navigation by freely moving rats by using calcium imaging. GitHub. https://github.com/rufusmitchellheggs/Neural-Predictive-Spatial-Coding. Deposited 7 October 2022.

Chapter 5

Appendix

5.1 Keggin-type polyoxometalates as Cu(II) chelators in the context of Alzheimer's disease

Prior to my PhD, I worked as a research assistant at the Laboratoire de Chimie de Coordination (LCC) - Centre Nationale de la Researche Scientifique (CNRS) - Toulouse, France. I researched the in-vitro interaction of a chemical agent with Aβ plaques (one of the key hallmarks of AD). Progressing to my PhD, this early work was put forward for publication and I was invited to review my updated work. The details of the paper are outlined below.

A key pillar of AD research is the study of the formation of Aβ plaques and how they induce neurotoxicity. First, amyloid precursor protein (APP) breaks down into Aβ monomers which go on to aggregate into toxic oligomers and eventually senile Aβ plaques. Importantly, Aβ plaques possess metal binding residues that often coordinate metal ions such as Copper (Cu), Zinc (Zn) and Iron (Fe). Not only do these metal ions aid the assembly of Aβ plaques, but in the presence of oligomers, they have been linked to the production of reactive oxygen species (ROS) and downstream neurotoxicity (Das et al., 2021). Therefore, targeting these metal ions may present a candidate for diminishing the negative impact of Aβ plaques.

The (Atrián-Blasco et al., 2022) study explores how in-vitro Aβ plaques can be targeted and reduced by removing metal ions such as Cu(II) that are involved in Aβ aggregation and ROS generation. Specifically, the paper aimed to analyse the effectiveness of a class of compounds called Keggin-type polyoxometalate (POM) chelators in the presence of Aβ plaques in-vivo. To achieve this, two candidate POMS were investigated on their ability to bind free Cu(II) ions and Cu(II) ions in the presence of Aβ40 and Aβ16 sub-types. By studying their UV-vis and absorption spectra, the study discovered that both POMs were able to successfully remove Cu(II) from Aβ peptides.

This in turn was found to guide Aβ peptides into more stable mature fibrils. This study adds to the understanding of the role of metal coordination in Aβ aggregation and highlights its importance when developing novel therapies. The chelating capacity of POMS, coupled with the fact that they are non-toxic and can pass the blood-brain barrier thus presents them as a potential drug candidate for metal-targeted AD therapy. Furthermore, with the pursuit of effective therapies still underway, it is paramount that additional angles of treatment are explored.

Personal contribution: In this study, my contribution required that I leverage my background in Biochemistry to run wet-lab protocols. These included preparing in-vitro Aβ assays in the presence of POMS and running UV-vis spectroscopy and absorption experiments at distinct time points to define their effectiveness. I also contributed to the analysis of the results and reviewed the main text.

ChemComm

COMMUNICATION

View Article Online
View Journal | View Issue

Cite this: *Chem. Commun.*, 2022, **58**, 2367

Received 14th October 2021,
Accepted 13th January 2022

DOI: 10.1039/d1cc05792h

rsc.li/chemcomm

Keggin-type polyoxometalates as Cu(II) chelators in the context of Alzheimer's disease†

Elena Atrián-Blasco,‡[ab] Lucie de Cremoux,‡[a] Xudong Lin,[a] Rufus Mitchell-Heggs,[a] Laurent Sabater,[a] Sébastien Blanchard *[c] and Christelle Hureau *[a]

Two Keggin polyoxometalates were used as new copper ligands to counteract the effects of Cu^{II}(Amyloid-β) interaction. Their ability to remove Cu^{II} from Cu^{II}(Amyloid-β), to stop Cu^{II}(Amyloid-β) induced formation of reactive oxygen species and to restore apo-like self-assembly of Cu^{II}(Amyloid-β) was shown.

Alzheimer's disease (AD) is a debilitating and devastating mental disorder and the most widespread kind of dementia. Due to the aging of the population and the lack of curative treatments, the number of AD patients will increase dramatically in the near future, putting the health care system under an incredibly huge pressure.[1] This underlines the need for alternatives to the current therapeutic options. AD is characterized by the presence of extra-cellular deposits of highly ordered supra-molecular assemblies of the Amyloid-β (Aβ) peptide, the so-called senile or amyloid plaques in specific regions of the brain. The Aβ peptide indeed belongs to the amyloid-forming peptide family that also includes amylin and α-synuclein, involved in Type II diabetes and Parkinson's diseases respectively.[2] The main forms of Aβ peptides are made of 39 to 43 amino acid residues, with the 40 amino-acids sequence being the most studied. Apart from the N-terminal hydrophilic part (up to the 16 residues), the peptide is mainly hydrophobic with the LVVF moiety and the C-terminal sequence involved in its self-assembly. This process known as aggregation finally leads to the formation of highly stable β-sheets rich structures (amyloids) that gather into the senile plaques.[3] The 16 residues N-terminal sequence contains several metal binding residues (mainly histidine and carboxylate-containing residues) involved in the coordination of d-block ions, mainly Copper and Zinc.[2] Based on that ability and the abnormally high level of Cu, Zn and Fe found in the senile plaques, and in line with many *in vitro* studies that have shown a role of metal ions in the modulation of Aβ self-assembly, metal ions are regarded as biologically relevant partner of amyloid formation and related toxicity.[2,4,5] Cu-bound to Aβ can catalyze the production of reactive oxygen species (ROS) and thus may contribute to the overall oxidative stress observed in the disease.[6]

Polyoxometalates (POMs) are oxoclusters of early transition metal ions that have found applications in various fields from catalysis to material science. They result from the polycondensation in acidic media of oxoanions such as WO_4^{2-}, templated or not by *p*-oxoanions (PO_4^{3-}, SiO_4^{4-}, *etc.*). Controlled basic degradation of complete POMs can lead to lacunary POMs, which are very efficient all-inorganic ligands. Among the proposed biochemical and medical applications of POMs,[7–9] their interactions with peptides and proteins have been gaining interest over the last years.[10,11] For example, Prusiner and co-workers have studied the ability of different POMs, mainly Keggin-type (Scheme 1), to promote the aggregation of the toxic form of the prion protein.[12] The modulating activity of the POMs relies on their electrostatic interactions with the positively charged amino acids of the protein, while their size may also play a role.[13] While it has been proposed that various types of POMs could modulate Aβ aggregation *via* electrostatic interaction,[14–16] Qu *et al.* reported that transition metal substituted POMs (MS-POMs) were even more efficient, presumably *via*

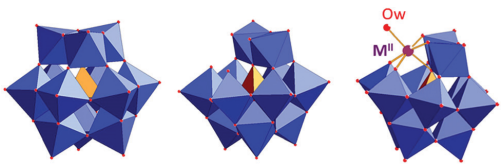

Scheme 1 K^{4-}, K_V^{8-} and K_M^{6-} structures (M^{II} is a d-metal dication, w = water molecule).

[a] *LCC-CNRS, Université de Toulouse, CNRS, Toulouse, France. E-mail:*
[b] *Instituto de Nanociencia y Materiales de Aragón (INMA), Consejo Superior de Investigaciones Científicas-Universidad de Zaragoza, Zaragoza 50009, Spain*
[c] *CNRS, Institut Parisien de Chimie Moléculaire, IPCM, Sorbonne Université, 4 Place Jussieu, Paris F-75005, France. E-mail:*

† Electronic supplementary information (ESI) available. See DOI: 10.1039/d1cc05792h
‡ Contribute equally to the work.

additional coordination bond between metal ion and the histidine residues of Aβ.[17] While POMs, including MS-POMs, were used to tune Aβ self-assembly, there is no report on the use of POMs as chelating agents (in the context of AD), although giant POMs were shown to alter Cu^{II}(Aβ) and Zn^{II}(Aβ) aggregation due to multiple weak electrostatic interactions with the metal ions.[16]

Up to now, no lacunary POM has been studied for its ability to remove Cu^{II} bound to Aβ and to prevent resulting effects with respect to Aβ aggregation and Cu(Aβ)-induced ROS production and thus to act as a classical chelator but with the extra ability to modify Aβ aggregation on its own. This is the core of the present communication, where we present a detailed study of the influence of $K_4[\alpha\text{-}SiW_{12}O_{40}]$ ($K_4\alpha[\mathbf{K}]\cdot 10H_2O$) and its monolacunary derivative $K_8[\alpha\text{-}SiW_{11}O_{39}]$ ($K_8\alpha[\mathbf{K}_\gamma]\cdot 18H_2O$) on Cu and Cu(Aβ)-induced ROS production and on aggregation of Aβ (with or without Cu^{II}). This first study may open new routes of research with POMs as efficient chelating agents in the AD context.

$\mathbf{K}^{4-}$ and $\mathbf{K}_\gamma^{8-}$ (Scheme 1) are composed of a central Si(IV) surrounded by four atoms of oxygen, which connect the central Si to twelve ($\mathbf{K}^{4-}$) or eleven ($\mathbf{K}_\gamma^{8-}$) W(VI) cations each in an octahedral WO_6 environment. Since $\mathbf{K}^{4-}$ is known to generate $\mathbf{K}_\gamma^{8-}$ at pH > 4,[18] we probed this transformation under our working conditions. Evolution of the O to W charge transfer bands around 240 nm in a pH 6.9 HEPES buffer shows that this conversion takes place over 90 minutes (Fig. S1A, ESI†) while $\mathbf{K}_\gamma^{8-}$ is stable (Fig. S1B, ESI†) in line with reported aqueous solution stability properties.[19] In the presence of Cu(II), the formation of the $[\alpha\text{-}SiW_{11}O_{39}Cu(OH_2)]^{6-}$ ($\mathbf{K_{Cu}}^{6-}$) anion from $\mathbf{K}^{4-}$ or $\mathbf{K}_\gamma^{8-}$, respectively takes about one hour or is instantaneous as attested by the kinetic monitoring of the appearance of a new band at 253 nm corresponding to the generation of the MS-POM (Fig. S1, ESI,† panels C and D). Coordination of Cu^{II} to the POM anion is also confirmed by a broad and weak d–d band with maximum at 865 nm (ε = 40 M^{-1} cm^{-1}) and an EPR spectrum characteristic of a Cu^{II} ion lying in a D_{4h} geometry surrounded by five oxygen atoms from the POM and a water molecule (Fig. 1A and C), in line with literature.[20]

Once the ability of $\mathbf{K}^{4-}$ and $\mathbf{K}_\gamma^{8-}$ to coordinate Cu(II) was checked, their ability to retrieve Cu(II) bound to Aβ was studied. The evolution of the characteristic d–d band of the Cu(Aβ) complex at 625 nm was followed by UV-vis spectroscopy after the addition of either $\mathbf{K}_\gamma^{8-}$ or $\mathbf{K}^{4-}$ (Fig. 1, panels A and B). The observed full disappearance of the Cu(Aβ) signature indicates that both POMs can completely remove Cu(II) from the peptide to form the $\mathbf{K_{Cu}}^{6-}$. While the removal has a time of half completion of 40 minutes with $\mathbf{K}^{4-}$, it is instantaneous with $\mathbf{K}_\gamma^{8-}$. This was also observed by EPR, where $\mathbf{K}^{4-}$ completely removes Cu^{II} from Aβ after a 3 hours incubation time while the EPR spectrum measured just after addition of $\mathbf{K}_\gamma^{8-}$ to a Cu(Aβ) solution shows already signatures of the $\mathbf{K_{Cu}}^{6-}$ as a largely predominant species (Fig. 1, panel C).

The thorough inspection of the UV-Vis but mainly the EPR spectrum of the complex formed by the addition of $\mathbf{K}^{4-}$ or $\mathbf{K}_\gamma^{8-}$ to Cu(Aβ) slightly differs from that of the *in situ* generated $\mathbf{K_{Cu}}^{6-}$ (without Aβ). An additional small peak at 335 mT is indeed detected (Fig. 1, panel C, blue vertical line). Linear combinations of the EPR spectra of Cu(Aβ) and $\mathbf{K_{Cu}}^{6-}$, which could mirror the incomplete removal of Cu^{II} from Aβ by the POMs, failed to reproduce this EPR signal thus pointing strongly toward the formation of a ternary species. We propose that this species corresponds to a complex between $\mathbf{K_{Cu}}^{6-}$ and Aβ, where Aβ may bind the Cu^{II} ion on its sixth labile position. This is confirmed by the increase of the relative intensity of the peak induced by the presence of higher ratio of Aβ *versus* $\mathbf{K_{Cu}}^{6-}$ (Fig. 1, panel C). This proposition is in line with the lability of the water molecule bound to the MS-POMs,[21] and with reported interaction of Cu^{II} in MS-POM with the imidazole from histidine side-chains of Aβ peptides.[17]

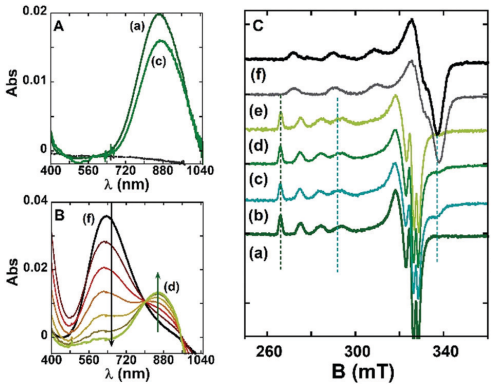

Fig. 1 (A) UV-Vis spectra of Cu^{II} + $\mathbf{K}_\gamma^{8-}$ (a, dark green) and Cu(Aβ) + $\mathbf{K}_\gamma^{8-}$ -(c, green), (B) Kinetic monitoring of Cu(Aβ) + $\mathbf{K}^{4-}$; (f, black) starting spectrum and (d, green) last spectrum, once the reaction is completed. Spectrum measured at 5 (brown), 20 (red), 40 (dark orange), 70 (light brown), 110 (dark brown) and 170 minutes (light green, d) after the addition of $\mathbf{K}^{4-}$ to Cu(Aβ). Conditions: [$Aβ_{16}$] = [$\mathbf{K}^{4-}$] = 500 μM, [Cu^{II}] = 450 μM, [HEPES] = 100 mM pH 6.9, ℓ = 1 cm, under stirring, T = 25 °C. (C) EPR spectra of: Cu(Aβ) (f, black); Cu(Aβ) + $\mathbf{K}^{4-}$ at t_0 (e, grey) and t_f (d, light green); Cu(Aβ) + $\mathbf{K}_\gamma^{8-}$ (c, green, at t_0 or t_f), Cu(II) + 4 equiv. (Aβ) + 1 equiv. $\mathbf{K}_\gamma^{8-}$ (b, turquoise) and Cu(II) + $\mathbf{K}_\gamma^{8-}$ (a, dark green). Spectra at t_0 were taken just after the addition of $\mathbf{K}_\gamma^{8-}$ or $\mathbf{K}^{4-}$ to the Cu(Aβ) solution, and after 1 day of incubation for t_f. Conditions: [$Aβ_{16}$] = [$\mathbf{K}_\gamma^{8-}$ or $\mathbf{K}^{4-}$] = 200 μM, [$^{65}Cu^{II}$] = 180 μM, [HEPES] = 100 mM pH 6.9, 10% glycerol as cryoprotectant. ν = 9.47 GHz, T = 120 K, microwave power = 20 mW, modulation amplitude = 0.5 mT.

Since $\mathbf{K}^{4-}$ and $\mathbf{K}_\gamma^{8-}$ can bind Cu^{II}out from the Aβ peptide, their ability to stop the Cu(Aβ)-induced ROS production was assayed, using a well-established ascorbate (Asc) consumption experiment that mirrors the production of ROS.[22] Briefly, under aerobic conditions, Asc fuels the incomplete reduction of dioxygen and thus the formation of ROS. The Asc consumption is catalysed by the presence of Cu^{II} or Cu^{II}(Aβ) leading to the decrease of the absorbance at 265 nm (corresponding to Asc, ε = 14 500 M^{-1} cm^{-1}). Two experiments were performed, either starting from the +II redox state and including a short incubation with the POM (*ca.* 60 s) or with the POM added in the course of Asc consumption (when absorbance equals 1), thus in presence of both Cu^{I} and Cu^{II} ions. $\mathbf{K}_\gamma^{8-}$ can prevent the Asc

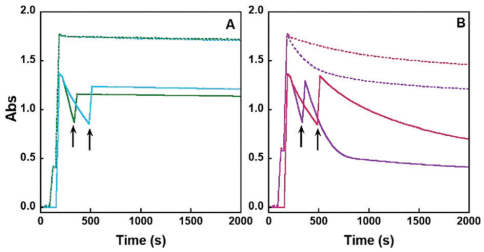

Fig. 2 Absorption (measured at 265 nm) monitoring of the effect $\mathbf{K}_{\gamma}^{8-}$ (panel A) and $\mathbf{K}^{4-}$ (panel B) on Cu^{II} and $Cu^{II}(A\beta)$-induced Asc consumption. (A) dotted lines: data with Cu^{II} (green) and $Cu^{II}(A\beta)$ (blue) incubated first with $\mathbf{K}_{\gamma}^{8-}$ during 60 s; plain lines: data with $\mathbf{K}_{\gamma}^{8-}$ added when Abs is at *ca.* 1 (indicated by arrows), during Asc consumption. Before POM addition the curves corresponds to Asc consumption by Cu^{II} and $Cu^{II}(A\beta)$. (B) Dotted lines: data with Cu^{II} (purple) and $Cu^{II}(A\beta)$ (pink) incubated first with $\mathbf{K}^{4-}$ during 60 s; plain lines: data with $\mathbf{K}^{4-}$ added when Abs is at *ca.* 1, during Asc consumption. $[A\beta_{16}] = [\mathbf{K}_{\gamma}^{8-}, \mathbf{K}^{4-}] = 10\ \mu M$, $[Cu^{II}] = 9\ \mu M$, [HEPES] = 100 mM pH 6.9, $\ell = 1$ cm, $T = 25\ ^{\circ}C$.

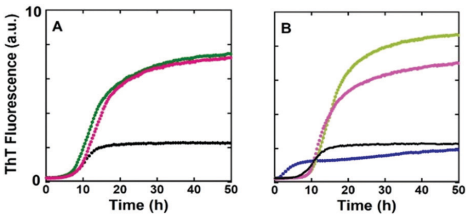

Fig. 3 Selection of representative ThT curves of the $A\beta_{1-40}$ peptide (A) or the $Cu(A\beta_{40})$ complex (B) in absence or presence of POMs. Panel A: apo-$A\beta_{40}$ (black), $A\beta_{40}$ + 1 equiv. $\mathbf{K}^{4-}$ (pink), $A\beta_{40}$ + 1 equiv. $\mathbf{K}_{\gamma}^{8-}$(green). Panel B: $Cu(A\beta_{40})$ (blue) formed at 0.9 equiv. of Cu^{II}, $Cu(A\beta_{40})$ + 1 equiv. $\mathbf{K}^{4-}$ (light green), $Cu(A\beta_{40})$ + 1 equiv. $\mathbf{K}_{\gamma}^{8-}$ (light pink) and apo-$A\beta_{40}$ (black) for direct comparison. Conditions: $[A\beta_{40}] = 20\ \mu M$, $[\mathbf{K}_{\gamma}^{8-}$ or $\mathbf{K}^{4-}] = 0$ or 20 μM, $[Cu^{II}] = 0$ or 18 μM, [ThT] = 10 μM, [EDTA] = 0.1 μM, [HEPES] = 50 mM, pH 6.9, T = 37 °C. The pH, controlled after the completion of the aggregation process, remains at 6.9 for all conditions. All the curves corresponding to this experiment (noted N°1), are given in the ESI† along with simulated curves.

consumption, both starting from Cu^{II} and $Cu^{II}(A\beta)$ or when added in the course of the experiment. There is indeed no decrease in the Asc UV band in presence of $\mathbf{K}_{\gamma}^{8-}$ (Fig. 2, panel A)w. In contrast, $\mathbf{K}^{4-}$ is active only if incubated before Asc addition (Fig. 2, panel B), in line with the longer time required to form $\mathbf{K}_{Cu}^{6-}$.

In addition to its participation to oxidative stress, Cu^{II} also affects the aggregation path of the Aβ peptide.[23] The self-assembly of Aβ is a very complex and multi-step mechanism, which can be viewed as a nucleation–elongation supramolecular assembly, in which secondary nucleation by formed amyloids takes a predominant part.[24,25] The low molecular weight intermediates present during the aggregation are currently regarded as the most toxic species (compared to the starting monomer and the final fibrils) and Cu^{II} has been proposed to promote their formation.[26] To monitor Aβ aggregation, the thioflavin-T (ThT) fluorescence screening assay was used,[27] and the morphology of the aggregates formed was observed after 6 days using transmission electronic microscopy (TEM). Note that as recently pointed out, due to the intrinsic auto-catalytic nature of the aggregation process, the reproducibility of aggregation experiments is fairly weak.[28] To secure robust results, we have thus repeated several times the aggregation assays and have changed several environmental parameters, mainly to avoid the so-called "batch-dependent" effect. The results are described based on the data shown in Fig. 3 that are representative of the trends observed in all the experiments, and the range of values of the key kinetic parameters of the 3 mathematically-analysed experiments are given in Table S1 (ESI†) (see also Fig. S2, ESI† for an illustration of the fitting). The aggregation curves for the apo-Aβ peptide§ show the expected sigmoidal shape (Fig. 3, black line) characteristic of amyloids formation,[25,28] with the time evolution of the fluorescence intensity being described by

$$F(t) = \frac{\Delta F}{\left(1 + e^{-k\left(t - t_{1/2}\right)}\right)} \quad (1)$$

$t_{1/2}$ is the time necessary to reach half of ΔF, the variation of ThT fluorescence intensity; k is the growth rate mirroring the formation of fibrils. Overall, in presence of $\mathbf{K}_{\gamma}^{8-}$ or $\mathbf{K}^{4-}$, the maximum of fluorescence intensity is increased by about 2 to 3-fold and the $t_{1/2}$ is increased by about 10 to 20% compared to Aβ (Fig. 3, panel A). The important increase in the final fluorescence reflects the formation of more fibrils and/or the formation of more ordered fibrils inducing a higher enhancement of the ThT fluorescence. No statistically-meaningful differences were observed between $\mathbf{K}_{\gamma}^{8-}$ or $\mathbf{K}^{4-}$ in line with the quite rapid evolution of $\mathbf{K}^{4-}$ to $\mathbf{K}_{\gamma}^{8-}$ compared to the time scale of the aggregation (Table S1, ESI†). By TEM (Fig. S3, ESI†), the pictures show long and twisted Aβ fibrils in absence of POM; while in presence of POM, more abundant and longer fibrils are observed. In presence of Cu^{II}, the aggregation curve shows a two-step path where the ThT fluorescence increases during the first five hours followed by a second ill-defined and smooth sigmoid-like increase. The resulting fluorescence is weaker than in absence of Cu^{II} by about 15%. This kinetic profile is reminiscent of published data on Cu^{II} modulation of Aβ aggregation,[23] and mirrors the formation of less-ordered aggregates. In presence of $\mathbf{K}_{\gamma}^{8-}$ or $\mathbf{K}^{4-}$, the kinetic of the ThT fluorescence is dramatically changed with curves that resemble those obtained upon addition of $\mathbf{K}_{\gamma}^{8-}$ or $\mathbf{K}^{4-}$ on the apo Aβ (Fig. 3, panel B). In the TEM pictures, in presence of Cu^{II}, the Aβ fibrils are shorter, thicker and less abundant than with the apo-peptide, but in presence of POM very long and thin fibrils are recovered. This indicates that the *in situ* generated $\mathbf{K}_{Cu}^{6-}$ has a similar effect on Aβ aggregation than its apo counterparts, $\mathbf{K}_{\gamma}^{8-}$ or $\mathbf{K}^{4-}$, *id est* redirecting the Aβ aggregation towards more fibrillar species. Deeper inspection of the ThT fluorescence curves reveals that the $t_{1/2}$ value of the Cu(Aβ) aggregation in presence of $\mathbf{K}_{\gamma}^{8-}$ or $\mathbf{K}^{4-}$ is increased by about 20% (Table S1, ESI†) compared to those of Aβ in presence of $\mathbf{K}_{\gamma}^{8-}$ or $\mathbf{K}^{4-}$. Hence, the *in situ* generated $\mathbf{K}_{Cu}^{6-}$ has a slightly increased ability to delay Aβ self-assembly effect compared $\mathbf{K}_{\gamma}^{8-}$ (or $\mathbf{K}^{4-}$). This may be linked to the difference in the net charge and/or in the possibility to form coordination bond between $\mathbf{K}_{Cu}^{6-}$ (but not $\mathbf{K}_{\gamma}^{8-}$ nor $\mathbf{K}^{4-}$) and some of the amino-acid

side chains of the Aβ peptide. Under our working conditions, $\mathbf{K}_{\gamma}^{8-}$/$\mathbf{K}^{4-}$ and $\mathbf{K}_{\mathbf{Cu}}^{6-}$ interact with Aβ promoting the formation of highly ordered fibrils. This is different to previous data on other POMs and MS-POMs, which were shown to reduce ThT intensity by 40 to 80% depending on the substituted cations.[15,17] The origin of such discrepancy has to be understood but will require an in-depth investigation of the modes of interaction of POM with Aβ peptide (currently under investigation) that is beyond the scope of the present communication, while the exact nature of the POM and different working conditions may be part of the explanation. The enhancement of amyloid formation is however highly reminiscent to what has been observed for linear polyphosphates, a biological polyanion.[29] The most remarkable effect of the studied POMs on Cu^{II} modulated Aβ aggregation is their double mode of action. Indeed they (i) remove Cu^{II} from Aβ preventing the formation of ill-defined Cu(Aβ) aggregates, regarded as the most deleterious with respect to AD,[30] and (ii) then the *in situ* generated $\mathbf{K}_{\mathbf{Cu}}^{6-}$ reshapes the aggregation kinetic and species towards a better defined sigmoidal process and the formation of mature fibrils, respectively. Most of the ligands reported in the literature can restore apo-aggregation if they are able to retrieve Cu^{II} from Aβ,[31] but have no additional effect.

In summary, our results provide new insights on the use of POMs in the context of AD. Their ability to coordinate Cu^{II} out of the Aβ was first assessed: $\mathbf{K}_{\gamma}^{8-}$ is readily effective, while $\mathbf{K}^{4-}$ needs first to lose one WO^{4+} unit to form $\mathbf{K}_{\gamma}^{8-}$. Once the $\mathbf{K}_{\mathbf{Cu}}^{6-}$ has formed, a redox inert and stable complex is obtained. Both POMs induce the formation of more-ordered Aβ aggregates (higher β-sheet contents) including in the presence of Cu^{II}. Hence the two POMs studied here fulfil criteria to be appropriate Cu^{II} chelators in the context of AD. Indeed preventing Cu^{II} interaction with Aβ is of interest for metal-based therapy against AD, as this prevents the formation of toxic oligomers and the deleterious production of ROS. In fact, the POMs studied ''kill two birds with one stone'' since they not only stop Cu(Aβ) ROS production but also redirect aggregation towards mature fibrils regardless of the presence of Cu. Previous studies have shown that POMs do not produce toxicity and are capable of passing the blood–brain barrier.[17] Therefore, $\mathbf{K}^{4-}$ and $\mathbf{K}_{\gamma}^{8-}$ could be promising drug candidates. The effects of POMs with different shape/size both on prevention of Cu^{II}- and Cu^{II}(Aβ)-induced ROS and on the modulation of Aβ assembly are currently under study in our group.

Dr V. Borghesani is acknowledged for her participation in recording preliminary data. E. A. B., L. de C, L. S. and C. H. thank the ERC StG grant 638712, aLzINK for financial support.

Conflicts of interest

There are no conflicts to declare.

Notes and references

§ The shorter $A\beta_{16}$ peptide has been used as a valuable model for Cu(II) binding to the full length $A\beta_{40}$ or $A\beta_{42}$ peptides for the experiments studying the coordination and the ROS production. The longer $A\beta_{40}$ peptide has been used for the experiments involving aggregation. No differences between the short and full-length Aβ peptides have been observed for their binding Cu(II) coordination, binding affinity or ROS production.[5]

1 Alzheimer's Association, Facts and Figures, https://www.alz.org/alzheimers-dementia/facts-figures.
2 E. Atrian-Blasco, P. Gonzalez, A. Santoro, B. Alies, P. Faller and C. Hureau, *Coord. Chem. Rev.*, 2018, **375**, 38.
3 Z. L. Almeida and R. M. M. Brito, *Molecules*, 2020, **25**, 1195.
4 T. J. Huat, J. Camats-Perna, E. A. Newcombe, N. Valmas, M. Kitazawa and R. Medeiros, *J. Mol. Biol.*, 2019, **431**, 1843.
5 C. Hureau in *Alzheimer's Disease: Recent Findings in Pathophysiology, Diagnostic and Therapeutic Modalities*, ed. T. Govindaraju, The Royal Society of Chemistry, 2021, p. in press.
6 C. Cheignon, M. Jones, E. Atrian-Blasco, I. Kieffer, P. Faller, F. Collin and C. Hureau, *Chem. Sci.*, 2017, **8**, 5107.
7 L. S. Van Rompuy and T. N. Parac-Vogt, *Curr. Opin. Biotechnol*, 2019, **58**, 92.
8 A. Bijelic, M. Aureliano and A. Rompel, *Angew. Chem., Int. Ed.*, 2019, **58**, 2980.
9 N. I. Gumerova and A. Rompel, *Inorg. Chem.*, 2021, **60**, 6109.
10 M. Arefian, M. Mirzaei, H. Eshtiagh-Hosseini and A. Frontera, *Dalton Trans.*, 2017, **46**, 6812.
11 P. Gao, Y. Wu and L. Wu, *Soft Matter*, 2016, **12**, 8464.
12 D. J. Levine, J. Stöhr, L. E. Falese, J. Ollesch, H. Wille, S. B. Prusiner and J. R. Long, *ACS Chem. Biol.*, 2015, **10**, 1269.
13 A. Bijelic and A. Rompel, *Coord. Chem. Rev.*, 2015, **299**, 22.
14 Y. Zhou, L. Zheng, F. Han, G. Zhang, Y. Ma, J. Yao, B. Keita, P. de Oliveira and L. Nadjo, *Colloids Surf., A*, 2011, **375**, 97.
15 J. Geng, M. Li, J. Ren, E. Wang and X. Qu, *Angew. Chem., Int. Ed.*, 2011, **50**, 4184.
16 Q. Chen, L. Yang, C. Zheng, W. Zheng, J. Zhang, Y. Zhou and J. Liu, *Nanoscale*, 2014, **6**, 6886.
17 N. Gao, H. Sun, K. Dong, J. Ren, T. Duan, C. Xu and X. Qu, *Nat. Commun.*, 2014, **5**, 3422.
18 G. Hervé, A. Tézé and R. Contant, in *Polyoxometalate Molecular Science*, ed. J. J. Borrás-Almenar, E. Coronado, A. Müller and M. Pope, Springer, Netherlands, Dordrecht, 2003, p. 33.
19 N. I. Gumerova and A. Rompel, *Chem. Soc. Rev.*, 2020, **49**, 7568.
20 G. Scholz, R. Lück, R. Stößer, H.-J. Lunk and F. Ritschl, *J. Chem. Soc., Faraday Trans.*, 1991, **87**, 717.
21 J. A. Gamelas, I. C. M. S. Santos, C. Freire, B. de Castro and A. M. V. Cavaleiro, *Polyhedron*, 1999, **18**, 1163.
22 B. Alies, I. Sasaki, O. Proux, S. Sayen, E. Guillon, P. Faller and C. Hureau, *Chem. Commun.*, 2013, **49**, 1214.
23 M. G. M. Weibull, S. Simonsen, C. R. Oksbjerg, M. K. Tiwari and L. Hemmingsen, *J. Biol. Inorg. Chem.*, 2019, **24**, 1197.
24 M. Törnquist, T. C. T. Michaels, K. Sanagavarapu, X. Yang, G. Meisl, S. I. A. Cohen, T. P. J. Knowles and S. Linse, *Chem. Commun.*, 2018, **54**, 8667.
25 G. Meisl, J. B. Kirkegaard, P. Arosio, T. C. T. Michaels, M. Vendruscolo, C. M. Dobson, S. Linse and T. P. J. Knowles, *Nat. Protoc.*, 2016, **11**, 252.
26 M. Rana and A. K. Sharma, *Metallomics*, 2019, **11**, 64.
27 S. Noël, S. Cadet, E. Gras and C. Hureau, *Chem. Soc. Rev.*, 2013, **42**, 7747.
28 P. Faller and C. Hureau, *Front. Chem.*, 2021, **8**, 1236.
29 C. M. Cremers, D. Knoefler, S. Gates, N. Martin, J.-U. Dahl, J. Lempart, L. Xie, M. R. Chapman, V. Galvan, D. R. Southworth and U. Jakob, *Mol. Cell*, 2016, **63**, 768.
30 S. J. C. Lee, E. Nam, H. J. Lee, M. G. Savelieff and M. H. Lim, *Chem. Soc. Rev.*, 2017, **46**, 310.
31 C. Esmieu, D. Guettas, A. Conte-Daban, L. Sabater, P. Faller and C. Hureau, *Inorg. Chem.*, 2019, **58**, 13509.

